

CONFORMAL SYMMETRIES
AND
CONSTRAINED CRITICAL PHENOMENA

PROEFSCHRIFT

ter verkrijging van de graad van doctor
aan de Technische Universiteit Delft,
op gezag van de Rector Magnificus prof. dr. ir. J. T. Fokkema,
voorzitter van het College voor Promoties,
in het openbaar te verdedigen op dinsdag 14 december 2004 om 10:30 uur
door

Youjin DENG

Master of Science (Beijing Normal University),
geboren te Zhangping, Fujian (P.R. China)

Dit proefschrift is goedgekeurd door de promotor:

Prof. dr. H. W. J. Blöte

Samenstelling promotiecommissie:

Rector Magnificus,	voorzitter
Prof. dr. H. W. J. Blöte,	Technische Universiteit Delft, promotor
Prof. dr. J. M. J. van Leeuwen,	Technische Universiteit Delft
Prof. dr. F. Y. Wu,	Northeastern University, USA
Prof. dr. B. Nienhuis,	Universiteit van Amsterdam
Prof. dr. H. W. F. Knops,	Katholieke Universiteit Nijmegen
Prof. dr. I. M. de Schepper,	Technische Universiteit Delft
Dr. J. R. Heringa,	Technische Universiteit Delft

Published and distributed by:

Delft University Press

Mekelweg 4

2628 CD Delft

The Netherlands

Copyright ©2004 by Youjin Deng

ISBN 90-407-2548-9

Preface

This book presents my research in the past four years during my stay in the Computational Physics Group of the Faculty of Applied Sciences (the first two years) and later in the Theoretical Physics Group at the same Faculty. It covers a number of subjects in the field of critical phenomena, including 1), a systematic test of the three-dimensional (3D) Ising universality class, 2), cluster simulations of quantum transverse q -state Potts models, 3), simulations in curved geometries and conformal symmetries in $d > 2$ dimensions, 4), constrained critical and tricritical phenomena, 5), spontaneous edge order of the 2D Potts model, 6), Monte Carlo investigations of backbone exponents, and 7), geometric properties of 2D and 3D Potts models, etc.

During this research, several novel computer algorithms were developed and applied. Even though the computer power has increased rapidly over the past decades, efficient algorithms still play an important role in the numerical study of phase transitions. On the other hand, I feel that numerical work is an efficient approach to solve physical problems only if it is combined with theoretical knowledge. Subjects 5) and 7), which arose from my curiosity in predictions by the Coulomb gas theory and conformal field theory, serve as two good examples. Naturally, my insight in the renormalization group theory and in critical phenomena has increased over time and by the research activities.

These scientific activities and achievements make my life full of joy and happiness.

Youjin Deng

Contents

1	Introduction and outline	1
1.1	Examples of phase transitions	1
1.2	The renormalization group theory	2
1.3	Conformal field theory	2
1.4	Outline	3
2	Simultaneous analysis of three-dimensional Ising models	11
2.1	Introduction	11
2.2	Models and algorithms	13
2.3	Dimensionless ratio Q	14
2.4	Other quantities	18
2.5	Discussion	20
	Bibliography	21
3	Cluster simulation of the transverse Ising model	25
3.1	Introduction	25
3.2	Anisotropic limit of the Ising model	26
3.3	Algorithm	28
3.4	Test of the algorithm	30
3.5	Applications	33
	3.5.1 Critical points of several TIM's	33
	3.5.2 The Binder ratio and the determination of the length scale	34
	Bibliography	35
4	Conformal invariance: The Ising model	37
4.1	The Ising model on a spheroid	37
	4.1.1 Introduction	37
	4.1.2 Conformal mappings	38
	4.1.3 Exact calculations	41
	4.1.4 Models and algorithms	43
	4.1.5 Numerical results	46
	4.1.6 Discussion	50
4.2	Bulk and surface criticality: three-dimensional Ising model	51
	4.2.1 Introduction	51
	4.2.2 Conformal mappings	52

4.2.3	Models and algorithms	53
4.2.4	Numerical results	55
4.2.5	Discussion	60
	Bibliography	61
5	Conformal invariance: The percolation model	63
5.1	Introduction	63
5.2	Models and algorithms	64
5.2.1	Quantum transverse q -state Potts models	64
5.2.2	Algorithms	66
5.3	Simulations in flat geometries	68
5.3.1	Two dimensions	68
5.3.2	Three dimensions	69
5.3.3	Restoration of isotropy	69
5.4	Conformal invariance	70
5.5	Simulations in curved geometries	73
5.5.1	Monte Carlo methods in curved geometries	73
5.5.2	Numerical results	74
5.6	Discussion	76
	Bibliography	76
6	Critical phenomena under energy-like and magnetic constraints	79
6.1	Introduction	79
6.2	Models and sampled quantities	80
6.2.1	The Blume-Capel model	81
6.2.2	Baxter's hard-core lattice gases	81
6.2.3	Two-dimensional Potts model with vacancies	81
6.2.4	Data sampled	82
6.3	Results for energy-like constraints	82
6.3.1	Hard-hexagon lattice gas	83
6.3.2	Critical Blume-Capel model	85
6.3.3	Dilute $q = 4$ Potts model	85
6.4	Results for magnetic constraints	87
6.4.1	Critical Ising model	87
6.4.2	Critical $q = 3$ Potts model	87
6.4.3	Tricritical Blume-Capel model	88
6.4.4	Tricritical $q = 3$ Potts model	88
6.4.5	Dilute $q = 4$ Potts model	88
6.5	Finite-size scaling in the presence of a constraint	90
6.5.1	Energy-like constraint	90
6.5.2	Magnetic constraint	90
6.6	Discussion	93
	Bibliography	94
7	Constrained tricritical Ising model in three dimensions	97
7.1	Introduction	97
7.2	Mean-field Blume-Capel model	100
7.2.1	Unconstrained systems	100
7.2.2	Monte Carlo simulations	102
7.2.3	Constrained systems	104
7.3	Fisher renormalization mechanism at tricriticality	104
7.4	Monte Carlo simulations	106

7.4.1	Unconstrained BC model	106
7.4.2	Constrained BC model	108
7.5	Discussion	112
	Bibliography	113
8	Constrained tricritical phenomena in two dimensions	115
8.1	Introduction	115
8.2	Models, simulations, and sampled quantities	117
8.2.1	Models	117
8.2.2	Monte Carlo methods	119
8.2.3	Sampled quantities	119
8.3	Finite-size scaling behavior in constrained systems	120
8.4	Results	122
8.4.1	Tricritical $q = 1$ Potts model	122
8.4.2	Tricritical Blume-Capel model	123
8.4.3	Baxter's hard-square model	128
8.4.4	Tricritical $q = 3$ Potts model	129
8.4.5	Dilute $q = 4$ Potts model	130
8.5	Discussion	131
	Bibliography	133
9	Monte Carlo study of backbone exponents	135
9.1	The q -state Potts model in two dimensions	135
9.1.1	Introduction	135
9.1.2	Models	137
9.1.3	Algorithms	138
9.1.4	Results	141
9.1.5	Discussion	145
9.2	The percolation and the Ising model in three dimensions	145
9.2.1	Introduction	145
9.2.2	Models	147
9.2.3	Results	148
9.2.4	Discussion	150
	Bibliography	151
10	Geometric properties of Potts configurations	155
10.1	The critical and tricritical Potts model in two dimensions	155
10.1.1	Introduction	155
10.1.2	General analysis	156
10.1.3	Monte Carlo investigation	161
10.1.4	Discussion	164
10.2	The critical and the tricritical Ising model in three dimensions	167
10.2.1	Introduction	167
10.2.2	Monte Carlo methods and sampled quantities	170
10.2.3	Results	171
10.2.4	Discussion	174
	Bibliography	174

11 Edge transitions of two-dimensional tricritical Potts models	177
11.1 Introductions	177
11.2 Dilute 1-state Potts model	180
11.3 Blume-Capel model	181
11.3.1 Bulk criticality $K < K_t$	183
11.3.2 Bulk tricriticality: $K = K_t, D = D_t$	184
11.3.3 Bulk first-order range: $K > K_t$	191
11.4 Tricritical 3-state Potts model	193
11.4.1 Special phase transitions	193
11.4.2 Field-driven edge transitions	193
11.5 Discussion	194
Bibliography	196
Curriculum Vitae	201

Introduction and outline

1.1 Examples of phase transitions

Nature is full of phase transitions. Well-known examples are contained in the phase diagram in the material H_2O , as sketched in Fig. 1.1(a). The material H_2O can be a solid (ice), a liquid, or a vapor; transitions between different phases can be induced by changing the temperature T or the pressure P . From our everyday experience, the liquid and the vapor phase coexist at $T = 373^\circ\text{K}$ and $P = 1 \text{ atm}$. Thus, at this point, the density ρ of H_2O is not fixed but can have a high value (liquid) or a low value (vapor). The transition is said to be *first-order*, because ρ , which can be expressed as the first derivative of the free energy density, has a discontinuity. However, as T increases, this density difference becomes smaller along the transition line, and at some point it vanishes completely. This point is named the *critical* point, and the associated phenomena are referred to as *critical phenomena*. Another example is the ferromagnetic state of materials like iron and nickel, of which the phase diagram is sketched in Fig. 1.1(b). At low temperature, the material is in the ferromagnetic state: a spontaneous magnetization m exists. The magnetization m can point in different directions when the external magnetic field h is zero. As T increases, the magnitude of m becomes smaller, and vanishes at the Curie temperature T_c . For $T > T_c$, the material becomes paramagnetic: $m = 0$ for $h = 0$. The Curie point is the ferromagnetic critical point.

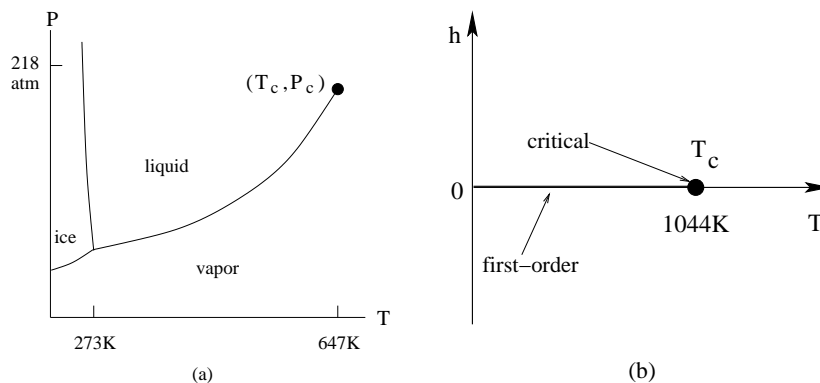


Figure 1.1: (a) The liquid-vapor critical point of H_2O : $T_c = 647^\circ\text{K}$ and $P_c = 218 \text{ atm}$. (b). The ferromagnetic point of Fe: $T_c = 1044^\circ\text{K}$, $h_c = 0$.

There are many other kinds of critical points, such as the antiferromagnetic critical point of Cs_3CoCl_5 , the superfluid critical point of liquid helium, and the superconductivity critical points of many metals and alloys. It turns out that the asymptotic behavior near a critical point can be described by a limited number

of critical indices. For instance, at the ferromagnetic critical point, the magnetization m , referred to as the order parameter, vanishes *algebraically* as

$$|m| \propto (T_c - T)^\beta, (T \uparrow T_c, h = 0), \quad \text{and} \quad m \propto h^{1/\delta}, (T = T_c). \quad (1.1)$$

The magnetic susceptibility $\chi = (\partial m / \partial h)_T$ and the specific heat C diverge with a power law

$$\chi \propto (T_c - T)^{-\gamma} \quad \text{and} \quad C \propto (T_c - T)^{-\alpha} \quad (h = 0). \quad (1.2)$$

The critical exponents, α , β , γ , and δ , are generally not integers, i.e., critical behavior is *singular*. Moreover, it turns out that these exponents are *universal*: various kinds of critical models can share a common set of critical exponents. For instance, the critical points in Fig. 1.1 (a) and (b) are believed to belong to the same universality class.

The universal properties of the transitions in Fig. 1.1 (a) and (b) are named after the Ising model, and those of the superfluid transitions are said to be described by the XY model.

1.2 The renormalization group theory

For the simplified models such as the aforementioned Ising and the XY model, typically, there are two approaches:

(1), direct solution approach. This means calculation of physical quantities of interest in terms of parameters, i.e., solving the model. The calculation may be done analytically or numerically, exactly or approximately.

(2), exploiting symmetries and/or approximations. This approach tries to deduce some characteristics of physical quantities from various symmetry operations, e.g., reflections, translations, and rotations.

The approach (1) is often a very difficult task. While (2) is not a substitute for (1), a great deal can be learned from (2) even without attempting (1). Onsager's solution of the two-dimensional Ising model is an example of (1), and the mean-field theory is an example of (2).

The contemporary physics of critical phenomena started with the invention of the renormalization group (RG) theory. This technique also takes approach (2): the renormalization group is a set of symmetry transformations. The essence of the RG is the hypothesis of the *scale invariance* at a critical point. This can be phenomenologically understood as follows. Consider a sample of magnetic material. At low temperature, a large fraction of magnetic spins points in the same direction. As T increases, this fraction is reduced, and it vanishes at the critical temperature T_c . However, for $T = T_c$, there are large patches (much larger than crystal unit cells) in which a net fraction of spins are lined up. The distribution of the sizes of these patches has a diverse range, such that, in principle, *all length scales* occur. Suppose that we look at this material through a microscope, and that our eyes can see spin variations down to a size b . If the sample is shrunk by a factor s , we shall *not see any change* at criticality if the sample is sufficiently large.

In other words, critical fluctuations occur at all length scales, and the correlation length, which measures the size of the largest fluctuations, *diverges*. In the momentum space, the RG deals with one length scale at one time: the short-distance fluctuations are integrated out, and then the remaining part of the Hamiltonian is rescaled. Upon iteration, this Hamiltonian approaches a fixed point, and universality emerges from the existence of such fixed points in the space of Hamiltonians.

Since the invention of the RG, enormous progress has been achieved in the understanding of phase transitions. In two dimensions, an important application is the Coulomb gas theory. This theory transforms a number of two-dimensional models into an electromagnetic Coulomb gas model. Then, a hierarchy of critical exponents can be expressed in terms of a *single* parameter. These models include the q -state Potts model, the anti-ferromagnetic Potts model, the $O(n)$ model, and frustrated Ising models, etc.

1.3 Conformal field theory

Besides RG transformations, a larger group of symmetry operations, the *conformal* transformations, can be applied to critical phenomena. Roughly speaking, a conformal mapping is a generalization of a scale

transformation in which the length-rescaling factor depends continuously on position; it can be further understood as a combination of the *local* scale and rotation transformations. The connection between scale and conformal invariance has been known to field theorists for a long time. In two dimensions, the conformal group algebra had been studied in the late 1960s by particle theorists in the context of the dual string model, where it was known as the Virasoro algebra. The connection of such quantum field theories and statistical mechanics close to a critical point has been proved to be very fruitful. It was shown, by Belavin, Polyakov, and Zamolodchikov, that each ‘primary’ scaling operator of a two-dimensional system at criticality corresponds to a representation of the Virasoro algebra. If these representations are of a particularly simple kind, corresponding to the vanishing of a certain quantity called the Kac determinant, then not only the critical exponents but all the multi-point correlation functions at criticality can be obtained. Further, Friedan, Qiu, and Shenker showed that these representations are indeed allowed, if the theory is to be unitary and if a certain quantity c called the conformal anomaly satisfies $c < 1$. In two dimensions, the conformal field theory has already predicted a series of exact values, listed in the so-called Kac table, for a number of critical systems.

Despite of their great success, the renormalization group approach and the conformal field theory still lack a firm mathematical foundation. There has been a lot of work recently by mathematicians in the context of the so-called Stochastic Loewner Evolution (SLE). The basic idea is to try to prove the physicists’ predictions for the critical exponents.

Naturally, neither the RG technique, the Coulomb gas theory, or the conformal field theory could supply the immediate solution of all outstanding problems in the field of critical phenomena. In the first place, the RG theory relies on several nontrivial assumptions, and the formalism is thus not rigorously justified, as mentioned above. Second, in general, these theories do not provide information on nonuniversal aspects of critical phenomena. Third, although the basic abstract ideas of the RG are easy to understand, to carry out these ideas and verify them turns out to be difficult. Furthermore, although these theories have yielded a large amount of exact information for two-dimensional critical systems, exact information is still very scarce for spatial dimensionality $d > 2$. An alternative tool is provided by computer simulations, of which the application has been greatly stimulated by the rapid development of the computer technology. It is even considered that, together with theoretical and experimental physics, computational physics form a triangular framework in the research of modern physics.

However, since numerical investigations are restricted to systems with finite extent, the diverging correlation length at a critical point is truncated, such that critical singularities are rounded off. Due to the scale invariance at criticality, the linear size of a finite system can be simply regarded as a scaling field in the RG approach. The corresponding theory is called the *finite-size scaling* theory, in which the finite-size dependence of physical quantities is derived at and near a critical point.

1.4 Outline

This thesis is organized on the basis of a number of drafts which have been published or are intended for publication. As a consequence, there exists some redundancy in related chapters.

In Chapter 2, the universality hypothesis is systematically tested for eleven three-dimensional lattice models believed to be in the Ising universality class by means of Monte Carlo methods and finite-size scaling. After verification of this hypothesis within narrow numerical margins, we assume that universality holds exactly. Then, we can analyze the numerical data near the critical points of these systems simultaneously such that the universal parameters occur only once. As an example, we consider the dimensionless ratio $Q = \langle m^2 \rangle^2 / \langle m^4 \rangle$, where m is the profile of order parameter. The finite-size dependence of this ratio near criticality can be expressed as

$$Q(t, v, L) = Q^{(0,0)} + Q^{(1,0)} t L^{y_t} + Q^{(2,0)} t^2 L^{2y_t} + Q^{(0,1)} v L^{y_i} + \dots, \quad (1.3)$$

where L is the linear system size, and t and v are the relevant and irrelevant thermal fields, respectively. The renormalization exponents of t and v are denoted as y_t and y_i , respectively. The scaling fields, t and v , are analytical functions of physical parameters, and the amplitudes can assume different values in different

systems. The symbol $Q^{(i,j)}$ represents i and j differentiations of Q with respect to t and v , respectively. In addition to the critical exponents y_t and y_i , the numbers $Q^{(i,j)}$ are also universal. Thus, they occur only once in the simultaneous fit of the Monte Carlo data. The 11 systems included in this chapter are chosen such that they reflect a wide range of positions on the critical surface in the language of the Landau-Ginzburg-Wilson description of the Ising model. This particular choice, together with the simultaneous fitting technique, yields the thermal, magnetic, and irrelevant exponents as $y_t = 1.5868(3)$, $y_h = 2.4816(1)$, and $y_i = -0.821(5)$, respectively.

In Chapter 3 we formulate a cluster Monte Carlo simulations of the quantum transverse Ising model (TIM), which is believed to be relevant to the superconductivity phase transitions. It is known that the d -dimensional quantum TIM is equivalent with the anisotropic limit of a $(d+1)$ -dimensional lattice Ising model. This equivalence was displayed by Schultz and Mattis in 1964, and later was shown in a reverse path by Suzuki using the Trotter formula. However, the numerical application of this equivalence leads to practical difficulties due to singular behavior in the anisotropic limit of the classical Ising model. When the Hamiltonian limit is approached, the coupling constant and the correlation length diverge in one direction, while the couplings in other directions vanish. In this Chapter, we increase the number of spins in the strong-coupling direction and meanwhile rescale it by a *divergent* number. This rescaling renders this direction *continuous*, while the weak-coupling dimensions remain discrete. A continuous cluster algorithm is then developed, and the efficiency is comparable to the Swendsen-Wang and the Wolff method for discrete lattices. Applications of this algorithm yield the critical points of the TIMs on several two- and three-dimensional lattices with the statistical uncertainties in the fifth decimal place.

Chapter 4 investigates the critical properties of the Ising model in curved geometries by applying conformal transformations. In particular, the conformal invariance of the Ising model is confirmed in three dimensions. In two dimensions, the consequences of conformal invariance in critical systems have been studied extensively, and a large amount of results has been achieved. A well-known example is Cardy's mapping between an infinite plane and the surface of an infinitely long cylinder, which covariantly transforms, at criticality, the algebraic decay of correlations in the plane into an exponential decay along the cylinder. Since a cylinder pseudo-one-dimensional, its numerical investigation is simpler than that of a two-dimensional plane. For spatial dimensionality $d > 2$, however, conformal transformations generally lead to curved geometries or geometries with curved boundaries. For instance, in three dimensions, Cardy's mapping transforms the infinite space \mathbb{R}^3 into a pseudo-one-dimensional geometry $S^2 \times \mathbb{R}^1$. This geometry can be obtained by extending the surface of a sphere S^2 into another dimension \mathbb{R}^1 , and is referred to as the spherocylinder in this chapter. Another example is the conformal mapping between the semi-infinite space $\mathbb{R}^{(d-1)} \times \mathbb{R}^+$ and the interiors of a unit d -dimensional sphere. This mapping can be expressed as

$$\vec{r}'/r'^2 = \vec{r}/r^2 + \hat{I}/2, \quad (1.4)$$

where \hat{I} is an arbitrary fixed unit vector in d dimensions. This formula maps spheres onto spheres, so that the d -dimensional space \mathbb{R}^d is transformed into itself. Under the mapping (1.4), the $(d-1)$ -dimensional plane $\hat{I} \cdot \vec{r} = 0$, which corresponds to a spherical surface of an infinite radius, is conformally mapped onto the surface of a unit d -dimensional sphere with the center at \hat{I} . Meanwhile, the half spaces $\hat{I} \cdot \vec{r} > 0$ and $\hat{I} \cdot \vec{r} < 0$ are transformed respectively into the interior and exterior of this unit sphere, which reduces to a unit circle for $d = 2$.

For the geometries like the spherocylinder or the unit sphere, the nonzero net curvature poses a serious obstacle for numerical investigations: a sequence of regular lattices cannot be readily accommodated. For discrete spin models, this problem can be solved by using the Hamiltonian limit of the lattice model and the continuous cluster Monte Carlo algorithm developed in Chapter 2. The key ingredient of this infinitely anisotropic model is that one of its dimensions is continuous, so that the problem of discretization for one of the lattice dimensions is avoided.

In Sec. 4.1, we describe a conformal mapping of an infinite plane in two dimensions onto a spheroid. By rotating an ellipse about the minor or the major axis, one obtains an oblate or prolate spheroid, respectively. The special cases include the surface of an infinitely long cylinder, of a sphere, and of a two-sided flat disc. The latter case is obtained when the polar diameter of the spheroid approaches zero, so that one has the interiors of two circles connected at their perimeters. Thus, this transformation includes Cardy's mapping as

a special case. From the known two- and four-point correlation functions in the plane, and the assumption of covariance of the multipoint correlations under conformal mappings, the critical value of the dimensionless ratio Q is calculated for the Ising model on the sphere and on the flat disc. Further, cluster Monte Carlo simulations are performed, and the numerical estimations of Q , determined from the finite-size scaling, agree precisely with the above exact calculations. At criticality, we also sampled two- and one-point correlation functions on spheroids and half spheroids, respectively. The thermal and magnetic exponents, as obtained from the numerical data and the prediction of conformal invariance, are in good agreement with the exact results.

In Sec. 4.2, we simulate the Hamiltonian limit of the critical three-dimensional Ising model. First, from the ratio of the magnetic correlations in the strong- and weak-coupling directions, we numerically determined the length ratio relating the isotropic Ising model and the anisotropic limit. On this basis, we simulate the critical Ising model on a spherocylinder $S^2 \times \mathbb{R}^1$. From the prediction of conformal invariance and the sampled correlation lengths along the spherocylinder, we determine the magnetic and thermal exponents as $y_h = 2.4818(6)$ and $y_t = 1.581(7)$, respectively. Then, free boundary conditions are imposed on the equators of the spherocylinder, and we obtain the surface magnetic exponent $y_{hs}^{(o)} = 0.737(5)$, with the superscript (o) for the *ordinary* phase transition. The precision of these results reveals that, as in two dimensions, conformal mappings provide a powerful tool to investigate three-dimensional critical phenomena.

Chapter 5 investigates the anisotropic limit of the bond-percolation model in two and three dimensions, in which the critical bond-occupation probability p_{\parallel} in one of the directions (longitudinal) approaches 1, and the probability p_{\perp} in the other $(d - 1)$ dimensions (transverse) vanishes. Thus, near criticality, one has $p_{\parallel} = 1 - \epsilon$ and $p_{\perp} = \epsilon/t$, where $\epsilon \rightarrow 0$ is an infinitely small constant and t is a temperature-like parameter. In the same way as for the Hamiltonian limit of the Ising model, we rescale the system with an infinite factor in the longitudinal direction, so that a continuous percolation model is obtained. It can be simply reformulated as follows. Suppose that a sequence of lines originate from the vertices of a $(d - 1)$ -dimensional lattice, through which a current can flow. For each pair of nearest-neighboring lines, they are connected through a set of conducting ‘bridges’, which are uniformly distributed; moreover, a fraction of ‘barriers’, which have infinite resistance, is uniformly distributed on these lines. Thus, if a potential difference is applied to a pair of points with a large distance r , the probability $P(r)$ that a current can flow between these two points is determined by the *relative* abundance of the bridges and the barriers. For $t \gg 1$, there are so ‘many’ barriers that $P(r) \rightarrow 0$ as $r \rightarrow \infty$; for $t \ll 1$, one has a nonzero probability $P(r)$ as $r \rightarrow \infty$. A continuous phase transition occurs at some point t_c . This transition is referred to as the critical point of the transverse percolation model. It can be shown that a d -dimensional version is equivalent with the limit $q \rightarrow 1$ of the quantum q -state Potts model in $(d - 1)$ dimensions.

We formulate an efficient Monte Carlo method for this model, and its application confirms that it fits well in the percolation universality class of the isotropic case. In two dimensions, the dual symmetry yields the critical point as $t_c = 1$. For the three-dimensional rectangular geometry, we numerically obtain $t_c = 8.6429(4)$.

Next, we simulate critical systems in several two- and three-dimensional curved geometries including a spheroid and a spherocylinder. Using finite-size scaling and the predictions of conformal invariance, we determine the bulk and surface magnetic exponents, in agreement with the existing results.

Chapter 6 summarizes the influence of two types of annealed constraints on a number of critical and tricritical systems. The first type of constraint is energy-like and fixes the total number of vacancies or particles. We find that these constraints affect the leading finite-size behavior of energy-like quantities, while the effect on magnetic quantities is restricted to correction terms. The second type applies to the magnetization, and appears to suppresses the finite-size divergences of a quantity that normally scales as the magnetic susceptibility.

In an attempt to explain the observed finite-size scaling properties, we make use of the well-known Fisher renormalization mechanism. However, we do not always find a satisfactory agreement with our numerical results for constrained critical systems. For instance, for most energy-like constraints, the exponents describing the finite-size dependence of the specific heat are twice the expected values.

We also sample specific-heat-like and susceptibility-like quantities, which account for large-scale spatial inhomogeneities of energy and magnetization fluctuations. The finite-size behavior of these quantities

resembles that of the specific heat and the susceptibility of unconstrained systems.

In Chapter 7, we investigate the three-dimensional tricritical Blume-Capel model under an energy-like constraint. Since three is the upper tricritical dimensionality of the Ising model, we expect that the mean-field theory correctly predicts a number of universal parameters including the critical exponents and the Binder ratio. Therefore, we calculate the partition sum of the mean-field tricritical Blume-Capel model, and accordingly obtain the exact value of the Binder ratio. Further, we show that, under the constraint, this mean-field *tricritical* system reduces to the mean-field *critical* Ising model. However, our three-dimensional data do not agree with this mean-field prediction. Instead, they are successfully explained by the Fisher renormalization mechanism generalized to include the effect of the subleading thermal field.

Chapter 8 systematically investigates the constrained phenomena of the tricritical Potts model in two dimensions. Some of the results have been included in Chapter 6. Near a d -dimensional tricritical point, we show that the leading thermal exponent y_{t1} is renormalized to $d - y_{t1}$, while the subleading exponent y_{t2} remains unchanged.

Chapter 9 determines the backbone exponents of several critical and tricritical q -state Potts models in two dimensions and the percolation and the Ising model in three dimensions. For the general q -state Potts model, the nature of the bulk critical singularities is well established in two dimensions. Nevertheless, the Potts model continues to be a subject of much research interest. There is still a number of critical exponents, of which the exact values have not been obtained even in two dimensions. These exponents characterize geometric properties of the Potts model at criticality, and seem to have no analog in the thermodynamics. One of them is the fractal dimension of “backbones”, whose definition can be illustrated as follows. Consider the random-cluster representation of a Potts model, the probability that a pair of points with distance r belongs to the same Kasteleyn-Fortuin cluster, denoted as $P_1(r)$, behaves asymptotically as $P_1(r) \propto r^{-2X_h}$ at criticality, where $X_h = d - y_h$ is the magnetic scaling dimension. In other words, $P_1(r)$ can be understood as the probability that these two points are connected by *at least one* path which consists of occupied bonds in the random-cluster model. Analogously, one can ask the question what is the asymptotic critical behavior of the probability $P_k(r)$ that these two points are connected via *at least k independent* paths without any bond in common. At criticality, the behavior of $P_k(r)$ is governed by a family of exponents X_k , of which X_2 is the so-called backbone scaling dimension X_b . In percolation theory the backbone problem is considered to be of some physical relevance. In the past decades, this subject has attracted much research attention. Numerous theoretical attempts have been carried out to predict the exact values of X_b for the two-dimensional Potts model, particularly for the percolation model. In parallel, several numerical techniques have been developed for the determination of X_b , including Monte Carlo simulations and transfer-matrix methods.

In this chapter, we formulate an efficient numerical procedure to sample the probability $P_2(r)$, and thus to determine the backbone dimension X_b for several two- and three-dimensional models from a finite-size scaling analysis of $P_2(r)$. The precision of these results is favorable in comparison with the existing determinations. Moreover, from a scaling argument, we derive that, for two-dimensional tricritical Potts models, X_b reduces to the magnetic exponent X_h . This is confirmed by the numerical results.

In Chapter 10, we investigate geometric properties of several systems. It is known that a second-order phase transition is generally accompanied by diverging correlation lengths both in time and space. It has been suspected long time ago that, near a critical point, thermodynamic singularities can be represented by some sort of ‘geometric’ clusters. Consider a Potts model with ferromagnetic interactions between nearest-neighbor (NN) Potts variables, for each pair of NN sites in the same Potts state, one places a bond with probability $0 \leq p \leq 1$. Thus, the whole lattice is decomposed into groups of spins connected via the occupied bonds, to which we refer as the geometric clusters. For the special case $p = p_r = 1 - \exp(-K)$ with the Potts interaction strength K these geometric clusters reduce to the well-known Kasteleyn-Fortuin (KF) clusters. The critical Potts singularities can be correctly represented by the size distribution of the KF clusters (the so-called random-cluster model). For instance, the fractal dimension of KF clusters at the critical point K_c is just the magnetic scaling dimension X_h of the Potts model. In the parameter space (p, K) , the point (p_{rc}, K_c) , $p_{rc} = 1 - \exp(-K_c)$, can be generally regarded as a fixed point, which is referred to as the random-cluster fixed point. For $K = K_c$, renormalization flows in the p direction are governed by the bond-dilution field, whose exponent is called the red-bond exponent y_r .

Section 10.1 investigates the general q -state Potts model in two dimensions. We find that, in addition

to the random-cluster fixed point (K_c, p_{rc}) , there exists another fixed point on the critical line $K = K_c$, to which we refer as the geometric cluster fixed point p_{gc} . For the critical branch, the fixed point p_{rc} is unstable ($y_r > 0$) and the point $p_{gc} > p_{rc}$ is stable. In contrast, for the tricritical Potts model, the fixed points p_{rc} and p_{gc} are stable and unstable, respectively. In this case, one has $p_{gc} < p_{rc}$, so that the percolation threshold of the geometric clusters does not coincide with the KF clusters. We conjecture that the fixed point p_{gc} of a critical and a tricritical q -state Potts model can be regarded to correspond to p_{rc} of a tricritical and a critical q' -state Potts model, respectively. In terms of the coupling constant g of the Coulomb gas particle, these two models are related as $gg' = 16$. This conjecture is confirmed by the numerical results.

Along similar lines, Sec. 10.2 investigates the critical Ising and the tricritical Ising model in three dimensions. For the critical Ising model, exact information is scarce. Nevertheless, many numerical techniques have been developed, and a considerable amount of results has been obtained. Since the upper tricritical dimensionality of Ising systems is three, many universal parameters can be exactly obtained. However, the number of research activities carried out thus far for the geometric properties of both models is rather limited. By means of Monte Carlo simulations, we observe that, unlike two-dimensional tricritical Potts systems, the percolation threshold of geometric clusters coincides with KF clusters in three dimensions. We determine the corresponding red-bond exponents as $y_r = 0.757(2)$ and $0.501(5)$ for the critical Ising and the tricritical Ising model, respectively. On this basis, we conjecture $y_t = 1/2$ for the latter model, which is further confirmed by the numerical determination of y_r for the mean-field version of the tricritical Blume-Capel model (not reported in this section).

Chapter 11 investigates critical and tricritical surface phenomena of the general q -state Potts model in two dimensions. Near a critical point, the effect of a surface can be drastic, since the bulk correlation lengths become long-ranged. For instance, for the Ising model in a semi-infinite three-dimensional space, as the surface coupling K_s is varied, the bulk transition $K = K_c$ can occur in the absence or the presence of a spontaneous surface magnetization: the ‘ordinary’ or the ‘extraordinary’ transition, respectively. For disordered bulk $K < K_c$, there is a critical line of ‘surface’ transitions terminating at $K = K_c$ in a multicritical point, the so-called ‘special’ transition.

In two dimensions, the ‘surfaces’ are just one-dimensional *edges*, it may then seem natural that surface critical phenomena are less rich than those in three dimensions. In particular, for systems with short-range interactions only, it may seem plausible that *spontaneous edge* order cannot exist. However, our numerical results show otherwise. Using suitable Monte Carlo methods and finite-size scaling, we show that, for the two-dimensional tricritical Potts model, application of a sufficiently strong surface coupling or a surface magnetic field can induce a continuous phase transition. At even larger surface couplings, pseudo-one-dimensional order occurs on the edges. We determine several critical exponents describing these edges transitions. On the basis of these results and conformal field theory, we conjecture exact expressions of these exponents.

List of publications

- **Published:**

1. L.Y. Liu and Y. Deng,
Scientific knowledge for the Youth (in Chinese),
(China International Broadcast Press, Beijing, 1999).
2. Y. Deng and H.W.J. Blöte,
‘Conformal Invariance of the Ising Model in Three Dimensions’,
Phys. Rev. Lett. **88** 190602, p.1-4, (2002).
3. H.W.J. Blöte and Y. Deng,
‘Cluster Monte Carlo simulation of the transverse Ising model’,
Phys. Rev. E **66** 066110, p.1-8, (2002).

4. Y. Deng and H.W.J. Blöte,
'Conformal invariance and the Ising model on a spheroid',
Phys. Rev. E **67** 036107, p.1-10, (2003).
 5. H.W.J. Blöte and Y. Deng,
'Conformal invariance and simulations in curved geometries',
Physica A **321** 59, p.59-70, (2003).
 6. Y. Deng and H.W.J. Blöte,
'Bulk and surface critical behavior of the three-dimensional Ising model and conformal invariance',
Phys. Rev. E **67** 066116, p.1-8, (2003).
 7. Y. Deng and H.W.J. Blöte,
'Simultaneous analysis of several models in three-dimensional Ising universality class',
Phys. Rev. E **68** 036125, p.1-9, (2003).
 8. Y. Deng, H.W.J. Blöte, and B. Nienhuis,
'Backbone exponents of the 2D q-state Potts model: a Monte Carlo study',
Phys. Rev. E **69** 026114, p.1-9, (2004).
 9. Y. Deng, H.W.J. Blöte, and B. Nienhuis,
'Geometric properties of 2D critical and tricritical Potts model',
Phys. Rev. E **69** 026123, p.1-7, (2004).
 10. Y. Deng and H.W.J. Blöte,
'Anisotropic limit of the bond-percolation and conformal invariance in curved geometry',
Phys. Rev. E **69** 066129, p.1-10, (2004).
 11. Y. Deng and H.W.J. Blöte,
'Spontaneous edge order and geometric aspects of two-dimensional Potts models',
Phys. Rev. E, **70** 035107(R), p.1-4, (2004).
 12. Y. Deng and H.W.J. Blöte,
'Magnetic and backbone exponents of the percolation and the Ising model in three dimensions',
Phys. Rev. E, **70** 046106, p.1-6, (2004).
 13. Y. Deng and H.W.J. Blöte,
'Constrained tricritical Blume-Capel model in three dimensions',
Phys. Rev. E, **70** 046111, p.1-11, (2004).
- **Accepted for publication:**
 14. Y. Deng and H.W.J. Blöte,
'Red-bond exponents of the critical and the tricritical Ising model in three dimensions',
Phys. Rev. E, to appear in Nov. (2004).
 - **Submitted for publication:**
 15. X.F. Qian, Y. Deng, and H.W.J. Blöte,
'Simulation algorithms for the random-cluster model'.
Phys. Rev. E (2004).
 16. Y. Deng, H.W.J. Blöte, and J.R. Heringa,
'Constrained tricritical phenomena in two dimensions'.
Phys. Rev. E (2004).

17. Y. Deng and H.W.J. Blöte,
'Edge phase transitions of the tricritical Potts model in two dimensions'.
Phys. Rev. E (2004).
18. Y. Deng and H.W.J. Blöte,
'Surface phase transitions in three-dimensional percolation'.
Phys. Rev. E (2004).
19. X.F. Qian, Y. Deng, and H.W.J. Blöte,
'Percolation in one of q colors near criticality'.
Phys. Rev. Lett. (2004).

Simultaneous analysis of three-dimensional Ising models

We investigate several three-dimensional lattice models believed to be in the Ising universality class, by means of Monte Carlo methods and finite-size scaling. These models include spin- $\frac{1}{2}$ models with nearest-neighbor interactions on the simple-cubic and on the diamond lattice. For the simple-cubic lattice, we also include models with third-neighbor interactions of varying strength, and some 'equivalent-neighbor' models. Also included are a spin-1 model and a hard-core lattice gas. Separate analyses of the numerical data confirm the Ising-like universal critical behavior of all these systems. On this basis, we analyze all these data simultaneously such that the universal parameters occur only once. This leads to an improved accuracy. The thermal, magnetic, and irrelevant exponents are determined as $y_t = 1.5868(3)$, $y_h = 2.4816(1)$, and $y_i = -0.821(5)$, respectively. The Binder ratio is estimated as $Q = \langle m^2 \rangle^2 / \langle m^4 \rangle = 0.62341(4)$.

2.1 Introduction

The Ising model has been investigated extensively, and thus serves as a testing ground for theories of phase transitions. Many physical systems can be described by this simple but nontrivial model. It is believed that continuous phase transitions in systems with short-range interactions and a scalar order parameter belong to the Ising universality class. These include a variety of magnetic systems, alloys, gas-liquid systems, and liquid mixtures. For instance, magnetic systems can be described by a spin- $\frac{1}{2}$ or spin-1 Ising model depending on the nature of the elementary magnetic moments; gas-liquid systems can be modeled by means of hard-core particles, which exclude one another within a non-zero range. Furthermore, the particle coordinates may be restricted to the vertices of regular lattices.

In two dimensions, the evidence supporting the universality hypothesis is rather solid. One underlying reason is that exact results are available. For instance, exact analysis of Onsager's spin- $\frac{1}{2}$ model [1] and related models yields the thermal and magnetic scaling exponents as $y_t = 1$ and $y_h = 15/8$ [2], respectively. In three dimensions, however, such exact results are absent. Therefore, investigation of critical behavior has to depend on approximations. These include techniques such as ϵ - and series expansions, the coherent-anomaly method, and Monte Carlo methods etc. Extensive studies have been carried out [3–14], and there is some consensus that the values of y_t and y_h are, respectively, 1.587 and 2.482, with differences only in the last decimal place. Compared to the case of two dimensions, the three-dimensional results are indeed less satisfactory. Apart from the limited accuracy, the absence of exact results leaves, at least in principle, some room for severe disagreements. For instance, a very recent investigation by García and coworkers [15] claims that $y_t = 1.600(2)$ and $y_h = 2.501(5)$.

Many factors are responsible for this unsatisfactory situation. First, due to the restriction of current computer capacity, one can only explore rather limited system sizes in three dimensions. Second, corrections-to-scaling are much more serious than that in two dimensions. For the two-dimensional Ising model, the exponent of the leading irrelevant thermal field is $y_i = -2$, while in three dimensions $y_i \simeq -0.82$. Moreover,

the determination of y_i is not very accurate so far. A better estimation of y_i thus seems justified and is one of the purposes of the present work.

In the language of renormalization group technique, the critical behavior of systems within a universality class is governed by a common fixed point. In terms of scaling fields, the function of the free energy, and thus of physical observables, is universal near the critical points. By means of finite-size scaling, such universal functions are extended to finite systems. As an example, we concern the dimensionless ratio $Q = \langle m^2 \rangle^2 / \langle m^4 \rangle$, where m is the profile of order parameter. The quantity Q is related to Binder cumulant [16], and has been reported [11] to be a good choice to estimate y_i and locate criticality. Near the critical points Q behaves as

$$Q(t, v, L) = Q(tL^{y_t}, vL^{y_i}, 1) + \dots, \quad (2.1)$$

where L is the linear system size, t is the thermal scaling field, and the irrelevant field v reflects the distance of criticality of corresponding systems and the fixed point. Here, we have not yet specified contributions due to the analytic part of the free energy. Taylor-expansion of the right-hand-side of Eq. (2.1) yields

$$Q(t, v, L) = Q^{(0)} + Q^{(1,0)} tL^{y_t} + Q^{(2,0)} t^2 L^{2y_t} + Q^{(0,1)} vL^{y_i} + \dots, \quad (2.2)$$

where the derivatives of the universal function Q with respect to t and v are denoted as $Q^{(i,j)}$. Apart from the scaling exponents y_t and y_i , the amplitudes of $Q^{(0)}$ and $Q^{(i,j)}$ are equal for systems in the same universality class.

However, from the Monte Carlo data of a single model only, the estimation of y_i is rather difficult. The reason is as follows. In Eq. (2.2), the amplitude v is coupled to the exponent y_i , and thus a reasonable estimation of y_i requires systems with a large value of v . However, the large value of v excludes an accurate determination of $Q^{(0)}$, so that the accuracy of y_i is also limited. On the other hand, although a system with a small amplitude v helps to estimate $Q^{(0)}$, it does not allow a good determination of y_i either. This is one of the reasons why, in many numerical investigations, the exponent y_i is fixed at a constant taken from other sources.

This problem can be avoided by a simultaneous analysis of several systems with a diversity of the irrelevant fields v . Given a reasonable value of y_i , Monte Carlo data of systems with a small irrelevant field v determine $Q^{(0)}$ with a narrow margin; this information, together with models with a significant amplitude v , greatly helps the estimation of y_i , which in return improves the determination of $Q^{(0)}$.

In the present work, we investigate eleven Ising-like lattice models in three dimensions, of which the amplitudes v have a wide range of values. These models include the spin- $\frac{1}{2}$ Ising model with nearest-neighbor interactions K_{nn} on the simple-cubic and on the diamond lattice. On the simple cubic lattice, models with further-neighbor interactions are also investigated. In particular, third-neighbor interactions K_{3n} are included in several models with various ratios K_{3n}/K_{nn} . Further, we study some 'equivalent-neighbor' models, originally introduced by Domb and Dalton [17–19]. In such systems, each spin interacts equally strongly with all its neighbors within a certain distance. The model with the interactions till the r th shell of neighbors is referred to as the equivalent-neighbor model of order r . Also included are a spin-1 model [20] and a hard-core lattice gas with nearest-neighbor exclusion.

For these models, we analyze the numerical data both separately and simultaneously. The separate analyses are in a good agreement with the Ising universality hypothesis for all these systems. This provides the basis of the simultaneous analysis, in which we assume that universality is *exactly* satisfied so that universal parameters occur only once. This feature of the simultaneous analysis, combined with the aforementioned discussion in Sec. 2.1, leads to a significantly improved estimation of the critical points of these systems and the universal quantities including scaling exponents and the Binder ratio $Q^{(0)}$.

A difficulty is that such a simultaneous analysis requires a large amount of accurate Monte Carlo data. Fortunately, some numerical data are already available and were published elsewhere [9–11, 21–24]. The data generated by the Cluster Processor [11] are not included and will be published elsewhere. Our new Monte Carlo simulations mainly focus on larger system sizes, and were performed on a cluster of 6 PCs with a frequency of 2100 MHz.

Table 2.1: Definitions of the models.

Model	$\frac{K_{2n}}{K_{nn}}$	$\frac{K_{3n}}{K_{nn}}$	$\frac{K_{4n}}{K_{nn}}$	D	Lattice	Description of models
1	0	0	0	$-\infty$	d.	Spin- $\frac{1}{2}$ with nn couplings
2	0	0	0	$-\infty$	s.c.	Spin- $\frac{1}{2}$ with nn couplings
3	0	0.1	0	$-\infty$	s.c.	Spin- $\frac{1}{2}$ with nn and $3n$ couplings
4	0	0.2	0	$-\infty$	s.c.	Spin- $\frac{1}{2}$ with nn and $3n$ couplings
5	0	0.3	0	$-\infty$	s.c.	Spin- $\frac{1}{2}$ with nn and $3n$ couplings
6	0	0.4	0	$-\infty$	s.c.	Spin- $\frac{1}{2}$ with nn and $3n$ couplings
7	1	0	0	$-\infty$	s.c.	Equivalent-neighbor of order two
8	1	1	0	$-\infty$	s.c.	Equivalent-neighbor of order three
9	1	1	1	$-\infty$	s.c.	Equivalent-neighbor of order four
10	0	0	0	$\ln 2$	s.c.	Spin-1 with nn couplings
11	—	—	—	—	s.c.	Lattice gas with nn exclusion

d. – diamond lattice; s.c. – simple-cubic lattice.

2.2 Models and algorithms

As mentioned earlier, the present Monte Carlo analyses include eleven Ising-like models. Except the hard-core lattice gas, these models can be represented in terms of a spin-1 Hamiltonian

$$\mathcal{H}/k_{\text{B}}T = -K_{nn} \sum_{\langle nn \rangle} \sigma_i \sigma_j - K_{2n} \sum_{(2n)} \sigma_i \sigma_j - K_{3n} \sum_{[3n]} \sigma_i \sigma_j - K_{4n} \sum_{\{4n\}} \sigma_i \sigma_j + D \sum_i \sigma_i^2, \quad (2.3)$$

where the sums $\langle nn \rangle$, $(2n)$, $[3n]$, and $\{4n\}$ are respectively over nearest-, second-, third-, and fourth-neighbor pairs, and the associated couplings are denoted as K_{nn} , K_{2n} , K_{3n} , and K_{4n} , respectively. The spins can assume three discrete values $s_i = 0, \pm 1$, where spins $s = 0$ may be referred to as vacancies. The detailed definitions are specified in Tab. 2.1, where ten models are defined on the simple cubic lattice, and one on the diamond lattice. We define the finite-size parameter L by its relation with the total number N of lattice sites as $N = L^3$. Thus, the linear size of the 8-site elementary cell of the diamond lattice is taken to be $L = 2$. Periodic boundary conditions are applied. The systems sizes were taken in the range $4 \leq L \leq 128$.

For $D = -\infty$, the vacancies are excluded, so that the model reduces to the spin- $\frac{1}{2}$ model. This applies to the first nine models in Tab. 2.1. Models 1 and 2 have nearest-neighbor interactions K_{nn} only. Models 3-6 include, in addition, third-neighbor interactions K_{3n} . Various ratios are applied: $K_{3n}/K_{nn} = 0.1, 0.2, 0.3$, and 0.4 . Models 7-9 are the equivalent-neighbor models [17–19] of order two, three, and four, respectively. We choose these models because they cover a wide range of amplitudes of the irrelevant field v in Eq. (2.2). In particular, v is positive for models 1-4 and negative for models 5-9. This reflects that the critical points of these systems lie on opposite sides of the Ising fixed point in the direction of v on the critical surface. Moreover, the absolute value of v is relatively large for models 1, 2, 8, and 9, and relatively small for models 4, 5 and 7. This will be shown later in the numerical analysis.

During the Monte Carlo simulations, one can in principle apply the standard form of the Swendsen-Wang or of the Wolff cluster algorithm. However, the efficiency of these methods decreases rapidly as the number of interacting neighbors increases. This difficulty is avoided by an algorithm described in Ref. [9]. Here, we summarize the essential points. During the formation of a cluster, a bond between equal spins coupled with strength K is frozen with probability $p = 1 - \exp(-2K)$, or broken with probability $1 - p$. Sites connected by frozen bonds belong to the same cluster. The distribution $P(k) = p(1 - p)^{k-1}$ expresses the probability that $(k - 1)$ subsequent bonds are broken while the k th bond is frozen. The algorithm generates this distribution from a uniformly distributed random number $0 < r < 1$ as follows

$$k = 1 + [\ln(r)/\ln(1 - p)], \quad (2.4)$$

where the square brackets denote the integer part. By repeated evaluation of k , one may set up a complete list of frozen bonds, and thus a cluster is formed. The efficiency of this procedure is almost independent of

the range of the interactions. An example was shown in Ref. [21] by simulating the mean-field Ising model, in which each spin is interacting with every other spin.

We also include a spin-1 model with $D = \ln 2$, which is important to our purposes due to its very small amplitude of v [9]. However, for a general spin-1 model, it is not obvious how cluster algorithms can produce transitions between vacancies and non-vacancies. One can in principle follow a hybrid algorithm in which Metropolis sweeps alternate with cluster steps. As long as the spin-1 model is not close to the tricritical point where the ordered Ising phases meet the phase dominated by vacancies, serious critical slowing down is not expected.

Here, due to the special choice $D = \ln 2$ (model 10), a full cluster algorithm [9, 11, 21] becomes possible. First, the spin-1 model is mapped onto a spin- $\frac{1}{2}$ model with two variables, of which the Hamiltonian is

$$\mathcal{H}/k_{\text{B}}T = -M_1 \sum_{\langle ij \rangle} (t_i + u_i)(t_j + u_j) - M_2 \sum_m t_m u_m, \quad (2.5)$$

where two $s = \frac{1}{2}$ spins $t_i = \pm 1$ and $u_i = \pm 1$ sit on each site i of the simple-cubic lattice. Using the transformations $\sigma_i = (t_i + u_i)/2$ and $v_i = (1 + t_i)(1 - u_i)/4$, it has been shown [9] that the partition function is, up to a constant factor,

$$Z = \sum_{\sigma_k} \exp \left[4M_1 \sum_{\langle ij \rangle} \sigma_i \sigma_j + (2M_2 - \ln 2) \sum_m \sigma_m^2 \right]. \quad (2.6)$$

This is precisely the partition function of the spin-1 model. The special choice $D = \ln 2$ leads to $M_2 = 0$ so that there are no interactions between variables on the same site. On this basis, the Wolff algorithm is applied to flip the variables t_i and/or u_i . This costs a little price, i.e., two arrays have to be stored in computer memory for the variables t_i and u_i . In the present work, we improve this algorithm by using one variable only. This improvement is based on the equivalence of the variables t_i and u_i . Because of this symmetry, only the sum of t_i and u_i on the same site needs to be stored. This leads to a cluster algorithm for $D = \ln 2$, which allows flips between nonzero and zero spins.

Another model (model 11) investigated in the present work is the hard-core lattice gas on the simple-cubic lattice, of which the Hamiltonian is

$$\mathcal{H}/k_{\text{B}}T = -K \sum_{\langle nn \rangle} \sigma_i \sigma_j - \mu \sum_m \sigma_m. \quad (2.7)$$

Here, the variable $\sigma_i = 1, 0$ represents the presence and the absence of a particle, respectively. The nearest-neighbor coupling $K \rightarrow -\infty$ implies that no nearest-neighbor sites are allowed to be occupied simultaneously. The chemical potential of the particles is denoted as μ . This lattice gas was Monte Carlo simulated by means of a combination of the Metropolis and a geometric cluster method. This cluster algorithm is based on geometric symmetries, such as the spatial inversion symmetry of the simple-cubic lattice. The full description of this algorithm is given in Refs. [22–24].

As mentioned in Sec. 2.1, the critical behavior of the hard-core lattice gas is expected to belong to the Ising universality class. Surprisingly, significant differences have been reported. The investigations by Yamagata [25, 26] yielded critical exponents $\beta/\gamma = 0.311(8)$ and $\gamma/v = 2.38(2)$, which would imply $y_h = 2.689(8)$. These results, however, could not be confirmed by later investigations which did reveal a relatively large irrelevant field, but no deviations from the Ising universality class [22, 23].

2.3 Dimensionless ratio Q

For the aforementioned eleven systems, Monte Carlo simulations took place very close to critical points for $L > 20$, while ranges of temperature-like parameters are wider for smaller systems. Table 2.2 presents the number of ten millions of samples taken per system size and the number of simulation sweeps before taking each sample.

Table 2.2: Number of samples (in ten millions) and simulation steps per sample. We use the notation $M \times N$ to indicate that $10^7 M$ samples have been taken at intervals of N Monte Carlo steps. Smaller system sizes $L < 20$ are also included in the analysis. For the lattice gas, simulations steps include one Metropolis sweep for each sample.

Model \ L	20	22	24	28	32
1	50×10	50×10	50×10	50×10	40×10
2	10×10	10×10	10×10	12×10	20×10
3	10×10				
4	10×10				
5	10×10				
6	10×10				
7	20×20	15×22	17×24	15×28	12×32
8	20×20	15×22	12×24	10×28	8×32
9	20×20	17×22	12×24	10×28	7×32
10	128×6	92×6	92×6	92×6	87×8
11	150×7	20×8	52×10	50×10	30×12

	40	48	64	128
1	40×10	20×20	10×20	5×40
2	10×10	5×20	5×32	1.8×64
3	10×10	5×20	5×32	2×64
4	10×10	5×20	5×32	2×64
5	10×10	5×20	5×32	2×64
6	10×10	5×20	5×32	2×64
7	8×40	6×48	5×64	3×128
8	6×40	4×48	3×64	2×128
9	6×40	4×48	3×64	1.5×128
10	55×10	22×12	2×16	5.4×25
11	15×14	12×16	15×64	4.4×128

During the simulations, the universal ratio $Q = \langle m^2 \rangle^2 / \langle m^4 \rangle$ was sampled, where m is the order parameter. For the spin systems (models 1 - 10) and the lattice gas (model 11), the magnetization density and the staggered particle density assume this role, respectively. Near the critical points, we analyzed Q both separately and simultaneously.

I. Separate analyses

The finite-size behavior of Q near the critical points is described by Eq. (2.2). Here, the thermal scaling field t depends on temperature-like parameters. For the spin- $\frac{1}{2}$ models (models 1-9), these are the spin-spin interactions K_{nn} , K_{2n} , K_{3n} , and K_{4n} . Since fixed ratios apply between these couplings, it is sufficient to select K_{nn} as the only temperature parameter K_i for the i th model. For the spin-1 model (model 10), both the nearest-neighbor couplings K_{nn} and the chemical potential D are temperature-like parameters. In this work, D is fixed at $\ln 2$ so that K_i is again represented by K_{nn} . For the hard-core lattice gas (model 11), the chemical potential μ of the particles assumes this role. For later convenience, near the critical points, we express the dependence of the scaling field t on the physical temperature parameter K_i as $t = a_i(K_i - K_{ci}) + b_i(K_i - K_{ci})^2 + \dots$. The amplitudes of the quantities with the subscript i depend on specific models. On this basis, Eq. (2.2) becomes

$$Q = Q^{(0)} + Q^{(1)}a_i(K_i - K_{ci})L^{y_t} + Q^{(2)}a_i^2(K_i - K_{ci})^2t^2L^{2y_t} + Q^{(3)}a_i^3(K_i - K_{ci})^3t^3L^{3y_t} + Q^{(4)}a_i^4(K_i - K_{ci})^4t^4L^{4y_t} + c_i(K_i - K_{ci})^2L^{y_1} + b_{1i}L^{y_1} + b_{2i}L^{y_2} + b_{3i}L^{y_3} + \dots \quad (2.8)$$

Here, we have written $Q^{(i,0)}$ as $Q^{(i)}$ for simplicity. The term with the coefficient c_i reflects the nonlinear dependence of t on K_i . The exponents of the correction terms, as obtained in earlier analyses of Q in Refs. [9, 11], are $y_1 = y_i = -0.82(3)$, $y_2 = d - 2y_h = -1.963(3)$, and $y_3 = y_t - 2y_h = -3.375(3)$. The correction with the exponent y_2 is due to the field dependence of the analytic part of the free energy. The last term arises from nonlinear dependence of the temperature scaling field on the physical magnetic field. Finite-size scaling also predicts further contributions. For a single model, since both the quantities $Q^{(i)}$ and other parameters such as a_i and K_{ci} are unknown, we may simplify Eq. (2.8) as

$$Q = Q_0 + q_{1i}(K_i - K_{ci})L^{y_t} + q_{2i}(K_i - K_{ci})^2L^{2y_t} + q_{3i}(K_i - K_{ci})^2L^{3y_t} + q_{4i}(K_i - K_{ci})^2L^{4y_t} + c_i(K_i - K_{ci})^2L^{y_t} + b_{1i}L^{y_1} + b_{2i}L^{y_2} + b_{3i}L^{y_3} \quad (2.9)$$

where q_{ij} is the product of $Q^{(j)}$ and a_i^j .

According to the least-squares criterion, Eq. (2.9) was fitted to the Monte Carlo data separately for the aforementioned eleven models. First, we fixed y_1 , y_2 , and y_3 at the aforementioned values with the error margins neglected, and y_t was taken as 1.587 [3–13]. We applied a cutoff for small system sizes $L < 10$ for model 8, $L < 12$ for model 9, and $L < 8$ for the rest. For the equivalent-neighbor model of order three and four, the Monte Carlo data for small system sizes may be affected by crossover effects due to the proximity of the mean-field fixed point [21]. This is the reason why we applied different cutoffs at small system sizes for models 8 and 9. The results are shown in Tab. 2.3. The numerical uncertainties quoted between parenthesis represent one standard deviation. The excellent agreement of the universal quantity $Q^{(0)}$ in the third column confirms that these eleven systems belong to the Ising universality class. Furthermore, according to Eqs. (2.8) and (2.9), the quantity $q_1^2/q_2 = [Q^{(1)}]^2/Q^{(2)}$ is the same for all Ising-like models. This is confirmed by the last column of Tab. 2.3, which reveals that the values q_1^2/q_2 are consistent with each other within two standard deviations.

The amplitudes of the irrelevant field for these models are shown, up to a constant factor, in the sixth column of Tab. 2.3. As mentioned in Sec. 2.1, they reflect the positions of the critical points of these systems on the critical surface. For clarity, we start from the Landau-Ginzburg-Wilson description [27] of the Ising model:

$$-\mathcal{H}(\phi)/k_B T = \int d\mathbf{r} [r\phi^2(\mathbf{r}) + v\phi^4(\mathbf{r}) + \nabla^2\phi(\mathbf{r}) + h\phi(\mathbf{r})], \quad (2.10)$$

where the square-gradient term represents short-range interactions, r and v together determine the temperature-like and irrelevant parameters, and h is the magnetic field. For spatial dimensionality $d < 4$, a renormalization

Table 2.3: Separate fits of the dimensionless ratio Q with y_1 fixed.

	K_c	$Q^{(0)}$	q_1	q_2	b_1	q_1^2/q_2
1	.36973976(16)	.62338(8)	0.4906(5)	0.19(1)	0.1150(10)	1.26(7)
2	.22165452(8)	.62327(10)	0.885(10)	0.58(5)	0.097(2)	1.35(15)
3	.18562459(10)	.62351(10)	0.995(1)	0.80(3)	0.051(2)	1.24(4)
4	.16073242(15)	.62364(15)	1.128(13)	1.07(4)	0.0118(20)	1.19(5)
5	.14230189(10)	.62355(14)	1.250(13)	1.26(5)	-0.018(2)	1.24(5)
6	.12800424(12)	.62350(16)	1.385(30)	1.85(18)	-0.048(2)	1.03(15)
7	.06442225(5)	.62338(10)	2.854(40)	7.5(2)	-0.019(2)	1.08(19)
8	.04303818(3)	.62324(15)	4.02(30)	15.1(9)	-0.107(2)	1.07(16)
9	.03432687(4)	.62337(26)	4.99(40)	23.2(15)	-0.212(4)	1.08(23)
10	.3934222(2)	.62344(5)	0.6617(8)	0.360(2)	-0.0015(7)	1.21(6)
11	.0544853(20)	.62316(20)	0.0593(1)	.0027(4)	0.212(4)	1.29(12)

– the first column is the number of the models

Table 2.4: Some results of separate fits of Q with y_1 as a free parameter.

Model	1	2	8	9	11
K_c	0.3697399(4)	0.2216545(2)	0.0430382(7)	0.0343268(1)	0.05449(3)
Q_0	0.6238(7)	0.6231(8)	0.625(1)	0.623(2)	0.625(3)
y_i	-0.87(6)	-0.800(15)	-0.68(16)	-0.80(2)	-1.0(3)

analysis [28] shows that there are two fixed points, i.e., the mean-field $(0, 0)$ and the Ising fixed points (r^*, v^*) (Fig. 2.1). The crossover behavior of the Binder ratio $Q^{(0)}$ is displayed by a data collapse in Fig. 10 in Ref. [29]. This provides a scale for the irrelevant Ising field v on the whole range from the Ising to the mean-field fixed point. Using this scale and the value of b_{1i} for the i th model (Tab. 2.3), we schematically illustrate the positions of the critical point of the eleven systems in the present work (Fig. 2.1).

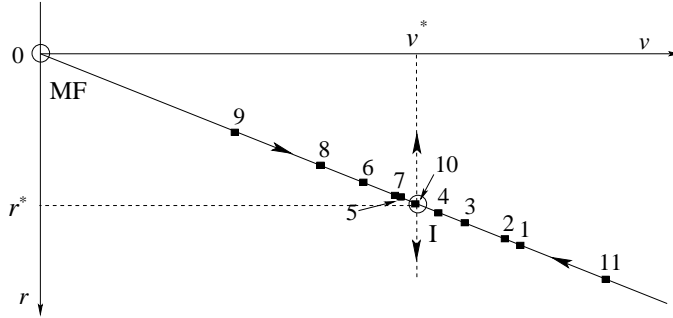


Figure 2.1: Schematic illustration of positions of models 1-11 in the parameter space (r, v) , where r is a temperature-like parameter and u reflects the amplitude of the irrelevant field. The mean-field and Ising fixed points, denoted as \bigcirc , sit at $(0, 0)$ and (r^*, v^*) , respectively.

The results in Tab. 2.3 rely on the choice that the irrelevant exponent y_i was fixed at -0.82 . As discussed in Sec. 2.1, without such an assumption of the value of y_i , the accuracy of $Q^{(0)}$ and y_i will be very limited. As a test, we left the exponent y_1 as a free parameter. We find that the uncertainties of y_1 are then almost as big as the absolute value of y_1 itself for models with relatively small amplitude b_1 . For the rest, the results in Tab. 2.3 are also affected in the sense that the accuracy decreases significantly, as shown in Tab. 2.4.

II. Simultaneous analysis

Table 2.5: Simultaneous fit of the ratio Q .

$Q^{(0)}$	$Q^{(1)}$	$Q^{(2)}$	$Q^{(3)}$	$Q^{(4)}$
0.62342(3)	1 (fixed)	0.826(6)	-3.32(9)	-9.4(14)
y_i	$K_c^{(1)}$	$K_c^{(2)}$	$K_c^{(3)}$	$K_c^{(4)}$
-0.821(5)	0.36973981(8)	0.22165455(5)	0.18562452(6)	0.16073229(5)
$K_c^{(5)}$	$K_c^{(6)}$	$K_c^{(7)}$	$K_c^{(8)}$	$K_c^{(9)}$
0.14230186(5)	0.12800417(5)	0.06442222(2)	0.04303821(2)	0.03432687(2)
$K_c^{(10)}$	$K_c^{(11)}$	a_1	a_2	a_3
0.39342225(9)	0.0544876(8)	0.5203(8)	0.853(1)	0.9930(12)
a_4	a_5	a_6	a_7	a_8
1.132(2)	1.261(3)	1.390(3)	2.77(3)	4.031(14)
a_9	a_{10}	a_{11}	$b_{1\ 1}$	$b_{1\ 2}$
4.92(3)	0.6603(3)	0.05944(4)	0.114(2)	0.094(2)
$b_{1\ 3}$	$b_{1\ 4}$	$b_{1\ 5}$	$b_{1\ 6}$	$b_{1\ 7}$
0.052(1)	0.0147(7)	-0.016(1)	-0.046(1)	-0.014(1)
$b_{1\ 8}$	$b_{1\ 9}$	$b_{1\ 10}$	$b_{1\ 11}$	
-0.113(2)	-0.219(4)	-0.0012(5)	0.207(4)	

On the basis of the universality hypothesis, we analyze the Monte Carlo data of these systems simultaneously. The data were fitted, instead of to Eq. (2.9), to Eq. (2.8). As a result, each of the amplitudes q_{ji} is decomposed in a universal factor $Q^{(j)}$ and a nonuniversal factor a_i . Since the $Q^{(j)}$ are shared by all the systems, the number of unknown parameters decreases significantly, in comparison of the total number in the separate fits. This decomposition also leads to an additional free parameter since numerical data can only determine the product of $Q^{(1)}$ and a_i , so that one of the parameters $Q^{(j)}$ ($j \neq 0$) and a_i has to be fixed as an arbitrary constant. Here, we simply set $Q^{(1)} = 1$. Together with the mechanism discussed in Sec. 2.1, this effect leads to a substantially improved accuracy of the unknown parameters, despite that y_i was left as a free parameter. This includes the determination of the critical points, the universal ratio $Q^{(0)}$, the irrelevant exponent y_i , and the amplitudes b_{1i} . The results are shown in Tab. 2.5. The amplitude $[Q^{(1)}]^2/Q^{(2)} = 1/0.826(6) = 1.211(9)$ is in good agreement with those in the separate fits (Tab. 2.3).

2.4 Other quantities

The Monte Carlo simulations also yielded the susceptibility as $\chi = L^3 \langle m^2 \rangle$. Furthermore, we sampled the energy density and its cross products with $\langle m^2 \rangle$ and $\langle m^4 \rangle$. Thus, we obtained derivative of Q , denoted as Q_p . Analysis of χ and Q_p yields an estimation of the magnetic and thermal exponents, y_t and y_h , respectively.

I. Simultaneous analysis of χ

According to finite-size scaling, the magnetic susceptibility χ behaves as

$$\chi(t, v, L) = x(t) + L^{2y_h - d} \left(\frac{\partial h}{\partial H} \right)^2 \chi(L^{y_t} t, L^{y_i} v, 1), \quad (2.11)$$

where $x(t)$ arises from the differentiation of the analytical part of the free energy density, h is the magnetic scaling field, and H is the physical magnetic field. The dependence of h on H is not universal and is linearized as $h = \sqrt{w_i} H$. Taking into account that $t = a_i(K_i - K_{ci}) + b_i(K_i - K_{ci})^2 + \dots$, Taylor-expansion of Eq. (2.11) yields

$$\begin{aligned} \chi = & x_i + s_i(K_i - K_{ci}) + L^{2y_h - d} w_i [\chi^{(0)} + \chi^{(1)} a_i(K_i - K_{ci}) L^{y_t} + \\ & \chi^{(2)} a_i^2(K_i - K_{ci})^2 L^{2y_t} + \chi^{(3)} a_i^3(K_i - K_{ci})^3 L^{3y_t} + \\ & \chi^{(4)} a_i^4(K_i - K_{ci})^4 L^{4y_t} + b_i L^{y_i} + c_i(K_i - K_{ci}) L^{y_t + y_i}]. \end{aligned} \quad (2.12)$$

Table 2.6: Simultaneous fit of the magnetic susceptibility χ .

$\chi^{(0)}$	$\chi^{(1)}$	$\chi^{(2)}$	$\chi^{(3)}$	$\chi^{(4)}$
1 (fixed)	1 (fixed)	0.409(2)	-0.043(1)	-0.075(2)
y_h	$K_c^{(1)}$	$K_c^{(2)}$	$K_c^{(3)}$	$K_c^{(4)}$
2.4816(1)	0.3697398(1)	0.22165457(3)	0.18562459(7)	0.16073233(6)
$K_c^{(5)}$	$K_c^{(6)}$	$K_c^{(7)}$	$K_c^{(8)}$	$K_c^{(9)}$
0.14230183(12)	0.12800422(5)	0.06442225(3)	0.04303821(2)	0.03432690(3)
$K_c^{(10)}$	$K_c^{(11)}$	w_1	w_2	w_3
0.3934221(1)	0.054487(1)	1.75(2)	1.55(2)	1.38(2)
w_4	w_5	w_6	w_7	w_8
1.266(2)	1.187(2)	1.127(2)	1.156(2)	0.989(2)
w_9	w_{10}	w_{11}	a_1	a_2
0.875(1)	0.933(1)	0.2192(4)	2.00(4)	3.32(2)
a_3	a_4	a_5	a_6	a_7
3.87(2)	4.45(4)	4.96(6)	5.63(6)	10.64(4)
a_8	a_9	a_{10}	a_{11}	
16.16(3)	19.7(2)	2.65(8)	0.2236(2)	

Table 2.7: Results for the ratio r_i .

Model	1	2	3	4	5
r	0.259(5)	0.258(5)	0.257(6)	0.256(6)	0.254(7)
6	7	8	9	10	11
0.253(8)	0.259(7)	0.252(8)	0.252(8)	0.259(6)	0.258(6)

Here, the j th thermal derivative of χ at criticality is denoted as $\chi^{(j)}$. For the i th model, the amplitude a_i is the same as in Eq. (2.8). This will be confirmed later. Equation (2.12) was fitted to the Monte Carlo data, and the result is shown in Tab. 2.6. According to similar arguments as mentioned above, there are two extra free parameters in Eq. (2.12) during the fit. Here, we simply fixed $\chi^{(0)}$ and $\chi^{(1)}$ equal to 1. The magnetic renormalization exponent is estimated as $y_h = 2.4816(1)$. This is in excellent agreement with most available results [3–13], and its precision is comparable with the best known value $y_h = 2.48180(15)$, obtained from a 25th-order high-temperature expansion [30]. The critical points are consistent with those in Tab. 2.5. We also calculated the ratio $r_i = (a_i)^{(Q)} / (a_i)^{(\chi)}$, where the superscripts Q and χ represent that the value of a_i is taken from Tabs. 2.5 and 2.6, respectively. The result is shown in Tab. 2.7. The consistency of r_i among these eleven models confirms that the function of t of K is independent of the type of physical observable.

II. Simultaneous analysis of Q_p

During the Monte Carlo simulations, the energy density e was sampled as the nearest-neighbor sum for models 1-10:

$$e = \langle S_{nn} \rangle = \sum_{\langle nn \rangle} \langle \sigma_i \sigma_j \rangle. \quad (2.13)$$

For the hard-core lattice gas (model 11), the nearest-neighbor couplings are infinitely repulsive, and the quantity e is thus defined, instead, as a sum over the next-nearest-neighbor pairs. On this basis, we sampled a quantity Q_p which correlates the magnetization distribution with the energy density:

$$Q_p = 2 \frac{\langle m^2 S_{nn} \rangle}{\langle m^2 \rangle} - \frac{\langle m^4 S_{nn} \rangle}{\langle m^4 \rangle} - \langle S_{nn} \rangle = \frac{1}{Q} \frac{\partial Q}{\partial t} \frac{\partial t}{\partial K_{nn}}. \quad (2.14)$$

Little additional effort is required for this task since m^2 and e are already sampled during the Monte Carlo

Table 2.8: Result of simultaneous fit of Q_p .

L_{\min}	$Q_p^{(0)}$	$Q_p^{(1)}$	$Q_p^{(2)}$	$Q_p^{(3)}$	$Q_p^{(4)}$
8	1 (fixed)	0.1 (fixed)	-4.4(5)	-1.2(2)	9.3(23)
y_t	p_1	p_2	p_3	p_4	p_5
1.58684(14)	0.825(5)	1.355(2)	1.335(2)	1.334(2)	1.343(2)
p_6	p_7	p_8	p_9	p_{10}	p_{11}
1.351(2)	1.422(1)	1.428(1)	1.441(2)	1.058(1)	0.662(1)

simulations. The quantity Q_p has been reported [9–11] to be a good choice in determining the thermal scaling dimension. The reason will be discussed later on the basis of its scaling behavior. For models 3-10, apart from nearest neighbors, the spin-spin interactions occur between second-, third- and fourth-neighbor pairs. In those cases, the amplitude of $\partial t/\partial K_{nn}$ is different from the value of a_i in the function $t = a_i(K_i - K_{ci})$. According to Eq. (2.1), near the critical point the quantity Q_p behaves as

$$Q_p(t, v, L) = L^{y_t} \frac{\partial t}{\partial K_{nn}} Q_p(L^{y_t} t, L^{y_i} v, 1). \quad (2.15)$$

Taking into account contributions of $d_i L^{y_2}$ due to the analytic part of the free energy, we Taylor-expand this equation as

$$Q_p = L^{y_t} p_i [Q_p^{(0)} + Q_p^{(1)} a_i (K_i - K_{ci}) L^{y_t} + Q_p^{(2)} a_i^2 (K_i - K_{ci})^2 L^{2y_t} + Q_p^{(3)} a_i^3 (K_i - K_{ci})^3 L^{3y_t} + Q_p^{(4)} a_i^4 (K_i - K_{ci})^4 L^{4y_t} + b_i L^{y_i} + d_i L^{y_2} + c_i (K_i - K_{ci})], \quad (2.16)$$

where the parameters $Q_p^{(j)}$ are universal, and $\partial t/\partial K_{nn}$ is denoted as p_i for the i th model. Compared to the specific heat, the divergence of Q_p with respect to the system size L at criticality is much stronger. According to finite-size scaling, the critical specific heat C behaves approximately as $C - C_0 \propto L^{2y_t - 3}$, where C_0 arises from the analytical part of free energy. The exponent $2y_t - 3 \simeq 0.174$ is so small that the term with this exponent is normally difficult to separate from the background contribution C_0 in numerical analyses. Therefore, the quantity Q_p serves as a better choice than C to estimate the thermal exponent y_t . We fitted Eq. (2.16) to the Monte Carlo data, using the critical points as taken from Tab. 2.5. This is in line with the relatively weak dependence of Q_p on the temperature-like parameters K . The results are shown in Tab. 2.8. As possible alternatives, we have included more terms such as $L^{y_t + y_i} (K_i - K_{ci})$ within the square brackets of Eq. (2.16). However, this does not improve the residual χ^2 of the fit. The dependence on the cutoff at small system sizes in the fit was also determined. Taking into account these dependences and the uncertainties of the critical points, we estimate the thermal exponent as $y_t = 1.5868(3)$.

2.5 Discussion

We have performed extensive Monte Carlo simulations of several Ising-like models in three dimensions. These models were selected such that they span a wide range of the irrelevant field, as illustrated in Fig. 1. In order to enable a meaningful test of universality, the models are also chosen according to quite different microscopic Hamiltonians. On the basis of finite-size scaling, we analyze the Monte Carlo data both separately and simultaneously. These systems are confirmed to be within the Ising universality class. Compared to other methods, our simultaneous analyses yield more accurate estimations for the critical points, renormalization exponents, and the Binder cumulant. In particular, we determine the irrelevant exponent as $y_i = -0.821(5)$. Tables 2.9 and 2.10 show a comparison between some existing results and our estimations.

In order to interpret numerical data correctly, it is necessary to include appropriate corrections to scaling. We find that, normally, a single power-law correction is not sufficient to account for all finite-size corrections.

Table 2.9: Summary of results of the scaling exponents and the universal quantity $Q^{(0)}$ for the three-dimensional Ising universality class.

	Year	y_t	y_h	y_i	$Q^{(0)}$	Method
[5]	1980	1.587(4)	2.485(2)	-0.79(3)		RG
[31]	1990	1.587(4)	2.4821(4)	-0.83(5)		HTE
[32]	1991	1.587	2.4823	-0.84		HTE
[33]	1992	1.602(5)	2.4870(15)	-0.8		MCRG
[34]	1994	1.590(2)	2.482(7)			MC
[7]	1995	1.586(4)	2.482(4)			CAM
[9]	1995	1.587(2)	2.4815(15)	-0.82(6)	0.6233(4)	MC
[11]	1996	1.585(2)	2.4810(10)			MCRG
[14]	1998	1.586(3)	2.483(2)	-0.799(11)		HTE
[10]	1999	1.5865(14)	2.4814(5)	-0.82(3)	0.62358(15)	MC
[30]	2002	1.5869(4)	2.48180(15)	-0.82(5)		HTE
Now	2003	1.5868(3)	2.4816(1)	-0.821(5)	0.62341(3)	MC

RG – renormalization of ϕ^4 model; HTE – high-temperature series expansion; MC – Monte Carlo and finite-size scaling; MCRG – Monte Carlo renormalization; CAM – coherent-anomaly method.

For instance, if one neglects the term $b_3 L^{y_3}$ in Eq. (2.9), which is decaying relatively fast, one finds a considerable increase of the residual χ^2 both in the separate and simultaneous fits. In three dimensions, Monte Carlo simulations are restricted to linear system sizes L in the order of 100. Even for $L \approx 100$, corrections-to-scaling are still significant. For instance, we consider the contribution of $b_1 L^{y_1}$ in Eq. (2.9) for the spin- $\frac{1}{2}$ model on the simple-cubic lattice (model 2). From Tab. 2.3 ($b_1 \approx 0.094$), we find that the term $b_1 L^{y_1}$ contributes about 0.002 to Q for $L = 90$. Compared to the accuracy 0.00003 of $Q^{(0)}$ in Tab. 2.5, this contribution is huge and may not be neglected. Another example of corrections due to the irrelevant field is provided in Ref. [8], where the spontaneous magnetization density M was analyzed as $M(t) = f(t)t^\beta$ for the Ising model on simple-cubic lattices with linear sizes up to $L = 256$. Here, t is the reduced temperature $t = (K - K_c)/K_c$, the exponent β is equal to $(3 - y_h)/y_t$, and $f(t)$ is some function of t that contains the corrections to scaling. It was found that, without including a correction $\sim t^{y_i/y_t}$ due to the irrelevant field in the function $f(t)$, one cannot successfully describe the numerical data ($0.0005 < t < 0.26$), even when $f(t)$ is defined as $f(t) = p_0 + p_1 t + p_2 t^2 + p_3 t^3$. Another analysis involving the spontaneous magnetization density was recently carried out by García *et al* [15]. Remarkably, they claimed that, for $L > 90$ and $t > 0.004$, corrections to scaling are invisible. They did not comment on the nature of the discrepancy with Ref. [8], and did not provide details about their error estimation. Therefore, some doubt concerning the precision of their results ($y_t = 1.600(2)$ and $y_h = 2.501(5)$) seems justified.

For the spin-1 model and the lattice gas, another quantity of interest is the density of vacancies ρ_v at the critical points. Finite-size analysis yields $\rho_v = 0.400694(1)$ and $0.789516(1)$ for these two models, respectively.

Bibliography

- [1] L. Onsager, Phys. Rev. **65**, 117, (1944).
- [2] B.M. McCoy and T.T. Wu, *The Two-Dimensional Ising Model* (Harvard University Press, Cambridge, Massachusetts, 1968), and references therein.
- [3] J.H. Chen, M.E. Fisher, and B.G. Nickel, Phys. Rev. Lett. **48**, 630 (1982).
- [4] J. Adler, J. Phys. A **16**, 3585 (1983).

Table 2.10: Summary of results for the critical points

Model	K_c (present)	K_c	K_c
1	0.36973980(9)	0.36978(4) [35]	0.3697(8) [36]
2	0.22165455(3)	0.221656(10) [9]	0.2216576(22) [34]
3	0.18562452(6)	0.18562466(52) [11]	
4	0.16073229(5)	0.16073235(12) [11]	
5	0.14230186(5)	0.14230187(12) [11]	
6	0.12800417(5)	0.12800393(40) [11]	0.1280039(4) [9]
7	0.06442222(2)	0.0644220(5) [29]	0.06450 [17–19]
8	0.04303821(2)	0.0430381(5) [29]	0.0432 [17–19]
9	0.03432687(2)	0.03432685(15) [29]	
10	0.39342225(5)	0.3934220(7) [9]	
11	0.0544876(8)	0.05443(7) [23]	0.057136(8) [25]

- [5] J.C. Le Guillou and J. Zinn-Justin, *J. Physique* **48**, 19 (1987).
- [6] A.J. Guttmann and I.G. Enting, *J. Phys. A* **27**, 8007 (1994).
- [7] M. Kolesik and M. Suzuki, *Physica A* **215**, 138 (1995).
- [8] A.L. Talapov and H.W.J. Blöte, *J. Phys. A* **29**, 5727 (1996).
- [9] H.W.J. Blöte, E. Luijten, and J.R. Heringa, *J. Phys. A* **28**, 6289 (1995).
- [10] H.W.J. Blöte, J.R. Heringa, A. Hoogland, E.W. Meyer, and T.S. Smit, *Phys. Rev. Lett.* **76**, 2613 (1996).
- [11] H.W.J. Blöte, L.N. Shchur, and A.L. Talapov, *Int. J. Mod. Phys. C* **10**, 1137 (1999).
- [12] M. Hasenbusch, K. Pinn, and S. Vinti, *Phys. Rev. B* **59**, 11471 (1999).
- [13] P. Butera and M. Comi, *Phys. Rev. B* **56**, 8212 (1997).
- [14] R. Guida and J. Zinn-Justin, *J. Phys. A* **31**, 8103 (1998).
- [15] J. García, J.A. Gonzalo, and M.I. Marqués, preprint, cond-mat/0211270.
- [16] K. Binder, *Z. Phys. B* **43**, 119 (1981).
- [17] C. Domb, in *Phase Transitions and Critical Phenomena*, edited by C. Domb and M.S. Green (Academic Press, London, 1974), Vol. 3, p.357.
- [18] N.W. Dalton and C. Domb, *Proc. Phys. Soc.* **89**, 873 (1966).
- [19] C. Domb and N.W. Dalton, *Proc. Phys. Soc.* **89**, 859 (1966).
- [20] J.W. Essam and M.F. Sykes, *Physica* **29**, 378 (1963).
- [21] E. Luijten, *Interaction Range, Universality and the Upper Critical Dimension* (Delft University Press, 1997), p.16.
- [22] J.R. Heringa and H.W.J. Blöte, *Physica A* **232**, 369 (1996).
- [23] J.R. Heringa and H.W.J. Blöte, *Physica A* **251**, 224 (1998).
- [24] J.R. Heringa and H.W.J. Blöte, *Phys. Rev. E* **57**, 4976 (1998).
- [25] A. Yamagata, *Physica A* **222**, 119 (1995).

- [26] A. Yamagata, *Physica A* **231**, 495 (1996).
- [27] For an introduction, see e.g., S.K. Ma, *Modern Theory of Critical Phenomena* (Addison-Wesley, Redwood, California, 1976), and references therein.
- [28] K.G. Wilson and M.E. Fisher, *Phys. Rev. Lett.* **28**, 240 (1972).
- [29] E. Luijten, *Phys. Rev. E* **59**, 4997 (1999).
- [30] M. Campostrini, A. Pelissetto, P. Rossi, and E. Vicari, *Phys. Rev. E* **65**, 066127 (2002).
- [31] B.G. Nickel and Rehr, *J. Stat. Phys.* **61**, 1 (1990).
- [32] B.G. Nickel, *Physica A* **177**, 189 (1991).
- [33] C.F. Baillie, R. Gupta, K.A. Hawick, and G.S. Pawley, *Phys. Rev. B* **45**, 10 438 (1992).
- [34] L.D. Landau, *Physica A* **205**, 41 (1994).
- [35] M.F. Sykes and D.S. Gaunt, *J. Phys. A* **6**, 643 (1973).
- [36] O.G. Mouritsen, *J. Phys. C* **13**, 3909 (1980).

Cluster simulation of the transverse Ising model

We formulate a cluster Monte Carlo method for the anisotropic limit of Ising models on $d + 1$ -dimensional lattices, which in effect, are equivalent with d -dimensional quantum transverse Ising models. Using this technique, we investigate the transverse Ising models on the square, triangular, Kagome, honeycomb, and simple-cubic lattices. The Monte Carlo data are analyzed by finite-size scaling. In each case we find, as expected, that the critical behavior fits well in the $d + 1$ -dimensional Ising universality class. For the transverse Ising model on the square lattice, we determine the Binder cumulant of the classical counterpart for a range of aspect ratios between the system sizes in the third or ‘classical’ direction and that in the other two directions. Matching this universal function with the case of the isotropic Ising model yields the length ratio relating the isotropic Ising model with the anisotropic limit. The efficiency of the present algorithm is reflected by the precision of its results, which improves significantly on earlier analyses.

3.1 Introduction

It is well known that the d -dimensional quantum transverse Ising model (TIM) is equivalent with the anisotropic limit of $d + 1$ -dimensional lattice Ising model. As early as in 1964, Schultz and Mattis [1] displayed this equivalence by mapping the classical Ising model on a quantum model that reduces to the TIM. The reverse path, i.e. from quantum spin models to anisotropic lattice models, was shown by Suzuki [2, 3], by using the Trotter formula [4].

This equivalence enables one to explore the properties of the TIM by the study of its classical counterpart. In this way, one can take advantage of the insight and results that have been obtained from the theory of classical critical phenomena, including the renormalization theory. For instance, one can study the TIM in any number of dimensions, by means of the discretized path integral approach [5, 6], or by applying standard Monte Carlo techniques to its classical counterpart [7].

However, these numerical techniques lead to practical difficulties due to singular behavior in the anisotropic limit of the classical Ising model. When this Hamiltonian limit is approached, the coupling strengths and the correlation length in one of the directions in the classical model diverge, while the couplings in the other directions approach zero. Possibilities to deal with this problem are to approximate the anisotropic limit by a properly strong anisotropy, or extrapolate by taking the anisotropy stronger and stronger [7]. Such simulations tend to be difficult as a consequence of the considerable requirements of computer time and memory.

In this work, we tackle this problem by means of the direct application of a continuous cluster algorithm in the anisotropic limit of the Ising model. As the correlation length in the strong-coupling direction diverges when the Hamiltonian limit is approached, we increase the number of spins in this direction and meanwhile rescale it by a divergent number such that the physical size of the system remains constant. This rescaling renders the strong-coupling dimension continuous, while the other dimensions remain discrete. Thus, there is an infinite number of spins per physical length unit along the strong-coupling direction. In this continuous

limit, cluster algorithms can be formulated [8] whose efficiencies are comparable to the conventional cluster methods for the isotropic case.

The precision of the results obtained by this continuous algorithm indicates that it is efficient in comparison with other methods that have been used to investigate transverse Ising models. These results are in agreement with the expectation that quantum transverse Ising models belong to the universality class of the classical Ising model with one more dimension. An interesting property of this continuous cluster algorithm is that it can be applied to systems in curved geometries [9].

3.2 Anisotropic limit of the Ising model

Using $d = 1$ as an example, we briefly recall the relation between the $d + 1$ -dimensional classical Ising model and the d -dimensional TIM. In view of its relevance for Monte Carlo analyses, we put some emphasis on the behavior of the length scale in the $d + 1$ -st direction. The Hamiltonian of a classical 2-dimensional Ising model on a $N \times M$ square lattice with periodic boundary conditions is defined by

$$\mathcal{H}/k_B T = - \sum_{x,y} [K_x s_{x,y} s_{x+1,y} + K_y s_{x,y} s_{x,y+1}] , \quad (3.1)$$

where the integer coordinates x and y , which are defined modulo N and M respectively, label the lattice sites, and K_x, K_y are the coupling strengths in the x - and y -directions respectively. The spins can assume the values $s_{x,y} = \pm 1$. The critical line of this model is given by [10]

$$\sinh(2K_x) \sinh(2K_y) = 1 . \quad (3.2)$$

Therefore, in the anisotropic limit $\epsilon \rightarrow 0$, the couplings can be written

$$K_x = \epsilon/t, \quad \exp(-2K_y) = \epsilon , \quad (3.3)$$

where t parametrizes the temperature; the critical point is $t_c = 1$.

The evaluation of the partition function $Z(M, N)$ of this model by means of the transfer matrix \mathbf{T} is expressed by

$$Z(M, N) = \sum_{\vec{s}_1, \vec{s}_2, \dots, \vec{s}_M} \langle \vec{s}_1 | \mathbf{T} | \vec{s}_2 \rangle \langle \vec{s}_2 | \mathbf{T} | \vec{s}_3 \rangle \cdots \langle \vec{s}_M | \mathbf{T} | \vec{s}_1 \rangle , \quad (3.4)$$

where the transfer direction is taken along the strong bonds K_y , and the elements of \mathbf{T} are

$$\langle \vec{s}_k | \mathbf{T} | \vec{s}_{k+1} \rangle = \prod_x \exp [K_x s_{x,y} s_{x+1,y} + K_y s_{x,y} s_{x,y+1}] . \quad (3.5)$$

Here \vec{s}_k and \vec{s}_{k+1} are the spin configurations in two adjacent rows respectively. Eq. (3.4) is just the trace of \mathbf{T}^M , so that the partition function is the sum over the M -th powers of the eigenvalues of \mathbf{T} . For large M , the contribution from the largest eigenvalue dominates. Since every different spin contributes a factor ϵ , \vec{s}_k and \vec{s}_{k+1} must be nearly identical. Thus, up to order ϵ we may represent the transfer matrix as

$$\langle \vec{s}_k | \mathbf{T} | \vec{s}_{k+1} \rangle = \langle \vec{s}_k | \exp(-\frac{\epsilon}{t} \mathcal{H}_{\text{qm}}) | \vec{s}_{k+1} \rangle \exp(NK_y) , \quad (3.6)$$

in which \mathcal{H}_{qm} is the 1-dimensional quantum Hamiltonian

$$\mathcal{H}_{\text{qm}} = - \sum_x (s_x^z s_{x+1}^z + t s_x^x) , \quad (3.7)$$

where s^z and s^x are Pauli matrices. \mathcal{H}_{qm} contains non-commuting operators and represents a quantum system with Ising interactions between the nearest-neighboring spins along the chain, and a transverse field t in the x -direction. This establishes the relation between the 2-dimensional Ising model and the 1-dimensional TIM.

As mentioned earlier, one can also derive this equivalence by using the Trotter formula [4], which can be written as:

$$\exp[-\beta\mathcal{H}_{\text{qm}}] = \lim_{M \rightarrow \infty} \left\{ \exp\left[-\frac{\beta}{M}\mathcal{H}_{\text{qm}}\right] \right\}^M, \quad (3.8)$$

where β is the inverse temperature of the quantum system.

A comparison of Eqs. (3.6) and (3.8) yields the relation between the inverse temperature β of the TIM and the lattice size M for the classical Ising model as

$$M = \beta t / \epsilon. \quad (3.9)$$

The equivalence of the TIM and the classical model thus requires that M diverges as $1/\epsilon$ even at nonzero temperatures. This is a serious complication for simulations, especially at low quantum temperatures $\beta \rightarrow \infty$.

For $d \geq 2$, we use the example of the Ising model on the simple cubic lattice. Its Hamiltonian is

$$\mathcal{H}/k_{\text{B}}T = - \sum_{x=1}^N \sum_{y=1}^N \sum_{z=1}^{M_{\text{p}}} [K_{xy} s_{x,y,z} (s_{x+1,y,z} + s_{x,y+1,z}) + K_z s_{x,y,z} s_{x,y,z+1}], \quad (3.10)$$

where $1 \leq x, y \leq N$ and $1 \leq z \leq M_{\text{p}}$ label the lattice sites. The label p emphasizes that M_{p} refers to the *physical* system size; its ratio with N defines the aspect ratio of the 3-dimensional system. Periodic boundary conditions apply. The coupling strengths K_{xy} and K_z in the xy -plane and in the z -direction respectively are initially chosen to be of order one. The behavior of the length scales in the Hamiltonian limit, where K_z diverges while K_{xy} approaches zero, is illustrated by means of a Migdal-type renormalization [11] in the z -direction, without rescaling the x - and y -directions. We expect that this procedure, although only valid as an approximation, will yield a qualitatively correct picture. Each bond in the z -direction is decorated with $n-1$ Ising spins and the bond strength K_{xy} is distributed accordingly among the newly inserted spins. This leads to a model with a lattice spacing along the z -direction which is smaller by a factor n . It is described by the same Hamiltonian Eq. (3.10) but with new couplings $K_{xy}^{(n)}$ and $K_z^{(n)}$, and the z -coordinate is represented by integers $z' = nz$ which run from 1 to $M' = nM_{\text{p}}$:

$$\mathcal{H}'/k_{\text{B}}T = - \sum_{x=1}^N \sum_{y=1}^N \sum_{z'=1}^{M'} [K_{xy}^{(n)} s_{x,y,z'} (s_{x+1,y,z'} + s_{x,y+1,z'}) + K_z^{(n)} s_{x,y,z'} s_{x,y,z'+1}], \quad (3.11)$$

The new couplings satisfy

$$K_{xy}^{(n)} = K_{xy}/n \quad \text{and} \quad \tanh K_z^{(n)} = [\tanh K_z]^{1/n}. \quad (3.12)$$

For large n , one may write $\exp[-2K_z^{(n)}] = \epsilon$, and substitute $\tanh K_z^{(n)}$ in Eq. (3.12) accordingly. One finds $1/n = a [\ln(1+\epsilon) - \ln(1-\epsilon)] \simeq a\epsilon[2 + O(\epsilon^2)]$, where $a = -1/\ln(\tanh K_z)$. This leads to

$$K_{xy}^{(\infty)} = \frac{\epsilon}{t} [1 + O(\epsilon^2)], \quad \exp[-2K_z^{(\infty)}] = \epsilon, \quad (3.13)$$

which has a same form as Eq. (3.3). It also suggests that for nonzero ϵ the critical point $t_c(\epsilon)$ deviates from $t_c(0)$ as ϵ^2 .

This model is equivalent with the TIM on the square lattice with Hamiltonian

$$\mathcal{H}_{\text{qm}} = - \sum_{x,y} [s_{x,y}^z (s_{x+1,y}^z + s_{x,y+1}^z) + t s_{x,y}^x]. \quad (3.14)$$

The inverse proportionality of n and ϵ , together with Eq. (3.9), shows that the physical size $M_{\text{p}} = M'/n$ is proportional to the inverse quantum temperature β .

3.3 Algorithm

As mentioned earlier, a Monte Carlo method for the Hamiltonian limit will have to deal with singular aspects such as the divergent coupling strength K_z , the vanishing coupling strength K_{xy} , and the divergence of the system size M . Using ideas from existing cluster methods [12–14], we introduce procedures to improve the efficiency for the system described by Eqs. (3.1) and (3.3) with small but nonzero ϵ . Then we discuss how to deal with the divergence of the system size M in the y -direction, and finally describe the continuous Wolff algorithm (CWA) for the limit $\epsilon = 0$.

Now, let us recall the cluster algorithm for the isotropic lattice Ising model with nearest-neighbor interactions. If two nearest-neighboring spins on sites m and n , coupled with strength K_{mn} , have the same sign the algorithm will ‘freeze’ the bond between m and n with a probability $p_{mn} = [1 - \exp(-2K_{mn})]$, or ‘break’ the bond with the probability $1 - p_{mn}$. Sites connected by ‘frozen’ bonds are included in the same cluster. One can introduce bond variables $b_{mn} = 0$ or 1 ; frozen bonds have $b_{mn} = 1$ and broken bonds have $b_{mn} = 0$. A pair of opposite spins always has $b_{mn} = 0$. The conventional way to simulate this is to draw a uniformly distributed random number r ($0 < r < 1$) for each bond b_{mn} , set $b_{mn} = 1$ if the spins on sites m and n have the same sign and $r < p_{mn}$.

For the anisotropic model defined by Eqs. (3.1) and (3.3), there are two types of bond variables b_{mn} . For small ϵ , the bond probability between a pair of equal spins in the y -direction is $p_y = 1 - \exp(-2K_y) \propto 1 - \epsilon$, so one has to draw of order $1/\epsilon$ random numbers r before finding a bond variable $b_y = 0$. For the weak bonds in the x -direction, the probability $p_x = 1 - \exp(-2K_x) \propto \epsilon$ that a pair of equal neighbors is connected by a frozen bond is small, and many random numbers are needed before such a ‘bridge’ is found.

A more efficient procedure follows. We first write $b_{mn} = \tilde{b}_{mn} \delta_{s_m s_n}$ where the \tilde{b}_{mn} are independent random variables equal to 0 or 1; $\tilde{b}_{mn} = 1$ with probability $p_x = 1 - \exp(-2K_x)$ or $p_y = 1 - \exp(-2K_y)$ for bonds in the x or y direction respectively. Counting the bond variables sequentially in the y -direction, the distribution $P_y(k_y) \equiv (1 - p_y) p_y^{k_y - 1}$ expresses the probability that $(k_y - 1)$ subsequent bond variables \tilde{b}_{mn} are equal to one, while the k_y -th variable is zero: a ‘break’ occurs at the k_y -th position. Thus the cumulative distribution is

$$C_y(k_y) = \sum_{k=1}^{k_y} P_y(k) = 1 - (p_y)^{k_y}, \quad (3.15)$$

and by mapping the probability distribution $C_y(k_y)$ on the uniform distribution of the random number r , one can transform r into an integer k_y :

$$k_y = 1 + [\ln(r)/\ln(p_y)], \quad (3.16)$$

where $0 < r < 1$ and the square brackets denote the integer part. In contrast, in the x -direction, one uses the distribution $P_x(k_x) \equiv p(1 - p_x)^{k_x - 1}$ to express the probability that $(k_x - 1)$ subsequent variables \tilde{b}_{mn} are zero, while the k_x -th bond variable is one. Also in this case, one transforms a uniformly distributed random number r into an integer k_x :

$$k_x = 1 + [\ln(r)/\ln(1 - p_x)]. \quad (3.17)$$

This method avoids the problem that many random numbers have to be drawn before adding a new bridge or a new break.

For purpose of clarity, we describe in detail the steps in the formation of a Wolff cluster according to the description above.

1. Choose the origin (x, y) of the cluster randomly (see Fig. 3.1), denote its sign $s \equiv s_{x,y}$.
2. Count the neighboring sites on the left-hand side as $(x, y - 1)$, $(x, y - 2)$, \dots , $(x, y - a)$ till the nearest interface $s_{x,y-a-1} = -s$ (see Fig. 3.1). Draw a random number r and compute k_y according to Eq. (3.16). Define l_- as the smaller number of a and $k_y - 1$, and flip the spins from $(x, y - l_- + 1)$ to (x, y) . Do the same for the right-hand side such that the spins from $(x, y + 1)$ to $(x, y + l_+)$ are flipped. Thus, a range of $l_- + l_+$ strongly coupled spins on the x -th row is included in the cluster and flipped.

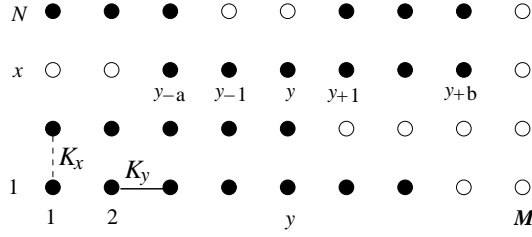


Figure 3.1: Illustration of the anisotropic Ising model on an $N \times M$ lattice. The vertical dashed line represents the weak coupling K_x , the horizontal line represents the strong coupling K_y . The black circles are + spins, and the open circles are -pins.

3. Include into the cluster spins on $(x - 1)$ -th and $(x + 1)$ -th rows connected to the above range by bridges in the weak-coupling direction. Compute k_x according to Eq. (3.17). If $k_x > l_- + l_+$, go to 4. Otherwise, if $s_{x-1, y-l_-+k_x} = s$, include this spin in the cluster and store its position in the ‘stack’ memory. Find a new random value k_x till all the $l_- + l_+$ bonds between x -th and $(x - 1)$ -th rows are accounted for. Do the same for the neighboring sites on the $(x + 1)$ -th row.
4. If the stack is empty, go to 5. Otherwise, read a site (x, y) from the stack, and erase it from the stack. Go to 2.
5. The cluster is completed and flipped.

Although the above procedures can improve the efficiency of the conventional Wolff algorithm, we still have to solve the problem of the divergence of the expectation values of k_x and k_y in parallel with that of M as $\epsilon \rightarrow 0$:

$$\langle k_y \rangle = \left\langle \frac{-1}{\ln(p_y)} \right\rangle \propto \frac{1}{\epsilon}, \quad \langle k_x \rangle = \left\langle \frac{-1}{\ln(1-p_x)} \right\rangle \propto \frac{1}{\epsilon}. \quad (3.18)$$

$\langle k_y \rangle$ and $\langle k_x \rangle$ can be recognized as the average distances, in the y -direction, of the breaks and of the bridges respectively.

To deal with the divergence of the system size M one can rescale the y -direction as $y_p = \epsilon y$, so that the total physical size $M_p = \epsilon M$ and the correlation length in this direction remain approximately constant (see Fig. 3.2). In the limit $\epsilon = 0$, the strong-coupling dimension becomes continuous, i.e., there are infinite number of spins per physical length unit, and the $+/-$ spins are replaced by ranges of sign $+/-$. Thus, the $N \times M$ square lattice reduces to N lines of physical length $M_p = \epsilon M$ (see Fig. 3.2), and Eqs. (3.16) and (3.17) change into

$$l_y = \epsilon k_y = -\ln(r), \quad (3.19)$$

and

$$l_x = \epsilon k_x = -\ln(r) t/2, \quad (3.20)$$

which indicate that the breaks and the bridges occur on a length scale of 1 so that the numbers of these breaks and bridges are finite in this continuous limit. These breaks can be recognized as interfaces separating the ranges of $+$ and $-$ spins, and the bridges serve as the connections between nearest-neighboring lines. Instead of the individual spins one may use the locations of these interfaces as the dynamical variables, and define a continuous Wolff algorithm (CWA) on this basis.

In the conventional Wolff algorithm, the spins are simply stored in an array. Since this information is no longer available, one has to determine the sign of a particular position (x, y) from the positions of the interfaces, supplemented with additional information on the sign at a given position on each continuous line, e.g. at the origin $y = 0$. The sign at position (x, y) is given by $s_x (-1)^n$, where n is the number of interfaces between the origin and position y on the x -th line, and s_x is the sign at the origin of this line.

The steps involved in the continuous Wolff algorithm (CWA) can now be expressed as follows:

1. Choose a random position (x, y) randomly, which means it is at x -th line and its y -coordinate is y , and obtain its sign s according to the directions given above.

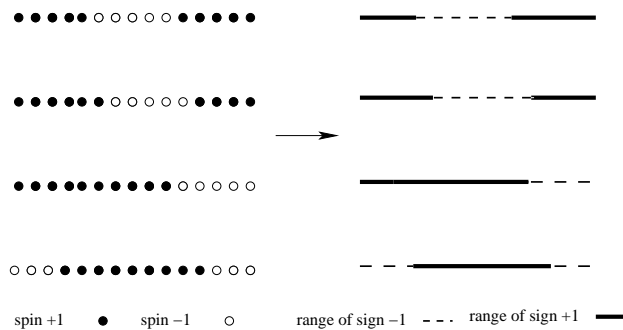


Figure 3.2: Illustration of the procedure leading to the Hamiltonian limit of the classical Ising model. The physical length scale is approximately conserved by reducing the horizontal size of $N \times M/\epsilon$ spins with a factor ϵ . This leads to N continuous lines of length M in the Hamiltonian limit. The left figure shows an anisotropic Ising model with small but nonzero ϵ , and the right one illustrates the $\epsilon = 0$ case.

2. Determine the distance d_l from y to the first interface on the left-hand side of y , and similarly the distance d_r on the right-hand side.
3. Include a range around (x, y) into the cluster as follows. Draw a random number r and obtain l_y from Eq. (3.19). If $l_y < d_l$, create an interface at position $(x, y - l_y)$; otherwise, annihilate the interface at $(x, y - d_l)$. So the left-hand end of the range to be flipped is set at $(x, y - c_l)$, where c_l is the smaller number of d_l and l_y ($c_l = \min(d_l, l_y)$). Find another number from Eq. (3.19) and obtain the right-hand end of the range $(x, y + c_r)$ analogously. Thus, the range from $(x, y - c_l)$ to $(x, y + c_r)$ is included in the cluster and flipped.
4. Create bridges between this range and its nearest-neighboring lines. For the $(x - 1)$ -th line, draw a random number and compute l_x by Eq. (3.20). If $l_x > c_l + c_r$, go to 5. Otherwise, if the sign at position $(x - 1, y - c_l + l_x)$ is equal to s , store the position into the stack. Repeat this procedure till the whole range has been visited. Do the same for the $(x + 1)$ -th line.
5. If the stack is empty, go to 6. Otherwise, read (x, y) from the stack, and erase it from the stack. Go to 2.
6. The cluster is completed and flipped.

In the CWA a spin range is flipped by the creation or annihilation of interfaces. When a range is flipped, there are three possibilities: two interfaces are created, two interfaces are annihilated, or one new interface is created and an existing one is annihilated. In all these cases, the number of interfaces per line remains even. One detail to be mentioned is that, if a flipped range includes the origin of that line, the corresponding array element containing the signs at the origins, should be changed.

It is straightforward to generalize the CWA for applications to d -dimensional TIM's with $d \geq 2$. Related continuous cluster algorithms, such as the Swendsen-Wang variety, can also trivially be formulated on the basis of the above description.

3.4 Test of the algorithm

To test the CWA, we investigated the anisotropic limit of the 2-dimensional Ising model defined by Eqs. (3.1) and (3.3), since it has been solved exactly [10]. The CWA was applied to simulate such systems with L lines of length L and with periodic boundary conditions, where $L = 8, 12, 16, 22$ and 24 . During the simulations, the dimensionless quantity Q_L , which is related to the Binder cumulant [15], was sampled:

Table 3.1: Results of the least-square fits of $Q_L(t)$ for the TIMs defined on the triangular, Kagome, honeycomb, square and cubic lattices.

	triangular	Kagome	honeycomb	square	cubic
L_{min}	6	8	10	2	7
L_{max}	20	20	20	48	14
Q	0.6238 (7)	0.6041 (4)	0.6149 (7)	0.6206 (2)	0.456947 (fixed)
t_c	4.76811 (9)	2.95265 (4)	2.13250 (4)	3.04438 (2)	5.15813 (6)
a_1	0.03138 (5)	0.0894 (1)	0.1027 (8)	0.0497 (2)	0.0235 (2)
a_2	0.0010 (1)	0.0082 (2)	0.0088 (2)	0.00207 (2)	0.0020 (4)
a_3	-0.00023 (7)	-0.0035 (5)	-0.0040 (2)	-0.00043 (6)	-0.0024 (6)
b_1	0.061 (5)	0.066 (2)	0.097 (4)	0.093 (2)	0.205 (2)
b_2	0.14 (2)	-	-	0.018 (6)	-0.118 (3)

$$Q_L(t) = \frac{\langle m^2 \rangle_L^2}{\langle m^4 \rangle_L} \quad (3.21)$$

where m is the magnetization density.

According to universality of the Binder cumulant, the asymptotic value of Q in such a system is equal to that for the lattice Ising model, with isotropic couplings $K_x = K_y$ and system sizes $L \times \alpha L$, where $\alpha = \lim_{\epsilon \rightarrow 0} 1/(\epsilon \sinh 2K_y) = 2$ [10, 16].

In the language of renormalization, the finite-size dependence of the singular part of the free energy density f is formulated as

$$f(t, h, v, \dots; L) = L^{-d} f(tL^{y_t}, hL^{y_h}, vL^{y_i}, \dots; 1), \quad (3.22)$$

where t is the transverse field, h the magnetic field, v the irrelevant field; y_t, y_h and y_i are the corresponding exponents, and d is the dimensionality. Therefore, one expects the following finite-size behavior of $Q_L(t)$ near critical point [17]:

$$Q_L(t) = Q + a_1(t - t_c)L^{y_t} + a_2(t - t_c)^2 L^{2y_t} + \dots \\ + b_1 L^{y_i} + b_2 L^{y_2} + c_1 L^{y_3} (t - t_c) + \dots, \quad (3.23)$$

where $y_2 = d - 2y_h$, $y_3 = y_i + y_t$, and a_1, a_2, b_1, b_2 and c_1 are unknown parameters. The Monte Carlo data were fitted on the basis of this formula, according to the least-squares criterion. The exponents y_t, y_h and y_i were set to the exact Ising values 1, 15/8 and -2 respectively. So $y_2 = d - 2y_h = -7/4$ and $y_3 = y_i + y_t = -1$. A fit including corrections with amplitudes a_1, a_2, a_3, a_4, b_1 and c_1 shows that $t_c = 0.99998$ (6) and $Q = 0.80976$ (22), in a good agreement with the known results $t_c = 1$ and $Q = 0.809678$ (3) [16]. When we set $t_c = 1$ and $Q = 0.809678$, and leave y_t to be fitted, we obtain $y_t = 1.01$ (1), in agreement with the known universal properties of the isotropic Ising model.

In order to compare the efficiency of the CWA with the conventional Wolff method, we investigated the $d = 2$ TIM on a $L \times L$ square lattice with periodic boundary conditions. The CWA was applied to simulate for the model defined by Eqs. (3.10) and (3.13) at the continuous limit $\epsilon = 0$. The length of the third direction is taken as L . The conventional Wolff algorithm was used to study such anisotropic lattice models with small but nonzero ϵ ($1/150 \leq \epsilon \leq 1/6$). The lattice size in the z -direction is taken as L/ϵ , and the couplings K_{xy} and K_z are obtained by substituting ϵ in Eq. (3.13). The transverse field was set as $t = 3.04440$, which is very close to the critical point t_c (see Table 3.1), and the system size at $L = 4$.

For several values of ϵ , the computer time needed for 5 million conventional Wolff steps, was compared to the time needed by the CWA for the same number of steps (see Fig. 3.3). As expected, the efficiency of the conventional Wolff method decreases proportionally for $\epsilon \rightarrow 0$. The efficiency of the CWA is lower than but still comparable to that of the conventional Wolff method for the isotropic Ising model. The reasons are

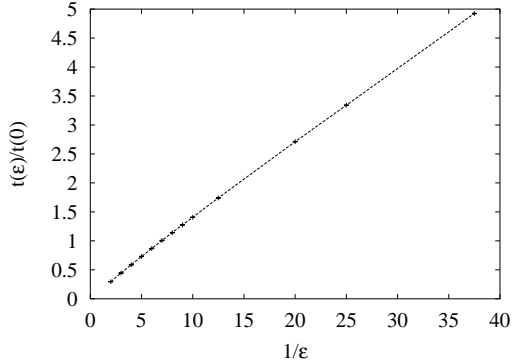


Figure 3.3: Ratio between the time used by the conventional Wolff algorithm and that by the present continuous algorithm, as a function of $1/\epsilon$. Five million Wolff steps are taken for every simulation. The system size and the transverse field are $L = 4$ and $t = 3.04440$ respectively.

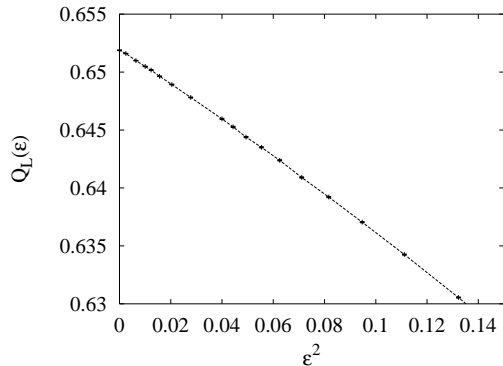


Figure 3.4: Dependence of $Q_L(\epsilon)$ on ϵ , as a function of ϵ^2 , for a system with sizes $L \times L/\epsilon$, with $L = 4$. The transverse field $t = 3.04440$ is set near its critical value. Error bars are approximately equal to the thickness of the lines.

as follows: first, floating-point operations are necessary in the anisotropic limit since the third dimension is continuous; and second, to find the sign at a particular position, one has to find the number of interfaces between this position and the origin of the line where it is located. The time consumption to find the signs is however still acceptable for the system sizes used in this work.

During these simulations, also the quantity $Q_L(\epsilon)$ was sampled as a function of ϵ . The results obtained by the conventional Wolff method as $\epsilon \rightarrow 0$, display satisfactory convergence to $Q_L(0)$ as obtained by the CWA (see Fig. 3.4). The convergence takes place approximately as ϵ^2 . The data for $Q_L(\epsilon)$ were fitted according to the least-squares criterion by the formula

$$Q_L(\epsilon) = Q_L(0) + q_1\epsilon + q_2\epsilon^2 + q_3\epsilon^3 + \dots, \quad (3.24)$$

where q_1 , q_2 and q_3 are unknown parameters. The largest ϵ included in the fit is 0.4, and we also let $Q_L(0)$ to be fitted. The resulting fit satisfied the χ^2 criterion ($\chi^2 = 18$ for 17 degrees of freedom); we obtain $q_1 = -0.0006$ (8), $q_2 = -0.1322$ (5), $q_3 = -0.0076$ (10) and $Q_L(0) = 0.65194$ (7), which is consistent with the Monte Carlo data obtained by the CWA $Q_L(0) = 0.65188$ (6). This fit suggests that the term with the amplitude q_1 vanishes.

This can be explained by Eq. (3.13). Since the critical points $t_c(\epsilon)$ for nonzero ϵ is expected to deviate from $t_c(0)$ as ϵ^2 , while the transverse field was always set as $t_c(0)$ during the simulations, it is not surprising that $Q_L(\epsilon) - Q_L(0) \propto \epsilon^2$.

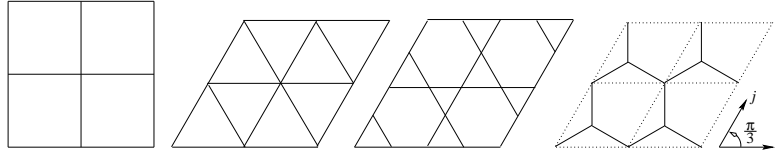


Figure 3.5: The two-dimensional lattices on which the TIM's are investigated. From left to right: square, triangular, Kagome and honeycomb lattices with finite size 2×2 . The geometries of the corresponding anisotropic limit of the classical Ising models are parallel lines which originate from these lattice sites and perpendicular to the planes.

3.5 Applications

3.5.1 Critical points of several TIM's

By means of the CWA, we have investigated the $d = 2$ TIMs on the square, triangular, honeycomb, and Kagome lattices (see Fig. 3.5), and the $d = 3$ TIM on the simple cubic lattice. System sizes were chosen as L^d , so that the physical length ϵM of the continuous direction is equal to L . Periodic boundary conditions were imposed. During the simulations, the Binder parameter $Q_L(t)$ was sampled.

For the $d = 2$ TIMs, the finite-size behavior of $Q_L(t)$ is expected to follow the usual scaling behavior of 3-D Ising system as expressed by Eq. (3.23). Moreover, we expect that the $d = 2$ TIMs on different lattices share the same exponents for the scaling fields t , h , and v , although the unknown amplitudes can be different. The Monte Carlo data for the systems on these different lattices were independently fitted on the basis of Eq. (3.23), according to the least-square criterion. The exponents y_t and y_i are set to the known values 1.587 (2) and -0.815 (4) respectively as reported in the literature, for instance [18–20] and in papers referenced therein. Results of these fits are shown in Table 3.1.

To test the universality of the $d = 2$ TIMs, we set $Q = 0.6206$ and $t_c = 3.04438$ as in Table 3.1 for the square lattice, and thus obtained $y_t = 1.583$ (6), which is in agreement with the known value 1.587. The corrections with amplitudes a_1, a_2, a_3, a_4, b_1 and b_2 were included, and the smallest system size used in the fit is $L = 2$.

For the $d = 3$ TIM, we have to deal with the numerical difficulties associated with the corrections due to the marginally irrelevant field as occur in 4-dimensional Ising-like models [21, 22]. The anomalously slow renormalization flow near the fixed point translates into a similarly slow finite-size convergence of the Binder ratio $Q_L(t)$, and leads to correction factors including small powers of logarithms of the linear system size L . Under these circumstances it is not feasible to determine many independent parameters in the fit. We thus make use of the theoretical predictions for the universal value Q at the critical point and the values of the exponents of the scaling fields. Expanding the finite-size scaling function for $Q_L(t)$, we expect the following behavior [22]:

$$Q_L(t) = Q + \sum_k a_k \{L^{y_t} (\ln L)^{\zeta_t} \left[t - t_c + v \frac{L^{-y_t}}{(\ln L)^{2/3}} \right]\}^k + b_1 L^{y_2} + b_2 (\ln L)^{-1} + b_3 (\ln L)^{-2} \dots, \quad (3.25)$$

where $k = 1, 2, \dots$, $\zeta_t = \frac{1}{6}$, $y_t = 2$ and $y_2 = 4 - 2y_h = -2$. The ‘shift’ term with amplitude v seems unimportant, and was taken to be zero. The universal value Q is taken as the analytical value: $Q = 0.456947$ [21, 23]. Results are shown in Table 3.1.

Thus, by applying the CWA to these 2- or 3-dimensional TIMs, we obtained the critical values of the transverse fields t_c (see Table 3.1). Table 3.2 compares these values to those obtained by other methods which include effective-field approximation [24, 25], effective-field renormalization group (EFRG) [26, 27], series expansion [28, 29] and density-matrix renormalization [31] results. The precision of the present results indicates that our algorithm contributes a useful tool for numerical studies of transverse Ising models. The total computer time consumed by the present simulations is about 5 processor-months at 750 MHz.

Table 3.2: Comparison of the critical values of the transverse field t_c , as obtained by several different methods, for the $d = 2$ TIMs on the square, Kagome, honeycomb and triangular lattices, and the $d = 3$ TIM in the simple cubic lattice.

lattice	Present work	EFA [*] [24, 25]	EFRG [†] [27]	SE [⊗] [28, 29]	PI [•] [6]	S-W [‡] [30]	DMRG [§] [31]
Square	3.04438 (2)	2.742	3.021	3.08	3.225	3.044 (1)	3.046
Kagome	2.95265 (4)	2.742	2.333	–	–	–	–
Honeycomb	2.13250 (4)	–	–	–	–	–	–
Triangular	4.76811 (9)	4.704	4.200	4.118	–	–	–
Cubic	5.15813 (6)	4.704	5.059	5.153	–	–	–

★ : Effective Field Approximation; †: Effective Field Renormalization Group; ⊗: Series Expansion; •: Path Integral Monte Carlo simulation; ‡: Swendsen-Wang in continuous time; §: Density Matrix Renormalization Group.

3.5.2 The Binder ratio and the determination of the length scale

For the isotropic Ising model on the simple cubic lattice, i.e. $K_{xy} = K_z$ in Eq. (3.10), the ratio Q defined by Eq. (3.23) is a universal function $Q(\alpha)$ of the aspect ratio $\alpha = M/N$. On the basis of symmetry arguments it is plausible that a maximum occurs at $\alpha = 1$.

For the corresponding anisotropic system, as obtained by extending the TIM on the square lattice in the Trotter direction, we expect a different dependence of the Binder ratio $Q_a(\alpha)$ on the aspect ratio $\alpha = M_p/N$, where $M_p = \epsilon M$ is the physical size in the continuous dimension. This can be attributed to the spatial anisotropy of the Hamiltonian density at the fixed-point of the anisotropic Ising model. However, the anisotropy of the fixed-point Hamiltonian can be suppressed by an anisotropic rescaling in the strong-coupling direction, i.e., $z \rightarrow z' = \beta z$ so that $0 < z' \leq \beta M_p$. Thus we expect that $Q_a(\alpha)$ of the anisotropic Ising model follows the same universal function Q , but with α replaced by $\alpha' = \beta\alpha = \beta M_p/N$, i.e. $Q_a(\alpha) = Q(\alpha\beta)$. Using instead the logarithm of the aspect ratio as the independent variable, one finds that $Q_a(\ln \alpha) = Q(\ln \alpha + \ln \beta)$, which expresses a shift on the $\ln \alpha$ scale with respect to the isotropic case.

We determined $Q_a(\ln \alpha)$ by means of Monte Carlo simulations for system sizes $L \times L \times \alpha L$, with $L = 8, 12, 16, 20$ and 24 , and several values of α in the range from 0.3 to 3.0. These data were analyzed on the basis of the scaling formula

$$Q_L(\ln \alpha + \ln \beta) = Q_\infty(0) + v_i L^{y_i} + v_2 L^{y_2} + (1 + dL^{y_i}) \sum_{k \geq 2} a_k (\ln \beta + \ln \alpha + cL^{y_a})^k, \quad (3.26)$$

obtained by Taylor expansion in the argument of Q_L to which a finite-size correction with amplitude c has been added. This term describes an L -dependent shift of the maximum of Q_L . The value of $Q_\infty(0)$ is known to be 0.62358 (15) [19]. Corrections with amplitudes v_i and v_2 describe the finite-size dependence of Q near its maximum. The term with amplitude d describes the influence of the anisotropy on the irrelevant finite-size correction.

Although the finite-size correction with amplitude c is clearly observable, we could not satisfactorily determine the associated exponent y_a . We have assumed that $y_a = y_i$ which is consistent with the data. First, we neglected the term with amplitude d and fixed the value of $Q_\infty(0)$ at 0.62358. A reasonable fit is obtained when we include terms up to $k = 7$ in the expansion. We then find $\beta = 0.880$ (6), which is slightly lower than the value $\beta = 0.8881$ (2) which was obtained from the spin-spin correlation function and quoted in Ref. [9, 20]. A reasonable data collapse of the numerical finite-size data for Q is thus obtained in the $Q'_L = Q_L - v_i L^{y_i} - v_2 L^{y_2}$ versus $x' = \ln \alpha - cL^{y_i}$ diagram, shown in Fig. 3.6. However, when we include the term with amplitude d in Eq. (3.26), we obtain a more satisfactory (on the basis of the χ^2 criterion) fit yielding $\beta = 0.886$ (7).

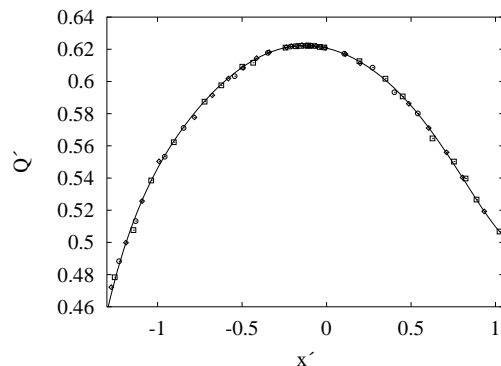


Figure 3.6: Data collapse of $Q_L(\ln \alpha + \ln \beta)$ shown as $Q' = Q_L - v_i L^{y_i} - v_1 L^{y_1}$ versus $x' = \ln \alpha - cL^{y_i}$. The system size are $L = 8$ (\diamond), $L = 12$ (\square), and $L = 16$ (\circ). The solid line is the corresponding fit.

In conclusion, the precision of the present results shows that the CWA is an efficient tool for the investigation of quantum models such as the TIM. The results of the data analysis agree with the general belief that the Hamiltonian limit of the Ising model belongs to the same universality class as the isotropic lattice Ising model. Furthermore, the special feature that one of the dimensions is continuous, makes the CWA suitable for applications to models defined in curved geometries [9].

Bibliography

- [1] T.D. Schultz, and D.C. Mattis, *Rev. Mod. Phys.* **36**, 856 (1964).
- [2] M. Suzuki, *Prog. Theor. Phys.* **46** 1337 (1971).
- [3] M. Suzuki, *Prog. Theor. Phys.* **56** 2454 (1976).
- [4] H.F. Trotter, *Proc. Am. Math. Soc.* **10** 545 (1959).
- [5] R.P. Feynman, *Statistical Mechanics* (Benjamin, Reading, MA, 1972).
- [6] R.M. Strat, *Phys. Rev. B* **33** 1921 (1986).
- [7] A. Wiesler, *Phys. Lett. A* **89**, 352 (1982).
- [8] A continuous time algorithm for discrete quantum systems is due to B.B. Beard and U.-J. Wiese, *Phys. Rev. Lett.* **77**, 5130 (1996). The present algorithm for the Ising model was presented by one of us (H.B.) at the Statphys 20 Conference; see P001/21 in *Livre des Résumés*, ed. A. Gervois, M. Gingold and D. Iagolnitzer (UNESCO Sorbonne, Paris 1998). A related algorithm of the Swendsen-Wang type was described in Ref. [30].
- [9] Y.J. Deng and H.W.J. Blöte, *Phys. Rev. Lett.* **88**, 190602 (2002).
- [10] L. Onsager, *Phys. Rev.* **65**, 117 (1944).
- [11] A.A. Migdal, *Zh. Eksp. Teor. Fiz.* **69**, 1457 (1975); *Sov. Phys. JETP* **42**, 743 (1976).
- [12] R.H. Swendsen and J.-S. Wang, *Phys. Rev. Lett.* **58**, 86 (1987); J.-S. Wang and R.H. Swendsen, *Physica A* **167**, 565 (1990).
- [13] U. Wolff, *Phys. Rev. Lett.* **62**, 361 (1989); *Phys. Lett. B* **228**, 379 (1989).
- [14] E. Luijten and H.W.J. Blöte, *Int. J. Mod. Phys. C* **6**, 359 (1995).

- [15] K. Binder Phys. B **43**, 119 (1981).
- [16] G. Kamieniarz and H.W.J. Blöte, J. Phys. A **26**, 201 (1992).
- [17] H.W.J. Blöte, E. Luijten and J.R. Heringa, J. Phys. A **28**, 6289 (1995).
- [18] R. Guida and J. Zinn-Justin, J. Phys. A **31**, 8103 (1998).
- [19] H.W.J. Blöte, L.N. Shchur and A.L. Talapov, Int. J. Mod. Phys. C **10**, 1137 (1999).
- [20] Y.J. Deng and H.W.J. Blöte, unpublished.
- [21] E. Luijten, *Interaction Range, Universality and the Upper Critical Dimension* (Delft University Press, Delft, 1997).
- [22] J.R. Heringa, H.W.J. Blöte and E. Luijten, J. Phys. A **33**, 2929 (2000).
- [23] E. Brézin and J. Zinn-Justin Nucl. Phys. B **257**,867 (1985).
- [24] E.F. Samento and T. Kaneyoshi, J. Phys. C **21**, 3933 (1988).
- [25] P.A. Slotte, J. Phys. A **20**, L177 (1987).
- [26] Q. Jiang and Z.Y. Li, Phys. Rev. B **40**, 11264 (1989).
- [27] Q. Jiang and X.F. Jiang, Phys. Lett. A **224**, 196 (1997).
- [28] R.J. Elliott and A.P. Young, Ferroelectrics **7**, 23 (1974).
- [29] W.H. Zheng, J. Oitmaa, and C.J. Hamer, J. Phys. A **27**, 5425 (1994).
- [30] R. Rieger and N. Kawashima, Eur. Phys. J. B **9**, 233 (1999).
- [31] M.S.L. du Croo de Jongh and J.M.J. van Leeuwen, Phys. Rev. B **57**, 9494 (1998).

4

Conformal invariance: The Ising model

We apply conformal transformations to the two-dimensional Ising model (4.1) and to the three-dimensional Ising model (4.2).

4.1 The Ising model on a spheroid

We formulate conformal mappings between an infinite plane and a spheroid, and one between a semi-infinite plane and a half spheroid. Special cases of the spheroid include the surface of an infinitely long cylinder, of a sphere, and of a flat disc. These mappings are applied to the critical Ising model. For the case of the sphere and the flat disc, we derive analytical expressions for the second and the fourth moments of the magnetization density, and thus for the Binder cumulant. Next, we investigate Ising models on spheroids and half spheroids by means of a continuous cluster Monte Carlo method for simulations in curved geometries. Fixed and free boundary conditions are imposed for half spheroids. The Monte Carlo data are analyzed by finite-size scaling. Critical values of the Binder cumulants and other ratios on the sphere and on the flat disc agree precisely with the exact calculations mentioned above. At criticality, we also sample two- and one-point correlation functions on spheroids and half spheroids. The magnetic and temperature scaling dimensions, as determined from the Monte Carlo data and the theory of conformal invariance, are in good agreement with exact results.

4.1.1 Introduction

In two dimensions, the consequences of conformal invariance for critical systems have been studied extensively. These studies have produced a large amount of results for both bulk and surface critical phenomena [1–4]. One of the reasons is that the conformal group in two dimensions is an infinite-parameter group, so that the restrictions imposed by conformal invariance are strong. As a result, the forms of the bulk and surface correlation functions, and thus the critical exponents are limited by conformal invariance. Under Cardy’s mapping between an infinite plane and the surface of a cylinder [5], the algebraic decay of correlations in the plane is transformed into an exponential decay along the cylinder. By utilizing the Schwarz-Christoffel formula, Burkhardt et al. conformally mapped the infinite plane onto a rectangular geometry [2]. Furthermore, Cardy and Burkhardt investigated the semi-infinite plane and the parallel-plate geometry with uniform or mixed boundary conditions [4, 6]. The universal properties of a system inside a circle with free or fixed boundary conditions have been studied both exactly and numerically [2, 3, 7].

However, as far as we know, no applications of conformal mappings onto curved geometries have been reported in two dimensions. In this work, we use a conformal mapping of an infinite plane onto a spheroid. By rotating an ellipse about the minor or the major axis, one obtains an oblate or a prolate spheroid, respectively. Special cases include the surface of an infinitely long cylinder, of a sphere, and of a flat disc. The latter case is reached when the polar diameter of the spheroid approaches zero, so that one obtains the

interiors of two circles connected at their perimeters. Thus, this transformation includes Cardy's mapping as a special case. We also perform a different conformal mapping from a semi-infinite plane onto a half spheroid.

We apply these mappings to the critical Ising model. From the known bulk two- and four-point correlation functions in the plane, and the assumption of covariance of the multi-point correlations under conformal mappings, the second and the fourth moments of the magnetization density σ on the sphere and on the flat disc can be expressed in terms of integrals. Since a direct analytic calculation of most of these integrals is not feasible, we evaluated them by means of Monte Carlo integration. As a result, we obtain the universal quantity $Q = \langle \sigma^2 \rangle^2 / \langle \sigma^4 \rangle$, and ratios $r_2 = \langle \sigma^2 \rangle_s / \langle \sigma^2 \rangle_d$ and $r_4 = \langle \sigma^4 \rangle_s / \langle \sigma^4 \rangle_d$, where the subscripts s and d represent the sphere and the flat disc, respectively.

The nonzero net curvature of a spheroid poses a problem for numerical applications of conformal invariance. The difficulty is that a system defined on the spheroid seems to defy any acceptable discretization. Even if the net curvature of a given geometry is zero, numerical simulations may be complicated due to the presence of curved boundaries. An example is a system inside a circle. Badke and Reš et al. have approximated this geometry for the Ising model. A circle is drawn on a square lattice and then free or fixed boundary conditions are imposed by removing or freezing the spins outside the circle, respectively [3, 7]. The effectivity of this approximation is, however, somewhat limited because of irregular finite size behavior, as shown later.

Recently, a continuous cluster Monte Carlo algorithm has become available for the anisotropic limit of the lattice Ising model [8, 9]. One of the interesting properties of this model is that one of its dimensions is continuous, which enables one to apply the continuous cluster method to curved geometries such as a spheroid. Using a Wolff-like version of this algorithm [9], we investigate the Ising model on several spheroids, including a sphere, a flat disc, and a prolate spheroid. Near the critical point, we sampled the moments of the magnetization density and the quantity Q . The Monte Carlo data were analyzed by means of finite-size scaling. For the sphere and the flat disc, the numerical results for the ratios Q , r_2 and r_4 are in excellent agreement with the aforementioned exact calculations, which will be presented in detail in Sec. 4.1.5. At criticality, the two-point magnetic correlations were sampled. Moreover, the Ising model on half spheroids was studied, including that on a half sphere and inside a circle. Both fixed and free boundary conditions were used. The density profiles of the magnetization and of the energy, i.e., one-point correlations, were sampled. From the Monte Carlo data and the theory of conformal invariance, we determined the magnetic and temperature scaling dimensions with a satisfactory precision.

4.1.2 Conformal mappings

In three-dimensional Cartesian coordinates (x, y, z) , a spheroid can be defined by

$$\frac{x^2}{a^2} + \frac{y^2}{a^2} + \frac{z^2}{b^2} = 1, \quad (a, b > 0), \quad (4.1)$$

where a and b are the equatorial and the polar radii, respectively. The parametric equations for the spheroid are therefore

$$x = a \sin \theta \sin \psi, \quad y = a \sin \theta \cos \psi, \quad z = b \cos \theta, \quad (4.2)$$

in which $0 \leq \theta \leq \pi$ and $0 < \psi \leq 2\pi$. Thus, the line element of the spheroid is

$$\begin{aligned} ds'^2 &= dx^2 + dy^2 + dz^2 = (a^2 \cos^2 \theta + b^2 \sin^2 \theta) d\theta^2 + a^2 \sin^2 \theta d\psi^2 \\ &= dw^2 + f(w) d\psi^2. \end{aligned} \quad (4.3)$$

Here, we have defined a new coordinate w to specify the distance along the ellipse from the 'north pole' as a function of θ (see Fig. 4.1). The coordinate w is related to the parameter θ by $w = \int_0^\theta \sqrt{a^2 \cos^2 v + b^2 \sin^2 v} dv$, which is an elliptic integral of the second kind, and $f(w) = a^2 \sin^2 \theta$.

In polar coordinates (r, φ) , the line element in an infinite plane is

$$ds^2 = dr^2 + r^2 d\varphi^2. \quad (4.4)$$

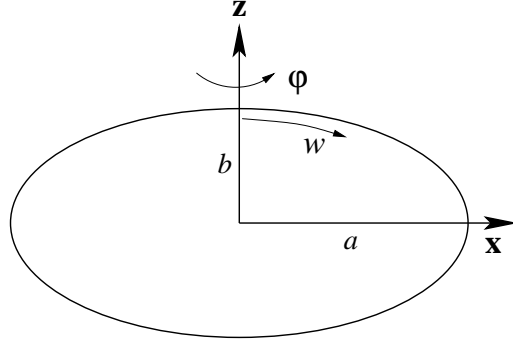


Figure 4.1: Example of an ellipse with $1/e = a/b = 2$. The corresponding oblate spheroid is obtained by the rotation of the ellipse about the z direction. The new coordinate w specifies the distance along the ellipse from the north pole.

A conformal transformation from the infinite plane into the spheroid is thus established by the equations

$$r = e^{-g(\theta)}, \text{ and } \varphi = \psi, \quad \text{with } g(\theta) = \int^{\theta} \sqrt{(b/a)^2 + \cot^2 v} dv, \quad (4.5)$$

and by the requirement that the points $r = 0$ and $r = \infty$ are mapped onto points $\theta = \pi$ and 0 , respectively. The transformation (4.5) is conformal, because the line elements (4.4) and (4.3) differ only by a position-dependent factor:

$$ds^2 = ds'^2 [e^{-2g(\theta)}/a^2 \sin^2 \theta]. \quad (4.6)$$

Under a conformal mapping ($\vec{r} \rightarrow \vec{r}'$), a multi-point correlation function covariantly transforms as [1]

$$\langle \sigma_1(\vec{r}_1) \sigma_2(\vec{r}_2) \cdots \rangle_{\vec{r}} = b(\vec{r}_1)^{-X_1} b(\vec{r}_2)^{-X_2} \cdots \langle \sigma_1(\vec{r}'_1) \sigma_2(\vec{r}'_2) \cdots \rangle_{\vec{r}'}, \quad (4.7)$$

where σ_i is a scaling operator (e.g., associated with the magnetization density or the energy density), X_i is the corresponding scaling dimension, and $b(\vec{r})$ is the rescaling factor, which reads $b(\vec{r})^2 = ds^2/ds'^2$.

In the infinite plane, the bulk two-point correlation function at criticality behaves as [10]

$$\langle \sigma(\vec{r}_1) \sigma(\vec{r}_2) \rangle_{\text{plane}} = B |\vec{r}_2 - \vec{r}_1|^{-2X}, \quad (4.8)$$

where B is a constant. Thus, according to Eqs. (4.5)-(4.8), one obtains the correlation function $g_1(\theta)$ of two points (θ, ψ) and $(\theta, \psi + \pi)$ on a spheroid ($\psi \leq \pi$)

$$g_1(\theta) = B(2a \sin \theta)^{-2X}. \quad (4.9)$$

The evaluation of the mapping formula (4.5) is complicated in general. However, for the special cases mentioned above, it simplifies and yields more results.

1. Surface of a cylinder

As the polar radius $b \rightarrow \infty$, the spheroid approaches the surface of an infinitely long cylinder. The substitutions of a new coordinate $u = b\theta$ and the radius $R = a$ of the cylinder lead to

$$ds'^2 = du^2 + R^2 d\psi^2, \quad (-\infty < u < \infty, 0 < \psi \leq 2\pi), \quad (4.10)$$

and the mapping formula (4.5) simplifies to

$$r = e^{-u/R}, \quad \text{and} \quad \varphi = \psi. \quad (4.11)$$

Thus, Cardy's mapping is restored [5]. The critical two-point correlation functions along the cylinder are then

$$\langle \sigma(u_1, \psi) \sigma(u_2, \psi) \rangle = BR^{-2X} e^{-X|u_1 - u_2|/R} (1 - e^{-|u_1 - u_2|/R})^{-2X}. \quad (4.12)$$

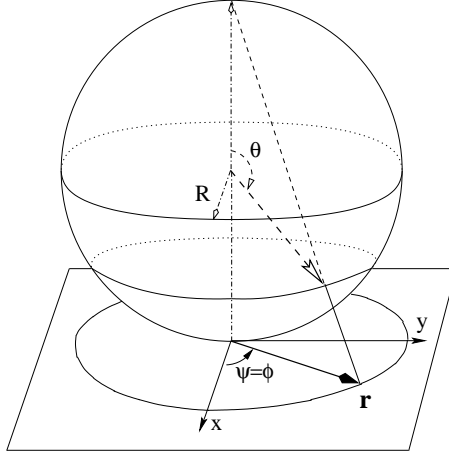


Figure 4.2: Illustration of the conformal mapping of an infinite plane on the surface of a sphere.

So the correlations decay exponentially for $|u_1 - u_2| \gg 0$.

II. Surface of a sphere

One obtains a sphere when the polar and the equatorial radii are equal, i.e., $b = a = R$. The line element (4.3) reduces to $ds'^2 = R^2 (d\theta^2 + \sin^2 \theta d\psi^2)$, and the mapping formula becomes

$$r = 2R \cot(\theta/2), \quad \text{and} \quad \varphi = \psi. \quad (4.13)$$

A geometric picture of this mapping involves the placement of a sphere with radius R on top of an infinite plane (Fig. 4.2). The mapping of a point \vec{r} in the plane on the sphere is defined as the intersection between the sphere and the line connecting the north pole and the point \vec{r} . Here, the vector \vec{r} stands for the point (r, φ) in Eq. (4.13). According to Eqs. (4.7), (4.8), and (4.13), one has the pair correlation function on the sphere as

$$\langle \sigma(\theta_1, \psi_1) \sigma(\theta_2, \psi_2) \rangle = BR^{-2X} 2^{-X} [1 - \sin \theta_1 \sin \theta_2 \cos(\psi_1 - \psi_2) - \cos \theta_1 \cos \theta_2]^{-X}. \quad (4.14)$$

If one introduces \vec{R} to represent the vector from the center of the sphere to the point (θ, ψ) , equation (4.14) reduces to

$$\langle \sigma(\vec{R}_1) \sigma(\vec{R}_2) \rangle = B |\vec{R}_1 - \vec{R}_2|^{-2X}, \quad (4.15)$$

which, interestingly, has the same form as Eq. (4.8).

III. Surface of a flat disc

In the limit $b \rightarrow 0$ of an oblate spheroid, a flat-disc geometry is reached. The coordinate w and the element (4.3) respectively reduce to

$$w = a \sin \theta \quad \text{and} \quad ds'^2 = dw^2 + w^2 d\psi^2, \quad (w \leq R = a), \quad (4.16)$$

and the mapping formula becomes

$$r = \begin{cases} w/R & 0 \leq r < 1 \\ R/w & r \geq 1 \end{cases}. \quad (4.17)$$

This mapping can be generalized to any number of dimensions.

Under the mapping (4.17), one finds two formulas for $g(\vec{w}_1, \vec{w}_2) = \langle \sigma(\vec{w}_1) \sigma(\vec{w}_2) \rangle$, of which the applicability depends on whether or not the two points \vec{r}_1 and \vec{r}_2 lie in the same face of the flat disc:

$$g(\vec{w}_1, \vec{w}_2) = \begin{cases} B[w_1^2 + w_2^2 - 2w_1 w_2 \cos(\psi_1 - \psi_2)]^{-X} & (\vec{w}_1, \vec{w}_2 : \text{same face}) \\ B[(w_1 w_2)^2 + R^2 - 2w_1 w_2 \cos(\psi_1 - \psi_2)]^{-X} & (\vec{w}_1, \vec{w}_2 : \text{opposite faces}) \end{cases} \quad (4.18)$$

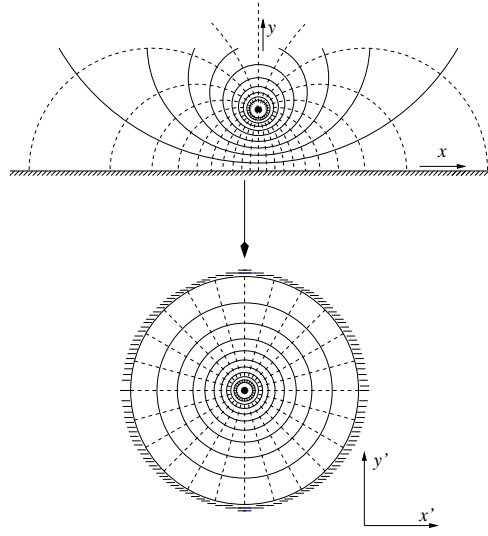


Figure 4.3: Illustration of the conformal mapping from a semi-infinite plane on a single disc.

where we have introduced \vec{w} to represent the vector from the center of the disc to the point (w, ψ) .

The derivative $\partial r/\partial w$ in Eq. (4.17) is discontinuous at the edge $w = R$. One may thus expect that finite-size corrections arise for the critical behavior near the edge.

Next, we describe the conformal transformation between a semi-infinite plane and a half spheroid. The latter object is defined by Eq. (4.1) but with $z \leq 0$. The mapping can conveniently be described in two steps. First, one parameterizes the plane complex numbers $z = x + iy$, so the formula $z' = (z - i)/(z + i)$ maps the semi-infinite plane $\mathbb{R} \times \mathbb{R}^+$ onto the interior of a unit circle (Fig. 4.3) [1]. This conformal mapping yields the profile of a scaling operator inside a unit circle as

$$\langle \sigma(r') \rangle = (1 - r'^2)^{-2X} . \quad (4.19)$$

This result can be generalized to any number of dimensions [1, 2]. Second, the interior of the unit circle is conformally mapped on the half spheroid under the transformation (4.5). In the limit $b \rightarrow \infty$, a semi-infinite cylinder (Eq. (4.10) but with $u \geq 0$) is reached, on which the profile of a scaling operator behaves as

$$\langle \sigma(u) \rangle \propto R^{-X} e^{-uX/R} (1 - e^{uX/2R})^{-X} . \quad (4.20)$$

For $b = a = R$ a half spheroid reduces to a half sphere, and one has

$$\langle \sigma(\theta) \rangle \propto (R \cos \theta)^{-X} . \quad (4.21)$$

4.1.3 Exact calculations

Since the transformations between the plane and the special cases of the spheroid (Eqs. (4.11), (4.13), and (4.17)) are relatively simple, it is possible to derive the expressions for $\langle \sigma^2 \rangle$ and $\langle \sigma^4 \rangle$ from the exact solution of the Ising model in the infinite plane [10]. For the case of an infinitely long cylinder, Burkhardt has evaluated these expressions by means of Monte Carlo integration [11]. The result is consistent with that obtained from direct simulations of systems on the cylinder [11]. Here, we follow analogous procedures for the surface of a sphere and of a flat disc.

In the continuum limit, the second and fourth moments of the magnetization density $\langle \sigma^2 \rangle$ and $\langle \sigma^4 \rangle$ can be given in terms of the two- and four-spin correlation functions, respectively:

$$\langle \sigma^2 \rangle = \rho^2 \int dS_1 dS_2 g(\vec{r}_1, \vec{r}_2) , \text{ and } \langle \sigma^4 \rangle = \rho^4 \int dS_1 \cdots dS_4 g(\vec{r}_1, \vec{r}_2, \vec{r}_3, \vec{r}_4) , \quad (4.22)$$

where ρ is the areal density of the spins, and dS_i represents the number of spins in an infinitesimal area. For a sphere, ρ and dS_i can be written as $1/(4\pi R^2)$ and $R^2 \sin\theta_i d\theta_i d\psi_i$, respectively. For a flat disc, $\rho = 1/(2\pi R^2)$ and $dS_i = r_i dr_i d\psi_i$. R is the radius of the sphere or the flat disc. $g(\vec{r}_1, \vec{r}_2)$ and $g(\vec{r}_1, \vec{r}_2, \vec{r}_3, \vec{r}_4)$ are the two- and four-spin correlation functions.

The two-point correlation function is known exactly (Eq. (4.8)). An exact result is also available for the bulk four-spin correlation of the two-dimensional critical Ising model, which is given in terms of pair correlations by [12]

$$g(1, 2, 3, 4) = \frac{1}{2} \left\{ \left[\frac{g(1, 2)g(2, 3)g(3, 4)g(4, 1)}{g(1, 3)g(2, 4)} \right]^2 + (2 \leftrightarrow 3) + (3 \leftrightarrow 4) \right\}^{1/2}. \quad (4.23)$$

Here, for simplicity, we have written $g(\vec{r}_1, \vec{r}_2)$ and $g(\vec{r}_1, \vec{r}_2, \vec{r}_3, \vec{r}_4)$ as $g(1, 2)$ and $g(1, 2, 3, 4)$, respectively. The notation $(i \leftrightarrow j)$ represents the expression between square brackets $[\]$ with i and j interchanged.

The universal amplitude ratio $Q = \langle \sigma^2 \rangle^2 / \langle \sigma^4 \rangle$ is simply related to the Binder cumulant [13].

I. Surface of a sphere

The substitution of the pair correlation on a sphere (Eq. (4.14)) leads to

$$\begin{aligned} \langle \sigma^2 \rangle &= \rho^2 4\pi R^2 \int_0^{2\pi} d\psi_2 \int_0^\pi d\theta_2 R^2 \sin\theta_2 g(0, 0; \theta_2, \psi_2) \\ &= BR^{-2X} 2^{-X-1} \int_0^\pi d\theta_2 \sin\theta_2 (1 - \cos\theta_2)^{-X} \\ &= BR^{-2X} 2^{-2X} / (1 - X), \end{aligned} \quad (4.24)$$

For the Ising model, $X = 2 - y_h = 1/8$ so that $\langle \sigma^2 \rangle = (2^{11/4}/7)BR^{-2X} \approx 0.961\,024\,5BR^{-2X}$.

Eqs. (4.22) and (4.23) and substitutions of the integration variables $x_i = \theta_i/\pi$ and $y_i = \psi_i/2\pi$ lead to

$$\langle \sigma^4 \rangle = BR^{-4X} \pi^3 2^{-2X-3} \int_0^1 dx_2 dx_3 dx_4 dy_3 dy_4 f(x_2; x_3, y_3; x_4, y_4), \quad (4.25)$$

with $f(x_2; x_3, y_3; x_4, y_4) = \sin(\pi x_2) \sin(\pi x_3) \sin(\pi x_4) g(1, 2, 3, 4)$, where the coordinates of these four points are $(0, 0)$, $(\pi x_2, 0)$, $(\pi x_3, 2\pi y_3)$, and $(\pi x_4, 2\pi y_4)$. This equation was evaluated with a Monte Carlo procedure, which approximates the integral by

$$\langle \sigma^4 \rangle = BR^{-4X} \pi^3 2^{-2X-3} N^{-1} \sum_{i=1}^N f(x_2^{(i)}; x_3^{(i)}, y_3^{(i)}; x_4^{(i)}, y_4^{(i)}), \quad (4.26)$$

where $x^{(i)}$ and $y^{(i)}$ are uniformly distributed random numbers in the interval $(0, 1)$. It yields $\langle \sigma^4 \rangle = BR^{-4X} (1.198\,78 \pm 0.000\,02)$, where the two decimal numbers are the average and standard error obtained from 1000 determinations of the integral. Each integral involves 10^6 Monte Carlo steps.

Thus, the value of the dimensionless quantity is obtained as $Q = 0.770\,42 \pm 0.000\,01$.

II. Surface of a flat disc

The critical pair correlations on a flat disc are given by Eq. (4.18). The evaluations both of $\langle \sigma^2 \rangle$ and $\langle \sigma^4 \rangle$ were done by means of Monte Carlo procedures because in this case the symmetry lower than that of a sphere. The calculation must allow for the fact that the form of the pair correlation depends on whether or not the two points are in the same face (Eq. (4.18)). Taking into account all possible distributions of the four correlated points, one finds

$$\langle \sigma^4 \rangle = \rho^4 \int_0^R dr_1 \cdots dr_4 \int_0^{2\pi} d\psi_1 \cdots d\psi_4 r_1 r_2 r_3 r_4 [2g_0(1, 2, 3, 4) + 8g_1 + 6g_2], \quad (4.27)$$

where $g_0(1, 2, 3, 4)$ defines correlations of four points on the same face, g_1 applies to three points on one face and one on the other, and g_2 applies to two points on one face and two on the other. From this calculation, we obtain $\langle \sigma^2 \rangle = R^{-2X}(1.041\,56 \pm 0.000\,01)$, $\langle \sigma^4 \rangle = R^{-4X}(1.412\,73 \pm 0.000\,05)$, and thus $Q = 0.767\,91 \pm 0.000\,03$.

The ratios of moments of the magnetization density on the sphere and on the flat disc are thus:

$$r_2 = \langle \sigma^2 \rangle_s / \langle \sigma^2 \rangle_d = 0.922\,68(2), \text{ and } r_4 = \langle \sigma^4 \rangle_s / \langle \sigma^4 \rangle_d = 0.848\,57(4), \quad (4.28)$$

where the number between parentheses stands for the estimated error in the last decimal place.

4.1.4 Models and algorithms

As mentioned before, simulations on a spheroid are difficult due to the incompatibility of regular lattices with curved geometries. Here, we tackle this problem by using the Hamiltonian limit of a two-dimensional lattice Ising model. For such a system, an efficient continuous Wolff-like method has been explained in detail [9]. Here, we describe the application of this algorithm to simulations in curved geometries.

The Hamiltonian of an Ising model on a $L \times L$ square lattice with periodic boundary conditions reads

$$\mathcal{H}/k_B T = - \sum_{x,y} [K_x \sigma_{x,y} \sigma_{x+1,y} + K_y \sigma_{x,y} \sigma_{x,y+1}] \quad (4.29)$$

where the integers $1 \leq x, y \leq L$ label the lattice sites. K_x and K_y are the coupling strengths along the x and y direction, respectively. The spins can assume the values $\sigma_{x,y} = \pm 1$. The critical line of this model is given by [10]

$$\sinh(2K_x) \sinh(2K_y) = 1. \quad (4.30)$$

In the anisotropic limit $\epsilon \rightarrow 0$, the couplings therefore are

$$K_x = \epsilon/t, \quad \exp(-2K_y) = \epsilon, \quad (4.31)$$

where t is a temperature-like parameter whose critical point is $t_c = 1$. It is known that in this limit the system is equivalent to the quantum transverse Ising chain [14,15] with nearest-neighbor couplings and an external field t :

$$\mathcal{H}_{\text{QM}} = - \sum_x (\sigma_x^z \sigma_{x+1}^z + t \sigma_x^x), \quad (4.32)$$

with σ^z and σ^x Pauli matrices.

Since our purpose is the application of conformal invariance, we have to restore isotropy asymptotically for the system with $K_x < K_y$. This can be done by increasing the number of spins in the y direction by a factor $L_y/L_x = \sinh 2K_y = 1/2\epsilon$ [16]. Meanwhile, one rescales the y direction as $y' = 2y/\epsilon$ so that the system sizes along the x and y direction are equal again: $L'_y = L_x$. As a result, the y dimension becomes continuous as $\epsilon \rightarrow 0$, i.e., there is an infinite number of spins per physical length unit, and the lattice structure transforms into L lines of length L . The spins form ranges of $+/-$ signs, and the number of interfaces in the system is of order L^2 .

For this anisotropic limit, a full description of the aforementioned continuous Wolff-like algorithm has been given in Ref. [9]. For the convenience of the reader, we summarize the essential points. During the formation of a cluster, a bond between nearest-neighboring spins with the same sign is 'frozen' with a probability $P = 1 - \exp(-2K)$ or 'broken' with $1 - P$. Sites connected by 'frozen' bonds are included in the same cluster. For the anisotropic limit, the probability P in the x and y direction will be of order ϵ and $1 - \epsilon$, respectively. Thus, the strong-coupling bonds will continue to connect spins in the y direction until a 'break' occurs with a probability of order ϵ per bond. Therefore, after the rescaling discussed above, the connected spins along the lines in the y direction form ranges of $+/-$ signs with lengths of order 1, and the breaks are just the aforementioned interfaces. Moreover, the average distance of the bonds between adjacent lines is also of order 1. These weak-coupling bonds serve as 'bridges' between neighboring lines to connect ranges of the same sign, and help to build clusters. Analogous to cluster methods for the discrete models, the aforementioned continuous cluster algorithm flips one or more clusters during a Monte Carlo step depending

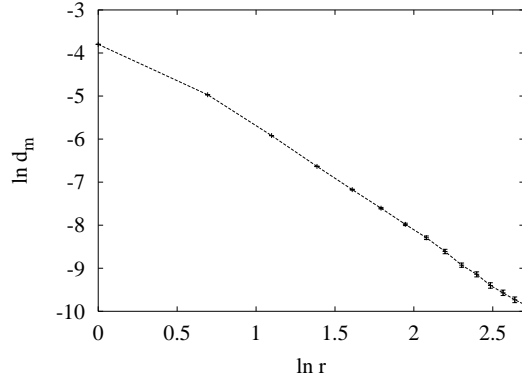


Figure 4.4: Decay of the difference $d_m(r)$ of the magnetic correlation functions in the x and y direction, shown as $\ln d_m$ vs $\ln r$. The system size is 40×40 .

on whether it is Wolff-like or Swendsen-Wang-like. The correctness and efficiency of this method has been demonstrated both in two and three dimensions [9].

Although the long-distance behavior of such an anisotropic system is the same in the x and y direction, corrections may exist at short distances. We investigate this problem in a system with size $L = 40$. We sampled the difference $d_m(r)$ of the magnetic correlation functions over distances r in the x and y direction

$$d_m(r) = \frac{1}{V} \sum_x \int dy \langle \sigma_{x,y} \sigma_{x+r,y} - \sigma_{x,y} \sigma_{x,y+r} \rangle, \quad (4.33)$$

where $V = \sum_x \int dy = L \times L$ is the area of the square. A plot of d_m as a function of r is shown in Fig. 4.4. The fact that the line becomes approximately straight at the right-hand side indicates that the leading correction behaves as r^{y_a} . From Fig. 4.4, we estimate the associated exponent $y_a \approx -2.25$, so we simply assume that $y_a = -2X_h + y_i$, where $y_i = -2$ is the correction-to-scaling exponent in the two-dimensional Ising model, and $X_h = 1/8$ is the magnetic scaling dimension. Taking into account the periodic boundary conditions, we fitted the Monte Carlo data according to the least-squares criterion on the basis of

$$d_m = r^{-2X_h} \{ a_1 [r^{y_i} + (L-r)^{y_i}] + a_2 [r^{y_1} + (L-r)^{y_1}] \}, \quad (4.34)$$

where a_1, a_2 are unknown parameters, and the term with $y_1 = -3$ is another significant correction. We obtain $a_1 = 0.0228(6)$ and $a_2 = 0.027(3)$.

Since the model is now continuous in the y direction, one can investigate it in curved geometries such as a spheroid. As an example, we consider the case of a sphere S^2 . The structure of the anisotropic model in the flat geometry defined by Eqs. (4.29) and (4.31) consists of L lines of length L . Each of these lines can be understood as a circle S^1 because of the periodic boundary condition. As a result, one can represent the 'lattice structure' on a sphere S^2 by L uniformly distributed circles with varying radius (Fig. 4.5), such that there are strong couplings along the circles while weak couplings occur between adjacent circles. The location of the k th circle is $\theta_k = (k - \frac{1}{2})\pi/L$, with $k = 1, 2, \dots, L$ (Fig. 4.5), and the corresponding circumference is $c_k = 2L \sin \theta_k$, which accounts for the S^2 curvature. Since the probability of a weak-coupling bond is defined *per unit of length*, and the adjacent circles on a sphere have different radii, the distribution of these weak-coupling bonds still requires a length scale. It was chosen as the average length scale of both circles. Self-interactions via weak bonds over the poles $\theta = 0$ or π could, in principle, occur at the circles with $k = 1$ and L , respectively. But these interactions may be set to zero because the circles at $\theta = 0$ and π have a zero length. By means of the continuous Wolff-like algorithm, we simulated the above model on a sphere. The magnetic correlation of diametrically opposite points was sampled,

$$g_0(\theta) = \frac{1}{\pi} \int_0^\pi d\psi \langle \sigma(\theta, \psi) \sigma(\pi - \theta, \psi + \pi) \rangle. \quad (4.35)$$

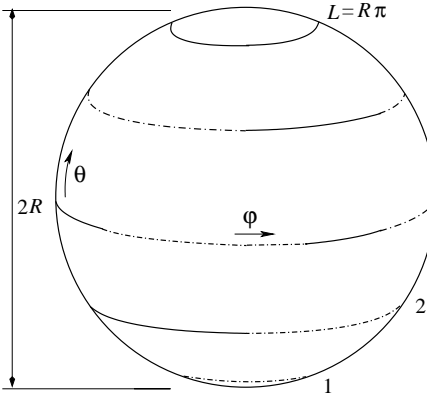


Figure 4.5: Example of 'lattice structure' on a sphere, on which $L = 5$ circles represent continuous lines of spins in the strong-coupling direction. The full and dash-dotted parts of the circles represent (arbitrarily chosen) ranges of spins with different signs.

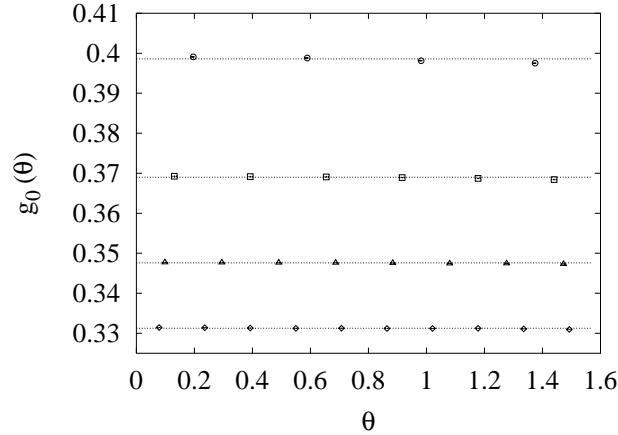


Figure 4.6: The magnetic correlation functions $g_0(\theta)$ on spheres vs θ . The Monte Carlo data are shown for system sizes $L = 8$ (\circ), $L = 12$ (\square), $L = 16$ (\triangle), and $L = 20$ (\diamond). The lines show the corresponding fits. The angle θ is given in radians.

An example for systems without self-interactions at $\theta = 0$ and π is shown in Fig. 4.6. As the number of the circles L increases, the pole $\theta = 0$ is approached, and the spacing of adjacent circles decreases. The lines are quite straight, which indicates that the spherical symmetry is restored asymptotically. We have also investigated the system with self-interactions over the poles. Significant deviations from isotropy occur in this case.

On a microscopic scale, the 'lattice' structure on a sphere is the same as that on a flat plane. However, for finite L , apart from microscopic deviations from the uniformity, the discretization in θ may lead to a global effect on the coupling strength. According to the trapezium rule, we expect that this deviation vanishes as L^{-2} . Under renormalization this effect leads to corrections proportional to L^{y_t-2} , where $y_t = 1$ is the temperature renormalization exponent. Thus, this effect vanishes when $L \rightarrow \infty$, and the critical point on a sphere is identical to the one on the flat plane. Moreover, since the exponent of the irrelevant field $y_i = -2$, it is expected that the term with L^{y_i-2} dominates over the corrections of order L^{y_i} , as will be confirmed later.

As an alternative way for the distribution of L circles on a sphere, the location of the k th circle can be given by $\theta_k = (k - 1)\pi/(L - 1)$, so that in this case the circumference of the sphere is $c = 2(L - 1)$. It was

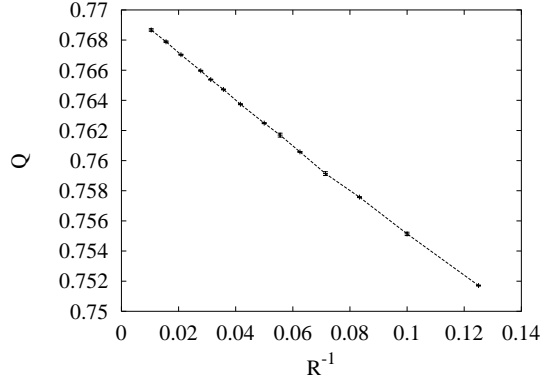


Figure 4.7: The dimensionless quantity Q_R at criticality vs R^{-1} .

found numerically that the spherical symmetry is less well restored in this case. That may be due to the singularity of the zero radii of the circles with $k = 1$ and L .

The same procedure can be applied to the disc geometry. The k th circle is simply located at $r_k = (k - 1)$ and its circumference is given by $c_k = 2\pi(k - 1)$, with $k = 1, 2, \dots, L$. For a general spheroid with constant ratio $e = b/a$, the problem that the circles should be evenly distributed is solved in two steps. First, since the circumference of the corresponding ellipse is $2L$, the value of the parameter a can be numerically calculated from the equation $L = a \int_0^L dw = a \int_0^\pi d\theta \sqrt{\cos^2 \theta + e^2 \sin^2 \theta}$. Second, the location of the k th circle can be obtained by solving for θ_k in equation $k - \frac{1}{2} = a \int_0^{\theta_k} d\theta \sqrt{\cos^2 \theta + e^2 \sin^2 \theta}$. The corresponding circumference is $c_k = 2\pi a \sin \theta_k$ ($k = 1, 2, \dots, L$).

4.1.5 Numerical results

By means of the continuous Wolff-like algorithm, we performed simulations of the Ising model on a sphere, on a flat disc, on a spheroid with $e = 2$, on a half sphere, and inside a circle.

1. Surface of a sphere

For systems on a sphere, we sampled $\langle \sigma^2 \rangle$, $\langle \sigma^4 \rangle$, and $Q_R(t)$ near the critical point. In addition, the two-point magnetic correlation function $g_1(\theta) = \langle \sigma(\theta, \psi) \sigma(\pi - \theta, \psi) \rangle$ was determined at criticality. The system sizes are taken as 15 values ranging from $L = 8$ to 96.

According to finite-size scaling, in the critical region, $Q_R(t)$ behaves as

$$Q_R(t) = Q_c + a_1 R^{y_t} (t - t_c) + a_2 R^{2y_t} (t - t_c)^2 + \dots + b_1 R^{y_c} + b_2 R^{y_i} + \dots, \quad (4.36)$$

where a_1 , a_2 , b_1 , and b_2 are unknown parameters, and Q_c is the universal value for the infinite system at criticality. The correction with exponent $y_c = y_t - 2 = -1$ is due to the discretization of the sphere as explained above. An example is shown in Fig. 4.7. The approximate linearity indicates that the approach of $Q_R(0)$ to Q_c occurs as R^{-1} . Formula (4.36) was fitted to Monte Carlo data according to the least-squares criterion. The value of the temperature parameter is fixed at $t_c = 1$. We obtain $Q_c = 0.770\,43(3)$, which is consistent with the exactly calculated value $0.770\,42(1)$ in Sec. 4.1.3.

Similarly, the finite-size behavior of $\langle \sigma^2 \rangle$ is

$$\langle \sigma^2 \rangle = R^{-2X_h} [m_2 + a_1 R^{y_t} (t - t_c) + a_2 R^{2y_t} (t - t_c)^2 + \dots + b_1 R^{y_c} + b_2 R^{y_i} + \dots], \quad (4.37)$$

and that of $\langle \sigma^4 \rangle$ is

$$\langle \sigma^4 \rangle = R^{-4X_h} [m_4 + a_1 R^{y_t} (t - t_c) + a_2 R^{2y_t} (t - t_c)^2 + \dots + b_1 R^{y_c} + b_2 R^{y_i} + \dots]. \quad (4.38)$$

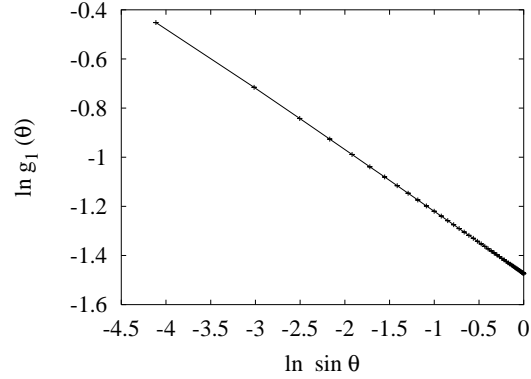


Figure 4.8: Decay of the magnetic correlation function $g_1(\theta)$, shown as $\ln g_1(\theta)$ vs $\ln \sin \theta$. The number of circles on the sphere is $L = 96$. The line shows the corresponding fit.

Table 4.1: Fits of the correlation functions $g_1(\theta)$ on spheres.

L_{\min}	L_{\max}	θ_{\max}	X_h	a_0	a_1	a_2
8	96	1.40	0.12497(4)	0.72215(5)	-0.026(2)	-0.023(4)
a_3	b_0	b_1	c
-0.0006(1)	-0.427(3)	0.21(2)	-0.209(3)

The exponents $-2X_h$ and $-4X_h$ of R are obtained by the substitution of $X_h = 1/8$. The fits yield $m_2 = 0.61988(3)$ and $m_4 = 0.49875(5)$.

According to Eq. (4.14), $g_1(\theta) \propto (L \cos \theta)^{-2X_h}$, which is confirmed numerically in Fig. 4.8. On the basis of finite-size scaling and conformal invariance, the correlation function $g_1(\theta, L)$ is expected to behave as

$$g_1(\theta, L) = L^{-2X_h} \{ (\cos \theta)^{-2X_h + cL^{y_c}} [a_0 + a_1(L\pi - L\theta)^{y_c} + a_2(L\pi - L\theta)^{y_i} + a_3(L \sin \theta)^{y_c}] + b_0L^{y_c} + b_1L^{y_i} \}, \quad (4.39)$$

where $a_0, a_1, a_3, b_0, b_1, c$ are unknown parameters. The corrections with amplitudes a_1 and a_2 are due to the deviations from isotropy at short distances; the term with a_3 accounts for the inhomogeneity because of the discretization of the θ direction. Equation (4.39) was fitted to the Monte Carlo data. As a consistency test, we choose X_h as a free parameter. We obtain $X_h = 0.12497(4)$, which is in a good agreement with the exact result $X_h = 1/8$ (see Table 4.1). Although the parameter a_3 is quite small, it is necessary to obtain a reasonable residual.

II. Surface of a flat disc

The system sizes on the flat-disc geometry were taken as values of 12 odd numbers ranging from $L = 13$ to 91. The corresponding radii are $L/2$. Near the critical point, we sampled Q_R , $\langle \sigma^2 \rangle$, and $\langle \sigma^4 \rangle$. The finite-size behavior of these quantities also follows from Eqs. (4.36), (4.37), and (4.38), respectively. The fits yield that $m_2 = 0.6719(1)$, $m_4 = 0.5879(1)$, and $Q_c = 0.76802(15)$, which agrees well with the exact calculation $Q_c = 0.76791(3)$. Thus, we also obtain the ratios $r_2 = 0.92263(13)$ and $r_4 = 0.84841(14)$, which are consistent with Eq. (4.28).

At criticality, three types of two-point magnetic correlation functions were sampled. We denote $g_1(r)$ as the one between two points with same coordinates (r, ψ) but on opposite faces, and $g_2(r)$ and $g_3(r)$ as those between two points (r, ψ) and $(r, \psi + \pi)$ on opposite and on the same faces, respectively. On the basis of Eq. (4.18), one expects that

$$g_1(r) \propto (L - 4r^2/L)^{-2X_h}, \quad g_2(r) \propto (L + 4r^2/L)^{-2X_h}, \quad g_3(r) \propto r^{-2X_h}. \quad (4.40)$$

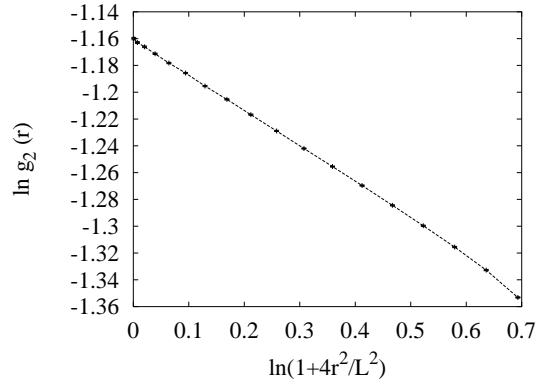


Figure 4.9: Decay of the magnetic correlation function $g_2(r)$, shown as $\ln g_2(r)$ vs $\ln(1 + 4r^2/L^2)$. The finite-size parameter of the flat disc is $L = 17$.

A plot for $g_2(r)$ is shown in Fig. 4.9. The curvature near $r = L/2$ is due to the discrete property of the derivative $\partial \vec{r} / \partial w$ in the mapping formula (4.17). We assume that this effect decays as in order of $(L/2 - r)^{y_c}$ when r approaches zero. Thus, one can obtain the finite-size behavior of these quantities by including corrections in Eq. (4.40). For instance, the quantity $g_3(r)$ follows

$$g_3(r) = r^{-2X_h + cL^{y_c}} [a_0 + a_1 r^{y_c} + a_2 r^{y_i} + d_1 (L/2 - r)^{y_c} + b_0 L^{y_c} + \dots]. \quad (4.41)$$

By introducing a cutoff at large r , we made fits for $g_1(r)$, $g_2(r)$, and $g_3(r)$ independently, and obtain $X_h = 0.124\,92(9)$, $X_h = 0.125\,01(16)$, and $X_h = 0.125\,05(7)$, respectively, in good agreement with the exact result.

III. Spheroids with $e = 2$

As an example, we performed Monte Carlo simulations for a prolate spheroid with the ratio $e = b/a = 2$. We sampled the universal ratio Q_R and the magnetic correlation function $g_1(\theta) = \langle \sigma(\theta, \psi) \sigma(\theta, \psi + \pi) \rangle$. The analysis of the finite-size behavior of Q_R leads to the result $Q_c = 0.764\,3(1)$. From the Monte Carlo data for $g_1(\theta)$ and Eq. (4.9), we obtain $X_h = 0.124\,9(2)$.

We also sampled the correlation functions $g_2(\theta) = \langle \sigma(\theta, \psi) \sigma(\pi - \theta, \psi) \rangle$. The mapping formula is relatively complicated in this case, and we did not work out the expression of $g_2(\theta)$. But we observe that a plot of the Monte Carlo data $\ln[g_2(\theta)]$ versus $\ln(1 + \sqrt{e^2 + 1} \tan^2 \theta)$ approximately follows a straight line (Fig. 4.10). By means of finite-size scaling, we obtain the value of the slope as $0.124\,1(8)$, which is close to the exact result $X_h = 1/8$.

IV. Half surface of a sphere with fixed boundary conditions

We also investigated the anisotropic limit of the Ising model on a half sphere. An infinite ordering field was applied at the equator. The system sizes are taken as 10 values ranging from $L = 4$ to 40. The corresponding radius is $R = (2L - 1)/\pi$. We sampled the magnetization density $m = \langle \sigma(\theta) \rangle$ and the energy density e as a function of θ . Since the interactions along the θ and ψ direction are of different forms, the energy density can be represented in two ways: the interactions due to the weak couplings $\langle \sigma(\theta) \sigma(\theta + 1) \rangle$, or the density of interfaces along the strong couplings $\langle n(\theta) \rangle$. We chose the latter because it needs much less computer time. The behavior of the magnetization density follows Eq. (4.20), and the energy density behaves as

$$e(\theta) = \langle n(\theta) \rangle = n_0 + a (L \cos \theta)^{-X_t}, \quad (4.42)$$

where n_0 is the bulk density, and X_t is the temperature scaling dimension. An example is shown in Fig. 4.11. Finite-size analyses of the quantities $\langle \sigma(\theta) \rangle$ and $\langle e(\theta) \rangle$ yield $X_h = 0.12499(2)$ and $X_t = 0.995(6)$ respectively, which are again in excellent agreement with the exact values.

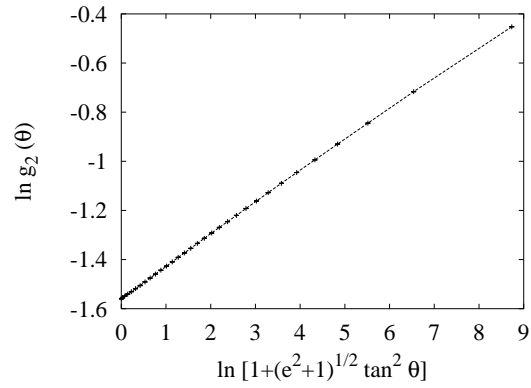


Figure 4.10: Decay of the magnetic correlation function $g_2(\theta)$, shown as $\ln g_2(\theta)$ vs $\ln(1 + \sqrt{e^2 + 1} \tan^2 \theta)$. The finite size of the spheroid is $L = 64$ and $e = b/a = 2$.

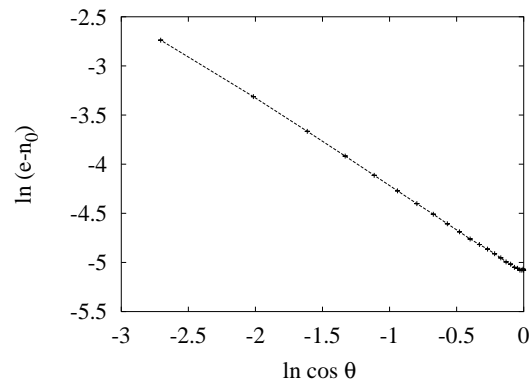


Figure 4.11: Decay of the fluctuation of the energy density $e(\theta) - n_0$ for half the surface of a sphere, shown as $\ln(e - n_0)$ vs $\ln \cos \theta$. The system size $L = 24$. n_0 is obtained from the Monte Carlo data for flat systems.

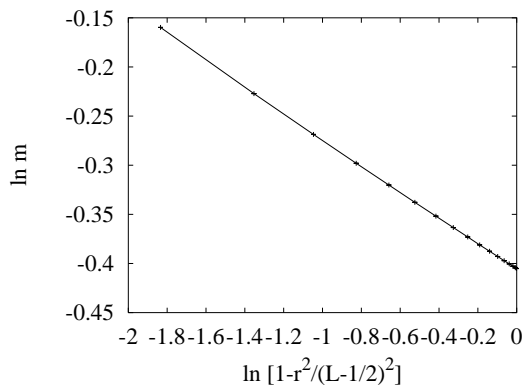


Figure 4.12: Decay of the magnetization density $m = \langle \sigma(r) \rangle$, shown as $\ln m$ vs $\ln[1 - r^2/(L - 1/2)^2]$. The system size is $L = 16$. Fixed boundary conditions were applied.

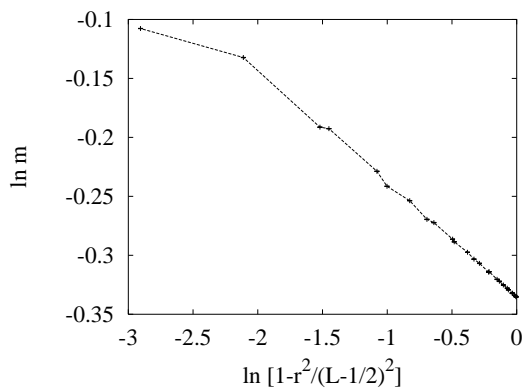


Figure 4.13: Decay of the magnetization density $m = \langle \sigma(r) \rangle$, shown as $\ln m$ vs $\ln[1 - r^2/(L - 1/2)^2]$. The circle was cut from a $L \times L$ square lattice with $L = 24$.

V. Interior of a circle

Conformal invariance on the interior of a circle with free and fixed boundary conditions has been numerically tested by Badke and Reš et al. [3, 7]. They approximated this geometry by drawing the circle from a squares lattice. In this way, the symmetry along the ψ direction is broken, and irregular finite-size effects arise (Fig. 4.13). Thus, it seems appropriate to simulate the interior of a circle by means of the continuous algorithm. We used both free and fixed boundary conditions. The system sizes are taken as 10 values ranging from $L = 8$ to 40. An example is shown in Fig. 4.12, and no irregular effects are observed. Analyses yield that $X_h = 0.124994(15)$ and $X_t = 1.002(7)$.

4.1.6 Discussion

Conformal invariance is known as a powerful tool to investigate critical behavior. Its applications in two dimensions have thus far been focused on flat systems. We have shown how one can apply it in curved geometries. The validity of our method is confirmed by the agreement between predictions based on conformal invariance and our numerical results. Moreover, in the case of the Ising model, the difficulty of numerical simulations in curved geometries is solved by the recently developed continuous cluster algorithm. Trivial modifications can generalize this algorithm to Potts models, including the percolation model [18].

Furthermore, since conformal mappings of three-dimensional systems usually lead to curved geometries, this algorithm enables us to investigate applications of conformal invariance in three dimensions [9, 17, 18].

4.2 Bulk and surface criticality: three-dimensional Ising model

Using a continuous cluster Monte Carlo algorithm, we investigate the critical three-dimensional Ising model in its anisotropic limit. From the ratio of the magnetic correlations in the strong- and the weak-coupling directions, we determine the length ratio relating the isotropic Ising model and the anisotropic limit. On this basis, we simulate the critical Ising model on a spherocylinder $S^2 \times \mathbb{R}^1$, i.e., a curved geometry obtained from a conformal mapping of the infinite space \mathbb{R}^3 . From correlation lengths along the spherocylinder, combined with the prediction of conformal invariance, we estimate the magnetic and thermal scaling dimensions as $X_h = 0.5182(6)$ and $X_t = 1.419(7)$, respectively. The behavior of the Binder cumulant is also determined in the limit of an infinitely long spherocylinder. Next, free boundary conditions are imposed on the equators of the spherocylinder, and thus the geometry $S^1 \times S^+ \times \mathbb{R}^1$ is obtained. The surface magnetic scaling dimension is estimated as $X_h^{(s)} = 1.263(5)$. The consistency of the aforementioned estimations and existing results confirms the three-dimensional Ising model is conformally invariant. Further, the precision of these results reveals that, as in two dimensions, conformal mappings provide a powerful tool to investigate critical phenomena. With the continuous cluster algorithm, we also perform simulations of systems inside a conventional solid cylinder. The surface magnetic correlation length differs, within the estimated error margin, by a factor $\pi/2$ from that along a half spherocylinder $S^1 \times S^+ \times \mathbb{R}^1$ with the same radius.

4.2.1 Introduction

Applications of conformal invariance in two dimensions have been explored extensively and produced fruitful results both for bulk and surface critical phenomena [1, 4, 19, 20]. Conformal mappings provide relations between critical systems in different geometries. A well-known and particularly useful example is Cardy's mapping between an infinite plane and the surface of an infinitely long cylinder, which transforms the algebraic decay of correlations in the plane into an exponential decay along the cylinder [5, 6]. Because a cylinder is pseudo-one dimensional, its numerical investigation is simpler than that of a two-dimensional plane. This mapping can be generalized to any number of dimensions [6]. In three dimensions, Cardy's mapping transforms an infinite space \mathbb{R}^3 into a pseudo-one-dimensional geometry $S^2 \times \mathbb{R}^1$, i.e., a curved geometry extending the surface of a sphere S^2 into another dimension \mathbb{R}^1 . Thus, one also expects that, as in two dimensions, Cardy's mapping also provides a significant help in numerical studies of critical phenomena. In particular, we need such studies because exact results are scarce in three dimensions. However, the nonzero net curvature of the geometry $S^2 \times \mathbb{R}^1$ poses a serious obstacle for numerical investigations.

Recently, we solved this problem for the case of the Ising model by using the Hamiltonian limit of the lattice Ising model and a continuous cluster Monte Carlo algorithm [9, 17]. The key ingredient of this infinitely anisotropic model is that one of its dimensions is continuous, so that the problem of discretization for one of the lattice directions is avoided. In two dimensions, we have numerically studied a conformal mapping between an infinite plane and a spheroid [21]. Special cases of the spheroid include the surfaces of an infinitely long cylinder, of a sphere, and of a flat disc. Thus, this mapping includes Cardy's transformation as a special case. A brief report has also been published about the confirmation of Cardy's mapping in three dimensions [17], in which the aforementioned geometry $S^2 \times \mathbb{R}^1$ was named a 'spherocylinder'. In the present work, the techniques involved in Ref. [17] will be described in more detail. Moreover, by mapping the semi-infinite space $\mathbb{R}^2 \times \mathbb{R}^+$ onto the half spherocylinder $S^2 \times \mathbb{R}^+$ and $S^1 \times S^+ \times \mathbb{R}^1$, respectively, we investigate the surface criticality of the Ising model in three dimensions.

The present work also includes simulations of the Ising model inside a conventional solid cylinder. Compared to the aforementioned half spherocylinder, the conventional solid cylinder has a zero net curvature. However, numerical simulations suffer from complications due to its curved surface. Such a difficulty is avoided by using the Hamiltonian limit of the lattice Ising model and the continuous cluster algorithm. Free boundary conditions are imposed on the surface of the conventional solid cylinder, and correlation functions along the cylinder are sampled. In fact, the conventional solid cylinder is closely related to the half spherocylinder $S^1 \times S^+ \times \mathbb{R}^1$. The former object is obtained by replacing the half-sphere of the latter object by the interior of a circle.

4.2.2 Conformal mappings

In two dimensions, one may parametrize the infinite plane as a complex number $z = x + iy$. Cardy's transformation is then expressed as $z' = R \ln z$ [5]. The geometry of z' can be interpreted as the surface of an infinitely long cylinder or a flat strip with periodic boundary conditions. For a critical system with a scaling dimension X , Cardy's mapping yields the correlation length along the cylinder as

$$\xi_R = R/X, \quad (4.43)$$

where R is the radius of the cylinder [1].

This mapping can be generalized to any number of dimensions [6]. In three dimensions, one may express the flat space \mathbb{R}^3 in spherical coordinates (r, φ) . Cardy's mapping is then described by the coordinate transformation:

$$(r, \theta, \varphi) = (e^{u/R}, \theta, \varphi) \quad (-\infty < u < \infty), \quad (4.44)$$

where R is a free parameter. Thus a geometry expressed by the variables (u, θ, φ) in Eq. (4.44) is reached. It is obvious that this geometry is analogous to the surface of an infinite cylinder as mentioned earlier. The latter object can be recognized as the extension of a circle S^1 into another dimension \mathbb{R} . Analogously, the former geometry can be obtained by extending a sphere S^2 into another dimension \mathbb{R} . This dimension is perpendicular to the surface of the sphere, which, unfortunately, cannot be visualized in three-dimensional space. Taking into account this analogy, we named in Ref. [17] the three-dimensional geometry $S^2 \times \mathbb{R}$ a 'spherocylinder'.

The reason why equation (4.44) is conformal is as follows. First, the metric of the flat space \mathbb{R}^3 is expressed, in spherical coordinates, by the invariant line element

$$ds^2 = dr^2 + r^2 (d\theta^2 + \sin^2 \theta d\varphi^2), \quad (0 \leq \theta \leq \pi, 0 \leq \varphi < 2\pi). \quad (4.45)$$

Under the formula (4.44), equation (4.45) transforms as [6]

$$ds^2 = R^{-2} e^{2u/R} [du^2 + R^2 (d\theta^2 + \sin^2 \theta d\varphi^2)], \quad (4.46)$$

where $ds'^2 = du^2 + R^2 (d\theta^2 + \sin^2 \theta d\varphi^2)$ reflects the natural metric of the spherocylinder $S^2 \times \mathbb{R}^1$. Equation. (4.46) shows that the line elements ds^2 and ds'^2 differ only by a position-dependent factor $R^{-2} e^{2u/R}$. Thus, the mapping (4.44) is conformal.

Under a conformal mapping ($\vec{r} \rightarrow \vec{r}'$), a multipoint correlation function covariantly transforms as [1]

$$\langle \sigma_1(\vec{r}_1) \sigma_2(\vec{r}_2) \cdots \rangle_{\vec{r}} = b(\vec{r}_1)^{-X_1} b(\vec{r}_2)^{-X_2} \cdots \langle \sigma_1(\vec{r}'_1) \sigma_2(\vec{r}'_2) \cdots \rangle_{\vec{r}'}, \quad (4.47)$$

where σ_i is a scaling operator (e.g., associated with the magnetization density or the energy density), and $b(\vec{r})$ is the rescaling factor, which reads $b(\vec{r})^2 = ds^2/ds'^2$.

In the infinite space \mathbb{R}^3 , the critical two-point correlation function behaves as

$$\langle \sigma(\vec{r}_1) \sigma(\vec{r}_2) \rangle_{\mathbb{R}^3} \propto |\vec{r}_2 - \vec{r}_1|^{-2X}. \quad (4.48)$$

Equations (4.44), (4.47) and (4.48) yield the correlation function along the spherocylinder as

$$\langle \sigma(u_1, \theta, \varphi) \sigma(u_2, \theta, \varphi) \rangle_{S^2 \times \mathbb{R}^1} \propto R^{-2X} \left(e^{|u_1 - u_2|/2R} - e^{-|u_1 - u_2|/2R} \right)^{-2X}. \quad (4.49)$$

For $|u_1 - u_2| \gg 0$, equation (4.49) reduces to

$$\langle \sigma(u_1, \theta, \varphi) \sigma(u_2, \theta, \varphi) \rangle \propto R^{-2X} e^{-X|u_1 - u_2|/R}, \quad (4.50)$$

so that the relationship (4.43) follows again.

However, applications of Eq. (4.43) in three dimensions are rather scarce so far. The reason is that the spherocylinder $S^2 \times \mathbb{R}^1$ has a non-zero net curvature. For numerical investigations, a curved geometry

does not readily accommodate a sequence of regular lattices. For the special case of the spherical model, equation (4.50) has been verified analytically by Cardy [6]. Weigel and Janke approximated the S^2 sphere by the surface of a cube [22]. Their results for the Ising model with finite size R satisfy Eq. (4.50) up to a proportionality constant, which has to be determined empirically.

Under the mapping (4.44), the half infinite space $\mathbb{R}^2 \times \mathbb{R}^+$ conformally transforms into the half spherocylinder $S^1 \times S^+ \times \mathbb{R}$, i.e., a geometry also described by the natural metric ds'^2 in Eq. (4.46), but with $0 \leq \theta \leq \pi/2$. Thus, this geometric object has a surface at the equators ($\theta = \pi/2$) of the spheres. The pair correlation on the surface of the half space $\mathbb{R}^2 \times \mathbb{R}^+$ follows from the formula (4.48), except that the bulk scaling dimension X is replaced by the surface dimension $X^{(s)}$ [1]. Thus, the surface correlation at the equators of the half spherocylinder is also described by Eq. (4.49) but with a substitution of X by $X^{(s)}$.

Next, we consider another conformal mapping between the semi-infinite space $\mathbb{R}^2 \times \mathbb{R}^+$ and a half spherocylinder $S^2 \times \mathbb{R}^+$, also described by the metric ds'^2 in Eq. (4.46), but with $u \geq 0$. This mapping is different from Eq. (4.44) and is conveniently described in two steps. First, the formula [2]

$$\vec{r}'/r'^2 = \vec{r}/r^2 + \hat{I}/2, \quad (4.51)$$

maps spheres onto spheres in three dimensions, and the space \mathbb{R}^3 is transformed into itself [2]. Here, \hat{I} is an arbitrary fixed unit vector. Under the mapping (4.51), the plane $\hat{I} \cdot \vec{r} = 0$, which corresponds to a spherical surface of an infinite radius, is conformally mapped onto the surface of a unit sphere with the center at \hat{I} . Meanwhile, the half spaces $\hat{I} \cdot \vec{r} > 0$ and $\hat{I} \cdot \vec{r} < 0$ are transformed respectively into the interior and exterior of this unit sphere. The homogeneous translation

$$\vec{r}'' = \vec{r} - \hat{I} \quad (4.52)$$

shifts the center of the sphere to the origin of the double-primed coordinate system.

The profile of a scaling operator σ in the semi-infinite space $\mathbb{R}^2 \times \mathbb{R}^+$ behaves as [1]

$$\langle \sigma(\vec{r}) \rangle_{\mathbb{R}^2 \times \mathbb{R}^+} \propto y^{-X}, \quad (4.53)$$

where $y \gg 0$ is the distance of a point \vec{r} to the surface. Equations (4.51) and (4.52) yield the rescaling factor $b(\vec{r})$ of the conformal mapping ($\vec{r} \rightarrow \vec{r}''$) as [2]

$$b(\vec{r}) = 1 + \hat{I} \cdot \vec{r} + r^2/4 = 4/(\vec{r}'' - \hat{I})^2. \quad (4.54)$$

From Eqs. (4.47) and (4.51)-(4.54), the quantity $\langle \sigma(\vec{r}'') \rangle$ inside a unit sphere follows from [1, 2]

$$\langle \sigma(\vec{r}'') \rangle \propto |1 - (r'')^2|^X, \quad (4.55)$$

where $r'' \leq 1$ is the distance of the point \vec{r}'' to the center of sphere.

Next, we apply Eq. (4.44) to conformally map this unit sphere onto the half spherocylinder $S^2 \times \mathbb{R}^+$. The profile (4.55) is then covariantly transformed into

$$\langle \sigma(u, \theta, \varphi) \rangle_{S^2 \times \mathbb{R}^+} \propto R^{-X} \left(e^{|u_1 - u_2|/2R} - e^{-|u_1 - u_2|/2R} \right)^{-2X}, \quad (4.56)$$

which differs from Eq. (4.49) by a factor R^{-X} .

Moreover, equations (4.51), (4.52) and (4.44) transform the quarter-infinite space $\mathbb{R}^1 \times \mathbb{R}^+ \times \mathbb{R}^+$ into a quarter of the infinite spherocylinder $S^1 \times S^+ \times \mathbb{R}^+$, described by ds'^2 in Eq. (4.46) but with $0 \leq \theta \leq \pi/2$ and $u \geq 0$. Therefore, the profile of the surface scaling operator at the equators should follow from Eq. (4.56) except that the exponent X is replaced by the surface scaling dimension $X^{(s)}$.

4.2.3 Models and algorithms

In this section, we briefly recall the Hamiltonian limit of the Ising model and the continuous cluster algorithm [9]. The applications to the spherocylinder and the conventional solid cylinder are also described.

The three-dimensional Ising model with anisotropic couplings is described by the Hamiltonian

$$\mathcal{H}/k_{\text{B}}T = - \sum_{x,y,z} [K_{xy} s_{x,y,z} (s_{x+1,y,z} + s_{x,y+1,z}) + K_z s_{x,y,z} s_{x,y,z+1}], \quad (4.57)$$

where the integers $1 \leq x, y \leq L$ and $1 \leq z \leq L'$ label the sites of a cubic lattice, K_{xy} and K_z are the coupling strengths along bonds perpendicular and parallel to the z direction, respectively. The spins can assume the values $s_{x,y,z} = \pm 1$.

In the limit that the interactions in the z direction are infinitely strong, the couplings K_{xy} and K_z become

$$K_{xy} = \epsilon/t, \quad \exp[-2K_z] = \epsilon, \quad (\epsilon \rightarrow 0), \quad (4.58)$$

where t parametrizes the temperature and ϵ is an infinitely small number. The anisotropic model defined by Eqs. (4.57) and (4.58) is equivalent to the quantum transverse Ising model on the square lattice [14, 15]:

$$\mathcal{H}_{\text{qm}} = - \sum_{x,y} [s_{x,y}^z (s_{x+1,y}^z + s_{x,y+1}^z) + t s_{x,y}^x], \quad (4.59)$$

where $s_{x,y}^z$ and $s_{x,y}^x$ are Pauli matrices, and t represents a transverse field in the x direction.

For such an infinitely anisotropic system, the physical size in the z direction diverges as $1/\epsilon$, because the correlation length in this direction is of order $1/\epsilon$ [14, 15]. In order to keep the correlation length finite, one may rescale as $z' = z\epsilon$ so that the z' dimension becomes continuous. This means that there is an infinite number of spins per physical length unit. As a result, the simple-cubic lattice reduces to L^2 lines originating from the sites of a $L \times L$ square lattice. The spins on these lines form ranges of $+/-$ signs, and the total number of interfaces between these ranges is of order L^3 .

Monte Carlo simulations of this continuous system are realized by the application of a continuous cluster algorithm. This algorithm uses the positions of the aforementioned interfaces as the dynamical variables. The full description has been given in Ref. [9]. Here, we summarize the essential points. We start from a discrete Ising model and use bond variables as defined in the random cluster model [23]. During the formation of a cluster, the bond between nearest-neighbor spins of the same sign is ‘frozen’ with a probability $P = 1 - \exp(-2K)$ or ‘broken’ with the probability $1 - P$. A cluster is then formed by spins connected to one another by these frozen bonds. The formation and flipping of these clusters leads to highly efficient Monte Carlo methods, which suppress the critical slowing down that is prominent in the Metropolis algorithm. In the Swendsen-Wang cluster method [24], the whole lattice is decomposed into a sequence of clusters. In the Wolff version of the cluster algorithm [25], only one cluster is formed and flipped during a Monte Carlo step. For the anisotropic Ising model defined by Eqs. (4.57) and (4.58), the probability P in the xy plane and z direction is of order ϵ and $1 - \epsilon$, respectively. Thus, the strong-coupling bonds connect many spins in the z direction until a ‘break’ occurs with a probability of order ϵ per bond. Spins between these breaks in the z direction form clusters of $+/-$ signs of with lengths of order $1/\epsilon$. After the rescaling described above, these z direction clusters reduce to ranges of $+/-$ signs, of which the length is now of order 1. Moreover, the average distance of the frozen weak-coupling bonds along the z direction is also of order 1. These weak-coupling bonds serve as ‘bridges’ between neighboring lines to connect ranges of the same sign, and help to build clusters in the xy plane. As a result, continuous Wolff-like and Swendsen-Wang-like cluster algorithms can be formulated for this anisotropic limit. The application of a continuous Wolff-like algorithm, combined with finite-size-scaling analysis, yields [9] the critical point as $t_c = 3.04438(2)$ for the model defined by Eqs. (4.57) and (4.58). The precision is good in comparison with existing results [8, 26], and reflects the efficiency of the aforementioned continuous cluster algorithm.

Since our purpose is the application of conformal mappings, we have to restore isotropy asymptotically. This can be done by choosing an appropriate aspect ratio $\alpha = L'_z/L_{xy}$, where L'_z and $L_{xy} = L$ are linear system sizes in the z' direction and the xy plane, respectively. In Ref. [9], we determined the critical Binder cumulant as a function of the length ratio α . Matching this universal function with the case of the isotropic Ising model [27–29], we showed that the asymptotic isotropy of this Hamiltonian limit is restored for $\alpha_0 = 0.886(7)$. Here, we proceed differently. We sampled the critical magnetic correlations over half

linear system sizes in the strong- and weak-coupling directions, respectively, of which the amplitude ratio d_m is defined as

$$d_m(\alpha, L) = \frac{\sum_{x,y} \int dz' \langle 2 \sigma(x, y, z') \sigma(x, y, z' + \alpha L/2) \rangle}{\sum_{x,y} \int dz' \langle \sigma(x, y, z') [\sigma(x + L/2, y, z') + \sigma(x, y + L/2, z')] \rangle}. \quad (4.60)$$

This amplitude ratio d_m is a function of the length ratio α and the linear size L . The aforementioned isotropy means that the magnetic correlations in the z direction are equal to those in the x and y directions, and thus $d_m(\alpha_0, L) = 1$. Taking into account finite-size effects, we Taylor-expand $d_m(\alpha, L)$, using logarithmic scales for d_m and α , as

$$\ln d_m(\alpha, L) = a_1(\ln \alpha - \ln \alpha_0) + a_2(\ln \alpha - \ln \alpha_0)^2 + bL^{y_a} + cL^{y_a}(\ln \alpha - \ln \alpha_0) + \dots, \quad (4.61)$$

where a_1, a_2, b and c are unknown parameters, and the correction with the exponent y_a is due to the microscopic deviations from isotropy of the Hamiltonian limit of the Ising model. In two dimensions, such a correction has been investigated in detail [21]. It was found that $y_a \approx -2 = y_i$, where y_i is the exponent of the irrelevant field for the two-dimensional Ising model. Here, we assume that this relation also holds in three dimensions so that $y_a = y_i = -0.821(5)$, where the value of y_i was taken from Refs. [21, 27–29]. On the basis of the least-squares criterion, equation (4.61) was fitted to the Monte Carlo data. We find that $a_1 = 0.505(2)$, $a_2 = 0.06(1)$, $b = 0.375(7)$, $c = 2.8(3)$, and $\alpha_0 = 0.8881(2)$, which provides a significant improvement over our previous result $\alpha_0 = 0.886(7)$ [9].

As a result, the new coordinate $z'' = z'/\alpha_0$ restores the isotropy asymptotically for systems consisting of L^2 lines with physical length L in the large- L limit. Due to periodic boundary conditions, each of these lines can be recognized as a circle S^1 . This enables one [17, 21] to represent the ‘lattice structure’ on a sphere S^2 by L evenly spaced circles with varying radius, such that the strong couplings are along the φ direction while the weak couplings are between the adjacent circles. The location of the k th circle is $\theta_k = (k - \frac{1}{2})\pi/L$ ($k = 1, 2, \dots, L$), and the corresponding circumference is $2L \sin \theta_k$, which accounts for the S^2 curvature. Since the probability of a weak-coupling bond is defined *per unit of length*, and the adjacent circles on a sphere have different radii, the distribution of these weak-coupling bonds still requires a length scale. It was chosen as the average length scale of both circles. Therefore, the circumference of the sphere is $2L$, and the radius is L/π [17, 21]. The validity of this method, i.e., asymptotic spherical symmetry of such systems, has been confirmed in Ref. [21]. Extension of this lattice structure of a sphere into another dimension yields the approximation of the spherocylinder $S^2 \times \mathbb{R}^1$ [17].

The critical point for systems on the spherocylinder is identical to that in the flat space \mathbb{R}^3 . Arguments are *a*), the lattice structures in these two geometries are same on a microscopic scale; *b*), for finite systems L , the discretization in θ leads to an integrated effect on the average coupling strength, which is proportional to L^{-2} according to the trapezium rule. Under renormalization, this effect leads to corrections proportional to L^{y_t-2} . Since the thermal scaling exponent $y_t < 2$ for the two- and three-dimensional Ising model, this effect will vanish for $L \rightarrow \infty$. In two dimensions, we have studied the Ising model on a sphere [17, 21], and confirmed that the leading corrections for finite systems are of order L^{y_t-2} .

Analogous procedures can be applied to the interior of a circle, i.e., a disc geometry. In this case, the lattice structure on the disc is also represented by L evenly distributed circles, but the k th circle is simply located at $r_k = (k - \frac{1}{2})$. Thus, the radius of the disc is just that of the largest circle $\pi(2L - 1)$. The conventional solid cylinder is obtained by extending this disc geometry into another dimension with a discrete lattice structure.

4.2.4 Numerical results

By applying the aforementioned continuous Wolff-like cluster algorithm, we have simulated the Hamiltonian limit of the Ising model in the following geometries.

I. Spherocylinder with periodic boundary conditions

For systems on a spherocylinder, the values of L were taken as 4, 6, 8, 10, 12, 14, 16, 20. The finite size in the \mathbb{R} direction was taken as $nL = 8L$. Periodic boundary conditions were imposed in the u direction ($u = 0$

and $u = 8L$). Later, we will show that $n = 8$ is large enough to approximate the geometry $S^2 \times \mathbb{R}^1$. We sampled the magnetic correlation function $g_m(r)$ in the u direction, which is defined by [17]

$$g_m(r) = \frac{1}{V} \sum_{u,\theta} \int_0^{2\pi} d\varphi \frac{L}{\pi} \sin \theta \langle \sigma(u, \theta, \varphi) \sigma(u+r, \theta, \varphi) \rangle. \quad (4.62)$$

Since the couplings are different in the φ direction and in the other two directions, there are two ways to represent the energy density: the density of the interfaces and the nearest-neighbor interactions in the weak-coupling directions. We chose the latter one

$$e_{nn} = \frac{1}{V} \sum_{u,\theta} \int_0^{2\pi} d\varphi \frac{L}{\pi} \sin \theta \langle \sigma(u, \theta, \varphi) \sigma(u+1, \theta, \varphi) \rangle, \quad (4.63)$$

in order to sample the energy-like correlation $g_e(r)$

$$g_e(r) = \frac{1}{V} \sum_{u,\theta} \int_0^{2\pi} d\varphi \frac{L}{\pi} \sin \theta \langle \sigma(u, \theta, \varphi) \sigma(u+1, \theta, \varphi) \times \sigma(u+r, \theta, \varphi) \sigma(u+r+1, \theta, \varphi) \rangle - e_{nn}^2. \quad (4.64)$$

For finite systems, there is a correction $\propto L^{y_t-2}$ as mentioned earlier. Compared to the irrelevant scaling exponent $y_i = -0.821(5)$ in three dimensions [21, 27–29], the correction with the power $y_c = y_t - 2 = -0.413$ is expected to dominate over that with y_i .

In the continuum limit, the behavior of the magnetic energy-like correlations, $g_m(r)$ and $g_e(r)$ respectively, follows from Eq. (4.49). Taking into account finite-size effects yields the correlation length ξ_L as

$$\xi_L^{-1} = \frac{X}{R} (1 + aL^{y_c} + bL^{y_i}) = \frac{\pi X}{L} (1 + aL^{y_c} + bL^{y_i}). \quad (4.65)$$

Due to the periodicity in the u direction, correlations build up over two distances r and $nL - r$. Thus, the correlation function $g(r, L)$ for finite systems behaves as

$$g(r, L) = L^{-2X} [Y(r) + Y(nL - r)] (A + BL^{y_c} + CL^{y_i}), \quad (4.66)$$

with the function

$$Y(r) = (e^{hr/2R} - e^{-hr/2R})^{-2X}, \quad (h = 1 + aL^{y_c}). \quad (4.67)$$

Here, the radius is $R = L/\pi$ as mentioned before.

Equations (4.66) and (4.67) was fitted to the Monte Carlo data. The value of y_c is fixed at -0.413 as specified above. For the magnetic and the energy-like correlations, the exponent X represents the bulk magnetic and thermal scaling dimensions, X_h and X_t respectively. We obtain $X_h = 0.5178(12)$ and $X_t = 1.423(19)$, in a good agreement with the existing results $X_h = 0.5185(3)$ and $X_t = 1.413(1)$ [21, 27–29]. This confirms the assumption of conformal invariance [17]. Including another correction cL^{y_i} in the function h does not improve the residual χ^2 of the fit significantly.

II. Binder cumulant on a spherocylinder

The dimensionless quantity originally introduced by Binder plays an important role in the study of critical phenomena [13]. An example is Ref. [9], in which we obtains the length ratio $\alpha_0 = 0.881(6)$ by sampling the Binder cumulant. For a system on a hyper-cubic lattice in general d dimensions, the universal ratio Q , which is closely related to the Binder cumulant [13], is defined as

$$Q(K) = \langle \sigma^2 \rangle^2 / \langle \sigma^4 \rangle. \quad (4.68)$$

For a system on a hypercylinder-like geometry $S^{d-1} \times \mathbb{R}^1$, however, another definition is desirable. The reason is as follows. If the length of the geometry $S^{d-1} \times \mathbb{R}^1$ is much larger than the correlation length,

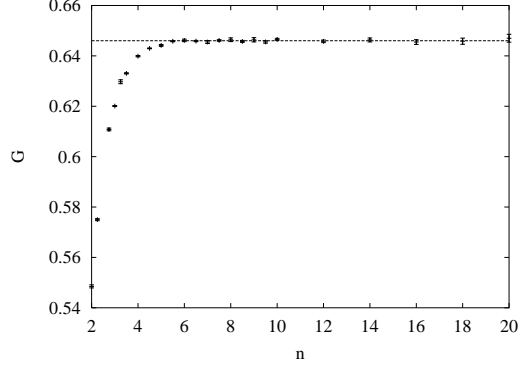


Figure 4.14: The dimensionless ratio G , shown as a function of n , where $n\pi$ is the ratio of the length and the radius of the spherocylinder. System size is $L = 8$.

i.e., $\gamma = L/R \rightarrow \infty$, the critical magnetization density is normally distributed, and thus the value of $Q(K)$ approaches $1/3$. The same value applies to a disordered system. As a consequence, little information can be obtained for critical phenomena. In this case, a useful dimensionless quantity can be defined as [1, 11]

$$G(K, \gamma) = (3 - \langle \sigma^4 \rangle / \langle \sigma^2 \rangle^2) \gamma / 3, \quad (4.69)$$

which plays a similar role as the aforementioned correlation length ξ_R . According to finite-size scaling, the critical quantity G is universal for infinite systems R and $\gamma \rightarrow \infty$.

In two dimensions, the critical bulk two- and four-point correlation functions are exactly known for the Ising model [10]. On this basis, the value of G for the surface of an infinitely long cylinder can be calculated according to the prediction of conformal invariance. This calculation has been performed by Burkhardt and Derrida [11] who evaluated the resulting integrals by a Monte Carlo method. Their result is

$$G(K_c, \infty) / 2\pi = 2.46044(2). \quad (4.70)$$

For an arbitrary model, it was shown by Cardy [30] that for the infinitely long strip

$$G(K_c, \infty) / 2\pi \sim (\pi X_h)^{-1}, \quad (4.71)$$

if X_h is small.

In three dimensions, no result for the quantity G is available yet. Here, we sampled both quantities Q/π and G/π on a spherocylinder as a function of the size L and the ratio $\gamma/\pi = n$. The system sizes were taken as $L = 8, 10, 12, 16, 20, 24, 30, 40$ and the largest value of n is 20. Periodic boundary conditions were applied in the u direction. Part of the results are shown in Figs. 4.15 and 4.14. The lattice figure suggests that $n = 8$ already provides a good approximation of the geometry $S^2 \times \mathbb{R}^1$.

For finite systems at the critical point, we fitted the following formula to the Monte Carlo data:

$$G(L, n) / \pi = G_\infty + \frac{a_1}{n} + \frac{a_2}{n^2} + v(nL)^{y_c} + \dots \quad (4.72)$$

In order to obtain an acceptable residual χ^2 of the fit, we applied a cutoff by excluding small system sizes $L \leq 6$ and $n \leq 5$. The result is $G/\pi = 0.6458(5)$, which differs significantly from that for a two-dimensional strip [11].

III. Spherocylinder with fixed boundary conditions

Fixed boundary conditions, i.e., infinitely strong fields, were imposed on both ends of the spherocylinder ($u = 0$ and $u = nL$). The finite system sizes were taken as $L = 4, 6, 8, 10, 12, 14, 16, 20, 24$ and $n = 8$. The magnetization and the energy densities,

$$m(r) = \frac{1}{V} \sum_{\theta} \int_0^{2\pi} d\varphi \frac{L}{\pi} \sin \theta \langle \sigma(r, \theta, \varphi) \rangle \quad (4.73)$$

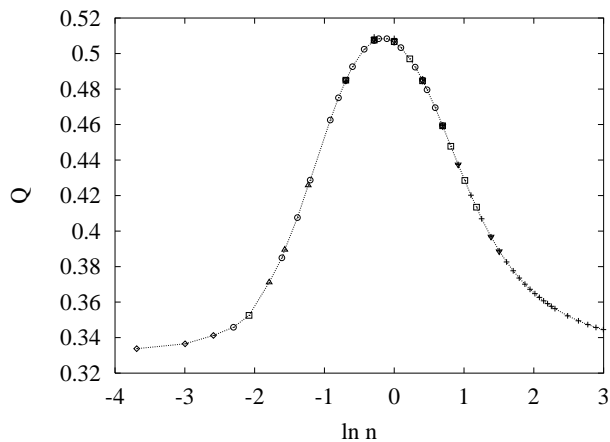


Figure 4.15: The dimensionless ratio Q , shown as a function of $\ln n$, where $n\pi$ is the ratio of the length and the radius of the spherocylinder. Systems sizes are $L = 8$ (+), $L = 12$ (∇), $L = 16$ (\square), $L = 20$ (\circ), $L = 24$ (\triangle), and $L = 40$ (\diamond). The data collapse indicates that corrections-to-scaling are small.

and

$$e(r) = \frac{1}{V} \sum_{\theta} \int_0^{2\pi} d\varphi \frac{L}{\pi} \sin \theta \langle n(r, \theta, \varphi) \rangle, \quad (4.74)$$

were sampled. Here, we have chosen the density of the interfaces $n(r, \theta, \varphi)$ as the energy density. Compared to the alternative definition of e in Eq. (4.63), sampling the density of the interfaces consumes much less computer time. This is due to the fact that, during the Monte Carlo simulations, the positions of these interfaces are stored in computer memory as the dynamical variables.

The scaling behavior of $m(r)$ and $e(r)$ follows from Eq. (4.56). According to Eqs. (4.56) and (4.49), the magnetization density $m(r)$ and the correlation $g_m(r)$ decay in a similar way with respect to the distance r . An example is shown in Fig. 4.16. For a given spherocylinder with radius R , however, the prefactor of $g_m(r)$ is R^{-2X_h} [Eq. (4.49)] while that of $m(r)$ is R^{-X_h} [Eq. (4.56)]. This effect, combined with the fact that less computer time is needed, shows that $m(r)$ is a better quantity than $g_m(r)$ to determine the magnetic scaling dimension. A similar argument holds for the energy density. Taking into account finite-size corrections and fixed boundary conditions at both ends, we have

$$m(r, L) = L^{-X_h} [Y(r) + Y(nL - r)] (A + BL^{y_c}), \quad (4.75)$$

and

$$e(r, L) = n_0 + L^{-X_t} [Y(r) + Y(nL - r)] (A + BL^{y_c}), \quad (4.76)$$

where n_0 is the bulk density of the interfaces at criticality, and the function $Y(r)$ is given in Eq. (4.67).

Formulas (4.75), (4.76) and (4.67) were fitted to the Monte Carlo data. An example of the energy density is shown in Fig. 4.17. The value of n_0 is fixed at 0.90160(5), as obtained from numerical simulations in a flat geometry. We obtain $X_h = 0.5182(6)$ and $X_t = 1.419(7)$. The precision of these results is comparable to that of other methods [21, 27–29].

IV. Half spherocylinder $S^1 \times S^+ \times \mathbb{R}^1$

For the half spherocylinder, fixed and free boundary conditions were applied on both ends ($u = 0$ and $u = nL$) and the equators ($\theta = \pi/2$) of $S^1 \times S^+$, respectively. The systems sizes were taken as $L = 8, 10, 12, \dots, 26$ and $n = 8$. The radius of the half spherocylinder is $R = (2L - 1)/\pi$, different from the formula $R = L/\pi$ for the spherocylinder. The magnetization density on the equators was sampled, defined

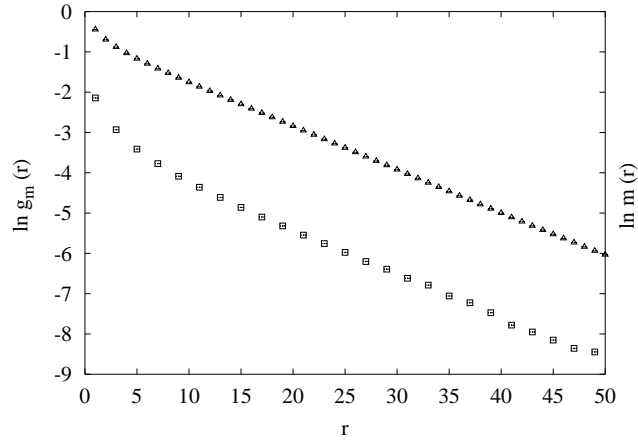


Figure 4.16: The quantities $\ln m(r)$ (\square) and $\ln g_m(r)$ (\triangle), the logarithm of the magnetization profile and of the magnetic correlation, respectively, vs. the distance r along a spherocylinder with $R = 16/\pi$ and $n = 8$. The error bars for $\ln m(r)$ are smaller than the symbol size; for $\ln g_m(r)$ they are at most approximately equal to the symbol size.

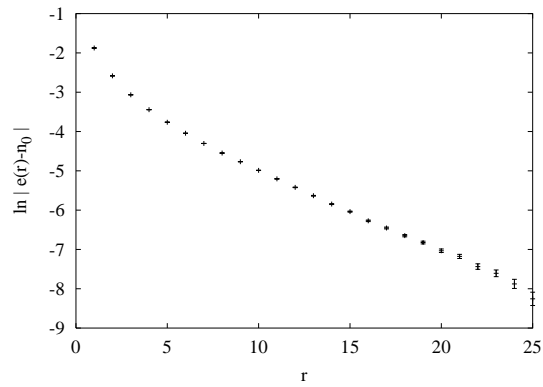


Figure 4.17: Exponential decay of the interface density, shown as $\ln |e(r) - n_0|$ vs. the distance r along a spherocylinder with $R = 24/\pi$ and $n = 8$. Error bars show the statistical uncertainty.

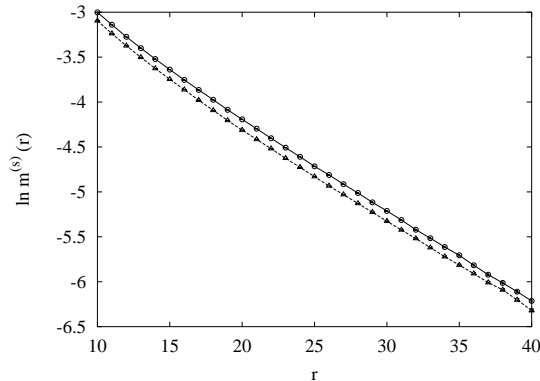


Figure 4.18: Exponential decay of the surface magnetization density, shown as $\ln m^{(s)}(r)$, vs. the distance r along a conventional solid cylinder (\triangle) and a spherocylinder (\circ). The radii of these two objects are $R = 19.5$ and $19.5 \times 2/\pi$, respectively; the ratio is $n = 8$.

as

$$m^{(s)}(r) = \frac{1}{2\pi} \int_0^{2\pi} d\varphi \langle \sigma(r, \pi/2, \varphi) \rangle. \quad (4.77)$$

The finite-size scaling behavior of this surface magnetization densities also follows from Eq. (4.75), except that the exponent X_h is replaced by the surface scaling dimension $X_h^{(s)}$. Equations (4.75) and (4.67) were fitted to the Monte Carlo data, and a short-distance cutoff was applied. The minimum system size included in the fit is $L = 14$. The result is $X_h^{(s)} = 1.263(5)$, of which the precision is good in comparison with the known value obtained by a different method $X_h^{(s)} = 1.259(15)$ [31].

V. Conventional solid cylinder

We have also performed simulations inside a conventional solid cylinder with fixed and free boundary conditions on both ends ($u = 0$ and $u = nL$) and the surface, respectively. The system sizes are $L = 8, 10, 12, 16, 18$ and $n = 8$. The radius of the cylinder is given by $R = L - 1/2$ in this case, which differs by a factor $\pi/2$ from that of the half spherocylinder with the same L . The surface magnetization density $m^{(s)}(r)$ along the cylinder was sampled. We found, empirically, that the decay of $m^{(s)}(r)$ along the conventional cylinder is very similar to that on the half spherocylinder $S^1 \times S^+ \times \mathbb{R}^1$ with the same finite size L . An example is shown in Fig. 4.18. Thus, we also fitted the Monte Carlo data on the basis of Eqs. (4.75) and (4.67), but with $h = \zeta + aL^{y_c}$. Here, the factor ζ accounts for the difference of the surface correlation length along the solid cylinder and that along the aforementioned half spherocylinder. The value of $X_h^{(s)}$ is fixed at 1.263 as specified earlier, and we obtain $\zeta = 1.585(9)$, very close to $\pi/2 \simeq 1.571$.

4.2.5 Discussion

We have shown how one can simulate the Ising model in curved geometries by means of a continuous cluster Monte Carlo algorithm. We confirm that the three-dimensional Ising model is conformally invariant. The satisfactory precision of the numerical results presented in this work shows that, as in two dimensions, conformal mappings also provide a useful tool to investigate critical phenomena (at least, if one takes the assumption of conformal invariance for granted). Further applications to other models, such as the bond percolation model, are also possible [32].

We have used the same algorithm for Monte Carlo simulations of a system inside a conventional solid cylinder. We found that the corresponding surface correlation length differs by a factor close to $\pi/2$ from that along a half spherocylinder. However, it is not obvious that this result can be supported by means of a conformal transformation.

Bibliography

- [1] J.L. Cardy, in *Phase Transitions and Critical Phenomena*, edited by C. Domb and J.L. Lebowitz (Academic Press, London, 1987), Vol.11, p.55, and references therein.
- [2] T.W. Burkhardt and E. Eisenriegler *J. Phys. A* **18**, L83 (1985).
- [3] R. Badke, V. Rittenberg, and H. Ruegg *J. Phys. A* **18**, L867 (1985).
- [4] T.W. Burkhardt and I. Guim *Phys. Rev. B* **47**, 14306 (1993), and reference therein.
- [5] J.L. Cardy, *J. Phys. A* **17**, L385 (1984).
- [6] J.L. Cardy, *Nucl. Phys. B* **240** 514 (1984); *Phys. Rev. Lett.* **65**, 1443 (1990).
- [7] I. Reš and J. P. Straley *Phys. Rev. B* **61**, 14425 (2000).
- [8] R. Rieger and N. Kawashima, *Eur. Phys. J. B* **9**, 233 (1999).
- [9] H.W.J. Blöte and Y. Deng, *Phys. Rev. E* **66**, 066110 (2002).
- [10] L. Onsager, *Phys. Rev.* **65**, 117 (1944).
- [11] T.W. Burkhardt and B. Derrida, *Phys. Rev. B* **32**, 7273 (1985), and references therein.
- [12] A. Luther and I. Peschel, *Phys. Rev. B* **12**, 3908 (1975).
- [13] K. Binder, *Phys. B* **43**, 119 (1981) (Academic Press, New York, 1982).
- [14] H.F. Trotter, *Proc. Am. Math. Soc.* **10**, 545 (1959).
- [15] M. Suzuki, *Prog. Theor. Phys.* **56**, 1454 (1976).
- [16] G. Kamieniarz and H.W.J. Blöte, *J. Phys. A* **26**, 201 (1993).
- [17] Y. Deng and H.W.J. Blöte, *Phys. Rev. Lett.* **88**, 190602 (2002).
- [18] H.W.J. Blöte and Y. Deng, to be published.
- [19] A.A. Belavin, A.M. Polyakov and A.B. Zamolodchikov, *J. Stat. Phys.* **34**, 763 (1984)
- [20] D. Friedan, Z. Qiu and S. Shenker, *Phys. Rev. Lett.* **52**, 1575 (1984)
- [21] Y. Deng and H.W.J. Blöte, to appear in *Phys. Rev. E* (2003).
- [22] M. Weigel and W. Janke, *Europhys. Lett.* **51**, 578 (2000).
- [23] P.W. Kasteleyn and C.M. Fortuin, *J. Phys. Soc. Japan. (Suppl.)* **26**, 11 (1969).
- [24] R.H. Swendsen and J.-S. Wang, *Phys. Rev. Lett.* **58**, 86 (1987); J.-S. Wang and R.H. Swendsen, *Physica A* **167**, 565 (1990).
- [25] U. Wolff, *Phys. Rev. Lett.* **62**, 361 (1989); *Phys. Lett. B* **228**, 379 (1989).
- [26] W.H. Zheng, J. Oitmaa and C.J. Hamer, *J. Phys. A* **27**, 5425 (1994).
- [27] H.W.J. Blöte, L.N. Shchur and A.L. Talapov, *Int. J. Mod. Phys. C* **10**, 1137 (1999).
- [28] P. Butera and M. Comi, *Phys. Rev. B* **56**, 8212 (1997).
- [29] R. Guida and J. Zinn-Justin, *J. Phys. A* **31**, 8103 (1998).
- [30] J.L. Cardy, *Nucl. Phys. B* **270**, [FS16], 186 (1986).
- [31] M.P. Nightingale and H.W.J. Blöte, *Phys. Rev. B* **48**, 13 678 (1993).
- [32] Y. Deng and H.W.J. Blöte, unpublished.

Conformal invariance: The percolation model

We investigate the anisotropic limit of the bond-percolation model in d dimensions, which is equivalent with a $(d-1)$ -dimensional quantum $q \rightarrow 1$ Potts model. We formulate an efficient Monte Carlo method for this model. Its application shows that the anisotropic model fits well with the percolation universality class in d dimensions. For three-dimensional rectangular geometry, we determine the critical point as $t_c = 8.6429(4)$, and determine the length ratio as $\alpha_0 = 1.5844(3)$, which relates the anisotropic limit of the percolation model and its isotropic version. On this basis, we simulate asymptotically isotropic critical systems in several curved geometries including a spheroid and a spherocylinder. Using finite-size scaling and the assumption of conformal invariance, we determine the bulk and surface magnetic exponents in two and three dimensions. They are in good agreement with the existing results. This confirms that the percolation model is conformally variant.

5.1 Introduction

Since their introduction in 1957 [1], percolation problems have been studied extensively, and a variety of applications has also been reported (see, *e.g.*, Refs. [2,3]). Percolation provides a simple picture of a second-order phase transition, and remains an active research subject [4–6]. We illustrate the problem of the bond-percolation on a regular lattice. Between each pair of lattice sites, a bond is occupied or empty with a probability p or $1-p$, respectively. Two sites connected through a chain of occupied bonds are said to be in the same cluster. Then, various questions can be asked concerning the critical cluster distribution and the percolation probability etc. Such percolation problems are now rather well understood; this can at least partly attributed to the well-known relationship [7] between the bond-percolation and the Potts model (for a review of the Potts model, see Ref. [8]). In this way, the phase transition that occurs in percolation problems can be described in the language of critical phenomena in statistical physics. As a consequence, a considerable number of critical exponents has exactly been obtained in two dimensions. For instance, the thermal and magnetic scaling exponents are $y_t = 3/4$ and $y_h = 91/48$. These exponents can be calculated from the Coulomb gas theory [9,10] and are also predicted by the conformal field theory [11–13].

Besides the above isotropic percolation model, it is of interest to understand the behavior of anisotropic systems in the percolation theory. For instance, an anisotropic random percolation model was demonstrated to be governed by new, random fixed points [14]. In the present paper, we shall consider the anisotropic bond-percolation model, which is defined on a d -dimensional rectangular lattice with a bond probability p_\perp within $(d-1)$ -dimensional layers perpendicular to the z direction, and with the probability $p_\parallel = Rp_\perp$ parallel to z . For $R = 0$, the system decouples into independent $(d-1)$ -dimensional layers, so that the percolation problem reduces to $(d-1)$ dimensions. Models with a finite and nonzero R have already received some attention [15], and it was shown that they are within the same universality class as the isotropic percolation model in d dimensions. In the present paper, we shall focus on the limit $R \rightarrow \infty$. In this anisotropic limit of the bond-percolation model, the probability p_\perp in the $(d-1)$ -dimensional layers approaches 0 near criticality,

and thus one can express p_{\perp} and p_{\parallel} as

$$p_{\parallel}(p_z) = 1 - \epsilon, \quad \text{and} \quad p_{\perp} = \epsilon/t \quad (\epsilon \rightarrow 0), \quad (5.1)$$

where t is a temperature-like parameter. When ϵ is precisely zero, the system becomes one-dimensional and this percolation problem is trivial. However, as we shall argue later, the anisotropic percolation model defined by Eq. (5.1) is equivalent with a quantum $q \rightarrow 1$ Potts model in $(d-1)$ dimensions, which fits in the d -dimensional percolation universality class.

For the anisotropic model defined by Eq. (5.1), the correlation length in the z direction is of the order of $1/\epsilon$. In order to maintain the d -dimensional character of the system, the lattice size in this direction must also diverge as $1/\epsilon$. Thus, we apply a rescaling $z' = z\epsilon$, so that the correlation length in the new unit and the physical size remain approximately constant. As $\epsilon \rightarrow 0$, the z' dimension becomes continuous, and we refer to the resulting continuous percolation problem as the transverse percolation model.

Next, we formulate a Monte Carlo method for the transverse percolation model. The numerical results confirm that the transverse percolation model belongs to the same universality class as the conventional percolation problem on a discrete lattice.

Another purpose of the present paper is the application of conformal mappings in curved geometries. In two dimensions, the theory of conformal invariance has yielded substantial results [11–13]. Conformal mappings yield relations between critical systems in different geometries, and thus provide useful tools for the determination of universal properties of critical models. A well-known example is Cardy’s mapping between an infinite plane and the surface of an infinitely long cylinder [16]. Since a cylinder is pseudo-one-dimensional, its numerical investigation is simpler than that of a two-dimensional plane. Cardy’s mapping can be generalized to any number of spatial dimensions, and in three dimensions it transforms an infinite space \mathbb{R}^3 into a pseudo-one-dimensional geometry $S^2 \times \mathbb{R}$. However, the nonzero curvature of the geometry $S^2 \times \mathbb{R}$ poses a serious obstacle for numerical simulations.

In applications to the Ising model, this problem was solved recently in Refs. [17–19]. The solution makes use of the Hamiltonian limit of the lattice Ising model, which renders one of the lattice directions continuous. Thus, one can perform Monte Carlo simulations in curved geometries, such as the surface of a sphere $S^1 \times S^1$ in two dimensions and the cylinder-like geometry $S^2 \times \mathbb{R}^1$ in three dimensions. It was reported [17,18] that, in three dimensions, the Ising model is conformally invariant and the corresponding estimations of critical exponents are compatible with existing results. In Ref. [17] the three-dimensional geometry $S^2 \times \mathbb{R}^1$ was named a spherocylinder. Here, we simulate the transverse percolation model in curved geometries, which provides another application of conformal mappings to investigate bulk and surface critical phenomena.

5.2 Models and algorithms

5.2.1 Quantum transverse q -state Potts models

The partition sum of the $q = 1$ Potts model is just a constant, so that its equivalence to the bond-percolation model has to be formulated [7] in terms of geometric properties of the random-cluster representation of the Potts model in the limit $q \rightarrow 1$. To explore the anisotropic limit of the bond-percolation model defined by Eq. (5.1), we start with the Hamiltonian limit of an Ising model on a $N \times M$ rectangular lattice with periodic boundary conditions

$$\mathcal{H}/k_{\text{B}}T = - \sum_{i,j} [K_x s_{i,j} s_{i+1,j} + K_y s_{i,j} s_{i,j+1}]. \quad (5.2)$$

The spins can assume the values $s_{i,j} = \pm 1$, the integer coordinates i and j label the lattice sites, and K_x and K_y are the coupling strengths in the x and y directions, respectively. The critical line of this model is given by [20]

$$\sinh(2K_x) \sinh(2K_y) = 1. \quad (5.3)$$

Thus, in the anisotropic limit $\epsilon \rightarrow 0$, the couplings can be written as

$$K_x = \epsilon/t, \quad \text{and} \quad \exp(-2K_y) = \epsilon, \quad (\epsilon \rightarrow 0), \quad (5.4)$$

where t parametrizes the temperature; the critical point is $t_c = 1$.

The Hamiltonian limit of the lattice Ising model defined by Eqs. (5.2) and (5.4) can be exactly mapped onto the *one*-dimensional quantum Ising model [21]. This equivalence was formulated in the reverse direction by Suzuki [22], using the Trotter formula [23]. The Hamiltonian of the quantum Ising chain reads

$$\mathcal{H}_{\text{qm}} = - \sum_i (\sigma_i^z \sigma_{i+1}^z + t \sigma_i^x), \quad (5.5)$$

where σ^z and σ^x are the Pauli matrices for the z and x spin components, respectively. The Hamiltonian \mathcal{H}_{qm} contains noncommuting operators and represents a quantum system with nearest-neighbor Ising interactions, and the temperature-like parameter t acts as a transverse field in the x direction.

This equivalence can be readily generalized to spatial dimensions $d > 2$, i.e., the Hamiltonian limit of a d -dimensional lattice Ising model is equivalent with the transverse Ising model in $(d - 1)$ dimensions.

Including the transverse Ising model as a special case, one can define a general quantum q -state Potts model [24, 25]. For instance, the Hamiltonian of a quantum q -state Potts chain (with integer q) can be written as

$$\mathcal{H}_{\text{qm}} = - \sum_i \sum_{k=0}^{q-1} (\mathbf{S}_i^k \mathbf{S}_{i+1}^{q-k} + t \mathbf{R}_i^k), \quad (5.6)$$

where \mathbf{S} and \mathbf{R} are $q \times q$ matrices satisfying the $Z(q)$ algebra

$$\begin{aligned} [\mathbf{S}_i, \mathbf{S}_j] = [\mathbf{R}_i, \mathbf{R}_j] = [\mathbf{S}_i, \mathbf{R}_j] &= 0, & i \neq j, \\ \mathbf{S}_j \mathbf{R}_j &= \exp(i2\pi/q) \mathbf{R}_j \mathbf{S}_j, & \text{and } \mathbf{R}_j^q = \mathbf{S}_j^q = \mathbf{I}. \end{aligned} \quad (5.7)$$

For the case of $q = 2$, the operators \mathbf{S} and \mathbf{R} reduce to the Pauli matrices σ^z and σ^x , respectively, and Eq. (5.6) simplifies to Eq. (5.5). The eigenspectra of these critical quantum q -state Potts chains ($0 < q \leq 4$) with free and periodic boundary conditions have already been explored in Refs. [24, 25], and it was shown that, indeed, they share the same critical exponents as the corresponding classical q -state Potts models in two dimensions.

For noninteger q or the limiting case $q \rightarrow 1$, equations (5.6) and (5.7) are not suitable to describe the Hamiltonian limit of the q -state Potts model. In this case, one can instead apply the transfer matrix of the random cluster model [26]. The evaluation of the partition function uses the transfer matrix as

$$Z = \sum_{s^{(1)}, s^{(2)}, \dots} \langle s^{(1)} | \mathbf{T} | s^{(2)} \rangle \dots \langle s^{(y)} | \mathbf{T} | s^{(y+1)} \rangle \dots, \quad (5.8)$$

where $s^{(y)}$ is the bond configuration at the y th row and the transfer is in the direction of the strong coupling. For the anisotropic bond percolation model described by Eq. (5.1), the transfer matrix reads

$$\langle s^{(y)} | \mathbf{T} | s^{(y+1)} \rangle = \mathbf{I} - \epsilon \sum_x [\mathbf{B}_x^{(y, y+1)} - \frac{1}{t} \mathbf{C}_{x, x+1}^{(y)}] + O(\epsilon^2), \quad (5.9)$$

where \mathbf{I} is the unit matrix. The symbol $\mathbf{B}_x^{(y, y+1)}$ represents that, between the y th and $(y + 1)$ rows, a ‘broken’ bond occurs at the site x while the remaining bonds are occupied, and $\mathbf{C}_{x, x+1}^{(y)}$ means that only *one* bond exists between x and $x + 1$ at the y th row. Once q is not precisely equal to 1, the operators \mathbf{B} and \mathbf{C} do not commute, and thus are quantum operators. For $t \ll 1$, most sites are connected so that the system is in an ‘ordered’ state; while for $t \gg 1$, they are independent of each other and the system is ‘disordered’. A phase transition occurs at $t = 1$.

Therefore, we simply expect that the anisotropic limit of the bond percolation model by Eq. (5.1) is within the same universality class with the corresponding isotropic version. This will be demonstrated further by means of Monte Carlo simulations.

5.2.2 Algorithms

We consider the anisotropic limit of the bond-percolation model [Eq. (5.1)] on a $N \times M$ rectangular lattice with periodic boundary conditions. The bond occupation probabilities in the x and y directions are p_{\perp} and p_{\parallel} in Eq. (5.1), respectively. For such a system, the correlation length in the y direction is of order $1/\epsilon$, as mentioned earlier. Thus, we have to take the lattice size M proportional to $1/\epsilon$ while if N is kept constant. Since computer memories are finite, it may not immediately be obvious how a Monte Carlo algorithm can be formulated.

Let us start with the procedures commonly used for the cluster decomposition of the isotropic version of the percolation model with the bond probability p . First, one introduces a bond variable b_{ij} for each bond between nearest-neighboring sites i and j . Occupied and empty bonds are represented by $b_{ij} = 1$ and 0 , respectively. For each bond variable b_{ij} , one draws a uniformly distributed random number r ($0 \leq r < 1$), and sets $b_{ij} = 1$ if $r < p$. The whole lattice is then decomposed into clusters of connected sites through the occupied bonds. These percolation clusters are analogous to the Swendsen-Wang clusters in the Potts model [27].

For the anisotropic limit of the percolation model defined by Eq. (5.1), the bond probability in the y direction is $p_y = 1 - \epsilon$, so that one has to draw of order $1/\epsilon$ random numbers r before finding an empty bond $b_y = 0$. This indicates that empty bonds are sparsely distributed in the y direction. In the x direction, the bond probability $p_x \propto \epsilon$, so that the task to find the next occupied bond $b_x = 1$ again involves of order $1/\epsilon$ random numbers.

A more efficient procedure follows [28]. Counting the bond variables sequentially in the y direction, the distribution $P_y(m) \equiv (1 - p_y)p_y^{m-1}$ expresses the probability that $(m - 1)$ subsequent bond variables b_{ij} are equal to 1, while the m th variable is zero, i.e., an empty bond occurs at m th position. Thus, the cumulative distribution can be written as

$$C_y(m) = \sum_{j=1}^m P_y(j) = 1 - p_y^m = 1 - (1 - \epsilon)^m, \quad (5.10)$$

which represents the probability that an empty bond $b_j = 0$ occurs in the range $1 \leq j \leq m$. Thus, by mapping the distribution $0 < C_y(m) < 1$ on the uniform distribution of the random number r , one transforms r into an integer m

$$m = 1 + [\ln(r) / \ln(1 - \epsilon)], \quad (5.11)$$

where $0 < r < 1$ and the square brackets denote the integer part of the number in between. The number m represents the distance of the current empty bond to the one to be generated. Thus, only *one* random number is needed to generate the next empty bond in the y direction.

In the x direction, one instead uses the distribution $P_x(n) \equiv p_x(1 - p_x)^{n-1}$ to express the probability that $(n - 1)$ subsequent variables b_{ij} are zero, while the n th bond variable is 1. We mention that, although the bond variables are now in the x direction, they are still counted sequentially along the y direction. Analogously, one can transform a uniformly distributed random number r into an integer n

$$n = 1 + [\ln(r) / \ln(1 - p_x)] \quad (p_x = \epsilon/t). \quad (5.12)$$

The average number of the y -dimensional empty bonds and that of the occupied bonds in the x direction are

$$\bar{m} \equiv \int_0^1 dr \ln(r) / \ln(1 - \epsilon) \propto \frac{1}{\epsilon}, \quad \text{and} \quad \bar{n} \propto \frac{t}{\epsilon}, \quad (5.13)$$

respectively. Now, suppose the $N \times M$ square lattice represents a conducting network, and the occupied bonds act as the elementary conducting units. According to Eq. (5.13), in the y direction, the current is allowed to flow along the conducting ‘lines’ until it occasionally encounters an empty bond, to which we shall refer as a barrier with an infinitely large resistance. In the x direction, since most bonds are empty, the areas between the neighboring conducting lines can be considered to be filled with an insulating material, and the electrical current has to rely on sparsely distributed ‘bridges’ (occupied bonds). If a potential difference is

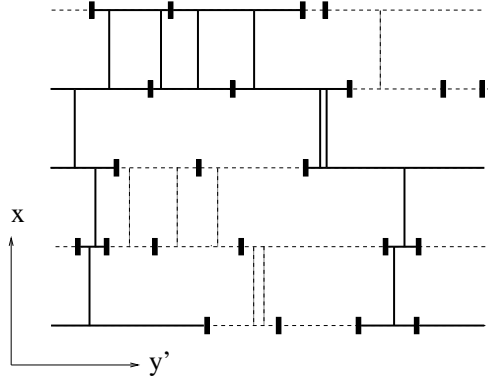


Figure 5.1: The anisotropic limit of the percolation model after the rescaling $y' = \epsilon y$. The horizontal lines represent ‘conducting’ lines in the y' direction, and the black bars are barriers with an infinitely large resistance on these lines; the vertical lines serve as ‘bridges’ between neighboring lines. One percolating cluster is shown by solid lines. This figure shows that the conducting lines on the left- and right-hand sides of a barrier may belong to the same cluster, but in that case they are via a detour. If this barrier is removed, the cluster size will remain unchanged.

applied to the up and down sides of the $N \times M$ network, the corresponding conductivity of this network then depends on the relative abundance of the bridges and barriers. According to Eq. (5.13), the average total numbers of the barriers and the bonds are $NM\epsilon$ and $NM\epsilon/t$, respectively, so that they remain finite in the limit $\epsilon \rightarrow 0$. Thus, the conductivity of the network depends only on the temperature-like parameter t . For $t \gg 1$, the sizes of conducting clusters are small, and the up and down sides are disconnected, so that no current exists; if the temperature t is sufficiently low, a percolating cluster which carries current may occur in the system.

Although one now needs only a finite number of random numbers, one still has to solve the problem of the infinite size M in the y direction, reflected by the divergence of \overline{m} and \overline{n} . This can be done by rescaling the y direction as $y' = \epsilon y$, so that the physical size $M' = M\epsilon$ remains approximately a constant. In the limit $\epsilon \rightarrow 0$, the y dimension becomes continuous, i.e., there is an infinite number of lattice sites per physical length unit, and the $N \times M$ square lattice reduces to N lines of physical length M' . Meanwhile, Eqs. (5.11) and (5.12) change into

$$m' = \epsilon m = -\ln(r), \quad \text{and} \quad n' = \epsilon n = -t \ln(r), \quad (\epsilon \rightarrow 0), \quad (5.14)$$

which indicates that the average distances of the barriers and bridges, \overline{m}' and \overline{n}' , are now of the order of 1. As a result, after the rescaling $y' = y\epsilon$, the anisotropic limit of the percolation model defined by Eq. (5.1) reduces to a continuous percolation model, to which we shall refer as the transverse percolation model. A typical configuration is shown in Fig. 5.1, where the horizontal lines are the aforementioned conducting lines and the vertical lines are the bridges in the transverse direction. The black bars represent the barriers, through which the current cannot penetrate. For clarity, in Fig. 5.1 we have outlined a cluster by means of solid lines.

Conventional Monte Carlo methods for discrete lattice percolation problems store the lattice sites simply in an array. For the transverse percolation, this is no longer applicable, since one of the dimensions is now continuous. However, as mentioned above, the total number of the barriers and bridges still remains finite, so that one can make use of their positions as the dynamical variables. On this basis, a procedure for the cluster decomposition and the sampling is formulated as:

First, *randomly distribute barriers and bridges over the $N \times M'$ geometry*. Starting from an arbitrarily chosen origin, the positions of the barriers and the bridges are sequentially generated by Eq. (5.14). For instance, suppose the current Monte Carlo step arrives at the i th barrier, whose position is stored as (x_i, y_i) . Here, the coordinates (x_i, y_i) represent that the i th barrier sits at the position y_i of the x_i th line. Then,

one draws a random number $0 < r < 1$ and evaluates m' by Eq. (5.14). If $y_i + m' \leq M'$, the $(i + 1)$ th barrier is placed at the same line as the i th one, and thus $x_{i+1} = x_i$ and $y_{i+1} = y_i + m'$; otherwise if $M' < y_i + m' \leq 2M'$, the $(i + 1)$ th barrier is at $(x_i + 1, y_i + m' - M')$; \dots . Repeat this procedure until the whole $N \times M'$ geometry is visited. The same procedure is applied to the distribution of the bridges, and the total numbers of the barriers and the bridges are denoted as B_l and B_r , respectively.

Second, *sample the sizes of the clusters*. After the first step, the geometry is now decomposed into clusters which consists of conducting lines connected through the bridges. The size of the i th cluster is the sum of the lengths of the conducting lines in it, which can be calculated from the positions of the barriers stored in the computer memory. If the size of the i th cluster is denoted as S_i , a quantity resembling the magnetic susceptibility χ and the corresponding Binder-like ratio Q [29] can be defined as

$$\chi = \frac{1}{V} \langle \sum_i S_i^2 \rangle \equiv V \langle m^2 \rangle, \quad \text{and} \quad Q = \frac{\langle \sum_i S_i^2 \rangle^2}{\langle (\sum_i S_i^2)^2 \rangle}, \quad (5.15)$$

where $V \equiv NM'$ is the volume of the system.

During the first step of the above algorithm, the function, $\ln r$, has to be frequently carried out, which decreases somewhat the efficiency of the algorithm. A different procedure can be applied as follows. From Eq. (5.14), the total number of the barriers and bridges is as $\langle B_l \rangle = V/\langle m' \rangle = V$ and $\langle B_r \rangle = V/\langle n' \rangle = V/t$, respectively. Instead of allowing the fluctuations of B_l and B_r during Monte Carlo simulations, one may fix them at their expectation values V and V/t , respectively. Since these barriers and bridges are uniformly distributed, their positions can now be *independently* calculated as $l_i = rV$ with the random number $0 < r < 1$. Then, the coordinates of the i th barrier is given by $x_i = [l_i/M'] + 1$ and $y_i = l_i - (x_i - 1)M'$, where the square brackets represent the integer part. Here, the word '*independently*' means that the position of the $(i + 1)$ th barrier does not depend on that of the i th one.

However, in this way, since the fluctuations of the energy-like quantities B_l and B_r are suppressed, an external constraint is effectively imposed on the system. A question arises how this energy-like constraint affects the critical behavior of the system. For the percolation model, since the thermal scaling exponent satisfies $2y_t - d < 0$, it can be shown [30] that the leading scaling behavior of the critical system is not modified. But new corrections to scaling can arise due to this constraint. To avoid this complication, we still use Eq. (5.14) to generate positions of the barriers and bridges in the present paper.

5.3 Simulations in flat geometries

5.3.1 Two dimensions

For the anisotropic limit of the percolation model in the two-dimensional rectangular geometry, the duality argument yields that the critical point is $t_c = 1$, since the critical bond probabilities satisfy $p_{xc} + p_{yc} = 1$. Furthermore, the thermal and magnetic critical exponents are exactly known, as mentioned earlier. Thus, this model provides a good test case for the Monte Carlo algorithm described above and the universality of the transverse percolation model.

The simulations used a rectangular geometry of L lines of length L in the range $6 \leq L \leq 32$. Periodic boundary conditions were applied, and the dimensionless Binder-like ratio Q and the susceptibility-like quantity χ defined in Eq. (5.15) were sampled. Near the critical point, the numerical data of Q were fitted [31] by

$$Q(t, L) = q_0 + \sum_{k=1}^4 q_k (t - t_c)^k L^{ky_1} + b_1 L^{y_1} + b_2 L^{y_2} + c_1 (t - t_c) L^{y_1 + y_1}. \quad (5.16)$$

The terms with $y_1 = -2$ and $y_2 = -3$ account for corrections to scaling. The fit with $y_t = 3/4$ yields $t_c = 0.9994(5)$, in good agreement with the exact result $t_c = 1$. If t_c is kept fixed at 1 while y_t is left free, we have $y_t = 0.752(3) \approx 3/4$ [9–13]. Moreover, we fitted the Monte Carlo data of χ at $t_c = 1$ by the formula

$$\chi(t_c) = x_0 + L^{2y_h - 2} (b_0 + b_1 L^{y_1} + b_2 L^{y_2}), \quad (5.17)$$

from which we obtain $y_h = 0.1043(4) \approx 5/48$ [9–13].

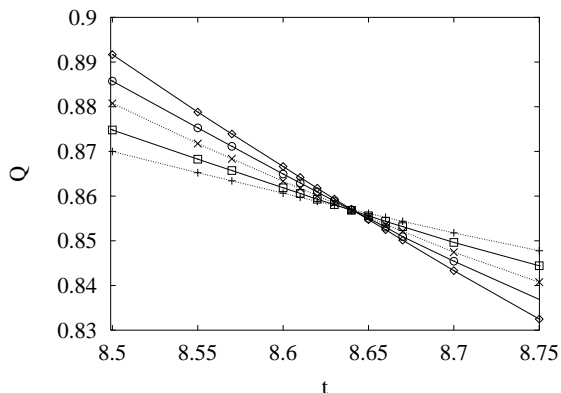


Figure 5.2: The Binder-like ratio Q vs the temperature-like parameter t for the transverse percolation model on the $L^2 \times L$ rectangular geometry. The system size L is 12 (+), 16 (\square), 20 (\times), 24 (\circ), and 28 (\diamond), respectively.

5.3.2 Three dimensions

As mentioned earlier, three-dimensional percolation models have been investigated extensively [2–6]. The most accurate results are provided by Monte Carlo simulations. For instance, for the isotropic bond-percolation model on the simple-cubic lattice, the percolation threshold is estimated [4] as $p_c = 0.248\,821\,6(5)$; the thermal and magnetic exponents are reported [4] as $y_t = 1.13(2)$ and $y_h = 2.523(4)$, respectively.

Using the aforementioned Monte Carlo algorithm, we simulated the transverse percolation model on the three-dimensional rectangular geometry: L^2 lines of length L originating from the $L \times L$ square lattice. The system sizes are in the range $6 \leq L \leq 40$, periodic boundary conditions were applied, and the quantities Q and χ in Eq. (5.15) were sampled. Part of the data for Q is shown in Fig. 5.2, indicating that the critical point is located at $t_c \approx 8.64$. The clean intersection of these lines suggests that corrections to scaling are rather small. Equation (5.16) was fitted to the data of Q , with y_1 and y_2 taken as -1.14 and -2 [4], respectively. For y_t fixed at 1.13, we obtain $t_c = 8.6428(2)$; if y_t is left free, we find $y_t = 1.135(8)$ and $t_c = 8.6429(4)$, with the error margin twice the standard deviation.

Moreover, the data for χ were fitted by [31]

$$\chi = x_0 + x_1(t - t_c) + x_2(t - t_c)^2 + L^{2y_h - 2} \left[\sum_{k=1}^4 a_k (t - t_c)^k L^{ky_t} + b_1 L^{y_1} + b_2 L^{y_2} + c_1 (t - t_c) L^{y_t + y_1} \right], \quad (5.18)$$

where the terms with x_i ($i = 0, 1, 2$) arise from the regular part of the free energy. With the thermal exponent $y_t = 1.13$, we obtain $y_h = 2.519(1)$, where the estimated error margin includes the uncertainty of y_t .

These investigations confirm the correctness of the Monte Carlo algorithm, and moreover confirm that the transverse percolation model belongs to the same universality class as the isotropic version of the percolation model on discrete lattices.

5.3.3 Restoration of isotropy

Although the transverse percolation model defined by Eq. (5.1) is intrinsically anisotropic, the correlation lengths in the longitudinal and transverse directions are of the same order. This can be demonstrated by the approximate isotropy of a cluster in Fig. 5.3. This arises from the rescaling $z' = \epsilon z$ in the longitudinal direction. In fact, one can asymptotically restore the isotropy by choosing an appropriate rescaling factor, i.e., $z' = \epsilon z / \alpha_0$ with α_0 a constant. The value of α_0 is important in the present investigation, since we are also interested in applications of conformal mappings, which rely on isotropy.

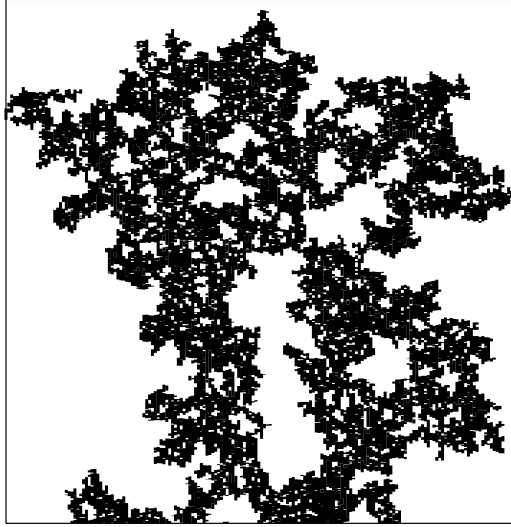


Figure 5.3: A cluster for the transverse percolation model on the $L \times L$ rectangular geometry with free boundary conditions and $L = 100$.

In two dimensions, we simulated the transverse percolation model precisely at $t_c = 1$ on the $L \times L$ rectangular geometry. The system sizes and the length ratio were taken as in the range $6 \leq L \leq 64$ and $0.65 \leq \alpha \leq 0.80$, respectively. Free boundary conditions were applied both in the x and y directions. During the Monte Carlo simulations, we sampled the percolation probabilities in both directions, denoted as P_x and P_y . Accordingly, we define a dimensionless ratio

$$r(\alpha, L) = \left\langle \frac{P_x}{P_y} \right\rangle. \quad (5.19)$$

Thus, the aforementioned isotropy means $r(\alpha_0, L) = 1$. Taking into account finite-size effects, we fitted the data of $r(\alpha, L)$ by

$$r(\alpha, L) = 1 + a_1(\alpha - \alpha_0) + a_2(\alpha - \alpha_0)^2 + \dots + b_1 L^{y_1} + b_2 L^{y_2} + c_1 L^{y_1}(\alpha - \alpha_0). \quad (5.20)$$

The terms with y_1 and y_2 describe corrections to scaling, due to small-scale deviations from isotropy of the transverse percolation model. The numerical data can be successfully described by Eq. (5.20) with $y_1 = -2$ and $y_2 = -3$, and the fit yields $\alpha_0 = 0.76978(7)$, in agreement with the number $4/3\sqrt{3}$ [25].

Similarly, for the three-dimensional rectangular geometry $L^2 \times L$ with free boundary conditions, one can define the ratio $r(\alpha, L)$ on the basis of the percolation probabilities in the discrete and continuous directions. Simulations were performed at the aforementioned estimated critical point $t_c = 8.6429(4)$, and the system sizes were taken in the range $6 \leq L \leq 40$. The data of $r(\alpha, L)$ were fitted by Eq. (5.20) with $y_i = -1.14$ [4]. After a cutoff for small system sizes $L \leq 10$, the fit yields $\alpha_0 = 1.5844(4)$.

5.4 Conformal invariance

In this section, we summarize the conformal mappings and the corresponding transformations of the pair correlation functions involved in the present paper. Most of these mappings have already been derived in Refs [13, 16–18].

Spherocylinder. In two dimensions, one may parametrize the infinite plane as a complex number $z = x + iy$, Cardy's well-known mapping [13, 16] is then expressed as $z' = R \ln z$. The geometry z' can be interpreted as the surface of an infinitely long cylinder $S^1 \times \mathbb{R}^1$ with a radius R . This mapping can be generalized to any number of dimensions. For instance, in spherical coordinates (r, θ, ϕ) , Cardy's mapping in three dimensions reads

$$(r, \theta, \phi) = (e^{u/R}, \theta, \phi), \quad (-\infty < u < \infty) \quad (5.21)$$

with $R > 0$ a free parameter. The geometry described by the variables (u, θ, ϕ) has a line element as

$$d s^2 = d u^2 + R^2(d \theta^2 + \sin^2 \theta d \phi^2), \quad (0 \leq \theta \leq \pi, 0 \leq \phi < 2\pi) \quad (5.22)$$

and thus can be recognized as the extension of a sphere S^2 into another dimension \mathbb{R} . In Ref. [17], this pseudo-one-dimensional geometry $S^2 \times \mathbb{R}$ was named a spherocylinder.

In the infinite flat space \mathbb{R}^3 , a critical two-point correlation function $g(r)$ behaves as

$$g(r)_{\mathbb{R}^3} \propto r^{-2X}, \quad (r \gg 0) \quad (5.23)$$

where X is the appropriate scaling dimension. Under the conformal mapping (5.23), this algebraic decay [Eq. (5.23)] is covariantly transformed into

$$g(u)_{S^2 \times \mathbb{R}} \propto R^{-2X} (e^{u/2R} - e^{-u/2R})^{-2X}, \quad (5.24)$$

where $u > 0$ is the distance between a pair of points on the spherocylinder, (u_0, θ, ϕ) and $(u_0 + u, \theta, \phi)$. For $u \gg 0$, the correlation function decays exponentially: $g(u) \propto R^{-2X} e^{-Xu/R} \equiv R^{-2X} e^{-u/\xi}$, so that the correlation length along the spherocylinder is equal to $\xi = R/X$.

Interior of a sphere. In two dimensions, the complex function $z' = (z - i)/(z + i)$ [13] maps the infinite plane onto itself, and meanwhile transforms the semi-infinite plane $\mathbb{R} \times \mathbb{R}^+$ into the interior of a *unit* circle. In fact, such a mapping can be generalized to spatial dimensions $d > 2$. It then reads

$$\vec{r}'/r'^2 = \vec{r}/r^2 + \hat{I}/2, \quad (5.25)$$

with \hat{I} an arbitrary fixed unit vector. Under Eq. (5.25), the infinite flat space \mathbb{R}^d is mapped onto itself, and the plane $\hat{I} \cdot \vec{r} = 0$, which corresponds to a spherical surface with an infinite radius, is conformally transformed into the surface of a d -dimensional unit sphere with the center at \hat{I} . The half spaces $\hat{I} \cdot \vec{r} > 0$ and $\hat{I} \cdot \vec{r} < 0$ are transformed into the interior and exterior of this unit sphere, respectively.

On the basis of the conformal transformation (5.25), it can be shown [13, 32] that, in the interior of a sphere with free or fixed boundary conditions, the profile of an operator $\langle \psi \rangle$ follows from

$$\langle \psi(r) \rangle \propto R^{-X} [1 - (r/R)^2]^{-X}, \quad (5.26)$$

where R is the radius of the sphere.

Furthermore, Eq. (5.21) transforms the interior of a unit sphere S^d into a semi-infinite spherocylinder $S^{d-1} \times \mathbb{R}^+$, with an end at $u = 0$. Thus, a conformal mapping between the semi-infinite flat space $\mathbb{R}^{d-1} \times \mathbb{R}^+$ and the half spherocylinder $S^{d-1} \times \mathbb{R}^+$ is established, and the profile (5.26) is covariantly transformed into

$$\langle \psi(u) \rangle \propto R^{-X} (e^{u/2R} - e^{-u/2R})^{-2X}, \quad (5.27)$$

which differs from Eq. (5.24) only by a factor R^{-X} .

Surface of a sphere. By rotating an ellipse about the minor or major axis, one obtains an oblate or a prolate spheroid, respectively. In three-dimensional Cartesian coordinates (x, y, z) , these spheroids are defined by

$$\frac{x^2}{a^2} + \frac{y^2}{a^2} + \frac{z^2}{b^2}, \quad (a, b > 0) \quad (5.28)$$

where a and b are the equatorial and the polar radii, respectively. Special cases of the spheroids include the surface of an infinitely long cylinder, of a sphere, and of a flat disc. The latter object is reached in the limit of an oblate spheroid $b \rightarrow 0$. It is already known [18] that a conformal transformation exists between the infinite plane \mathbb{R}^2 and the surface of a spheroid. For simplicity, we here only introduce the mappings of the infinite plane on the surface of a sphere and on that of a flat disc. Further, we generalize such conformal mappings to spatial dimensions $d > 2$.

The transformation between an infinite plane \mathbb{R}^2 and the surface of a sphere S^2 can be graphically understood as follows. A sphere with radius R is placed on the top of an infinite plane, i.e., only the south ‘pole’ of the sphere touches the plane. From the north ‘pole’, one draws an arbitrary line, such that this line penetrates through the sphere at \vec{R} and intersects with the plane at \vec{r} . The conformal transformation is simply obtained by setting an one-to-one correspondence between the point \vec{r} and \vec{R} . If one expresses the plane in polar coordinates (r, ϕ) , while parametrizes the surface of the sphere in spherical coordinates ($r = R, \theta, \phi$), the transformation reads

$$(r, \phi) = (2R \cot \frac{\theta}{2}, \phi) . \quad (5.29)$$

According to Eqs. (5.23) and (5.29), the pair correlation function $g(\vec{R}_1, \vec{R}_2)$ on the sphere follows from

$$\begin{aligned} g(\vec{R}_1, \vec{R}_2) &\propto 2^{-X} R^{-2X} [1 - \sin \theta_1 \sin \theta_2 \cos(\phi_1 - \phi_2) - \cos \theta_1 \cos \theta_2]^{-X} \\ &= |\vec{R}_1 - \vec{R}_2|^{-2X} , \end{aligned} \quad (5.30)$$

which, interestingly, has the same form as that in the infinite plane described by Eq. (5.23).

Application of Eq. (5.29) to the interior of a unit circle leads to the half sphere $S \times S^+$, so that a conformal transformation between the semi-infinite plane $\mathbb{R} \times \mathbb{R}^+$ and the half surface of a sphere is established. Accordingly, the profile of an operator in the geometry $S \times S^+$ behaves as

$$\langle \psi(\vec{R}) \rangle \propto (R \cos \theta)^{-X} . \quad (5.31)$$

In spherical coordinates (r, Ω) , where Ω is a set of angular variables specifying the surface of a d -dimensional sphere, the line element of the flat space \mathbb{R}^d can be written as

$$d s^2 = d r^2 + r^2 d \Omega^2 . \quad (5.32)$$

In three dimension, one simply has $d \Omega^2 = d \theta^2 + \sin^2 \theta d \phi^2$. On this basis, one can express the line element of the $(d + 1)$ -dimensional space \mathbb{R}^{d+1} as

$$d s'^2 = d r'^2 + r'^2 (d \theta'^2 + \sin^2 \theta' d \Omega^2) . \quad (5.33)$$

It is now obvious that, for $d > 2$, the generalization of Eq. (5.29) reads

$$(r, \Omega) = (2R \cot \frac{\theta'}{2}, \Omega) , \quad \text{with } r' = R . \quad (5.34)$$

Therefore, Eq. (5.34) transforms an infinite space \mathbb{R}^d into the surface of a $(d + 1)$ -dimensional sphere S^d , on which the pair correlation function follows from Eq. (5.30).

Surface of a hyper-disc. As mentioned earlier, the disc geometry is obtained in the limit $b \rightarrow 0$ of an oblate spheroid, composed of the interiors of two circles connected at their perimeters. This can be generalized to $d > 2$, and the surface of a hyper-disc consists of the interiors of two d -dimensional spheres with the surfaces of both spheres sewn together. Then, the conformal mapping between the space \mathbb{R}^d and the surface of the hyper-disc reads

$$\begin{cases} (r, \Omega) = (r'/R, \Omega) , & (0 \leq r < 1 , r' \leq R : \text{positive face}) \\ (r, \Omega) = (R/r', \Omega) , & (0 \leq r < 1 , r' \leq R : \text{negative face}) \end{cases} . \quad (5.35)$$

The first derivative of the mapping formula (5.35) is discrete at the edge of the hyper-disc ($r' = R$). For a pair of points on the same face of the hyper-disc, \vec{r}'_1 and \vec{r}'_2 , the correlation function has the same form as that in the infinite space \mathbb{R}^d , i.e., $g(\vec{r}'_1, \vec{r}'_2) \propto |\vec{r}'_1 - \vec{r}'_2|^{-2X}$.

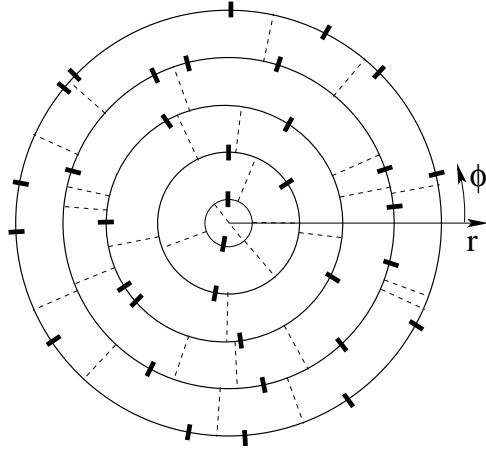


Figure 5.4: Example of transverse percolation model on the interior of a circle.

5.5 Simulations in curved geometries

For spatial dimensions $d > 2$, conformal mappings normally lead to a curved space or a geometry with curved boundaries. Even in two dimensions, curved geometries, such as the surface of a sphere, can also be obtained from conformal transformations. The nonzero curvature of these geometries poses a serious problem for numerical applications of conformal mappings, since they defy discretizations into regular lattices. As a consequence, the validity of Cardy's mapping was verified only for the special case of the spherical model [33]. Recently, for the case of the Ising model, this difficulty was avoided by making use of the Hamiltonian limit of the Ising model [17, 18], which renders one of the dimensions continuous. Since the aforementioned transverse percolation model also has one continuous dimension, we here provide further applications of conformal mappings to both the bulk and surface criticality.

5.5.1 Monte Carlo methods in curved geometries

As an example, we sketch a procedure for cluster decomposition of the interior of a circle. First, one divides the geometry into L concentric circles, with the L th circle precisely at the edge (Fig. 5.4). The location of the k th circle reads $r_k = k - \frac{1}{2}$, with the corresponding circumference $c_k = \pi(2k - 1)$. Then, let the continuous longitudinal dimension of the transverse percolation model be the ϕ direction, so that those concentric circles just represent the conducting lines mentioned above. Then, according to Eq. (5.14), one generates and uniformly distributes barriers at the concentric circles. We mention that, at the k th circle, the average number of the barriers is controlled by the length of its perimeter. The distribution of bridges follows an analogous way, but the total number of the bridges between the k th and $(k + 1)$ th circles ($1 \leq k \leq L - 1$) is now governed by the circumference of the circle in the middle. Furthermore, the diameter of the first circle is 1, and thus bridges can exhibit through the center, connecting different parts of the first circle. A typical configuration is shown in Fig. 5.4, where the bridges are denoted as the dashed lines.

Similarly, the 'lattice' structure on a sphere S^2 can be represented by L uniformly distributed circles with radii as chosen above. The transverse and longitudinal dimensions are the θ and ϕ directions, respectively. The location of the k th circle is $\theta_k = (k - \frac{1}{2})\pi/L$, and its circumference is $c_k = 2L \sin \theta_k$. Thus, the radius of the sphere is $R = L/\pi$. Analogously, the number of the barriers at the k th circle is dominated by the length of its perimeter, while that of the bridges is governed by the circumference of the circle in the middle of the k th and $(k + 1)$ th ones.

On a microscopic scale, the lattice structure on a sphere or the interior of a circle is the same as that on a flat plane, i.e., both of them are obtained in the anisotropic limit of the square lattice. Thus, one expects that the critical point is still $t_c = 1$. However, a global effect may arise due to the fact that the

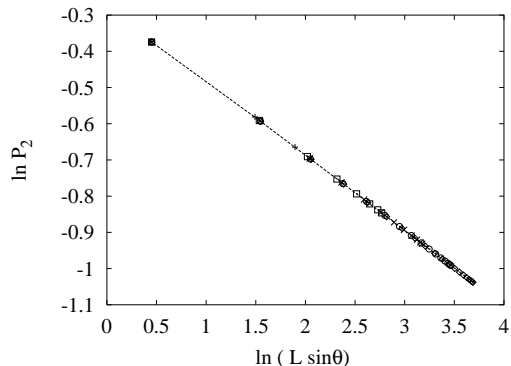


Figure 5.5: Data collapse of the quantity $P_2(\theta, L)$ for the transverse percolation model on the sphere. The system sizes are 8(+), 16(\square), 24(\times), 32(\circ), and 40(\diamond).

nonzero curvature cannot be fully accounted for by circles with varying radius. This has been investigated in Ref. [18], and it was argued that such a global effect can be described by a correction term proportional to L^{y_t-2} . Since the two- and three-dimensional percolation models have $y_t < 2$, this effect vanishes as $L \rightarrow \infty$.

It is now obvious that, in three dimensions, the spherocylinder $S^2 \times \mathbb{R}$ can be obtained by extending the aforementioned lattice structure of a sphere into another dimension. Meanwhile, in order to approximate the pseudo-one-dimensional geometry of the spherocylinder, the size of the \mathbb{R} direction should be taken as nL with a sufficiently large integer n .

5.5.2 Numerical results

With the Monte Carlo algorithms described above, we are now able to simulate the transverse percolation model in the following curved geometries in two and three dimensions.

Surface of a sphere. The system sizes were taken in the range $8 \leq L \leq 48$, with L the number of the circles on the sphere. The simulations occur precisely at the critical point $t_c = 1$, and the rescaling length ratio was set at $\alpha_0 = 0.76978$, such that the isotropy of the transverse percolation is asymptotically restored. We sampled the pair connectivity $P_2(\theta)$ of the points (θ, ϕ) and $(\theta, \phi \pm \pi)$ on the same circle. For both points in the same cluster, we say $P_2 = 1$; otherwise $P_2 = 0$. According to Eq. (5.30), the connectivity behaves as $\langle P_2(\theta) \rangle \propto (L \sin \theta)^{-2X_h}$ with X_h the magnetic scaling dimension, graphically shown in Fig. 5.5. The good quality of the data collapse for different system sizes (Fig. 5.5) indicates that corrections to scaling are relatively small. The data for P_2 were fitted by

$$\langle P_2(\theta) \rangle = (L \sin \theta)^{-2X_h + cL^{y_c}} [a_0 + a_2 L^{y_c} + a_3 (L \sin \theta)^{y_c} + \dots], \quad (5.36)$$

where the exponent $y_c = y_t - 2 = -5/4$, as explained above. For finite systems, the Hamiltonian may deviate from that at the fixed point, and we account for this by the terms with coefficients c and a_2 . Furthermore, we also include a term with a_3 , describing the inhomogeneity of a finite sphere. We found that the numerical data for $L \geq 12$ are successfully explained by Eq. (5.36), and the term cL^{y_c} cannot be well observed. The fit with $c = 0$ yields $X_h = 0.10418(4)$, in good agreement with the exact result $X_h = 5/48 = 0.104167\dots$

Interior of a circle. For the Ising model, the geometry inside a circle can be approximated [34] by drawing a circle on the square lattice. Applications of free or fixed boundary conditions are realized by removing or freezing the spins outside the circle, respectively. However, the symmetry along the ϕ direction is broken in this way, and thus irregular finite-size effects arise. The aforementioned Monte Carlo algorithm avoids this difficulty. The systems sizes were taken in the range $6 \leq L \leq 48$, and fixed boundary conditions were imposed: the whole edge is set within the same cluster. The fraction of the k th circle in this cluster $P_1(r)$

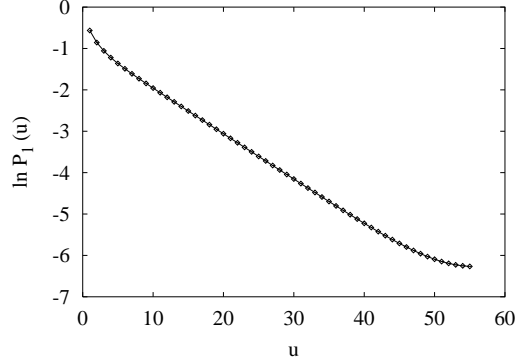


Figure 5.6: Exponential decay of $P_1(u)$ along the spherocylinder for the transverse percolation model. The system size is $L = 14$ and $n = 8$.

was sampled. The numerical data of $P_1(r)$ were fitted by Eq. (5.26) but with additional terms accounting for corrections to scaling. We obtain $X_h = 0.10413(4) \approx 5/48$.

Spherocylinder $S^2 \times \mathbb{R}$. The systems were taken as $L = 5, 7, \dots, 21$, and the finite-size in the \mathbb{R} direction was set as $nL = 8L$. Fixed boundary conditions were imposed at both ends $u = 0$ and $u = 8L$. The simulations were performed at the estimated critical point $t_c = 8.6429$, and the length rescaling ratio was fixed at $\alpha_0 = 1.5844$. The quantity $P_1(u)$ was sampled at the ‘equators’ only, in order to avoid inhomogeneity on finite spheres. The behavior of $P_1(u)$ follows from Eq. (5.27), decaying exponentially for $u \gg 0$. This is demonstrated in Fig. 5.6. The curved positions at the right-hand-side arise because fixed boundary conditions were applied at both ends, so that the correlations $P_1(u)$ build up over two distances u and $8L - u$.

As discussed above, there is a correction $\propto L^{y_c}$ in finite systems, due to the discretization of the θ direction. Compared to the irrelevant scaling exponent $y_i = -1.14$ in three dimensions, the correction with the exponent $y_c = y_t - 2 = -0.87$ is expected to dominate over that with y_i . Taking into account these effects, Eq. (5.27) yields

$$P_1(u, L) = L^{-X} [Y(u) + Y(8L - u)] (a_0 + a_1 L^{y_c} + a_2 L^{y_i} + a_3 L^{-2}), \quad (5.37)$$

with the function

$$Y(u) = (e^{uX/2R} - e^{-uX/2R})^{-2X}, \quad (X = X_h + cL^{y_c}) \quad (5.38)$$

where the radius of the spheres is $R = L\pi$ as mentioned earlier.

Equations (5.37) and (5.38) were fitted to the Monte Carlo data of $P_1(u)$. The fit yields $X_h = 0.479(1)$, which is in agreement with the existing estimation $y_h = 2.523(4)$ [4] and with our earlier determination $y_h = 2.519(1)$ on the $L^2 \times L$ rectangular geometry.

Half spherocylinder $S \times S^+ \times \mathbb{R}$. As an example of the applications of conformal mappings to surface criticality, we simulated the transverse percolation model on the half spherocylinder $S \times S^+ \times \mathbb{R}$. The system sizes were taken as $6, 8, \dots, 24$, and $n = 8$. The fixed and free boundary conditions were imposed on the ends of the spherocylinder and the equators, respectively. The quantity $P_1(u)$ was sampled. Analogously, the numerical data of $P_1(u)$ were fitted by Eqs.(5.37) and (5.38), but $X = X_{hs} + cL^{y_c}$, where X_{hs} is now the surface magnetic scaling dimension. After a cutoff for small system sizes $L \leq 10$, the fit yields $X_{hs} = 0.975(4)$, in good agreement with the existing results $X_{hs} = 0.96(5)$ [35] and $X_{hs} = 0.970(6)$ [36].

5.6 Discussion

We define a continuous percolation model: the transverse percolation model. This model is obtained by applying an infinite rescale factor to the longitudinal direction of the anisotropic limit of the bond percolation model, and is equivalent with the quantum transverse $q \rightarrow 1$ Potts model. We formulate and apply an efficient Monte Carlo method, and confirm that the transverse percolation model belongs to the same universality class as the conventional percolation problem on discrete lattices. For the two-dimensional rectangular geometry, the critical point is exactly available as $t_c = 1$, and that in the three-dimensional rectangular geometry is determined as $t_c = 8.6429(4)$. Furthermore, we restore the isotropy asymptotically by requiring that the correlation lengths in all Cartesian directions are identical to each other.

Moreover, the property that the longitudinal direction is continuous enables simulations of the transverse percolation model in curved geometries. The numerical data are analyzed by finite-size scaling according to the predictions of the theory of conformal invariance. It is shown that, in curved geometries, the predictions of conformal invariance are accurately satisfied. On the other hand, assuming conformal invariance, our method provides a powerful tool to investigate bulk and surface critical phenomena.

Bibliography

- [1] S.R. Broadbent and J.M. Hammersley, Proc. Cambridge Philos. Soc. **53**, 629 (1957).
- [2] D. Stauffer and A. Aharony, *Introduction to Percolation Theory* (Taylor and Francis, London, 1992), and references therein.
- [3] M. Sahimi, *Applications of Percolation Theory* (Taylor and Francis, London, 1994).
- [4] C.D. Lorenz and R.M. Ziff, Phys. Rev. E **57**, 230 (1997).
- [5] G. Paul, R.M. Ziff, and H.E. Stanley, Phys. Rev. E **64**, 026115 (2001).
- [6] C.K. Hu, J.A. Chen, N.S. Izmailian, and P. Kleban, Compt. Phys. Comm. **126**, 77 (2000).
- [7] P.W. Kasteleyn and C.M. Fortuin, J. Phys. Soc. Jpn. **26**, (Suppl.), 11 (1969).
- [8] see, e.g., F.Y. Wu, Rev. Mod. Phys. **54**, 235 (1982).
- [9] B. Nienhuis, J. Phys. A **15**, 199 (1982).
- [10] B. Nienhuis, in *Phase Transitions and Critical Phenomena*, edited by C. Domb and J.L. Lebowitz (Academic Press, London, 1987), Vol.11, p.1, and references therein.
- [11] A.A. Belavin, A.M. Polyakov and A.B. Zamolodchikov, J. Stat. Phys. **34**, 763 (1984)
- [12] D. Friedan, Z. Qiu and S. Shenker, Phys. Rev. Lett. **52**, 1575 (1984)
- [13] J.L. Cardy, in *Phase Transitions and Critical Phenomena*, edited by C. Domb and J.L. Lebowitz (Academic Press, London, 1987), Vol.11, p.55.
- [14] R. Juhász and F. Iglói, Phys. Rev. E **66**, 056113 (2002).
- [15] S. Redner and H.E. Stanley, J. Phys. A **12**, 1267 (1979).
- [16] J.L. Cardy, J. Phys. A **17**, L385 (1984).
- [17] Y. Deng and H.W.J. Blöte, Phys. Rev. Lett. **88**, 190602 (2002).
- [18] Y. Deng and H.W.J. Blöte, Phys. Rev. E **67**, 036107 (2003); **67**, 066116 (2003).
- [19] H.W.J. Blöte and Y. Deng, Phys. Rev. E **66**, 066110 (2002).

- [20] L. Onsager, Phys. Rev. **65**, 117 (1944).
- [21] T.D. Schultz and D.C. Mattis, Rev. Mod. Phys. **36**, 856 (1964).
- [22] M. Suzuki, Prog. Theor. Phys. **46**, 1337 (1971); **56**, 2454 (1976).
- [23] H.F. Trotter, Proc. Am. Math. Soc. **10**, 545 (1959).
- [24] C.J. Hamer, J. Phys. A **14**, 2981 (1981).
- [25] F.C. Alcaraz, M.N. Barber, and M.T. Batchelor, Phys. Rev. Lett. **58**, 771 (1987); F.C. Alcaraz, M.N. Barber, M.T. Batchelor, and R.J. Baxter, J. Phys. A **20**, 6397 (1987).
- [26] L. Mittag and H.J. Stephen, J. Math. Phys. **12**, 441 (1971); J. Sólyom and P. Pfeuty, Phys. Rev. B **24**, 218 (1981); J. Kogut, Rev. Mod. Phys. **51**, 659 (1979).
- [27] R.H. Swendsen and J.-S. Wang, Phys. Rev. Lett. **58**, 86 (1987); J.-S. Wang and R.H. Swendsen, Physica A **167**, 565 (1990).
- [28] E. Luijten and H.W.J. Blöte, Int. J. Mod. Phys. C **6**, 359 (1995).
- [29] K. Binder, Z. Phys. B: Condens. Matter **43**, 119 (1981).
- [30] M.E. Fisher, Phys. Rev. **176**, 257 (1968).
- [31] H.W.J. Blöte, E. Luijten, and J.R. Heringa, J. Phys. A **28**, 6289 (1995); Y. Deng and H.W.J. Blöte, Phys. Rev. E **68**, 036125 (2003).
- [32] T.W. Burkhardt and E. Eisenriegler, J. Phys. A **18**, L83 (1985).
- [33] J.L. Cardy, J. Phys. A **18**, L757 (1985).
- [34] R. Badke, V. Rittenberg, and H. Rugg J. Phys. A **18**, L867 (1985); I. Reš and J. P. Straley Phys. Rev. B **61**, 14425 (2000).
- [35] A. Hansen, P.M. Lam, and S. Roux, J. Phys. A **22**, 2635 (1989).
- [36] P. Grassberger, J. Phys. A **25**, 5867 (1992).

Critical phenomena under energy-like and magnetic constraints

We present a Monte Carlo study of several critical and tricritical systems in two dimensions under two types of constraint. The systems include Baxter’s hard-square and hard-hexagon lattice gases, the Blume-Capel model, and three- and four-state Potts models with vacancies. The first type of constraint is energy-like and fixes the number of particles or vacancies. We find that such constraints affect the leading finite-size-scaling properties of *energy-like* quantities, while the effect on magnetic quantities is restricted to correction terms. The second type of constraint applies to the magnetization, and appears to suppress the finite-size divergences of a quantity that normally scales as the magnetic susceptibility.

In an attempt to explain the observed finite-size scaling properties, we make use of the well-known Fisher renormalization mechanism. However, we do not always find a satisfactory agreement with our numerical results for constrained critical systems. For instance, for most energy-like constraints, the exponents describing the finite-size dependence of the specific heat are twice the expected values.

We also sample specific-heat-like and susceptibility-like quantities on the basis of the fluctuations of the long-wavelength Fourier components of the energy and magnetization densities of constrained systems. Their finite-size scaling behavior resembles that of the specific heat and the susceptibility of unconstrained systems respectively.

6.1 Introduction

In experiments or in simulations, systems undergoing a phase transition may be subject to a constraint. For instance, the total number of vacancies in the Blume-Capel (BC) model [1,2] can be kept constant. Likewise, in Baxter’s hard-square lattice gas [3], the total number of particles may be fixed.

Critical phenomena in these ‘annealed’ constrained systems have been of interest for decades. Investigations date back to 1965 when the exactly solvable Syozi model [4], a dilute spin- $\frac{1}{2}$ Ising model, was introduced. Syozi found that the critical indices α' , β' and γ' are related to the standard exponents of the Ising model as

$$\alpha' = -\alpha/(1 - \alpha), \quad \beta' = \beta/(1 - \alpha), \quad \gamma' = \gamma/(1 - \alpha), \quad \dots \quad (6.1)$$

Fisher suggested [5] that the relations (6.1) are not specific to the Syozi model, but are satisfied by equilibrium models with a divergent specific heat ($\alpha > 0$) in general. Since then, Fisher’s *renormalized critical exponents* have gained considerable acceptance. As a result of Eq. (6.1), the singularity of the constrained critical specific heat C assumes the form of a finite cusp instead of being divergent. For the marginal case of a logarithmic divergence ($\alpha = 0$), Fisher showed that $C - C_0 \propto 1/\ln t$ where t is the temperature-like distance to criticality.

Later, more general theories were formulated [6] for constrained systems, including a theory of tricritical constrained phenomena. Such restrictions can, besides the total number of vacancies, also involve the volume or pressure etc. It was concluded [6,7] that, depending on the type or strength of the constraint, a continuous transition may get Fisher-*renormalized*, remain unchanged, or become first-order. The special point where the transition remains unchanged corresponds to a ‘tricritical’ point [6], of which the critical singularity is the same as that of the unconstrained critical system. This theory was tested on the Baker-Essam model [8], an exactly solvable compressible Ising model.

On the basis of a renormalization-type analysis using a generalized Landau-Ginzburg-Wilson Hamiltonian and the ϵ -expansion technique, Imry and coworkers found four distinct fixed points [9]. These are the tricritical Ising (T) and critical Ising (I) fixed points for unconstrained systems, and the *renormalized* tricritical (RT) Ising and the *renormalized* Ising (RI) critical fixed point for constrained systems. In three dimensions, T and RT correspond to Gaussian and spherical fixed points, respectively [9]. The exponent relations between these fixed points are: $\alpha_{RI} = -\alpha_I/(1 - \alpha_I)$ and $\alpha_{RT} = -\alpha_T/(1 - \alpha_T)$, in agreement with Eq. (6.1). These relations have, for the 3D case, been used to explain experimental data for ^3He - ^4He mixtures [10].

Since the upper critical dimensionality of Ising-like tricritical systems is three, one may expect that mean-field theory yields a qualitatively correct scenario for such systems. We have thus performed an exact calculation for the tricritical mean-field Blume-Capel (BC) model [11] with a large but finite system size. We find that the finite-size scaling behavior of the constrained version of this model corresponds with the classical (mean-field) *critical* Ising model.

Although considerable work has already been done for critical constrained behavior, further investigations still seem appropriate. The reasons are as follows. First, although Fisher’s *renormalized exponents* have been used extensively, few reports have been published about the finite-size dependence of constrained systems. Second, it is not obvious how tricritical systems behave under the constraint. Third, it remains to be investigated how the constraint affects the long-wavelength fluctuations of quantities whose critical behavior is conserved or renormalized. Since the constraint does not eliminate the spatial fluctuations, one might expect that the unrenormalized behavior will persist.

Our investigations include several critical and tricritical 2D models: Baxter’s hard square (HS) and hard-hexagon (HH) lattice gases [3], the Blume-Capel (BC) model, and Potts models with vacancies. Also included is the tricritical BC model in three dimensions. The total number of vacancies (or particles) is fixed at the critical expectation value, while they still can move freely over the lattice. These models are defined in Section II. Here the problem arises what sort of Monte Carlo algorithm applies to such constrained systems. The Swendsen-Wang and Wolff methods are not suitable or sufficient, since they do not operate on the zero spins or lattice-gas particles. In principle, one can apply a particle-conserving Kawasaki-like Monte Carlo algorithm. But this method suffers from serious critical slowing down, so that such simulations are limited to small system sizes. In the present work, we realize two types of constraints by means of a particle-conserving geometric cluster algorithm [12], which moreover suppresses critical slowing down. This Monte Carlo method moves critical clusters of spins (both zero and nonzero) or particles over the lattice in accordance with the Boltzmann distribution. It also imposes a magnetic constraint: it conserves the magnetization. The latter constraint can be eliminated by including Wolff cluster steps. The results for the energy-like and for the magnetic constraint are presented in Sections III and IV, respectively. Section V presents an analytic approach to finite-size scaling in the presence of a constraint. A brief discussion and overview is given in Section VI.

6.2 Models and sampled quantities

All simulations of the models described below used $L \times L$ systems with periodic boundary conditions.

6.2.1 The Blume-Capel model

The Hamiltonian of the BC model [1, 2] on the square lattice is

$$\mathcal{H}/k_{\text{B}}T = -K \sum_{\langle nn \rangle} s_i s_j + D \sum_k s_k^2, \quad (6.2)$$

where the sum $\langle nn \rangle$ is over nearest-neighbor pairs, and the spins assume values $s = 0$ or ± 1 . We refer to zero spins $s = 0$ as vacancies. The parameter D acts as the chemical potential of the vacancies. In the $K - D$ parameter space, the BC model has a critical line $K_c(D)$ and a tricritical point (K_t, D_t) . The critical behavior along the line $K_c(D)$ is Ising-like, and thus the magnetic, thermal and irrelevant scaling exponents are $y_h = 15/8$, $y_t = 1$, and $y_i = -2$, respectively. At tricriticality, the BC model has different exponents, namely [13] $y_h = 77/40$, $y_t^{(1)} = 9/5$, $y_t^{(2)} = 1/5$, and $y_i = -1$. Using a sparse transfer-matrix method and finite-size scaling, we locate the tricritical point at $K_t = 1.6431759$ (1) and $D_t = 3.2301797$ (2). This result is based on the requirement that two types of correlation lengths (magnetic and energy-like) simultaneously reach their theoretical values. The corresponding vacancy density is $\rho_t = 0.4549506$ (2). Analogously, we determine an arbitrary critical point at $K_c = 1$ as $D_c = 1.70271780$ (2), with $\rho_c = 0.3495830$ (1). This point appears to be sufficiently far from the tricritical point; crossover effects were not seen in the scaling analysis of the transfer-matrix results.

6.2.2 Baxter's hard-core lattice gases

We consider a lattice gas on the square lattice defined by the Hamiltonian

$$\mathcal{H} = -K \sum_{\langle nn \rangle} \sigma_i \sigma_j - J \sum_{\{NE\}} \sigma_k \sigma_l - M \sum_{[SE]} \sigma_m \sigma_n + \mu \sum_k \sigma_k, \quad (6.3)$$

where $\sigma = 0, 1$ represents the absence and the presence of a particle, respectively, and the chemical potential of particles is denoted as μ . The sums labeled as $\{NE\}$ and $[SE]$ are over second-neighbor pairs (diagonals of the elementary faces) along the $(x, y) = (1, 1)$ and $(1, -1)$ directions, respectively. We focus on two exactly solved cases [3] in which the nearest-neighbor interaction $K \rightarrow -\infty$, *i.e.*, the particles are 'hard' and nearest-neighbor sites cannot be occupied simultaneously. The first case is Baxter's HS model at $J_t = M_t = \ln(3 + \sqrt{5})$ and $\mu_t = \ln[8(1 + \sqrt{5})]$ which is known [14] to belong to the same universality class as the tricritical BC model. The corresponding vacancy density is $\rho_t = (5 + \sqrt{5})/10$.

In the second case, one of the diagonal couplings becomes infinitely repulsive while the other one is zero: $M \rightarrow -\infty$ and $J = 0$. This leads to Baxter's hard-hexagon (HH) lattice gas, which has a critical point at $\mu_c = \ln[(11 + \sqrt{5})/2]$ that belongs to the three-state Potts universality class. The critical exponents are given by $y_h = 28/15$, $y_t = 6/5$ and $y_i = -4/5$ [3, 15]. The critical vacancy density is again $\rho_c = (5 + \sqrt{5})/10$ [3].

6.2.3 Two-dimensional Potts model with vacancies

We consider the Potts model on the square lattice defined by the Hamiltonian

$$\mathcal{H}/k_{\text{B}}T = -K \sum_{\langle i, j \rangle} \delta_{\sigma_i, \sigma_j} (1 - \delta_{\sigma_i, 0}) - D \sum_k \delta_{\sigma_k, 0} \quad (\sigma = 0, 1, \dots, q). \quad (6.4)$$

Here, the sum $\langle \rangle$ is over all nearest-neighbor sites, and the site is occupied by a Potts spin with $\sigma = 1, \dots, q$ or by a vacancy $\sigma = 0$. Nonzero couplings K occur only between equal Potts spins, *i.e.*, spins with $\sigma_k \neq 0$. The abundance of the vacancies is controlled by the chemical potential D . For $q < 4$ the phase diagram in the (K, D) plane resembles that of the Blume-Capel model: a tricritical point occurs between the continuous and the first-order range of the line of phase transitions. By means of a transfer-matrix method, we have located the $q = 3$ tricritical point at $K = 1.649913$ (5), $D = 3.152173$ (1). The corresponding density of the vacancies is $\rho = 0.34572$ (5).

For the generic $q = 4$ Potts case, analyses of the critical scaling behavior are hampered by logarithmic corrections induced by the marginally irrelevant dilution field associated with D . We suppress this dilution field by requiring that transfer-matrix results for both the temperature and the magnetic exponent lead to the exactly known values. Extrapolation of finite-size estimates leads to our estimate of the $q = 4$ critical fixed point in the (K, D) plane as $K = 1.45790$ (1), $D = 2.47844$ (2). The corresponding density of the vacancies is $\rho = 0.21207$ (2).

6.2.4 Data sampled

Several quantities were sampled during the Monte Carlo simulations, including the order parameter and the densities of the energy and the particles or vacancies when allowed to fluctuate. The magnetic susceptibility is obtained from the fluctuations of the order parameter m as $\chi = L^2 \langle m^2 \rangle$. For the BC model, m is just the magnetization density. For the HH model, we define $m^2 = \frac{1}{2} \langle (\rho_1 - \rho_2)^2 + (\rho_2 - \rho_3)^2 + (\rho_3 - \rho_1)^2 \rangle$ in terms of the vacancy densities ρ_1, ρ_2 and ρ_3 on the three sublattices.

Analogously, we have $m^2 = \langle (\rho_1 - \rho_2)^2 \rangle$ for the HS model. A universal Binder ratio [16] is then defined as $Q = \langle m^2 \rangle^2 / \langle m^4 \rangle$. An energy-like density e was sampled as the nearest-neighbor correlation for the BC model, and as the next-nearest-neighbor correlation for the HH and HS lattice gases. On this basis, a specific-heat-like quantity (equal to the second derivative of the reduced free energy to the parameter conjugate to e) is defined as $C = L^d \langle (e^2) - \langle e \rangle^2 \rangle$, where d is the dimensionality of the lattice.

In addition we also sample quantities describing the response of the model to spatially inhomogeneous temperature or magnetic fields. Just as C and χ they can be expressed in terms of fluctuations of the conjugate densities. For these conjugate densities we use the long-wavelength Fourier components of the energy or magnetization.

First, we define a susceptibility-like quantity χ_F on the basis of the fluctuations of the spatial order parameter distribution $m(x, y)$. The Fourier components of $m(x, y)$ for systems of size L are

$$m_{k_x, k_y} = \frac{1}{L^2} \int_0^L dx dy m(x, y) \exp[2\pi i(xk_x + yk_y)/L], \quad (6.5)$$

Obviously, the conventional susceptibility is just $\chi = L^2 \langle m^2 \rangle = L^2 \langle m_{0,0}^2 \rangle$, and the quantities m_{k_x, k_y} , for $k_x \neq 0$ or $k_y \neq 0$, represent spatial inhomogeneity of m . Thus, We define

$$\chi_F = L^2 \langle m_{-1,0} m_{1,0} + m_{0,-1} m_{0,1} \rangle. \quad (6.6)$$

We shall refer to χ_F as the structure factor of the susceptibility.

Analogously, we define a specific-heat-like structure factor as $C_F = L^2 \langle e_{-1,0} e_{1,0} + e_{0,-1} e_{0,1} \rangle$, where e_{k_x, k_y} denotes the Fourier components of the energy density e .

6.3 Results for energy-like constraints

The following simulations are performed exactly at the critical or tricritical point, unless specified otherwise.

According to finite-size scaling, for unconstrained critical systems, we expect, apart from finite-size corrections,

$$e - e_0 \propto L^{y_t - d}, \quad \chi \propto L^{2y_h - d}, \quad \text{and} \quad C - C_0 \propto L^{2y_t - d}, \quad (6.7)$$

where e_0 and C_0 arise from the analytic part of free energy. The scaling behavior of χ and C can be obtained by integration over space of the magnetic and energy-energy correlation functions respectively. These correlation functions depend on the distance r as $r^{2y_h - 2d}$ and $r^{2y_t - 2d}$ respectively. Since χ_F and C_F are determined by integrals with the same scaling properties, we expect finite-size behavior similar to χ and C respectively.

As a test, we simulated the unconstrained HH model ($y_t = 6/5$ and $y_h = 28/15$). In order to allow transitions between particles and vacancies, Metropolis sweeps were applied in addition to geometric cluster steps [12]. System sizes were taken as $L = 6, 9, \dots, 24$. Results are shown in Fig. 6.1, which confirms Eq. (6.7) and our expectation that C and C_F behave similarly.

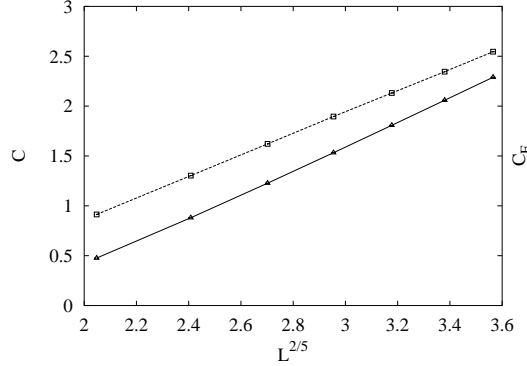


Figure 6.1: Specific-heat-like quantities C (\square) and C_F (\triangle) versus $L^{2/5}$ for the unconstrained HH model.

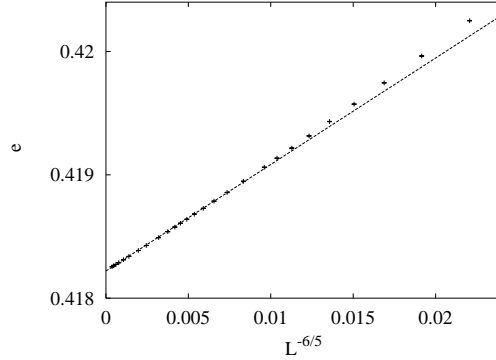


Figure 6.2: Energy-like quantity e for the constrained HH model versus $L^{-6/5}$.

6.3.1 Hard-hexagon lattice gas

For the constrained HH model, only geometric cluster steps [12] were used. In principle, the total number of the vacancies should be taken as $V_c = L^2 \rho_c$, with $\rho_c = (5 + \sqrt{5})/10$. For finite systems, however, V_c is not an integer. Therefore simulations were performed at two numbers $[V_c]$ and $[V_c + 1]$ where brackets $[\]$ denote the integer part. Data at V_c are obtained by linear interpolation between $[V_c]$ and $[V_c + 1]$. System sizes were chosen as 33 values ranging from 9 to 960. Examples of the Monte Carlo results are shown in following figures.

Figures 6.2-6.4 suggest that $e - e_0 \propto L^{-6/5}$, $C - C_0 \propto L^{-4/5}$, and $C_F \propto L^{2/5}$. Compared to unconstrained systems, the behavior of e and C is considerably modified. In particular, the specific-heat-like quantity C approaches a constant C_0 when L increases. The structure factor C_F remains, however, similar to that in the unconstrained system. It is also observed that the magnetic susceptibilities, as expected, approximately behave as $\chi \propto \chi_F \propto L^{2y_h - d} = L^{26/15}$ (not shown).

Although the leading behavior of susceptibility-like quantities remains unchanged, finite-size corrections due to the constraint appear. An example of such a quantity is the dimensionless Binder ratio (Fig. 6.5), indicating an associated exponent $y_1 = -2/5$.

To be more specific, we fitted the formula $Q_m = Q_{mc} + aL^{y_1}$ to the numerical data according to the least-squares criterion. Applying a cutoff for small system sizes $L \leq 15$ we found that $Q_{mc} = 0.7892(2)$, $a = 0.1025(9)$ and $y_1 = -0.397(5)$. Since the irrelevant exponent $y_i = -4/5$ is clearly different, it appears that new corrections are introduced by the constraint.

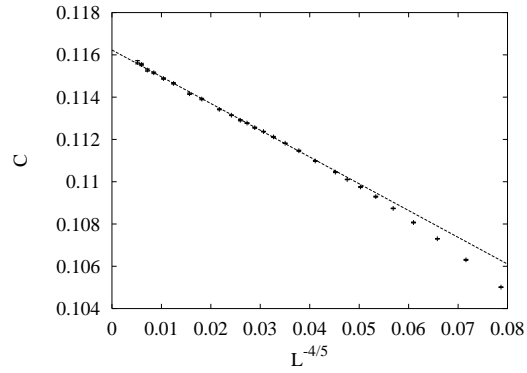


Figure 6.3: Specific-heat-like quantity C for the constrained HH model versus $L^{-4/5}$.

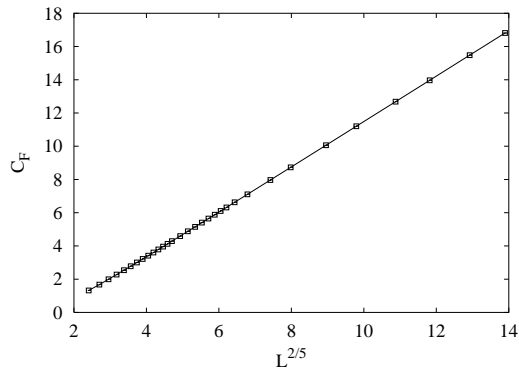


Figure 6.4: The structure factor C_F for the constrained HH model versus $L^{2/5}$.

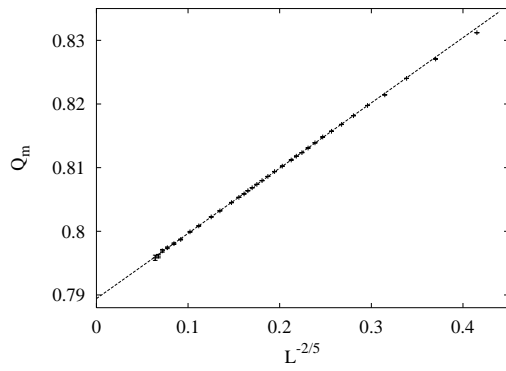


Figure 6.5: Binder ratio Q_m for the constrained HH model versus $L^{-2/5}$.

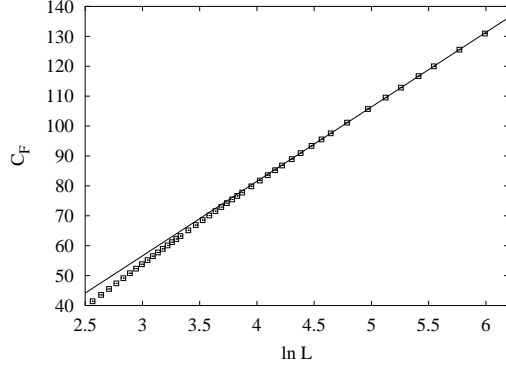


Figure 6.6: The structure factor C_F for the constrained critical BC model versus $\ln L$.

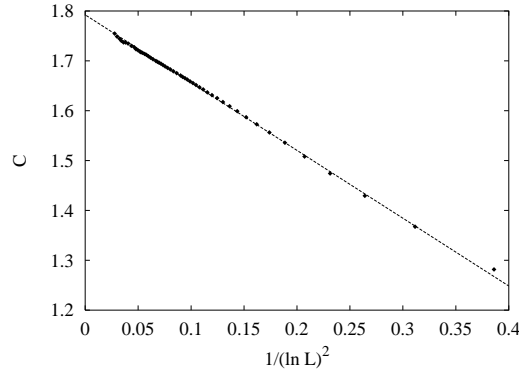


Figure 6.7: Specific-heat-like quantity C for the constrained critical BC model versus $1/(\ln L)^2$.

6.3.2 Critical Blume-Capel model

The critical BC model in two dimensions is a marginal case ($\alpha = 0$). The simulations used a combination of Wolff and geometric cluster steps in order to leave the magnetization free and impose the constraint that the number of vacancies is fixed. System sizes were chosen as 53 values ranging from 4 to 400. Under the constraint, the critical structure factor approximately behaves as $C_F - C_{F0} \propto \ln L$ (Fig. 6.6), and the scaling behavior of χ and χ_F is about $\propto L^{2y_h - d} = L^{7/4}$ (not shown). This scenario is analogous to that for the constrained HH model, *i.e.*, the critical behavior of C_F , χ and χ_F is not affected by the constraint.

The Monte Carlo data for C and e are shown in Figs. 6.7 and 6.8, respectively. They suggest that $C - C_0 \propto 1/(\ln L)^2$, and that a single power law is not sufficient to describe the behavior of the energy-like quantity e .

The Binder ratio Q_m is shown in Fig. 6.9 as $1/\ln L$, the approximate linearity at left-hand-side indicates that the leading finite-size correction may be of a logarithmic form. Compared to the irrelevant exponent $y_i = -2$ for unconstrained BC model, such a correction may arise from the constraint.

6.3.3 Dilute $q = 4$ Potts model

The simulations took place at the ‘fixed point’ where the logarithmic corrections are absent. The vacancy densities were kept fixed, and square systems were chosen in the range $12 \leq L \leq 280$. The numerical data for C were fitted by

$$C = c_0 + c_1 L^{-1} + c_2 L^{-3/2} + c_3 L^{-2}, \quad (6.8)$$

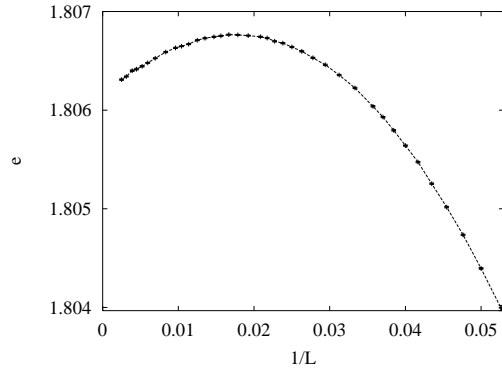


Figure 6.8: Energy-like quantity e for the constrained critical BC model versus $1/L$.

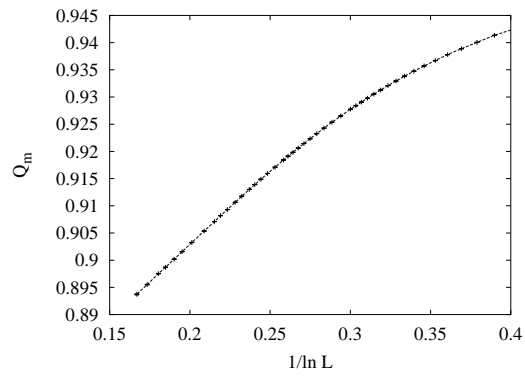


Figure 6.9: Binder ratio Q_m for the constrained critical BC model versus $1/\ln L$.

The amplitude c_3 was not significant. A two-parameter fit led to $c_1 = -2.1(5)$ and $c_2 = -23(1)$. It appears that the absolute value of c_2 is much larger than that of c_1 .

6.4 Results for magnetic constraints

In the presence of a constraint on the magnetization we still want to determine a susceptibility-like quantity. For the Ising model we may consider a local quantity defined as

$$m' \equiv L^{-d} \sum_{\text{triang}} s_i s_j s_k \quad (6.9)$$

where the sum is over three-spin products. These three spins are picked up from those on elementary units such as the elementary triangles and squares for the triangular and square lattices, respectively. This quantity has the same symmetry property as the magnetization m , *i.e.*, it changes sign when all spins are inverted. Its fluctuations are obviously reduced when the constraint $m = 0$ is imposed. We thus define the susceptibility-like quantity

$$\chi' \equiv L^d \langle m'^2 \rangle \quad (6.10)$$

In the more general context of the Potts model the magnetization is determined by the densities ρ_i defined as

$$\rho_i \equiv L^{-d} \sum_k \delta_{\sigma_k, i} \quad (6.11)$$

where $i = 1, 2, \dots, q$ denotes the Potts state. The normal Potts magnetic susceptibility χ is defined as

$$\chi = L^d \langle m^2 \rangle = \frac{1}{2} L^d \sum_{i=1}^q \sum_{j=i+1}^q \langle (\rho_i - \rho_j)^2 \rangle \quad (6.12)$$

Since the terms in the double sum do not depend on i and j one can just take the term $i = 1$ and $j = 2$. In the presence of the constraint $\rho_i = 1/q$ we may thus define the magnetization-like quantity

$$m' = L^{-d} \sum_{i,j,k} (\delta_{\sigma_i, 1} - \delta_{\sigma_i, 2})(\delta_{\sigma_j, 1} - \delta_{\sigma_j, 2})(\delta_{\sigma_k, 1} - \delta_{\sigma_k, 2}), \quad (6.13)$$

and the susceptibility-like quantity

$$\chi' = L^d \langle m'^2 \rangle \quad (6.14)$$

Without this constraint, the finite-size scaling behavior of χ' and χ is governed by the same exponents. This was numerically verified for several models.

6.4.1 Critical Ising model

The model is defined on the triangular lattice, and the system sizes were chosen in the range $8 \leq L \leq 660$. The simulations took place at the critical point $K_c = \frac{1}{4} \ln 3$ and at zero magnetization. The results for the susceptibility-like quantity χ' are shown in Fig. 6.10. The data for χ' were fitted by the formula

$$\chi' = c_0 + L^p (a_0 + a_1 L^{y_1}), \quad (6.15)$$

according to the least-squares criterion. The exponent p governs the leading singular behavior of χ' , and the term with y_1 purportedly accounts for finite-size corrections. We thus obtain $p = -1.008(12)$ and $y_1 = -1.05(6)$.

6.4.2 Critical $q = 3$ Potts model

The model is also defined on the triangular lattice, with system sizes ranging from 9 to 480. The densities of the three types of Potts variables were chosen equal and fixed. The data for χ' (not shown) were fitted by Eq. (6.15), which led to the results $p = -0.77(5)$ and $y_1 = -0.51(20)$.

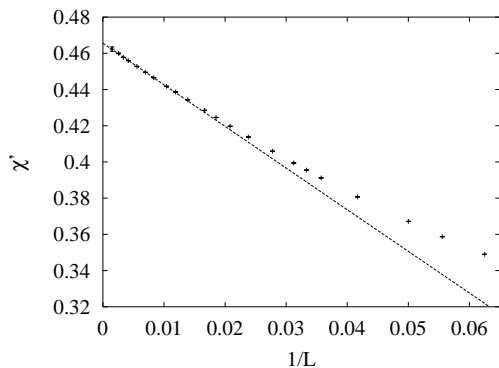


Figure 6.10: Susceptibility-like quantity χ' for the Ising model versus $1/L$.

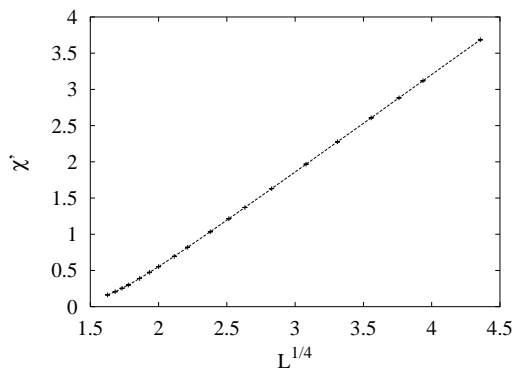


Figure 6.11: Susceptibility-like quantity χ' for the tricritical Blume-Capel model versus $L^{1/4}$.

6.4.3 Tricritical Blume-Capel model

The simulations took place at the tricritical point as given above, at zero magnetization and with the vacancy density fixed at its tricritical value, using square lattices with sizes in the range $8 \leq L \leq 360$. The results for χ' are shown in Fig. 6.11. The fits yielded that $p = 0.253(2)$ and $y_1 = -1.96(6)$.

6.4.4 Tricritical $q = 3$ Potts model

The simulations used the model on the square lattice, and took place at the tricritical point as given above. The vacancy density was fixed at its tricritical value, with the three Potts densities equal and fixed. The system sizes were in the range $10 \leq L \leq 480$. The three spins in the product sampled for χ' were chosen in the corners of each elementary square. The data are shown in Fig. 6.12. The fit yields $p = 0.126(2)$ and $y_1 = -2.0(3)$.

6.4.5 Dilute $q = 4$ Potts model

The simulations took place at the 'fixed point' where the logarithmic corrections are absent. The vacancy and Potts densities were kept fixed. Square systems were chosen in the range $12 \leq L \leq 480$. The data for χ' are shown in Fig. 6.13. The fits by Eq. (6.15) yields $p = 0.224(4)$ and $y_1 = -1.8(1)$.

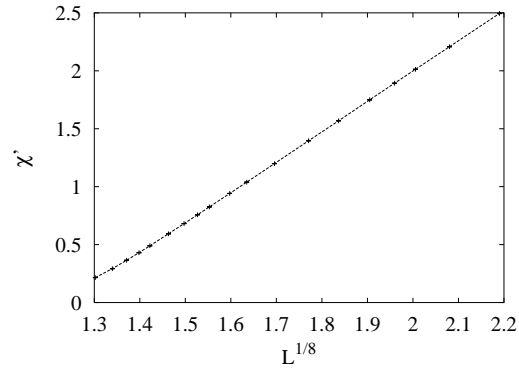


Figure 6.12: Susceptibility-like quantity χ' for the tricritical $q = 3$ Potts model versus $L^{1/8}$.

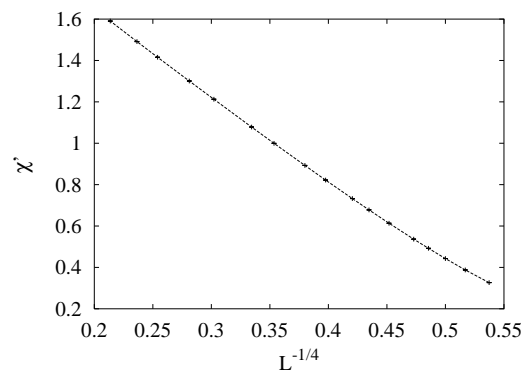


Figure 6.13: Susceptibility-like quantity χ' for the tricritical $q = 4$ Potts model versus $L^{-1/4}$.

6.5 Finite-size scaling in the presence of a constraint

As mentioned above, constrained critical behavior in infinite systems is explained by Fisher's *renormalized exponents* [5]. On this basis, we perform some calculations for finite-size constrained critical behavior.

6.5.1 Energy-like constraint

In the language of the Potts model with vacancies [Eq. (6.4)], the scaling behavior near the critical temperature of the reduced free energy density $f = \ln Z$ is

$$f(t, L) = L^{-d} f_s(tL^{y_t}, 1) + f_a(D), \quad (6.16)$$

where t is the thermal scaling field, and f_s and f_a are the singular and analytic parts of the free energy respectively. Here, we have neglected the irrelevant field in f_s . The analytic part f_a is expressed in D which parametrizes the critical line. The dependence of f_a on the distance t to the critical line is neglected. The constraint is thus $\rho(D, K, L) = \partial f / \partial D = \text{constant}$ where t is expressed in K and D . Solving this equation yields the path in the (D, K) plane. The solution can be written as $t \propto (K - K_c)L^{d-2y_t}$ if $2y_t - d > 0$, where K_c is the value of K where the path crosses the critical line at $t = 0$. Substitution of t in Eq. (6.16) leads to

$$f(t', L) = L^d f_s(t' L^{d-y_t}, 1) + f_a(t'). \quad (6.17)$$

where we have parametrized the distance to the critical point as $t' \equiv K - K_c$. On this basis, we expect that the leading critical singularities for constrained systems are

$$e - e_0 \propto L^{-y_t}, \text{ and } C - C_0 \propto L^{d-2y_t} + aL^{2(d-2y_t)}. \quad (6.18)$$

Equation (6.18) indicates that $e - e_0 \propto L^{-6/5}$ and $C - C_0 \propto L^{-2/5} + aL^{-4/5}$ for the constrained HH model, and that $e - e_0 \propto L^{-1}$ and $C - C_0 \propto 1/\ln L + a/(\ln L)^2$ for the constrained critical BC model. From a comparison with the numerical data in Sec. II, we find that the energy density is satisfactorily explained. However, for the specific heat, the amplitude of the leading term L^{d-2y_t} is very small if not absent. This result, as well as the aforementioned new finite-size corrections, suggests that some more reflection is desirable.

Our finite-size scaling results for models with an energy-like constraint, and our expectation on the basis of the Fisher renormalization scheme, are listed in Tab. I.

Tab. I: Summary of finite-size scaling properties in critical and tricritical models under the energy-like constraint that the number of vacancies or particles is conserved.

model	quantity	found	expected
hard-hexagon	e	$L^{-6/5}$	$L^{-6/5}$
hard-hexagon	$C - C_0$	$L^{-4/5}$	$L^{-2/5}$
hard-hexagon	C_F	$L^{2/5}$	$L^{2/5}$
crit. 2D Blume-Capel	e	L^{-1} (?)	L^{-1}
crit. 2D Blume-Capel	$C - C_0$	$1/(\ln L)^2$	$1/\ln L$
crit. 2D Blume-Capel	Q	$1/\ln L$ (?)	L^{-2}
dilute 2D $q = 4$ Potts	$C - C_0$	L^{-1} (?)	L^{-1}

6.5.2 Magnetic constraint

For Ising models we require $m = 0$, and for Potts models $\rho_1 = \rho_2 = \dots = \rho_q$. Without this constraint, the critical behavior of χ and χ' as defined above is governed by the same magnetic exponent. Under the constraint, χ is completely suppressed, and we may thus raise the question about the scaling behavior of χ' . We first note that χ and χ' can be written as the second derivatives of the free energy density f with

respect to fields H and H' respectively. The second derivative of f to H' will depend on the ‘path’ described by the constrained system in the H, H' plane. To find this path, we first assume that the magnetic scaling field h and a subleading field h' can be expressed as linear combinations of H and H' , and that h is the only relevant field governing the magnetic critical behavior. Following Fisher’s procedure applied earlier in the case of thermal behavior, we find that the path is determined by balancing the contributions of the singular and analytic parts of f to the magnetization so that the magnetic scaling dimension y_h is renormalized as $y'_h = X_h = 2 - y_h$. Thus, for critical systems with a zero magnetization, one would expect $\chi' \propto L^{p_1}$ with $p_1 = 2y'_h - 2 = 2 - 2y_h$. We refer to this as ‘Mechanism One’. It does not match our results given in Section IV: the observed singularities appear to be stronger.

We therefore tentatively assume instead that there is another relevant magnetic scaling field that plays a role in the Potts model. For the exponents associated with such scaling fields see *e.g.* Ref. [13]. Normally, this second field is considered redundant. The value of the second magnetic dimension is $X'_h = (g+1)(10-g)/8g$, with $q = 2 + 2 \cos(g\pi/2)$, where $2 \leq g < 4$ applies to the critical branch of the Potts model, and $4 \leq g \leq 6$ to the tricritical branch. The parameter g is called the coupling constant of the Coulomb gas. If the second field is not redundant, it will lead to a singularity according to $\chi' \propto L^{p_2}$ with $p_2 = 2 - 2X'_h$. We will refer to this as ‘Mechanism Two’. Comparison with Section IV tells us that it does not apply, as expected for redundant operators.

Next we investigate a third mechanism based on the nonlinearity of the scaling fields. In particular we expect that quadratic terms in the magnetic field may contribute to the temperature field t , *i.e.*, $t = K - K_c + wH^2 + w'H'^2 + \dots$. The scaling equation for the free energy then becomes

$$f(t, \dots, L) = L^{-d} f(L^{y_t}(K - K_c + wH^2 + w'H'^2 + \dots), \dots, 1) + \dots \quad (6.19)$$

The second derivative to H' will thus pick up contributions proportional to L^{p_3} with $p_3 = y_t - d$. For the case of the critical $q = 2$ and $q = 3$ Potts models, this agrees well with the numerical results, but not so for $q = 4$ and the tricritical systems.

A fourth mechanism is similar to the second, but with a second magnetic dimension assumed to be described by the Kac formula [17, 18]

$$X_{p,q} = \frac{[p(m+1) - qm]^2 - 1}{2m(m+1)}, \quad (1 \leq p < m, 1 \leq q \leq p) \quad (6.20)$$

for rotationally invariant operators. For the tricritical Blume-Capel model ($m = 4$), it is known [19] that $X_{h_2} = X_{2,1} = 7/8$ is a second relevant magnetic dimension. We assume that this can be generalized to the whole tricritical branch of the Potts model such that

$$X_{h_2} = X_{m/2, m/2-1} = (9m^2 - 4)/8m(m+1). \quad (6.21)$$

Thus, one has $X_{h_2} = 20/21$ and $9/8$ for the tricritical $q = 3$ ($m = 6$) and the $q = 4$ ($m \rightarrow \infty$) Potts model, respectively. Substitution of $g = 4(m+1)/m$ in Eq. (6.21) yields

$$X_{h_2} = [36 - (g-4)^2]/8g, \quad (6.22)$$

where g is the coupling constant of the Coulomb gas. We simply assume that Eq. (6.22) also applies to the critical branch of the Potts model, for which $g = 4m/(m+1)$. Thus, one has $X_{h_2} = X_{(m+3)/2, (m+1)/2} = (3m+5)(3m+1)/8m(m+1)$ for the critical Potts model. For $m = 5$, *i.e.*, the $q = 3$ Potts model, its value is $X_{h_2} = X_{4,3} = 4/3$. The case $m = 3$ applies to the critical Ising and tricritical $q = 1$ Potts models, which have $X_{h_2} = X_{3,2}$ and $X_{3/2, 1/2}$, respectively. Apparently, the coordinates of these exponents do not occur in the aforementioned Kac table (6.20), and the exponents may not be observable in thermodynamic quantities. The predictions of this mechanism (Mechanism Four) agree satisfactorily with the numerical results, except for the $q = 4$ Potts model and the tricritical $q = 3$ model.

The fits according to the above four mechanisms are summarized in Tab. II.

Tab. II: Summary of finite-size scaling results according to Mechanisms 1-4 outlined above. In those cases where p does not well agree with a single mechanism, better agreement is obtained by combining Mechanisms 3 and 4.

q	model	X_{h1}	X_{h2}	p	p_1	p_2	p_3	p_4
2	crit. Ising	1/8	7/6	-1.008(12)	-7/4	-1/3	-1	—
3	crit. $q = 3$	2/15	13/12	-0.77(5)	-26/15	-1/6	-4/5	-2/3
4	$q = 4$ with vac.	1/8	15/16	-0.224(4)	-7/4	1/8	-1/2	-1/4
3	tricer. $q = 3$	2/21	20/21	0.126(2)	-38/21	8/21	-2/7	2/21
2	tricer. $q = 2$	3/40	3/4	0.253(2)	-37/20	1/2	-1/5	1/4

Tab. III: Results of fits for several q -state Potts models with vacancies

	Fit1 (p_4, p_3 fixed)			Fit2		Fit3	
model	a_0	a_1	a_2	p_4	p_3	p_4	p_3
crit. $q = 3$	0.4198(4)	-0.83(5)	-1.08(7)	-0.7(2)	-4/5 (fixed)	-2/3 (fixed)	-0.7(2)
$q = 4$ with vac.	2.55(3)	-4.67(2)	0.78(3)	-0.249(5)	-1/2 (fixed)	-1/4 (fixed)	-0.49(8)
tricer. $q = 3$	-5.54(2)	4.40(2)	0.67(2)	0.094(5)	-2/7 (fixed)	2/21 (fixed)	-0.30(5)
tricer. Ising	-2.26(1)	1.356(2)	0.12(2)	0.250(5)	-1/5 (fixed)	1/4 (fixed)	-0.2(2)

Table II indicates that not all the numerical data can be explained by a *single* mechanism. It is obvious, however, that more than one mechanisms can simultaneously exist under the magnetic constraint. Thus, we fitted the data for χ' by

$$\chi' = a_0 + a_1 L^{p_4} + a_2 L^{p_3} + a_3 L^{p_4 + y_i}, \quad (6.23)$$

where the term with y_i arises from the irrelevant thermal scaling field. For the critical $q = 3$ Potts model, it is difficult to distinguish $p_3 = -4/5$ from $p_4 = -2/3$. However, if p_3 and p_4 are fixed and y_i is set to $-4/5$, both amplitudes a_1 and a_2 are indeed well determined as $a_1 = -0.83(4)$ and $a_2 = -1.08(5)$. For the tricritical Blume-Capel model, we also fixed $p_3 = -1/5$ and $p_4 = 1/4$ and obtained $a_1 = 1.356(3)$ and $a_2 = 0.12(2)$. If we leave p_4 free and keep p_3 fixed, we find $p_4 = 0.249(3)$, in agreement with the expected value. However, if p_3 is left free while p_4 is fixed at $1/4$, the error margin of p_3 is as big as the value itself. This may be due to the following. First, the amplitude a_2 is much smaller than a_1 as mentioned earlier. Second, the exponent $p_3 = -1/5$ is close to 0 such that the term with a_2 is difficult to distinguish from the background contribution a_0 . The fits of χ' for the $q = 3$ and $q = 4$ Potts models, and for the $q = 2$ tricritical model, are summarized in Tab. III.

6.6 Discussion

From our numerical results for several critical and tricritical systems under an energy-like constraint, we observe that *a)* the leading scaling behavior of susceptibility-like quantities remains the same as in unconstrained systems; *b)* critical behavior of structure factors, accounting for spatial fluctuations, is also not influenced by such a global constraint; *c)* the scaling behavior of energy-like quantities is modified significantly; and *d)* strong finite-size corrections arise due to the constraint.

On the basis of Fisher's theory, we have performed some analytical calculations, in order to compare with our numerical results. We find that constrained tricritical phenomena can be described satisfactorily. However, our understanding of constrained critical phenomena appears to be insufficient: the numerical results indicate that, for a number of models, the amplitude of the leading term in Eq. (6.18) is very small if not absent.

Our derivation of the constrained finite-size behavior does not provide us with an obvious reason why the leading term should vanish. Moreover, it has been observed [20] that the effective renormalization of the constrained specific heat in experiments is not as strong as the theoretical prediction, Eq. (6.1). This deviation from the expected scaling behavior is just in the opposite direction.

Furthermore, we have shown that, in comparison with unconstrained systems, new finite-size corrections for magnetic quantities arise due to the energy-like constraint. It appears that these corrections are not accounted for by the mechanism described in Ref. [21]. Thus, further investigation, in particular a theoretical analysis, seems desirable.

Our results for the constrained three-dimensional Blume-Capel model, while in agreement with the Fisher renormalization scheme, do not agree with the mean-field description [11] of the constrained model. Can we understand this? In the mean-field model, each spin interacts equally with every other spin. The presence of vacancies only reduces the number of Ising spins, leading to a smaller effective interaction. Thus, the vacancy fluctuations are coupled to the Ising fluctuations. The stability criterion of the coupled fluctuations determines the tricritical point. The constraint suppresses the fluctuations of the vacancies, and thus reduces the model to an 'ordinary' mean-field Ising model. It is clear that tricritical behavior is suppressed in the constrained mean-field model, but we find it puzzling that this result differs from that for the tricritical Blume-Capel model in three dimensions, the upper critical dimensionality.

For the magnetic constraint, the situation seems more satisfactory than for the energy-like constraints, but still involves assumptions that need further justification. For instance, our assumption for the value of the second magnetic scaling dimension of the Potts model deserves more attention, since no solid numerical evidence for this exponent is available, as far as we know.

For us the most remarkable result obtained above is the finite-size behavior of the constrained specific heat, which displays twice the expected exponent. In an attempt to obtain a further clue, we have done an

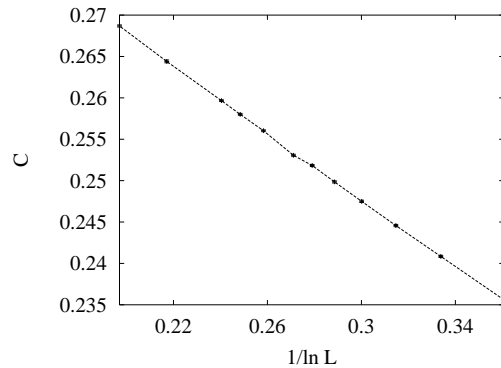


Figure 6.14: Specific heat C of the antiferromagnetic Ising model with a conserved magnetization versus $1/\ln L$.

additional investigation of the 2D antiferromagnetic critical Ising model at a conserved and nonzero magnetization. This case of a magnetic constraint stands clearly apart from the magnetic constraints described above. In the context of the Ising universality, the magnetic field acts as a temperature-like scaling field in the case of the antiferromagnet, so that the constraint should, within this context, be considered an *energy-like* one.

A transfer-matrix method was used to determine a rather arbitrary critical point at magnetization density $m = 0.199897148$. The associated coupling was found to be $K_c = -0.64599(1)$. The simulations by means of a geometric cluster algorithm used system sizes in the range $8 \leq L \leq 160$. The specific heat C was determined in the usual way from the fluctuations in time of the nearest-neighbor correlation. In this case, we found that $C - C_0 \propto 1/\ln L$ (shown in Fig. 6.14), which is, unlike the other cases involving an energy-like constraint, in a good agreement with our understanding of the Fisher renormalization mechanism.

Bibliography

- [1] M. Blume and V.J. Emery, Phys. Rev. A **4**, 1071, (1971).
- [2] H.W. Capel, Physica A **32** 966 (1966); Phys. Lett. **23** 327 (1966).
- [3] R.J. Baxter, J. Phys. A **13**, L61, (1980); J. Stat. Phys. **26**, 427, (1981).
- [4] I. Syozi, Prog. Theor. Phys. **34**, 189 (1965); I. Syozi and S. Miyazima, Prog. Theor. Phys. **36**, 1083 (1966).
- [5] M.E. Fisher, Phys. Rev. **176**, 257 (1968).
- [6] L. Gunther, D.J. Bergman and Y. Imry, Phys. Rev. Lett. **27**, 558 (1971); Y. Imry, O. Entin-Wohlman and D.J. Bergman, J. Phys. C **6**, 2846, (1973); O. Entin-Wohlman, D.J. Bergman and Y. Imry, J. Phys. C **7**, 496, (1974).
- [7] Y. Imry, private communications.
- [8] G.A. Baker and J.W. Essam, Phys. Rev. Lett. **24**, 447 (1969).
- [9] Y. Imry, Phys. Rev. Lett. **33**, 1304, (1974); J. Rudnick, D.J. Bergman and Y. Imry, Phys. Lett. A **46**, 448, (1974); Y. Achiam and Y. Imry, Phys. Rev. B **12**, 2768, (1975).
- [10] Y. Achiam and Y. Imry, J. Phys. C. **10**, 39, (1977).

- [11] Y. Deng and H.W.J. Blöte, unpublished. In this calculation, we use an interaction of each spin with the average magnetization, and use a finite but large number of spins such that binomial expansions etc. are valid while finite-size amplitudes remain accessible. The tricritical point follows by requiring that the expectation value of a spin is equal to the magnetization m up to the third order of m . Under the constraint that the density of the vacancies is fixed at its tricritical value, the tricritical transition reduces to an ordinary mean-field transition.
- [12] J.R. Heringa and H.W.J. Blöte, *Physica A* **232**, 369, (1996); *Phys. Rev. E* **57**, 4976, (1998).
- [13] B. Nienhuis, in *Phase Transitions and Critical Phenomena* Vol. 11, eds. C. Domb and J.L. Lebowitz (Academic, London, 1987).
- [14] D.A. Huse, *Phys. Rev. Lett.* **49**, 1121, (1982).
- [15] B. Nienhuis, A.N. Berker, E.K. Riedel, and M. Schick, *Phys. Rev. Lett.* **43**, 737, (1979).
- [16] K. Binder, *Phys. Rev. B* **43**, 119 (1981).
- [17] A.A. Belavin, A.M. Polyakov, and A.B. Zamolodchikov, *J. Stat. Phys.* **34**, 763 (1984); *Nucl. Phys. B* **241**, 333 (1984); D. Friedan, Z. Qiu, and S. Shenker, *Phys. Rev. Lett.* **52**, 1575 (1984).
- [18] J.L. Cardy, *Phase Transitions and Critical Phenomena*, edited by C. Domb and J.L. Lebowitz. (Academic Press, London, 1987), Vol. 11, p. 55, and references therein.
- [19] A. Klümper and P. A. Pearce, *J. Stat. Phys.* **64**, 13 (1991).
- [20] M.E. Fisher and P.E. Scesney, *Phys. Rev. A* **2**, 825 (1970).
- [21] V. Privman and M.E. Fisher, *J. Phys. A* **16**, L295 (1983).

Constrained tricritical Ising model in three dimensions

Using the Wolff and geometric cluster Monte Carlo methods, we investigate the tricritical Blume-Capel model in three dimensions. Since these simulations conserve the number of vacancies and thus effectively introduce a constraint, we generalize the Fisher renormalization for constrained critical behavior to tricritical systems. We observe that, indeed, the tricritical behavior is significantly modified under this constraint. For instance, at tricriticality, the specific heat has only a finite cusp and the Binder ratio assumes a different value from that in unconstrained systems. Since three is the upper tricritical dimensionality of Ising systems, we expect that the mean-field theory correctly predicts a number of universal parameters in three dimensions. Therefore, we calculate the partition sum of the mean-field tricritical Blume-Capel model, and accordingly obtain the exact value of the Binder ratio. Under the constraint, we show that this mean-field *tricritical* system reduces to the mean-field *critical* Ising model. However, our three-dimensional data do not agree with this mean-field prediction. Instead, they are successfully explained by the generalized Fisher renormalization mechanism.

7.1 Introduction

In the development of the theory of critical phenomena and phase transitions, a spin-1 Ising model known as the Blume-Capel (BC) model has played an important role. This model was originally introduced by Blume and Capel [1, 2], and the reduced Hamiltonian reads

$$\mathcal{H}/k_{\text{B}}T = -K \sum_{\langle ij \rangle} s_i s_j + D \sum_k s_k^2 \quad (s_i = \pm 1, 0), \quad (7.1)$$

where the sum $\langle \rangle$ is over all nearest-neighbor pairs of lattice sites. The spins assume values ± 1 and 0, and those in state 0 are referred to as vacancies. The abundance of vacancies is governed by the chemical potential D , which is also termed the crystal field parameter. The phase diagram is sketched in Fig. 7.1. For $D \rightarrow -\infty$, the vacancies are excluded, and the model (7.1) reduces to Onsager's spin- $\frac{1}{2}$ model [3]. The critical coupling $K_c(D)$ is an increasing function of D . For sufficiently large chemical potential, the transition then becomes first-order, separating the vacancy-dominated phase from those dominated by plus (+1) or minus (-1) spins. At the joint point, these three coexisting phases *simultaneously* become identical, and this point is then called [4] the tricritical point, denoted as (K_t, D_t) in Fig. 7.1.

In two dimensions, the nature of critical singularities of the BC model is now well established. For instance, as early as in 1942, the exact expression of the free energy was obtained by Onsager [3, 5] for the spin- $\frac{1}{2}$ model. The universal thermal and magnetic exponents are $y_t = 1$ and $y_h = 15/8$, respectively. At the tricritical point (K_t, D_t) , exact values of the universal exponents follow from Baxter's exact results for the hard-square lattice gas [6, 7], in the same universality class with the tricritical Blume-Capel model; further, these exponents can be calculated from the Coulomb gas theory [8, 9] and are also included in predictions of

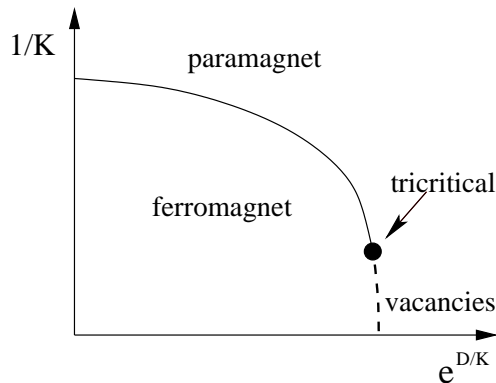


Figure 7.1: Sketch of the phase diagram of the BC model. The solid line represents the critical line, which separates the para- and ferromagnetic phases; and the first-order transition is shown as a dashed line. The two lines join at a tricritical point (black circle).

the conformal field theory [10,11]. The leading and subleading thermal exponents at tricriticality are [6–12] $y_{t1} = 9/5$ and $y_{t2} = 4/5$, respectively, and the magnetic ones are $y_{h1} = 77/40$ and $y_{h2} = 9/8$, respectively.

In three dimensions, exact results are absent for the BC model along the critical line $K_c(D)$, and investigations of critical behavior have to depend on approximations such as series and ϵ expansions, and Monte Carlo simulations [13–16]. However, the tricritical Ising model is somewhat special, in the sense that it is one of the rare cases in three dimensions that exact information is available about critical singularities [4]. This is possible because *three* is the upper tricritical dimensionality of Ising systems. As a consequence, critical exponents can be exactly obtained from renormalization calculations [17] of the Landau-Ginzburg-Wilson Hamiltonian. The thermal and magnetic tricritical exponents [4] are $y_{t1} = 2$ and $y_{t2} = 1$, and $y_{h1} = 5/2$ and $y_{h2} = 3/2$, respectively.

An experimental example of tricritical phenomena in three dimensions is the superfluid transition in ^3He - ^4He mixtures [4], which is sketched in Fig. 7.2. The transition at the tricritical point is known as the λ transition. In fact, the order parameter in the ^3He - ^4He mixtures is a vector of two components, so that the superfluid transition should in principle be described by the $O(2)$ model, the so-called XY model. Nevertheless, the renormalization calculations yield the same critical exponents for the $O(n)$ model with $n \geq 1$, apart from logarithmic corrections. Thus, in this sense, the BC model (7.1) is still qualitatively applicable [4] at the λ point. One would then simply expect that the tricritical specific heat C is *divergent*, with a critical index $\alpha = 2 - d/y_{t1} = 1/2$. However, this expectation does not agree with the existing experimental results: C was observed [18] to have only a *finite* cusp with $\alpha = -0.9(1)$ at the λ point.

This lack of agreement is the result of an important difference between the systems in the aforementioned theoretical and experimental contexts. This is reflected by the distinction between Figs. 7.1 and 7.2, of which the first deals with models in the space (K, D) . In contrast, Fig. 7.2 uses the mole fraction x of ^3He as an independent parameter [18]. The fraction x plays a similar role as the vacancy density in Eq. (7.1). Therefore, a correct theoretical description of the λ transition in Fig. 7.2 should be based on a restricted partition sum with a conserved number of vacancies. In other words, an external constraint is imposed on the system (7.1). This constraint is of the ‘annealed’ type [19] since vacancies are allowed to move freely over the lattice according to the Boltzmann distribution.

Constrained critical behavior has already been studied for decades. As earlier as 1965, Syozi [20] introduced a decorated Ising model on a d -dimensional lattice, which was shown [21] to be intimately connected with annealed systems. The Syozi model can be exactly transformed into the spin- $\frac{1}{2}$ model, and critical exponents of these two systems are related as

$$\alpha_s = -\alpha/(1 - \alpha), \quad \beta_s = \beta/(1 - \alpha), \quad \text{and} \quad \nu_s = \nu/(1 - \alpha), \dots \quad (7.2)$$

where α and β are the standard critical indices for the specific heat C and the magnetization density m for

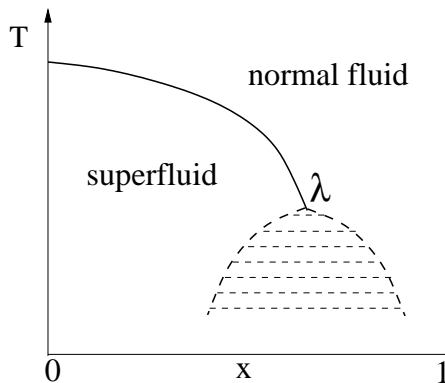


Figure 7.2: The schematic phase diagram of a ${}^3\text{He}$ - ${}^4\text{He}$ mixture in the plane of temperature T and mole fraction x of ${}^3\text{He}$. The temperature can be understood as the inverse coupling constant $1/K$ in Eq. (7.1).

the spin- $\frac{1}{2}$ model, respectively, and $\nu = 1/y_t$ is the inverse of the thermal exponent; those with the subscript s are for the Syozi model. It can be shown that the hyperscaling relations still hold among the critical indices α_s, β_s etc. In three dimensions, the spin- $\frac{1}{2}$ model has $\alpha > 0$, so that the specific heat C of the Syozi model does not diverge at criticality. In two dimensions, C of the spin- $\frac{1}{2}$ model is divergent in a logarithmic scale since $\alpha = 0$. For this marginal case, C of the Syozi model reaches a finite cusp, also of a logarithmic nature. Later, this was discussed in a more general context by Essam and Garelick [22] and by Fisher [23]. It was pointed out that relations (7.2) are not specific to the Syozi model, but are more generally satisfied by equilibrium models with a divergent specific heat ($\alpha > 0$). Since then, the so-called Fisher renormalization of constrained critical systems has gained considerable acceptance [24–27].

A description of constrained *tricritical* behavior was formulated by Imry and his coworkers [28] in the context of the renormalization group (RG) technique. Using the ϵ -expansion and a generalized Landau-Ginzburg-Wilson Hamiltonian, they found four distinct fixed points: the tricritical Ising (TI), critical Ising (CI), *renormalized* tricritical Ising (RTI), and *renormalized* critical Ising (RCI) fixed points. Renormalization flows deviating from TI can move into the fixed points CI or RTI , and those from CI can end at RCI . The critical exponents at these fixed points are related as $\alpha_{RCI} = -\alpha_{CI}/(1 - \alpha_{CI})$ and $\alpha_{RTI} = -\alpha_{TI}/(1 - \alpha_{TI})$, in agreement with Eq. (7.2). For the spatial dimensionality $d \geq 3$, TI and RTI correspond to Gaussian and spherical fixed points, respectively. Thus, one has the critical indices $\alpha_{TI} = 1/2$ and $\alpha_{RTI} = -\alpha_{TI}/(1 - \alpha_{TI}) = -1$ in three dimensions. If one assumes that constrained behavior of an annealed tricritical system is governed by the fixed point RTI , the theoretical prediction $\alpha_{RTI} = -1$ is then in good agreement with the experimental observation [18] $\alpha = -0.9(1)$.

At the upper critical dimensionality, the mean-field theory is generally believed to correctly describe some universal aspects of phase transitions. Indeed, for the tricritical BC model in three dimensions, a number of universal quantities, including the thermal and magnetic exponents y_{t1} and y_{h1} , can be exactly calculated [4] from a mean-field (MF) analysis. In the present paper, we also perform some exact calculations for the MF BC model. Under the constraint that the total number of vacancies is fixed, we show that the *tricritical* MF BC model reduces to the *critical* MF Ising model. However, this MF result is not what one would expect for the tricritical BC model in three dimensions, since the constraint should not change the universality class. Thus, the present paper also takes another approach: following the basic ideas in Ref. [23], we generalize the Fisher renormalization mechanism for constrained *critical* behavior to tricritical systems. In Particular, we derive finite-size scaling results based on this generalized mechanism.

In addition to these theoretical analyses, we perform a Monte Carlo study of the constrained three-dimensional (3D) BC model. For systems with a conserved number of vacancies, efficient simulations have only become possible after the introduction of the geometric cluster method [29–31]. This algorithm was developed on the basis of spatial symmetries, such as Hamiltonian invariance under spatial inversions and

rotations. It moves groups of magnetic spins and vacancies over the lattice in accordance with Boltzmann distribution, while the global magnetization and vacancy densities are conserved. Then, the aforementioned constraint can be realized by a combination of the geometric method and the Wolff algorithm [32], which acts only on nonzero spins and thus allows magnetization fluctuations.

7.2 Mean-field Blume-Capel model

In this section, we perform an asymptotic analysis of the finite mean-field (MF) BC model. On this basis, we hope to obtain some exact results for universal parameters describing constrained behavior of the tricritical BC model in three dimensions.

The mean-field (MF) version of a finite BC model (7.1) is expressed by the Hamiltonian

$$\mathcal{H}/k_{\text{B}}T = -\frac{K}{N} \sum_{i=1}^N \sum_{j=i+1}^N s_i s_j + D \sum_k s_k^2 \quad (s_i = \pm 1, 0), \quad (7.3)$$

where N is the total number of spins, and each spin is interacting with each other spin. Then, the local Hamiltonian of the i th spin, i.e., the terms in Eq. (7.3) involving that spin, reads

$$\mathcal{H}_i/k_{\text{B}}T = -K s_i m + D s_i^2 + \frac{K}{N} s_i^2 \quad \text{with } mN = \sum_{i=1}^N s_i, \quad (7.4)$$

where m is the global magnetization density. The last term in Eq. (7.4) vanishes as $1/N$, and will be neglected. The tricritical point [4] of this MF system can be calculated as follows. According to the Boltzmann distribution, Eq. (7.4) determines the statistical probability w of the local spin s_i as

$$w(s_i = 1) = \frac{1}{z} e^{Km}, \quad w(s_i = 0) = \frac{1}{z} e^D, \quad \text{and} \quad w(s_i = -1) = \frac{1}{z} e^{-Km}, \quad (7.5)$$

with a normalization factor $z = e^{Km} + e^D + e^{-Km}$. Thus, the local magnetization $\langle s_i \rangle$ and the global one m are related as

$$\langle s_i \rangle = 2 \sinh(Km) / [\exp(D) + 2 \cosh(Km)]. \quad (7.6)$$

At tricriticality, the stability criterion requires that $m = 0$, $\partial \langle s_i \rangle / \partial m = 1$, and $\partial^3 \langle s_i \rangle / \partial m^3 = 0$. From Eq. (7.6), solution of these requirements yields the tricritical point as $K_t = 3$ and $D_t = 2 \ln 2$, and the corresponding vacancy density as $\rho_v = \rho_{vt} = 2/3$.

7.2.1 Unconstrained systems

The Hamiltonian (7.3) depends only on the numbers of down spins and vacancies, which are denoted as N_d and N_v , respectively. Expression of the partition sum Z in these variables leads to

$$Z = \sum_{N_d=0}^N \sum_{N_v=0}^{N-N_d} c(N_d, N_v) \exp \left[\frac{K}{2} N \left(\frac{N - N_v - 2N_d}{N} \right)^2 - \left(D + \frac{K}{2N} \right) (N - N_v) \right], \quad (7.7)$$

where the combinatorial factor $c(N_d, N_v)$ counts the total number of configurations with N_d minus spins and N_v vacancies

$$C(N_d, N_v) = \frac{N!}{N_d! N_v! (N - N_d - N_v)!}. \quad (7.8)$$

After the substitution of the magnetization density $m = (N - N_v - 2N_d)/N$ and the vacancy density $\rho_v = N_v/N$ in Eqs. (7.7) and (7.8), one has

$$Z = 2N^2 \int_0^1 dm \int_0^1 d\rho_v c(m, \rho_v) \exp \left[\frac{K}{2} N m^2 - DN(1 - \rho_v) \right] [1 + \mathcal{O}(1/N)], \quad (7.9)$$

where we have replaced the sums in Eq. (7.7) by integrals over the magnetization and vacancy density m and ρ_v , and neglected correction terms of order $1/N$. Substitution of the tricritical values of K and D , application of the Stirling's formula $\ln(N!) = (N + \frac{1}{2}) \ln N - N$, and Taylor-expansion of $\ln c(m, \rho_v)$ yield

$$\begin{aligned} \ln c(m, \rho_v) = & -\frac{9}{4}N(\delta\rho_v + m^2)^2 - \frac{81}{4}N\delta\rho_v m^4 - \frac{27}{2}N\delta^2\rho_v m^2 - \frac{9}{8}N\delta^3\rho_v \\ & - \frac{81}{10}Nm^6 + N\mathcal{O}\left[\sum_{k=0}^4 m^{8-2k}(\delta\rho_v)^k\right] + \dots, \end{aligned} \quad (7.10)$$

where $\delta\rho_v = \rho_v - \rho_{vt}$ represents fluctuations of the vacancies. On this basis, the partition sum (7.9) can be written as

$$\begin{aligned} Z &= fN^2 \int_0^\infty dm e^{-\frac{81}{10}Nm^6} [1 + N\mathcal{O}(m^8)] \int_{-\infty}^\infty d\tilde{\rho} e^{-\frac{9}{4}N\tilde{\rho}^2} [1 + \frac{63}{8}Nm^6 + N\mathcal{O}(m^8)] \\ &= f'N^2 \int_0^\infty dm e^{-\frac{9}{40}Nm^6} \int_{-\infty}^\infty d\tilde{\rho} e^{-\frac{9}{4}N\tilde{\rho}^2} [1 + \mathcal{O}(1/N)] \quad (i + 2j = 6), \end{aligned} \quad (7.11)$$

where f and f' are constants and we have introduced a new variable $\tilde{\rho} = \delta\rho_v + m^2$. The integration boundaries have been extended to infinity, and this can be shown [33] to introduce only an error decaying exponentially with N . Equation (7.11) indicates that the tricritical fluctuations of the MF BC model (7.3) consist of two parts: Gaussian (normal) fluctuations of a combined variable $\tilde{\rho}$ and those of the magnetization described by a weight $\exp(-9Nm^6/40)$. The absence of m^2 and m^4 in Eq. (7.11) is an essential characteristic of the ϕ^6 theory and the mean-field description of tricritical phenomena. For later convenience, we rewrite Eq. (7.11) in the variables $x_m = 9Nm^6/40$ and $x_v = 9N\tilde{\rho}^2/4$ as

$$Z = B(N) \int_0^\infty dx_m x_m^{-\frac{5}{6}} e^{-x_m} \int_0^\infty dx_v x_v^{-\frac{1}{2}} e^{-x_v} [1 + \mathcal{O}(1/\sqrt[3]{N})], \quad (7.12)$$

where $B(N)$ is a function of N . Then, substitution of the Γ function, $\Gamma(z) = \int_0^\infty u^{z-1} e^{-u} du$, yields the partition sum (7.11) as

$$Z = B(N) \Gamma\left(\frac{1}{6}\right) \Gamma\left(\frac{1}{2}\right). \quad (7.13)$$

In the study critical phenomena, several universal ratios of finite-size scaling amplitudes, closely related to the quantity originally introduced by Binder [34], play an important role. Particularly, these dimensionless ratios are very useful in Monte Carlo determinations of critical points. Here, we consider two such ratios, which are defined on the basis of fluctuations of the magnetization m and vacancy density ρ_v as

$$Q_m = \frac{\langle m^2 \rangle^2}{\langle m^4 \rangle} \quad \text{and} \quad Q_v = \frac{\langle (\delta\rho_v)^2 \rangle^2}{\langle (\delta\rho_v)^4 \rangle}, \quad (7.14)$$

with $\delta\rho_v = \rho_v - \rho_{vt}$, as mentioned earlier.

From the probability distribution implied by the partition sum (7.12), the expectation values of the moments of the magnetization density m are then obtained as

$$\begin{aligned} \langle m^2 \rangle &= \frac{B(N)}{Z} \int_0^\infty dx_m m^2 x_m^{-\frac{5}{6}} e^{-x_m} \int_0^\infty dx_v x_v^{-\frac{1}{2}} e^{-x_v} \\ &= \left(\frac{40}{9N}\right)^{\frac{1}{3}} \frac{\Gamma(\frac{1}{2})}{\Gamma(\frac{1}{6})} + \mathcal{O}(N^{-\frac{2}{3}}), \\ \langle m^4 \rangle &= \left(\frac{40}{9N}\right)^{\frac{2}{3}} \frac{\Gamma(\frac{5}{6})}{\Gamma(\frac{1}{6})} + \mathcal{O}(N^{-1}), \\ \langle m^6 \rangle &= \left(\frac{40}{9N}\right) \frac{\Gamma(\frac{7}{6})}{\Gamma(\frac{1}{6})} + \mathcal{O}(N^{-\frac{4}{3}}), \quad \text{and} \\ \langle m^8 \rangle &= \left(\frac{40}{9N}\right)^{\frac{4}{3}} \frac{\Gamma(\frac{3}{2})}{\Gamma(\frac{1}{6})} + \mathcal{O}(N^{-\frac{5}{3}}). \end{aligned} \quad (7.15)$$

Therefore, the dimensionless ratio Q_m is

$$Q_m = \Gamma^2\left(\frac{1}{2}\right)/\Gamma\left(\frac{1}{6}\right)\Gamma\left(\frac{5}{6}\right) + \mathcal{O}(N^{-\frac{1}{3}}) = \frac{1}{2} + \mathcal{O}(N^{-\frac{1}{3}}), \quad (7.16)$$

where we have used formula $\Gamma\left(\frac{1}{2} + z\right)\Gamma\left(\frac{1}{2} - z\right) = \frac{\pi}{\cos(\pi z)}$, so that $\Gamma^2\left(\frac{1}{2}\right) = \pi$ and $\Gamma\left(\frac{1}{6}\right)\Gamma\left(\frac{5}{6}\right) = 2\pi$.

The exact value of Q_v can be obtained as follows. From the definition $\tilde{\rho} = \delta\rho_v + m^2$, one has

$$\begin{aligned} \langle \delta\rho_v \rangle &= \langle \tilde{\rho} \rangle - \langle m^2 \rangle, \\ \langle (\delta\rho_v)^2 \rangle &= \langle \tilde{\rho}^2 \rangle - 2\langle \tilde{\rho} \rangle \langle m^2 \rangle + \langle m^4 \rangle, \quad \text{and} \\ \langle (\delta\rho_v)^4 \rangle &= \langle \tilde{\rho}^4 \rangle - 4\langle \tilde{\rho}^3 \rangle \langle m^2 \rangle + 6\langle \tilde{\rho}^2 \rangle \langle m^4 \rangle - 4\langle \tilde{\rho} \rangle \langle m^6 \rangle + \langle m^8 \rangle. \end{aligned} \quad (7.17)$$

At the tricritical point, one has $\langle \delta\rho_v \rangle = 0$, so that $\langle \tilde{\rho} \rangle = \langle m^2 \rangle$. A detailed calculation then yields

$$Q_v^{-1} = \left(-3 + 6\frac{\langle m^4 \rangle}{\langle m^2 \rangle^2} - 4\frac{\langle m^6 \rangle}{\langle m^2 \rangle^3} + \frac{\langle m^8 \rangle}{\langle m^2 \rangle^4} \right) / \left[\frac{\langle m^4 \rangle}{\langle m^2 \rangle^2} - 1 \right]^2, \quad (7.18)$$

so that

$$Q_v^{-1} = 9 - \frac{1}{6} \left[\frac{\Gamma\left(\frac{1}{6}\right)}{\Gamma\left(\frac{1}{2}\right)} \right]^3 \simeq 3.8348, \quad (7.19)$$

and $Q_v = 0.2608\dots$

The aforementioned calculations implicitly yield the mean-field (MF) thermal and magnetic exponents. Equation (7.4) indicates that the mean-field quantity $\langle m^2 \rangle$ can be regarded as a type of energy density. From the definition of the magnetic susceptibility $\chi = N\langle m^2 \rangle$, one has then the scaling behavior at tricriticality $\langle m^2 \rangle \propto N^{\tilde{y}_t - 1} = N^{2\tilde{y}_h - 2}$. Here, we have introduced the mean-field critical exponents \tilde{y}_t and \tilde{y}_h , which are related to the standard leading thermal and magnetic exponents in finite dimensions as $y_{t1} = d\tilde{y}_t$ and $y_{h1} = d\tilde{y}_h$ with $d \geq 3$, respectively. The above scaling formula gives the mean-field relation $\tilde{y}_t = 2\tilde{y}_h - 1$, which generally holds for mean-field systems. On this basis, Eq. (7.15) yields $\tilde{y}_t = 2/3$ and $\tilde{y}_h = 5/6$ for the tricritical MF BC model, so that one has $y_{t1} = 2$ and $y_{h1} = 5/2$ in three dimensions, in agreement with the existing RG results [4].

7.2.2 Monte Carlo simulations

The mean-field (MF) calculations in the above subsection rely on the limit $N \rightarrow \infty$, and thus we have performed numerical tests for finite N . Using the standard Metropolis method, which is adequate for this purpose, we simulated the unconstrained model (7.3) for $D = D_t = 2 \ln 2$ in the range $2.96 \leq K \leq 3.04$. The system sizes were taken as $N = 100, 200, 400, 600, 800$, and 1000 . The MF result for the tricritical point is confirmed by the clear intersection of the Q_m versus K data, shown in Fig. (7.3) at $K = 3$. Then, we simulated precisely at the tricritical point (K_t, D_t) , with system sizes $10 \leq N \leq 16000$. The sampled quantities include the magnetic susceptibility $\chi = N\langle m^2 \rangle$, the vacancy density ρ_v , and the Binder ratios Q_m and Q_v . Here, the quantity Q_v is defined by Eq. (7.14), but $\delta\rho_v = \rho_v - \rho_{vt}$ is replaced by $\delta\rho_v = \rho_v - \langle \rho_v \rangle$ for finite systems. The latter definition of Q_v is more natural in the sense that, for finite-dimensional systems, the exact value of ρ_{vt} is generally unknown. Further, at tricriticality, since the quantity $\langle \rho_v \rangle$ approaches ρ_{vt} as $N \rightarrow \infty$, these two definitions do not have qualitative difference. The data for ρ_v , Q_m , and Q_v are shown in Tab 7.1. According to the least-square criterion, we fitted the Monte Carlo data by

$$\begin{aligned} \chi(N) &= \chi_0 + N^{2\tilde{y}_h - 1} (x_0 + x_1 N^{\tilde{y}_i} + x_2 N^{2\tilde{y}_i} + x_3 N^{3\tilde{y}_i}), \\ \rho_v(N) &= \rho_{vt} + N^{\tilde{y}_t - 1} (p_0 + p_1 N^{\tilde{y}_i} + p_2 N^{2\tilde{y}_i} + p_3 N^{3\tilde{y}_i}), \\ Q_m(N) &= Q_{mt} + q_{m1} N^{\tilde{y}_i} + q_{m2} N^{2\tilde{y}_i} + q_{m3} N^{3\tilde{y}_i}, \quad \text{and} \\ Q_v(N) &= Q_{vt} + q_{v1} N^{\tilde{y}_i} + q_{v2} N^{2\tilde{y}_i} + q_{v3} N^{3\tilde{y}_i}. \end{aligned} \quad (7.20)$$

The terms with the exponent \tilde{y}_i account for finite-size corrections, with $\tilde{y}_i = -1/3$, as indicated from Eq. (7.16). Results are given in Tab. 7.2, where the estimation of \tilde{y}_i was obtained from the fit of Q_m with

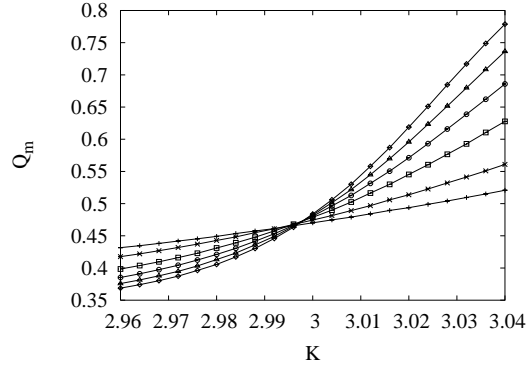


Figure 7.3: The Binder ratio Q_m of the MF BC model at $D_t = 2 \ln 2$ for $2.96 \leq K \leq 3.04$. The data points are $N = 100$ (+), 200 (x), 400 (\square), 600 (\circ), 800 (\triangle), and 1000 (\diamond).

Table 7.1: Monte Carlo data for ρ_v , Q_m , and Q_v for the MF BC model at the tricritical point $K_t = 3$ and $D_t = 2 \ln 2$. The numbers in in parentheses represent the error margins in the last decimal place.

N	10	20	40	60	100
ρ_v	.53364(3)	.54314(3)	.55756(3)	.56666(2)	.57804(2)
Q_m	.45159(5)	.45815(6)	.46352(6)	.46644(6)	.46992(6)
Q_v	.40132(5)	.36988(6)	.34546(7)	.33388(7)	.32129(8)
N	200	300	400	600	1000
ρ_v	.59251(2)	.60027(2)	.60541(2)	.61211(2)	.61970(1)
Q_m	.47449(7)	.47694(8)	.47853(8)	.4806(1)	.4831(1)
Q_v	.30746(8)	.30099(9)	.29683(9)	.2918(1)	.2865(1)
N	2000	4000	8000	16000	
ρ_v	.62852(1)	.63587(1)	.64183(1)	.64678(2)	
Q_m	.4862(1)	.4886(1)	.4910(2)	.4922(2)	
Q_v	.2807(1)	.2763(1)	.2732(2)	.2700(2)	

Table 7.2: Results of a least-squares analysis of the Monte Carlo data for the MF BC model at the tricritical point $K_t = 3$ and $D_t = 2 \ln 2$. The numbers in parentheses represent the error margins in the last decimal place.

	\tilde{y}_h	\tilde{y}_t	\tilde{y}_i	ρ_{vt}	Q_{mt}	Q_{vt}
Theory	5/6	2/3	-1/3	2/3	1/2	0.2608...
Fit	0.833(2)	0.667(2)	-0.332(1)	0.66664(6)	0.4998(3)	0.2609(3)

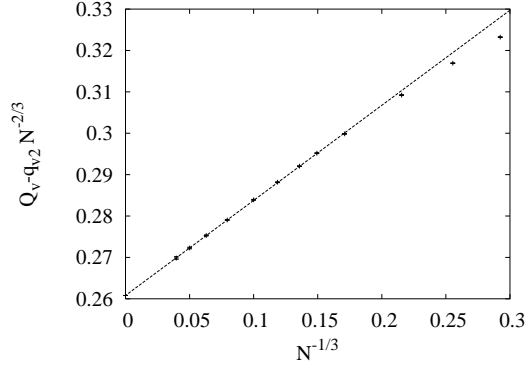


Figure 7.4: The Binder ratio Q_v of the MF BC model at tricriticality. The data $Q_v - q_{v2}N^{-2/3}$ are shown vs. $N^{-1/3}$, where $q_{v2} = 0.26(2)$ was taken from the fit.

Q_{mt} fixed at $1/2$. The theoretical predictions and the numerical determinations are in fine agreement. For clarity, the data for Q_v is shown in Fig. 7.4 as $Q_v - q_{v2}N^{-2/3}$ versus $N^{-1/3}$, with q_{v2} taken from the fit.

These exact results are not only theoretically interesting, but also practically useful. For instance, the exact values of Q_{mt} and Q_{vt} are very helpful in a Monte Carlo determination [35] of the tricritical point of BC models in three dimensions.

7.2.3 Constrained systems

For the MF BC model (7.3) with a conserved number of vacancies, the reduced partition sum is obtained from Eq. (7.9) by excluding the integration over vacancy fluctuations:

$$Z' = N^2 \int dm \delta_{\rho_v, 2/3} c(m, \rho_v) \exp\left[\frac{K}{2}Nm^2 - DN(1 - \rho_v)\right] [1 + \mathcal{O}(1/N)]. \quad (7.21)$$

Following the procedure in Ref. [33], it can be shown that, at the tricritical point (K_t, D_t) , Eq. (7.21) reduces to

$$Z' = N^2 \int dm e^{-\frac{3}{4}Nm^4} [1 + \mathcal{O}(Nm^6)], \quad (7.22)$$

which characterizes the *critical* mean-field Ising model [17, 33].

The reduction to the *critical* MF Ising model can be further understood as follows. In mean-field systems, each spin interacts with each other spin. Only the number of vacancies, not their positions, matters. One can then rearrange the labels of the Ising spins and those of the vacancies, such that all Ising spins are counted from 1 to $N/3$ and vacancies from $N/3 + 1$ to N . Then, the constrained Hamiltonian reads

$$\mathcal{H}/k_B T = -\frac{K'}{N'} \sum_{i=1}^{N'} + 2DN' \sum_{j=i+1}^{N'} s_i s_j \quad (s_i = \pm 1), \quad (7.23)$$

where the sum is now only over $N' = N/3$ Ising spins, and $K' = K/3$ is the coupling constant in Eq. (7.23). For $K = K_t = 3$, Eq. (7.23) describes a MF critical Ising model with N' spins, and the critical point is at $K' = K'_c = 1$. In this case, the Binder ratio Q_m assumes $4\Gamma^2(\frac{3}{4})/\Gamma^2(\frac{1}{4}) = 0.4569 \dots$ [33].

7.3 Fisher renormalization mechanism at tricriticality

As mentioned earlier, constrained critical phenomena can be successfully explained by the Fisher renormalization mechanism [23–27]. The basic idea of this mechanism is straightforward and fundamental. It is based

on the thermodynamic relation that, in the language of the BC model, the vacancy density ρ_v and the chemical potential D are conjugate parameters. Let f be the reduced free energy of the unconstrained critical model as a function of K and D . The constraint equation is then expressed as $\rho_v = -\partial f/\partial D = \text{constant}$. This yields the path of the constrained system in the parameter space (K, D) , which appears to be singular at the critical point. In this section, we follow a similar procedure and generalize the Fisher renormalization mechanism such that it can describe constrained tricritical phenomena. Particularly, since the Monte Carlo simulations have to take place at finite systems, we shall first focus on the finite-size scaling behavior of constrained tricritical systems.

As a first step, we express the finite-size scaling formula of the reduced free energy f of an unconstrained system [4] near the tricritical point as

$$f(t_1, t_2, L) = L^{-d} f_s(t_1 L^{y_{t1}}, t_2 L^{y_{t2}}) + f_a(t_1, t_2). \quad (7.24)$$

Here, L is the linear system size, and it can also be recognized as a scaling factor in the context of the renormalization group theory. The leading and subleading thermal scaling fields t_1 and t_2 represent the distance to the tricritical point at $t_1 = t_2 = 0$. The functions f_s and f_a are singular and analytical parts of the free energy f , respectively. We have neglected irrelevant scaling fields and also suppressed magnetic scaling fields in Eq. (7.24). For the BC model described by Eq. (7.1), the thermal fields t_1 and t_2 are analytic functions of K and D . Thus, differentiation of Eq. (7.24) with respect to D yields

$$-\langle \rho_v(t_1, t_2) \rangle = \frac{\partial f}{\partial D} = a_1 L^{y_{t1}-d} f_s^{(1,0)}(t_1 L^{y_{t1}}, t_2 L^{y_{t2}}) + a_2 L^{y_{t2}-d} f_s^{(0,1)}(t_1 L^{y_{t1}}, t_2 L^{y_{t2}}) + a_1 f_a^{(1,0)}(t_1, t_2) + a_2 f_a^{(0,1)}(t_1, t_2), \quad (7.25)$$

where $a_1 = \partial t_1/\partial D$ and $a_2 = \partial t_2/\partial D$ are constants. The superscripts (i, j) represent i differentiations with respect to t_1 and j differentiations to t_2 . Here, we mention that, for finite systems L , the conjugate quantity of D is the expectation value of the vacancy density $\langle \rho_v(t_1, t_2) \rangle$ instead of $\rho_v(t_1, t_2)$ itself. Under the constraint $\langle \rho_v(t_1, t_2) \rangle = \langle \rho_v(0, 0) \rangle$, Taylor expansion of of Eq. (7.25) near the tricritical point leads to

$$0 = b_1 L^{2y_{t1}-d} t_1 + b_2 L^{y_{t1}+y_{t2}-d} t_2 + b_3 t_1 + b_4 t_2, \quad (7.26)$$

where b_1, b_2, b_3 , and b_4 are constants, and *only* the leading terms are kept in the expansions of f_s and f_a . The constraint equation (7.26) describes the approach of the constrained BC model to the tricritical point in the parameter space (t_1, t_2) . However, the analytic form of the path still depends on the relative values of y_{t1} , y_{t2} , and d , and so does the critical exponents describing the constrained critical singularities for $t_1, t_2 \rightarrow 0$. It follows from Eq.(7.26) that, near the tricritical point, the thermal fields t_1 and t_2 are related as

1. for $2y_{t1} - d > 0$ and $y_{t1} + y_{t2} - d > 0$, the first two terms in the right-hand side of Eq. (7.26) dominate as $L \rightarrow \infty$, so that one has $L^{y_{t1}} t_1 \propto L^{y_{t2}} t_2$, i.e., $t_2 \gg t_1$ and $K - K_{tc} \approx t_2$. Thus, the leading thermal exponent of the constrained system is equal to the subleading exponent y_{t2} .
2. for $2y_{t1} - d > 0$ but $y_{t1} + y_{t2} - d < 0$, one has $L^{y_{t1}} t_1 \propto L^{d-y_{t1}} t_2$. The leading exponent is renormalized as $y_{t1} \rightarrow d - y_{t1}$. This case was already correctly included as one of the possible outcomes of Imry's renormalization calculations [28].
3. for $2y_{t1} - d < 0$, i.e., the unconstrained specific heat does not diverge at tricriticality, t_1 is linearly related to t_2 as $t_1 \propto t_2$, and no exponent renormalization occurs.

In short, for a system with a divergent specific heat at tricriticality, critical exponents are renormalized under the constraint; otherwise, no renormalization occurs. However, since tricritical systems have two relevant thermal fields t_1 and t_2 , the tricritical renormalizations can appear in different ways, depending on whether or not $y_{t1} + y_{t2} > d$.

Then, the expression of the reduced free energy f' of the constrained tricritical BC model can be obtained by substitution of the above renormalization in Eq. (7.24), which yields

$$f'(t_1, t_2, L) = L^{-d} f'_s(t_1 L^{y_{t1}}, t_2 L^{y_{t2}}, 1) + f'_a(t_1, t_2), \quad (7.27)$$

where y'_{t_1} is equal to y_{t_2} , $d - y_{t_1}$, and y_{t_1} for $y_{t_1} + y_{t_2} > d$, $y_{t_1} + y_{t_2} < d$ but $2y_{t_1} > d$, and $2y_{t_1} < d$, respectively.

Next, we consider the effect of the constraint in an infinite system. We interpret the parameter L in Eq. (7.24) as a rescaling factor that can be arbitrarily chosen. Thus, we may set the rescaling factor $L = t_2^{-1/y_{t_2}}$ for case 1 and $L = t_2^{-1/(d-y_{t_1})}$ for case 2, so that the thermal fields t_1 and t_2 are related as $t_1 \propto t_2^{y_{t_2}/y_{t_1}}$ and $t_1 \propto t_2^{(d-y_{t_1})/y_{t_1}}$, respectively. Substitution of these relation in Eq. (7.27) yields the constrained reduced free energy f' of an infinite system as

$$f'(t_1, t_2) \propto t_1^{2-\alpha'} \Psi(t_2/t_1^\phi). \quad (7.28)$$

Here, the critical index is given by $\alpha' = 2 - d/y'_{t_1}$ and the crossover exponent by $\phi = y_{t_2}/y'_{t_1}$, with y'_{t_1} given earlier, and Ψ represents an analytical function. For the case $y'_{t_1} = d - y_{t_1}$, one has $\alpha' = -\alpha/(1 - \alpha)$, in agreement with Eq. (7.2).

During the derivation of these scaling equations, we have used Taylor expansions, for instance, of Eq. (7.25), and kept only the leading terms. Therefore, in addition to those from irrelevant thermal fields, we expect that new corrections are induced by the constraint.

As generally expected at the borderline dimensionality for mean-field-like behavior, logarithmic corrections-to-scaling occur in tricritical BC systems (7.1) in three dimensions. This has already been obtained in renormalization calculations of the Landau-Ginzburg-Wilson Hamiltonian. Near the tricritical point, the reduced free energy of the 3D BC model reads [4]

$$f(t_1, t_2, h_1, h_2, v, L) = L^{-3} f_s(t_1 L^2, t_2 L L_0^{-2/5}, h_1 L^{5/2}, h_2 L^{3/2} L_0^{-1/10}, v L_0^{-1}) + f_a(t_1, t_2). \quad (7.29)$$

where the parameter v , also an analytical function of K and D , describes the leading irrelevant thermal field. For completeness, we have also included the leading and subleading magnetic fields h_1 and h_2 . The amplitude $L_0 = 1 + 25v \ln L$ accounts for the aforementioned logarithmic corrections. Equation (7.29) indicates that these corrections occur not only in the irrelevant field v but also in the subleading fields t_2 and h_2 .

It follows from Eq. (7.29) that the unconstrained specific heat C in systems (7.1) is divergent ($2y_{t_1} - 3 > 0$) at tricriticality, and thus the critical exponents are renormalized under the constraint. However, the 3D tricritical BC model (7.1) is a marginal case in the sense the critical exponents $y_{t_1} + y_{t_2} - 3 = 0$, so that it is not immediately obvious how the renormalization occurs. Taking into account $L_0^{-2/5}$ in Eq. (7.29) for the subleading field t_2 , we conclude that in constrained systems the leading thermal exponent is renormalized as $y'_{t_1} = 3 - y_{t_1} = 1$.

7.4 Monte Carlo simulations

7.4.1 Unconstrained BC model

The tricritical BC model (7.1) has been investigated on several three-dimensional lattices, and various techniques have been developed, including the self-consistent Ornstein-Zernike approximation [36] and Monte Carlo simulations [35, 37].

In comparison with the well-known Swendsen-Wang [38] and Wolff [32] algorithms for the spin- $\frac{1}{2}$ Ising model, no cluster algorithm has so far been developed to efficiently flip between Ising spins and vacancies near the tricritical point. Thus, Monte Carlo simulations of the unconstrained tricritical BC model (7.1) suffer from critical-slowing-down. Using a combination of the Metropolis, Wolff, and aforementioned geometric cluster [29–31] steps, we simulated the BC model (7.1) on the simple-cubic lattice with periodic boundary conditions. The fluctuations between vacancies and Ising spins are realized by the standard Metropolis method; the Wolff algorithm flips between +1 and -1 Ising spins; and the geometric steps move groups of spins and vacancies over the lattice. In this way, critical-slowing-down is significantly suppressed. Making use of the exact values of Q_m and Q_v , we located [35] the tricritical point as $K_t = 0.7133(1)$ and $D_t = 2.0313(4)$; the expectation value of the tricritical vacancy density is $\rho_{vt} = 0.6485(2)$, rather close the

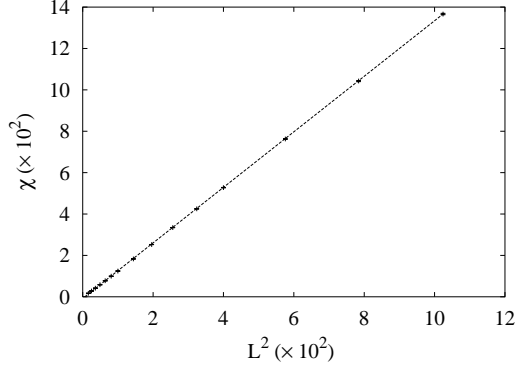


Figure 7.5: The unconstrained magnetic susceptibility χ of the 3D BC model at tricriticality, shown vs. $L^{2y_{h1}-3}$, with $y_{h1} = 5/2$.

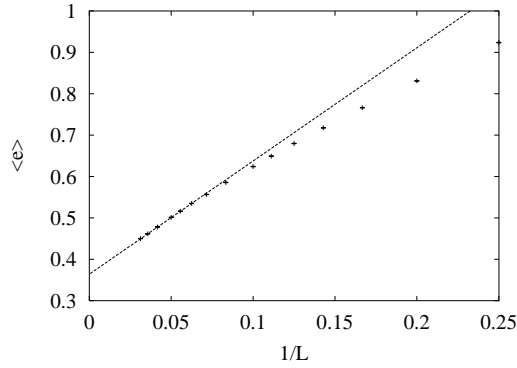


Figure 7.6: The unconstrained energy density $\langle e \rangle$ of the 3D BC model at tricriticality, vs. $L^{y_{t1}-3}$, with $y_{t1} = 2$.

mean-field value $2/3$. Consistency between these results and existing determinations [36, 37], $K_t = 0.706(3)$, $D_t = 2.01(1)$, and $\rho_{vt} = 0.655(6)$, exists within a margin of about twice the quoted errors. Here, we have applied other techniques, including a simultaneous analysis of various quantities for different systems such that parameters in common appear only once [16]; the details of these numerical analyses will be presented elsewhere [35].

For a comparison of constrained tricritical behavior, we simulated the constrained BC model at the tricritical point (K_t, D_t) , as determined earlier, with system sizes $6 \leq L \leq 32$. We sampled the magnetic susceptibility χ , the energy density $\langle e \rangle$, the specific heat C , and the Binder ratios etc, respectively. Here, the energy density $\langle e \rangle$ was defined as nearest-neighbor correlations, and the specific heat C reads

$$C = L^3 K^2 (\langle e^2 \rangle - \langle e \rangle^2), \quad (7.30)$$

representing the strength of critical fluctuations of $\langle e \rangle$. At tricriticality, the scaling behavior of these quantities can be derived from Eq. (7.29) as

$$\chi - x_0 \propto L^{2y_{h1}-3} = L^2, \quad \langle e \rangle - e_0 \propto L^{y_{t1}-3} = L^{-1}, \quad \text{and} \quad C - c_0 \propto L^{2y_{t1}-3} = L, \quad (7.31)$$

where the terms x_0 , e_0 , and c_0 arise from the analytical part of the free energy. The Monte Carlo data for χ , $\langle e \rangle$, and C are shown in Figs. 7.5, 7.6, and 7.7, respectively. The approximate linearity for large L in these figures confirms the tricritical finite-size scaling behavior described by Eq. (7.31).

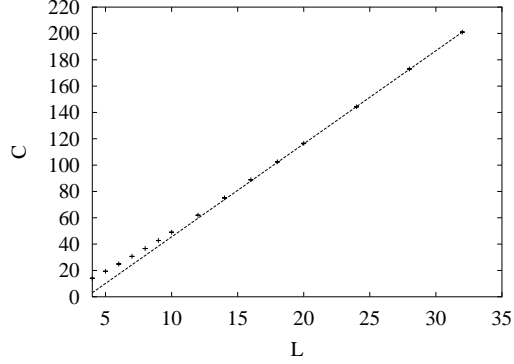


Figure 7.7: The unconstrained specific heat C of the 3D BC model at tricriticality, vs. $L^{2y_{t1}-3}$, with $y_{t1} = 2$.

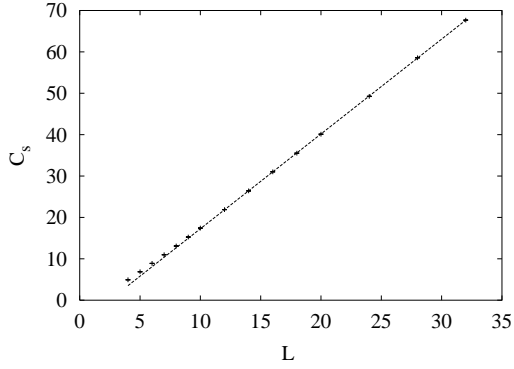


Figure 7.8: The unconstrained structure factor of the specific heat C_s of the 3D BC model at tricriticality, vs. $L^{2y_{t1}-3}$, with $y_{t1} = 2$.

Apart from the conventional specific heat C , we also sampled a related quantity C_s on the basis of the Fourier components of $e(x, y, z)$ for systems of size L :

$$e_{k_x, k_y, k_z} = \frac{1}{L^3} \int_0^L dx dy dz e(x, y, z) \exp[2\pi i(xk_x + yk_y + zk_z)/L]. \quad (7.32)$$

Obviously, $e_{0,0,0}$ is just the global energy density e ; and quantities e_{k_x, k_y, k_z} for $k_x \neq 0$, $k_y \neq 0$, or $k_z \neq 0$ represent spatial inhomogeneities of $e(x, y, z)$. Then, the quantity C_s can be defined in terms of e_{k_x, k_y, k_z} for the smallest wave numbers as

$$C_s = L^3 K^2 \langle e_{-1,0,0} e_{1,0,0} + e_{0,-1,0} e_{0,1,0} + e_{0,0,-1} e_{0,0,1} \rangle. \quad (7.33)$$

The physical meaning of C_s can be gleaned in comparison with the conventional specific heat C . First, as indicated by Eq. (7.30) and (7.33), both quantities represent fluctuation strengths of e_{k_x, k_y, k_z} , with $k_x = k_y = k_z = 0$ for C and $|k_x| + |k_y| + |k_z| = 1$ for C_s . Second, both C and C_s can be expressed in terms of a sum of energy-energy correlation functions. Thus, we expect that C_s behaves as a specific-heat-like quantity, and we refer to it as the structure factor of the specific heat C . Then, the tricritical scaling behavior of C_s is also governed by Eq. (7.31), and this is confirmed by Fig. 7.8.

7.4.2 Constrained BC model

For the three-dimensional BC model (7.1) with a conserved number of vacancies, we used a combination of the Wolff and geometric cluster steps only. The chemical potential D in Eq. (7.1) becomes implicit and does

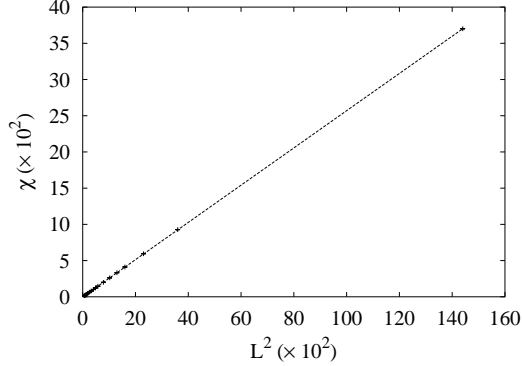


Figure 7.9: The constrained magnetic susceptibility χ of the 3D BC model at tricriticality, vs. $L^{2y_{h1}-3}$, with $y_{h1} = 5/2$.

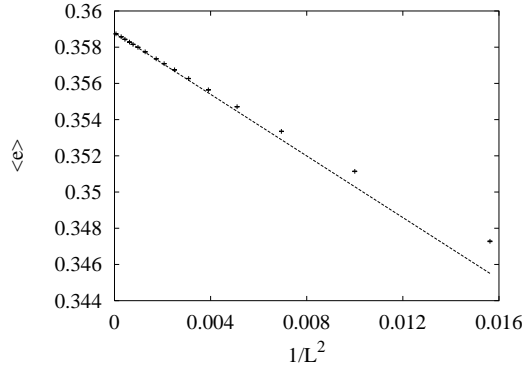


Figure 7.10: The constrained energy density $\langle e \rangle$ of the 3D BC model at tricriticality, vs. L^{-2} .

not play a role in constrained Monte Carlo simulations. One particular feature is that these simulations *hardly* suffer from critical-slowing-down even near the tricritical point. This may be attributed to the fact that the constrained specific heat C does not diverge at tricriticality, as discussed later. Therefore, we extensively simulated systems in the range $6 \leq L \leq 128$. The coupling constant K and the vacancy density ρ_v were set at $K_{tc} = 0.7133(1)$ and $\rho_{tc} = 0.6485(2)$ [35], respectively. For a finite system, however, the number of vacancies $N_{vt} = L^3 \rho_{tc}$ is not an integer, so that the actual simulations took place at $[N_{vt}]$ and $[N_{vt}] + 1$, where brackets $[\]$ denote the integer part. The value of a sampled quantity at N_{vt} was obtained by a linear interpolation between $[N_{vt}]$ and $[N_{vt}] + 1$.

The Monte Carlo data for χ , $\langle e \rangle$, and C are shown in Figs. 7.9, 7.10, and 7.11, respectively.

As illustrated by Figs. 7.5 and 7.9, the magnetic exponent describing the divergence of the susceptibility χ , i.e., y_{h1} , remains unchanged under the constraint, which indicates that the constraint on vacancies does not qualitatively influence magnetic quantities. However, the critical behavior of energy-like quantities is significantly modified. In particular, the tricritical specific heat C is strongly suppressed so that it only takes a finite value as $L \rightarrow \infty$. This constrained phenomenon is in agreement with the generalized Fisher renormalization mechanism. Further, from Eqs. (7.27) and (7.29), the quantitative finite-size behavior of $\langle e \rangle$ and C at tricriticality is described by

$$\langle e \rangle - e_0 \propto L^{y'_{t1}-3} = L^{-2}, \quad \text{and} \quad C - c_0 \propto L^{2y'_{t1}-3} = L^{-1}, \quad (7.34)$$

where $y'_{t1} = 3 - y_{t1} = 1$, as mentioned earlier. These theoretical predictions, i.e., Eq. (7.34), are reflected by

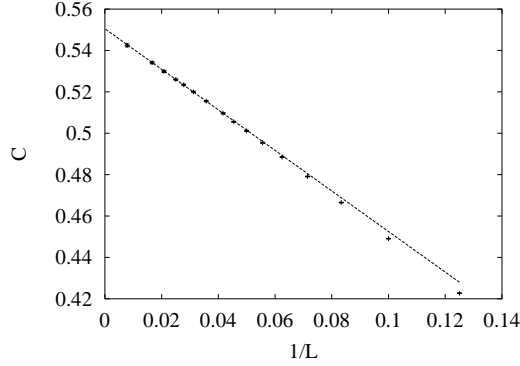


Figure 7.11: The constrained specific heat C of the 3D BC model at tricriticality, vs. L^{-1} .

the approximate linearity displayed by the data in Figs. 7.9 and 7.10. We fitted the data for $\langle e \rangle$ and C by

$$\langle e \rangle = e_0 + e_1 L^{y'_{t1}-3} (1 + b_1 / \ln L + b_2 / L + b_3 / L^2), \quad (7.35)$$

and

$$C = c_0 + c_1 L^{y'_{t1}-3} (1 + d_1 / \ln L + d_2 / L + d_3 / L^2), \quad (7.36)$$

respectively. The logarithmic corrections from the irrelevant fields are described by the terms with amplitudes b_1 and d_1 . The fits of $\langle e \rangle$ and C yield that $y'_{t1} = 0.99(2)$ and $1.02(2)$, respectively, with error margins of two standard deviations. This is consistent with the expectation $y'_{t1} = 3 - y_{t1} = 1$. We mention that Eqs. (7.35) and (7.36) are in fact neither complete nor “correct” in describing the scaling behavior of $\langle e \rangle$ and C . First, one has not taken into account the second relevant thermal fields t_2 , which can in principle introduce terms with $L_0^{-2/5}$ in the brackets of Eqs. (7.35) and (7.36). Second, the logarithmic corrections should be described by terms with $1/L_0$ instead of $1/\ln L$. However, as indicated by the fits of $\langle e \rangle$ and C , this ‘bias’ does not significantly affect the results of y'_{t1} due to the following reasons. The replacement of $1/\ln L$ by $(\ln L)^{-2/5}$ does not significantly change the result for y'_{t1} . Even neglecting the $1/\ln L$ term does not produce a large change. It appears that logarithmic corrections are not very serious in constrained tricritical systems. This is also illustrated by the clean intersection of the Q_m data for $K = K_t = 0.7133(1)$ and $0.645 \leq \rho_v \leq 0.651$, partly shown in Fig. 7.12. The data for Q_m in the range $6 \leq L \leq 128$ were fitted by

$$Q_m(K, L) = Q_{mt} + \sum_{k=1}^4 (\rho_v - \rho_{vt})^k L^{ky'_{t1}} + b_1 / \ln L + b_2 / L + b_3 / L^2 + c(\rho_v - \rho_{vt}) L^{y'_{t1}} / L, \quad (7.37)$$

where ρ_{vt} is the tricritical vacancy density. The renormalized thermal exponent was taken as $y'_{t1} = 1$, and we obtain $b_1 = 0.066(5)$ and $Q_{mt} = 0.687(6)$, with two standard deviations again. The value of Q_{mc} is in agreement neither with $Q_t = 1/2$ for unconstrained systems nor with the mean-field *critical* Ising value $Q_c = 0.4567 \dots$.

The influence of the annealed constraint on tricritical spatial fluctuations can be reflected by the constrained Monte Carlo data for C_s at the tricritical point, as shown in Fig. 7.13. As in unconstrained systems, C_s diverges as $C_s \propto L$ as $L \rightarrow \infty$, so that the leading thermal exponent y_{t1} still governs the scaling behavior of C_s . This is rather different from the constrained behavior of the conventional specific heat C , which is suppressed to be convergent at tricriticality. We fitted the data for C_s by

$$C_s = c_{s0} + c_{s1} L^{y_{t1}-3} (1 + d_{s1} / \ln L + d_{s2} / L + d_{s3} / L^2), \quad (7.38)$$

which yields $y_{t1} = 1.995(8)$, in fine agreement with the exact value $y_{t1} = 2$. Therefore, one can conclude that the tricritical spatial fluctuations remain unchanged under the constraint.

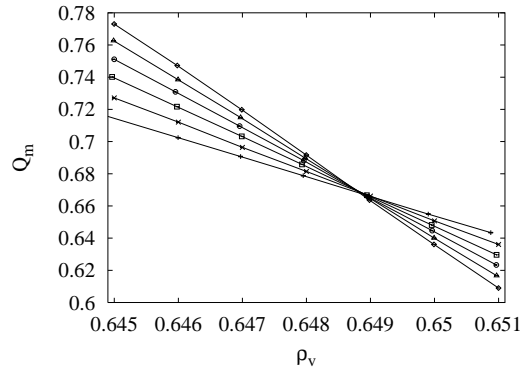


Figure 7.12: The constrained Binder ratio Q_m of the 3D BC model for $K = 0.7133(2)$, vs. the vacancy density ρ_v . The data points are $L = 16$ (+), 20 (\times), 24 (\square), 28 (\circ), 32 (\triangle), and 36 (\diamond).

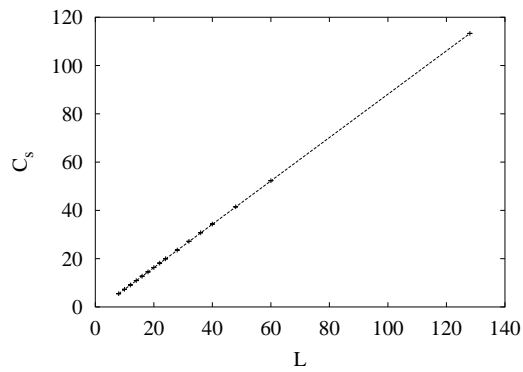


Figure 7.13: The structure factor C_s of the constrained specific heat of the 3D BC model at tricriticality, vs. L .

7.5 Discussion

Due to the geometric cluster algorithm, a full-cluster simulation becomes possible for the tricritical BC model with a conserved number of vacancies. We have performed an extensive investigation of constrained tricritical behavior in three dimensions, and observe that

- the leading finite-size scaling behavior of magnetic quantities remains unchanged under the constraint. This is as expected: the vacancy density ρ_v is conjugate to the chemical potential D , which contributes only to the thermal fields t_1 and t_2 .
- the critical behavior of energy-like quantities is renormalized; particularly, the constrained specific heat C has only a finite cusp at tricriticality. The leading thermal exponent $y_{t1} = 2$ is renormalized as $y'_{t1} = 3 - y_{t1} = 1$, while the second one $y_{t2} = 1$ remains unchanged under the constraint;
- the constrained magnetic Binder ratio at tricriticality is $Q_{mt} = 0.687(6)$, apparently different from the unconstrained value $Q_{mt} = 1/2$. This is understandable because the universal ratio Q_m still depends on boundary conditions, and the aspect ratios, etc, which influence magnetic correlation functions. The constraint also belongs to this category;
- structure factors such as C_s , accounting for spatial inhomogeneities of conventional quantities, display the same scaling behavior as in unconstrained systems. This indicates that the divergence of the spatial correlation length, one essential characterization of critical phenomena, remains unchanged under the constraint at least to a scale which is small in comparison with system sizes. In this sense, one can conclude that the annealed constraint does not modify the universality class of a tricritical system.

It is clear that the constrained tricritical BC model in three dimensions is *not* mean-field *critical* Ising-like. This indicates that the mean-field theory is not complete in describing universal critical phenomena even at the upper critical dimensionality. For a unconstrained mean-field BC model, the vacancy fluctuations are coupled to the Ising fluctuations. Then, the stability criterion of the coupled fluctuations, depending on the value of K and D , yields distinct types of phase transitions: a line of critical Ising points, a tricritical point, and a first-order transition line. However, in constrained mean-field systems, the fluctuations of vacancies are suppressed. Therefore, the presence of vacancies *only* serves to reduce the number of Ising spins, leading to a smaller effective interaction. As a consequence, the whole line of phase transitions in the space (K, D) , including the tricritical point and the first-order transition, reduces to mean-field *critical* Ising-like under the constraint. Since this does not agree with the constrained behavior of the investigated short-range model, we arrive at the somewhat surprising that mean-field theory does not describe the universal properties of the constrained tricritical at its upper critical dimensionality.

On the basis of the generalized Fisher renormalization mechanism, we finite-size analyzed several tricritical quantities of the constrained BC model in three dimensions. The agreement between the theoretical predictions and the Monte Carlo results is quite satisfactory.

The Fisher renormalization mechanism is rather straightforward and fundamental. Nevertheless, Imry's renormalization calculations [28] also give a correct prediction of the critical index α for tricritical $O(n)$ systems ($n \geq 1$) in three dimensions. However, we mention that the calculations in Ref. [28] did not take into account the effect of the subleading thermal field y_{t2} . It is then justified to ask the question how to include y_{t2} in these calculations.

A final remark follows. In a finite system, the vacancy density ρ_v needs not be equal to its expectation value $\langle \rho_v \rangle$, although this difference vanishes as $L \rightarrow \infty$. In the generalized Fisher mechanism for constrained tricritical behavior, it is only required that $\langle \rho_v(t_1, t_2) \rangle$ is equal to $\langle \rho_v(0, 0) \rangle$. However, the Monte Carlo simulations take place with $\rho_v = \rho_{vt}$, i.e., no fluctuation of ρ_v is allowed. In this sense, the constraint in our numerical studies is 'stronger' than the one in the generalized Fisher renormalization, although our present numerical results do not reveal the consequences of this fact.

Bibliography

- [1] M. Blume, Phys. Rev. **141**, 517 (1966).
- [2] H.W. Capel Physica **32**, 966 (1966); Phys. Lett. **23**, 327 (1966).
- [3] L. Onsager, Phys. Rev. **65**, 117 (1944).
- [4] For a review, see e.g., I.D. Lawrie and S. Sarbach, *Phase Transitions and Critical Phenomena*, edited by C. Domb and J.L. Lebowitz. (Academic Press, London, 1984), Vol. 9, p 1.
- [5] B.M. McCoy and T.T. Wu, *The Two-Dimensional Ising Model* (Harvard University Press, Cambridge, Massachusetts, 1968).
- [6] R.J. Baxter, J. Phys. A **13**, L61 (1980); J. Stat. Phys. **26**, 427 (1981).
- [7] D.A Huse, Phys. Rev. Lett. **49**, 1121 (1982); R.J. Baxter and P.A. Pearce, J. Phys. A **16**, 2239 (1983).
- [8] B. Nienhuis, A.N. Berker, E.K. Riedel, and M. Schick, Phys. Rev. Lett. **43**, 737 (1979).
- [9] B. Nienhuis, *Phase Transitions and Critical Phenomena*, edited by C. Domb and J.L. Lebowitz. (Academic Press, London, 1987), Vol. 11, p 1.
- [10] A.A. Belavin, A.M. Polyakov, and A.B. Zamolodchikov, J. Stat. Phys. **34**, 763 (1984); D. Friedan, Z. Qiu, and S. Shenker, Phys. Rev. Lett. **52**, 1575 (1984).
- [11] J.L. Cardy, *Phase Transitions and Critical Phenomena*, edited by C. Domb and J.L. Lebowitz. (Academic Press, London, 1987), Vol. 11, p. 55.
- [12] there is a typo in Ref. [9] about the second magnetic exponent; from private communications with B. Nienhuis, we have $y_{h_2} = 9/8$ for the tricritical BC model in two dimensions.
- [13] for a review, see e.g., K. Binder and E. Luijten, Phys. Rep. **344**, 179 (2001).
- [14] M. Campostrini, A. Pelissetto, P. Rossi, and E. Vicari, Phys. Rev. E **65**, 066127 (2002).
- [15] Y. Deng and H.W.J. Blöte, Phys. Rev. Lett. **88**, 190602 (2002).
- [16] Y. Deng and H.W.J. Blöte, Phys. Rev. E **68**, 036125 (2003).
- [17] For an introduction, see e.g., S.K. Ma, *Modern Theory of Critical Phenomena* (Addison-Wesley, Redwood, California, 1976).
- [18] Y. Achiam and Y. Imry, J. Phys. C **10**, 39 (1977).
- [19] R.B. Stinchcombe, *Phase Transitions and Critical Phenomena*, edited by C. Domb and J.L. Lebowitz. (Academic Press, London, 1984), Vol. 7, p. 152.
- [20] I. Syozi, Prog. Theor. Phys. **34**, 189 (1965); I. Syozi and S. Miyazima, Prog. Theor. Phys. **36**, 1083 (1966).
- [21] D.C. Rapaport, J. Phys. C **5**, 1830 (1977); **5**, 2813 (1977).
- [22] J.W. Essam and H. Garelick, Proc. Phys. Soc. **92**, 136 (1967).
- [23] M.E. Fisher, Phys. Rev. **176**, 257 (1968).
- [24] Y.N. Skryabin and A.V. Shchanov, Phys. Lett. A **234**, 147 (1997).
- [25] M. Krech, e-print, cond-mat/9903288 (1999).

- [26] I.M. Mryglod and R. Folk, *Physica A* **294**, 351 (2000).
- [27] I.M. Mryglod, I.P. Omelyan, and R. Folk, *Phys. Rev. Lett.* **86**, 3156 (2001).
- [28] Y. Imry, *Phys. Rev. Lett.* **33**, 1304, (1974); J. Rudnick, D.J. Bergman and Y. Imry, *Phys. Lett. A* **46**, 448, (1974); Y. Achiam and Y. Imry, *Phys. Rev. B* **12**, 2768, (1975).
- [29] J.R. Heringa and H.W.J. Blöte, *Physica A* **232**, 369 (1996).
- [30] H.W.J. Blöte, E. Luijten, and J.R. Heringa, *J. Phys. A* **28**, 6289 (1995).
- [31] J.R. Heringa and H.W.J. Blöte, *Phys. Rev. E* **57**, 4976 (1998).
- [32] U. Wolff, *Phys. Rev. Lett.* **62**, 361 (1989).
- [33] E. Luijten, *Interaction Range, Universality and the Upper Critical Dimension* (Delft University Press, 1997).
- [34] K. Binder, *Z. Phys. B: Condens. Matter* **43**, 119 (1981).
- [35] Y. Deng and H.W.J. Blöte, unpublished.
- [36] S. Grollau, E. Kierlik, M.L. Rosinberg, and G. Tarjus, *Phys. Rev. E* **63**, 041111 (2001).
- [37] M. Deserno, *Phys. Rev. E* **56**, 5204 (1997).
- [38] R.H. Swendsen and J.S. Wang, *Phys. Rev. Lett.* **58**, 86 (1987).

Constrained tricritical phenomena in two dimensions

We investigate several tricritical models on the square lattice by means of Monte Carlo simulations. These include the Blume-Capel model, Baxter's hard-square model, and the $q = 1, 3,$ and 4 Potts models with vacancies. We use a combination of the Wolff and geometric cluster methods, which conserves the total number of vacancies or lattice-gas particles, and suppresses critical slowing down. Several quantities are sampled, such as the specific heat C and the structure factor C_s which accounts for the large-scale spatial inhomogeneity of the energy fluctuations. We find that the constraint strongly modifies some of the critical singularities. For instance, the specific heat C reaches a finite value at tricriticality, while C_s remains divergent as in the unconstrained system. We are able to explain these observed constrained phenomena on the basis of the Fisher renormalization mechanism generalized to include a subleading relevant thermal scaling field. In this context, we find that, under the constraint, the leading thermal exponent y_{t1} is renormalized to $2 - y_{t1}$, while the subleading exponent y_{t2} remains unchanged.

8.1 Introduction

In experiments, many systems undergoing phase transitions are subject to external constraints such as the conservation of particle numbers in a mixture. Such systems are described in terms of the canonical ensemble, and thus typically display a behavior different from that of unconstrained models, which are described by the grand ensemble. An example is the superfluid transition in the ^3He - ^4He mixtures [1], whose universal properties can be described by a dilute XY model. The Hamiltonian of the lattice XY model reads

$$\mathcal{H}/k_{\text{B}}T = -K \sum_{\langle i,j \rangle} \vec{s}_i \vec{s}_j + D \sum_k |\vec{s}_k|^2, \quad (8.1)$$

where the spins can assume a unit vector of two components, $|\vec{s}_k| = 1$, or a vacancy $|\vec{s}| = \vec{0}$. The sum $\langle \rangle$ is over nearest-neighbor lattice pairs, and K and D are the coupling constant and the chemical potential of vacancies, respectively. The mole fraction of ^3He in the experiment corresponds with the vacancy density $\rho = \frac{1}{N} \sum_k (1 - |\vec{s}_k|^2)$, with N the total number of lattice sites. For $D \rightarrow -\infty$, the vacancies are excluded, and the model (8.1) reduces to the pure XY model. In three dimensions, this model undergoes a second-order phase transition, and the critical coupling constant $K_c(D)$ is an increasing function of D . The critical line terminates at a tricritical point (K_t, D_t) . Since the upper tricritical dimensionality of the $O(n)$ model ($n \geq 1$) is equal to three, significant exact information is available [1]. A set of universal parameters can be exactly obtained by means of mean-field analyses and also by renormalization group (RG) calculations of the Landau-Ginzburg-Wilson Hamiltonian. The leading and subleading thermal critical exponents are $y_{t1} = 2$ and $y_{t2} = 1$ [1]. Thus, as the tricritical point is approached, one simply expects that the specific heat C diverges with the index $\alpha = 2 - 3/y_{t1} = 1/2$. However, typical experiments take place at a constant density ρ instead at a constant chemical potential D . It was reported [2] that, at the tricritical point (K_t, ρ_t) , the

specific heat C has only a finite value with $\alpha = -0.9(1)$, apparently different from the aforementioned index $\alpha = 1/2$. Thus, the theoretical description of the experiment in Ref. [2] uses the dilute XY model with a *conserved* number of vacancies. This means that an external constraint is imposed on the system (8.1). Since the pertinent ^3He and ^4He mixtures are liquid, the constraint is of the ‘annealed’ type [3]. Therefore, the vacancies should be able to move freely over the lattice of model (8.1).

The effect of a constraint on a critical systems has already been studied for decades [3–6]. As early as in 1965, Szyzi introduced [4] a decorated Ising model, which is intimately connected with annealed systems. The Szyzi model can be exactly transformed into the spin- $\frac{1}{2}$ model, and for dimensionality $d > 2$ critical exponents of these two models are related as

$$\alpha_s = -\alpha/(1 - \alpha), \quad \beta_s = \beta/(1 - \alpha), \quad \text{and} \quad \nu_s = \nu/(1 - \alpha), \dots \quad (8.2)$$

where α and β are the standard critical indices for the specific heat C and the magnetization density m , respectively, and $\nu = 1/y_t$ is the inversion of the thermal exponent. The subscript s represents the Szyzi model. Later, this constraint mechanism was discussed in a more general context by Essam and Garelick [5] and by Fisher [6]. It was argued [5,6] that the relations (8.2) are not specific to the Szyzi model, but are more generally satisfied by equilibrium models with a divergent specific heat C . Thus, Eq.(8.2) predicts that, as long as $\alpha > 0$, the constrained critical specific heat C can at most reach a *finite* value instead of being divergent. For systems with a convergent specific heat $\alpha < 0$, Fisher [6] pointed out that no renormalization of critical exponents as Eq. (8.2) occurs, but additional corrections can be introduced by the constraint. Further, for the marginal case $\alpha = 0$, i.e., C normally diverges logarithmically in unconstrained systems, it was shown [6] that, again, the constraint leads to a convergent specific heat. Since then, Fisher’s *renormalized* critical exponents have been used extensively [3, 7–10].

More general theories were then formulated for constrained systems, including a theory of constrained tricritical phenomena [11,12]. Besides vacancies, constraints can be imposed on volumes or pressure, etc. It was argued [11,12] that, depending on the type or strength of the constraint, a continuous transition may become Fisher-renormalized, remain unchanged, or become first-order. The special point, where the transition remains unchanged was referred to as a special ‘tricritical’ point [11].

In the context of the renormalization group (RG) theory, Imry and coworkers [13] applied the ϵ -expansion technique to a generalized Landau-Ginzburg-Wilson Hamiltonian. The effect of the constraint is accounted for by an additional parameter, and they found four distinct fixed points: the tricritical Ising (TI), the critical Ising (CI), the *renormalized* tricritical Ising (RTI), and the *renormalized* critical Ising (RCI) fixed point. The critical exponents at these fixed points are related as: $\alpha_{\text{RCI}} = -\alpha_{\text{CI}}/(1 - \alpha_{\text{CI}})$ and $\alpha_{\text{RTI}} = -\alpha_{\text{TI}}/(1 - \alpha_{\text{TI}})$, in agreement with Eq. (8.2). For the spatial dimensionality $d \geq 3$, TI and RTI correspond to Gaussian and spherical fixed points, respectively [13]. Thus, at the fixed points TI and RTI, the critical index is equal to $\alpha_{\text{TI}} = 1/2$ and $\alpha_{\text{RTI}} = -1$, respectively. For the ^3He - ^4He mixtures, if one assumes that constrained tricritical behavior is governed by the fixed point RTI, the theoretical prediction $\alpha_{\text{RTI}} = -1$ is in good agreement with the experimental result $\alpha = -0.9(1)$ [2].

However, to our knowledge, numerical tests of these theories are still scarce; in particular, the finite-size behavior of constrained critical systems has only attracted limited attention. Thus, very recently, we performed [14] a Monte Carlo investigation of the constrained three-dimensional Blume-Capel (BC) model [15,16]. The phase diagram of the BC model is analogous to that of the dilute XY model, and, in three dimensions, the two tricritical models share a common set of critical exponents. At the tricritical point, the constrained specific heat reaches a finite value with the index $\alpha = -0.99(3)$ [14], in agreement with the experimental data [2] and the RG calculations in Ref. [13]. Nevertheless, the exponent of the power law describing the decay of the correlation function at tricriticality remains unchanged under the constraint. In this sense, the constraint does not lead to a change of the universality class. In Ref. [14], we also generalized Fisher’s approach [6] for application to *tricritical* systems. For the tricritical BC model in three dimensions, this mechanism also predicts that the unconstrained and constrained indices are related as $\alpha^{\text{co}} = -\alpha^{\text{un}}/(1 - \alpha^{\text{un}}) = -1$, in agreement with the RG calculations in Ref. [13]. Here, the superscripts ‘co’ and ‘un’ are for constrained and unconstrained systems, respectively. However, for a general tricritical system, it was predicted [14] that, in addition to the relation $\alpha^{\text{co}} = -\alpha^{\text{un}}/(1 - \alpha^{\text{un}})$, other cases can occur,

depending on the relative magnitude of the leading and subleading thermal exponents y_{t1} and y_{t2} , and the spatial dimensionality d .

In order to verify these theoretical predictions, the present paper presents a more extensive study of constrained tricritical phenomena in two dimensions. The systems investigated include the Blume-Capel (BC) model [15, 16], Baxter's hard-square model [17, 18], and the $q = 1, 3,$ and 4 Potts models with vacancies [19]. In comparison with the three-dimensional case, the investigation of two-dimensional systems has some advantages. First, Monte Carlo simulations can be performed for larger linear systems sizes. Second, the tricritical points of the tricritical $q = 1$ Potts model and Baxter's hard-square lattice gas are exactly known, and those of the other systems have been determined with a precision in the sixth or seventh decimal place. In contrast, for the three-dimensional BC model, the error estimation of the tricritical point is so far restricted to the fourth decimal place [14]. Third, Baxter's hard-square lattice gas [17, 18] is in the same universality class as the tricritical Blume-Capel model, so that the two models can serve for independent tests.

The outline of the remaining part of this paper is as follows. Section II reviews the models, the sampled quantities, and the geometric cluster algorithm, which plays an important role in the present investigation. In Sec. III, we apply the Fisher renormalization mechanism in the generalized context of tricritical scaling. Numerical results are presented in Sec. IV, and a brief discussion is given in Sec. V.

8.2 Models, simulations, and sampled quantities

8.2.1 Models

The Blume-Capel model. In the development of the theory of tricritical phenomena, the spin-1 model known as the Blume-Capel (BC) model has provided the foundation. The model was independently introduced by Blume and Capel [15, 16]. The reduced Hamiltonian reads

$$\mathcal{H}/k_B T = -K \sum_{\langle i,j \rangle} s_i s_j + D \sum_k s_k^2 \quad (s = 0, \pm 1). \quad (8.3)$$

This Hamiltonian is identical to Eq. (8.1) when the vector order parameter \vec{s} is replaced by a scalar s . Further, in three dimensions, the phase diagram of Eq. (8.3) is analogous to that of the dilute XY model (8.1). The universal tricritical exponents of the two-dimensional BC model (8.3) are known from exact solutions [17, 18]; they can also be calculated in the context of the Coulomb gas theory [20, 21] and are included in the predictions of conformal field theory [22, 23]. The leading and subleading thermal exponents are $y_{t1} = 9/5$ and $y_{t2} = 4/5$, and the magnetic ones are $y_{h1} = 77/40$ and $y_{h2} = 9/8$, respectively. Using a sparse transfer-matrix technique and the finite-size scaling, we have located [24] the tricritical point of the square-lattice BC model as $K_t = 1.6431759(1)$ and $D_t = 3.2301797(2)$; the tricritical vacancy density is $\rho_t = 0.4549506(2)$. These results are based on the requirement that both the leading magnetic and energy-energy correlation lengths simultaneously reach their theoretical values. They are consistent with the existing estimate $K_t = 1.64(2)$ and $D_t = 3.22(4)$ [25], and the precision is considered to be sufficient in the present investigation.

Baxter's hard-square model. We also investigate Baxter's tricritical hard-square lattice gas [17, 18], which belongs to the same universality class as the tricritical BC model. The Hamiltonian of a general lattice gas on the square lattice can be written as

$$\mathcal{H} = -K \sum_{\langle nn \rangle} \sigma_i \sigma_j - J \sum_{\{nmn\}} \sigma_k \sigma_l + D \sum_k \sigma_k, \quad (8.4)$$

where $\sigma = 0, 1$ represents the absence and the presence of a particle, respectively. The sums $\langle nn \rangle$ and $\{nmn\}$ are over nearest-neighbor and second-nearest-neighbor sites, respectively. For the hard-square lattice gas, it is required that $K \rightarrow -\infty$, i.e., the particles have a 'hard'-core so that nearest-neighbor sites cannot be occupied *simultaneously*. For this case, the tricritical point is exactly known [17, 18]: $J_t = \ln(3 + \sqrt{5})$ and $D_t = \ln[8(1 + \sqrt{5})]$. The corresponding vacancy density is $\rho_t = (5 + \sqrt{5})/10$.

The tricritical $q = 3$ Potts model. Just as the tricritical BC model, the tricritical $q = 3$ Potts model [19] can be obtained by including vacancies in the ‘pure’ $q = 3$ Potts model. The Hamiltonian of such a dilute q -state Potts model then reads

$$\mathcal{H} = -K \sum_{\langle nn \rangle} \delta_{\sigma_i, \sigma_j} (1 - \delta_{\sigma_i, 0}) - D \sum_k \delta_{\sigma_i, 0}, \quad (\sigma = 0, 1, \dots, q), \quad (8.5)$$

where the lattice site is occupied by a Potts variable $\sigma = 1, \dots, q$ or by a vacancy $\sigma = 0$. Nonzero couplings K occur only between nonzero Potts variables. For $q < 4$, the phase diagram in the (K, D) plane resembles that of the BC model: a tricritical point occurs between the continuous and the first-order line of transitions. At the tricritical point (K_t, D_t) , the critical exponents are [20–23] $y_{t1} = 12/7$, $y_{t2} = 4/7$, and $y_{h1} = 40/21$. Also for this model we used the sparse transfer-matrix method to locate [24] the tricritical point: $K_t = 1.649\,913(5)$, $D_t = 3.152\,173(10)$, with a corresponding vacancy density $\rho_t = 0.34572(5)$.

The dilute $q = 4$ Potts model. The $q = 4$ Potts model is a marginal case [19], since the subleading leading thermal exponent satisfies $y_{t2} = 0$. The leading thermal and magnetic exponents are [21, 22] $y_{t1} = 3/2$ and $y_{h1} = 15/8$, respectively. The phase transition of a pure Potts model with $q > 4$ is of the first-order type [17]. We investigate the dilute $q = 4$ Potts model at the point where the leading and the subleading thermal field vanish. We have located [24] this ‘fixed’ point as $K_t = 1.45\,790(1)$, $D_t = 2.47\,844(2)$, and the corresponding vacancy density is $\rho_t = 0.21\,207(2)$.

The tricritical $q = 1$ Potts model. It is already known for a long time [26] that the tricritical $q = 1$ Potts model is equivalent with the critical Ising model. The Ising clusters of the critical Ising model, a group of spins connected by bonds between equal nearest-neighbor spins, are described by the magnetic exponent of the tricritical $q = 1$ Potts model. Here, we shall illustrate this equivalence, starting from the dilute q -state Potts model (8.5), which, for the case $q = 1$, simplifies as

$$\mathcal{H} = -K \sum_{\langle nn \rangle} \sigma_i \sigma_j + D \sum_k \sigma_k, \quad (\sigma = 0, 1). \quad (8.6)$$

For $D \rightarrow -\infty$, the vacancies are excluded, and the random-cluster representation describes the ‘pure’ bond-percolation problem. Thus, the random-cluster representation of Eq. (8.6) corresponds with a mixed site-bond percolation model. Because of the attraction between the non-vacancies, this dilute model is different from the conventional site-bond percolation model [27], in which the vacancies are randomly distributed over the lattice, i.e., different sites are *uncorrelated*. Nevertheless, in general, one expects that the dilute $q \rightarrow 1$ Potts model, described by Eq. (8.6), is still in the percolation universality class, and the question arises if it has a tricritical point. The answer follows after substituting the relation $\sigma = (s + 1)/2$ in Eq. (8.6). Apart from a constant, the Hamiltonian (8.6) reduces to the Ising model in a magnetic field:

$$\mathcal{H} = -K^{(1)} \sum_{\langle nn \rangle} s_i s_j - H \sum_k s_k, \quad (s_i = \pm 1), \quad (8.7)$$

with the relations

$$K^{(1)} = K/4, \quad \text{and} \quad H = -D/2 + zK/4, \quad (8.8)$$

where z is the lattice coordination number. Thus, the Ising critical point at $K_c^{(1)}$ and $H = 0$ appears in the dilute $q \rightarrow 1$ Potts model (8.6) at $K_t = 4K_c^{(1)}$ and $D_t = 2zK_c^{(1)}$. Since the critical singularity is not percolation-like, this point qualifies as the tricritical point of the $q \rightarrow 1$ Potts model. The spin up-down symmetry of the critical Ising model yields the vacancy density of the dilute Potts model $\rho_t = 1/2$ at tricriticality. The relation (8.8) shows that the temperature-like parameters, K and D , contribute to $K^{(1)}$ and H in the Ising model. Therefore, the leading and subleading thermal exponents of the two-dimensional tricritical $q = 1$ Potts model simply follow as

$$y_{t1} = y_h^{(1)} = 15/8 \quad \text{and} \quad y_{t2} = y_t^{(1)} = 1. \quad (8.9)$$

The leading magnetic exponent of the two-dimensional tricritical $q = 1$ Potts model is $y_{h1} = 187/96$ [26].

8.2.2 Monte Carlo methods

The Hamiltonian for the q -state Potts model remains invariant under a global permutation of two of the q Potts states. Thus, one can apply the conventional Swendsen-Wang [28] and Wolff [29] cluster algorithms to simulate these models. However, for most tricritical models defined above (except for the tricritical $q = 1$ Potts model), these cluster algorithms are apparently not suitable or sufficient, since they do not operate on the vacancies. For unconstrained systems, a simple solution is to combine these conventional algorithms and the Metropolis method. However, the problem arises what sort of Monte Carlo algorithm is appropriate for constrained systems. In principle, one can apply a Kawasaki-like Monte Carlo method [30], which is particle-conserving. Unfortunately, this method suffers from serious critical-slowing-down, and thus simulations are restricted to small system sizes. This may be one of the reasons why the number of numerical investigations in this subject is rather limited.

In the present work, we make use of the so-called geometric cluster method [31–33], which is developed on the basis of spatial symmetries, such as invariance under the spatial inversion and rotation operations. This algorithm moves groups of spins/particles or vacancies over the lattice in accordance with the Boltzmann distribution, so that the total numbers of spins/particles and vacancies are conserved. It has been shown [31–33] for several models that the percolation threshold of the geometric clusters coincides with the phase transitions, so that critical-slowing-down is effectively suppressed.

Then, the constraint is fully realized by a combination of the Wolff and geometric cluster methods, of which the former flips between variables in different Potts states. A particular feature of such constrained simulations is that they *hardly* suffer from critical-slowing-down even near tricriticality.

8.2.3 Sampled quantities

Conventional quantities. During Monte Carlo simulations, we sampled several quantities, including the moments of the order parameter and the energy density etc. The magnetic susceptibility is then obtained from the fluctuations of the order parameter m as $\chi = L^2 \langle m^2 \rangle$. For the BC model (8.1), m is just the magnetization density; for Baxter’s hard-square lattice gas, m is the difference of the vacancy densities on the two sublattices of the square lattice, i.e., $m = \rho^{(1)} - \rho^{(2)}$; and for the tricritical $q = 3$ and 4-state Potts models, we define $m^2 = \frac{1}{2} \sum_{i \neq j} (\rho_i - \rho_j)^2$ where ρ_i is the density of the i th Potts state. An energy-like quantity e was sampled as nearest-neighbor correlations for the BC and the $q = 1, 3$, and 4-state Potts models with vacancies. For Baxter’s hard-square lattice gas, the nearest-neighbor sites cannot be occupied simultaneously, so that we sampled e as next-nearest-neighbor correlations. On this basis, a specific-heat-like quantity is defined as $C = L^2 (\langle e^2 \rangle - \langle e \rangle^2)$, which is proportional to the second derivative of the reduced energy with respect to the coupling constant K . Moreover, we sampled energy-energy correlations $g_e(r) = \langle e_0 e_r \rangle - \langle e \rangle^2$. For a lattice with linear system size L , the distance r was taken as the half diagonal distance, i.e., $r = \sqrt{2}L/2$. Since the vacancy density ρ also behaves energy-like, we define a compressibility-like quantity $P = L^2 (\langle \rho^2 \rangle - \langle \rho \rangle^2)$, which is expected to behave analogously as C .

In Monte Carlo studies of critical phenomena, the universal Binder ratio [34] plays a useful role. Thus, we sampled several dimensionless quantities as

$$Q_m = \frac{\langle m^2 \rangle^2}{\langle m^4 \rangle}, \quad Q_e = \frac{\langle (e - \bar{e})^2 \rangle^2}{\langle (e - \bar{e})^4 \rangle}, \quad \text{and} \quad Q_\rho = \frac{\langle (\rho - \bar{\rho})^2 \rangle^2}{\langle (\rho - \bar{\rho})^4 \rangle}, \quad (8.10)$$

where $\bar{e} = \langle e \rangle$ and $\bar{\rho} = \langle \rho \rangle$.

Structure factors. Apart from the singular behavior of physical observables, a second-order phase transition is generally accompanied by long-range correlations in time and space, and thus large-scale spatial fluctuations exist for the physical observables, such as the magnetization density m and the energy density e . It is thus justified to investigate the influence of the constraint on these spatial fluctuations. For this purpose, we define a set of quantities on the basis of spatial inhomogeneities of the magnetization, the energy, and the vacancy density. Consider the Fourier expansion of the order parameter $m(x, y)$ for a system of size L :

$$m_{k,l} = \frac{1}{L^2} \int_0^L dx dy m(x, y) \exp[2\pi i(xk + yl)/L]. \quad (8.11)$$

Obviously, $m_{0,0}$ is just the global magnetization density m , and the magnetic susceptibility is $\chi = L^2 \langle m^2 \rangle = L^2 \langle m_{0,0}^2 \rangle$; the number $m_{k,l}$ ($k \neq 0$ or $l \neq 0$) represents spatial inhomogeneity of $m(x, y)$. Since we are especially interested in fluctuations on the largest scales, we define a susceptibility-like quantity χ_s in terms of $m_{k,l}$ for the smallest wave numbers:

$$\chi_s = L^2 \langle m_{-1,0} \cdot m_{1,0} + m_{0,-1} \cdot m_{0,1} \rangle = L^2 \langle m_s^2 \rangle, \quad (8.12)$$

where, for later convenience, a quantity m_s has been introduced. We shall refer to χ_s as the structure factor of the susceptibility χ .

Analogously, we sampled the structure factor of the specific heat C as $C_s = L^2 \langle e_{-1,0} \cdot e_{1,0} + e_{0,-1} \cdot e_{0,1} \rangle = L^2 \langle e_s^2 \rangle$, and that of the compressibility P as $P_s = L^2 \langle \rho_{-1,0} \cdot \rho_{1,0} + \rho_{0,-1} \cdot \rho_{0,1} \rangle = L^2 \langle \rho_s^2 \rangle$, where $e_{k,l}$ and $\rho_{k,l}$ are obtained from Fourier expansions of the energy and the vacancy density, $e(x, y)$ and $\rho(x, y)$, respectively. On this basis, we sampled the following dimensionless ratios

$$Q_{sm} = \frac{\langle m_s^2 \rangle^2}{\langle m_s^4 \rangle}, \quad Q_{se} = \frac{\langle e_s^2 \rangle^2}{\langle e_s^4 \rangle}, \quad \text{and} \quad Q_{s\rho} = \frac{\langle \rho_s^2 \rangle^2}{\langle \rho_s^4 \rangle}. \quad (8.13)$$

The physical meaning of these structure factors can be gleaned from a comparison with the conventional quantities. For instance, both χ and χ_s represent fluctuation strengths of the order parameter m , and can be expressed in terms of a summation involving the magnetic correlation function, whose scaling behavior is described by the correlation function exponents η and ν . Thus, we expect that, in unconstrained systems, the structure factors, χ_s , C_s , and P_s , display the same scaling behavior as χ , C , and P , respectively. However, as we shall see, there are interesting differences in constrained systems.

8.3 Finite-size scaling behavior in constrained systems

A finite-size analysis of constrained phenomena precisely at tricriticality has recently been reported [14]. This analysis follows the basic idea of the Fisher renormalization mechanism, which has been formulated for *critical* systems [6]. In this section, we shall briefly review and moreover generalize the procedures in Ref. [14], such that we can also account for constrained scaling behavior due to deviations from the tricritical vacancy density.

As a first step, we express the finite-size scaling formula of the reduced free energy near tricriticality as

$$f(t_1, t_2, L) = L^{-d} f_s(L^{y_{t_1}} t_1, L^{y_{t_2}} t_2, 1) + f_a(t_1, t_2), \quad (8.14)$$

where t_1 and t_2 are the leading and subleading thermal fields, respectively. In the language of the BC model, t_1 and t_2 are analytic functions of the coupling constant K and the chemical potential D . The symbols f_s and f_a are the singular and analytical parts of the free energy, respectively. The expectation value of vacancy density $\langle \rho \rangle$ follows by differentiation as

$$\begin{aligned} -\langle \rho(t_1, t_2) \rangle = \frac{\partial f}{\partial D} &= a_1 L^{y_{t_1}-d} f_s^{(1,0)}(t_1 L^{y_{t_1}}, t_2 L^{y_{t_2}}) + a_2 L^{y_{t_2}-d} f_s^{(0,1)}(t_1 L^{y_{t_1}}, t_2 L^{y_{t_2}}) \\ &+ a_1 f_a^{(1,0)}(t_1, t_2) + a_2 f_a^{(0,1)}(t_1, t_2), \end{aligned} \quad (8.15)$$

where $a_1 = \partial t_1 / \partial D$ and $a_2 = \partial t_2 / \partial D$ are constants. The superscripts (i, j) represent i differentiations with respect to t_1 and j differentiations to t_2 . Linearization at the tricritical point yields

$$-\delta \rho = b_1 L^{2y_{t_1}-d} t_1 + b_2 L^{y_{t_1}+y_{t_2}-d} t_2 + b_3 t_1 + b_4 t_2 + \dots, \quad (8.16)$$

where b_1 , b_2 , b_3 , and b_4 are constants, and $\delta \rho = \langle \rho(t_1, t_2) \rangle - \langle \rho(0, 0) \rangle$ is the deviation of the vacancy density from its tricritical value. The constraint that the vacancy density is fixed at the tricritical value yields $\delta \rho = 0$ in Eq. (8.16). As a consequence, the thermal fields t_1 and t_2 are related, but in a way which still depends on which terms in the right-hand-side of Eq. (8.16) dominate. We consider the case of large L and then distinguish three cases:

1. for $2y_{t_1} - d > 0$ and $y_{t_1} + y_{t_2} - d > 0$, one has $L^{y_{t_1}} t_1 \propto L^{y_{t_2}} t_2$, i.e., $t_2 \gg t_1$ and $K - K_{tc} \simeq t_2$, so that the leading thermal exponent of the constrained systems is equal to the subleading exponent y_{t_2} ;
2. for $2y_{t_1} - d > 0$ but $y_{t_1} + y_{t_2} - d < 0$, one has $L^{y_{t_1}} t_1 \propto L^{d-y_{t_1}} t_2$. The leading thermal exponent is thus renormalized as $y_{t_1} \rightarrow d - y_{t_1}$. Again, we have $t_2 \gg t_1$ and $K - K_{tc} \simeq t_2$.
3. for $2y_{t_1} - d < 0$, i.e., the unconstrained specific heat does not diverge at tricriticality, t_1 is approximately proportional to t_2 , and no exponent renormalization occurs.

Therefore, for a tricritical system with a divergent specific heat ($2y_{t_1} - d > 0$), the leading thermal exponent y_{t_1} is renormalized to $d - y_{t_1}$ under the constraint, while the subleading one remains unchanged. Thus, the finite-size scaling relation for the difference of K to the tricritical point is $(K - K_t) \rightarrow (K - K_t)L^{d-y_{t_1}} + a_0(K - K_t)L^{y_{t_2}}$, with a_0 a constant.

Next, we consider the case that the fixed vacancy density ρ differs slightly from the tricritical value ρ_t , i.e., $\delta\rho = \rho - \rho_t \neq 0$ in Eq. (8.16). We first consider cases 1 and 2, i.e., $2y_{t_1} - d > 0$. We rewrite Eq. 8.16 as

$$L^{y_{t_1}} t_1 = -b_1^{-1}[(\delta\rho + b_4 t_2)L^{d-y_{t_1}} + b_2 t_2 L^{y_{t_2}} + \dots], \quad (8.17)$$

where we have omitted the term with amplitude b_3 which contributes a smaller power of L than the left-hand side. After substitution in Eq. (8.14), neglecting less relevant terms, we obtain

$$f(t_1, t_2, L) = L^{-d} f_s(-b_1^{-1} L^{d-y_{t_1}} (\delta\rho + b_4 t_2) - (b_2/b_1) L^{y_{t_2}} t_2, L^{y_{t_2}} t_2, 1) + f_a(0, t_2), \quad (8.18)$$

which can be written more simply as

$$f(t_1, t_2, L) = L^{-d} f'_s(L^{d-y_{t_1}} t'_1, L^{y_{t_2}} t_2) + f_a(0, t_2), \quad (8.19)$$

where $t'_1 \equiv \delta\rho + b_4 t_2$. This means that the deviation $(\rho - \rho_t)$ from the tricritical density combines with t_2 to act as a scaling field with a renormalization exponent $d - y_{t_1}$, i.e., the finite-size effect of this linear combination is multiplied by $L^{d-y_{t_1}}$.

In the constrained system, we wish to express the constrained free energy in K and ρ instead of t_2 and ρ . In cases 1 and 2, the constraint equation (8.16) shows that $t_1 \ll t_2$ for large L . Since t_1 and t_2 are written as linear combinations of K and D , we may write $K - K_t \simeq t_2$ apart from corrections with negative powers of L . Thus we have

$$t'_1 = \delta\rho + \alpha(K - K_t) \quad \text{and} \quad t_2 = K - K_t \quad (8.20)$$

Then, the scaling behavior of constrained quantities can be obtained from differentiations of Eq. (8.19) with respect to appropriate scaling fields.

For case 3, no exponent renormalization occurs and $\delta\rho$ approaches a linear combination of t_1 and t_2 , i.e., the distance $\rho - \rho_t$ behaves in leading order as the scaling fields t_1 and t_2 , independent of L .

The essential element of the above procedure is the solution of the constraint equation, $\delta\rho = \text{constant}$, in terms of a relation between K and D . In the parameter space (t_1, t_2) , this solution is sketched in Fig. 8.1. The path of the constrained system, the dashed line, is singular at tricriticality, and for the case $2y_{t_1} - d > 0$, renormalization of critical exponents occurs.

As mentioned earlier, in addition to uniform fluctuations, a second-order phase transition is also accompanied by inhomogeneous large-scale spatial fluctuations. Without the constraint, these two types of fluctuations display the same scaling behavior. However, their behavior becomes qualitatively different in constrained systems when the uniform fluctuations are sufficiently strongly suppressed by the constraint. A good test for such a difference is to compare the critical behavior of the structure factors χ_s , C_s , and P_s with χ , C , and P , respectively. According to Eq. (8.19), the exponents describing the behavior of C and P are modified as long as $2y_{t_1} - d > 0$. In contrast, since the constraint does not lead to a change of the universality class, one may expect that the leading finite-size scaling behavior of C_s and P_s remains unchanged at tricriticality. This will be confirmed by our numerical data later.

We conclude this section by pointing out the following implicit assumption. In the derivation of Eq. (8.16), we require that the expectation value $\langle \rho \rangle$ of the vacancy density is a constant; while, in fact, we should require

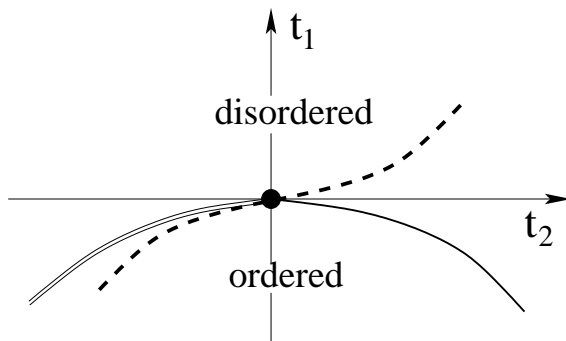


Figure 8.1: Illustration of the application of the Fisher renormalization mechanism to tricritical systems. The tricritical point (K_t, D_t) is denoted as the black circle, and the solid single and double lines represent the critical and the first-order-transition line, respectively. The variables t_1 and t_2 are the leading and subleading thermal fields at the tricritical point, respectively. The constraint that the vacancy density ρ is fixed at the tricritical value ρ_t is described by the dashed line, part of which coincides with the first-order transition line. As a consequence of the constraint, the scaling fields t_1 and t_2 are related, and this relation is singular at tricriticality.

that ρ itself is a constant. For $L \rightarrow \infty$, no difference exists between $\langle \rho \rangle$ and ρ . In a finite system, however, ρ need not be equal to $\langle \rho \rangle$, i.e., fluctuations of the vacancy density are allowed even if $\langle \rho \rangle$ is a constant. As mentioned earlier, the Monte Carlo simulations to be performed in this work conserve the number of vacancies, which leads to a ‘stronger’ constraint than $\langle \rho \rangle = \text{constant}$. Thus, the application of the Fisher renormalization mechanism in this paper used the assumption that suppressing the fluctuations of ρ about $\langle \rho \rangle$ does not lead to a qualitative change in the leading scaling behavior of the constrained system.

8.4 Results

8.4.1 Tricritical $q = 1$ Potts model

The tricritical $q = 1$ Potts model is particularly suitable to illustrate the Fisher renormalization mechanism for constrained tricritical phenomena. The equivalence of this model with the Ising model in a magnetic field, as mentioned in Sec. II, makes it possible to use the known properties of the latter model, and thus there is no obvious need for simulations. The energy density and the specific heat in the two models are related as

$$\langle e \rangle \propto \langle e^{(I)} \rangle + 2\langle m^{(I)} \rangle, \quad \text{and} \quad C \propto C^{(I)} + 4\chi^{(I)}, \quad (8.21)$$

where the superscript (I) is for the Ising model. Thus, the leading behavior of the Potts specific heat C is just that of the Ising magnetic susceptibility $\chi^{(I)}$. This illustrates the fact that the leading $q = 1$ Potts tricritical thermal exponent y_{t1} is equal to the magnetic exponent $y_h^{(I)}$ of the Ising model. However, the leading scaling behavior of $\langle e \rangle$ of the Potts model (8.6) is ‘accidentally’ governed by the exponent $y_t^{(I)}$, the subleading Potts thermal exponent y_{t2} . This is due to the symmetry between plus and minus Ising spins.

The dilute $q = 1$ Potts model with its vacancy density ρ fixed at $\rho_t = 1/2$, is equivalent with an Ising model with zero magnetization. Thus, the constrained susceptibility $\chi^{(I)}$ vanishes in Eq. (8.21), and the Potts and Ising specific heats, C and $C^{(I)}$, become identical. Further, the constraint on the Ising model is of the magnetic type, so that the scaling behavior of $C^{(I)}$ is not qualitatively influenced. Thus, one can conclude that, under the constraint, the Potts specific heat C is governed by the second thermal exponent y_{t2} , i.e., the Ising thermal exponent $y_t^{(I)} = 1$. This is as predicted in Sec. III for the case $2y_{t1} - d > 0$, $y_{t1} + y_{t2} - d > 0$.

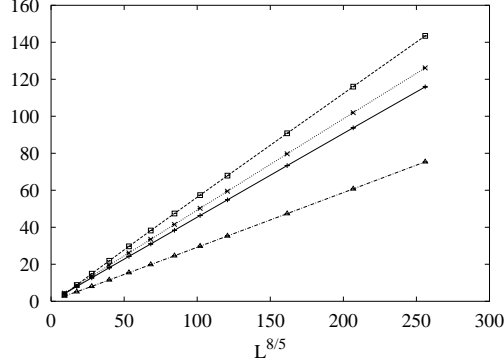


Figure 8.2: Specific-heat-like quantities in the unconstrained BC model at tricriticality vs. $L^{8/5}$. These quantities include $C/10$ (+), $2P$ (x), C_s (□), and $10P_s$ (Δ). The approximate linearity of the data illustrates that the leading behavior of these quantities is governed by the exponent $2y_{t1} - 2$, with $y_{t1} = 9/5$.

8.4.2 Tricritical Blume-Capel model

Unconstrained systems

For the unconstrained tricritical systems in the present paper, the nature of the critical behavior is now well established [20, 21]. The finite-size expression of the reduced free energy is given by Eq. (8.14), and the scaling behavior of the aforementioned conventional quantities is obtained by differentiating Eq. (8.14) with respect to appropriate scaling fields. These quantities include the energy density $\langle e \rangle$, the specific heat C , the magnetic susceptibility χ , and the energy-energy correlation function $g_e(r = L/\sqrt{2})$ etc. Precisely at tricriticality, one has

$$\begin{aligned}
 \langle e(L) \rangle &= e_0 + e_1 L^{y_{t1}-2} + e_2 L^{y_{t2}-2} + \dots, \\
 C(L) &= c_0 + c_1 L^{2y_{t1}-2} + c_2 L^{y_{t1}+y_{t2}-2} + c_3 L^{2y_{t2}-2} + \dots, \\
 P(L) &\propto C(L), \\
 \chi(L) &= \chi_0 + \chi_0 L^{2y_{h1}-4} + \dots, \quad \text{and} \\
 g_e(L) &= g_1 L^{2y_{t1}-4} + g_2 L^{y_{t1}+y_{t2}-4} + \dots.
 \end{aligned} \tag{8.22}$$

The constants, e_0 , c_0 , and χ_0 , arise from the analytic part of the free energy density. As discussed above, we expect that the structure factors, C_s , P_s , and χ_s , behave in a similar way as the physical quantities, C , P , and χ , respectively.

For a comparison with constrained phenomena investigated later, we simulated the tricritical BC model on the square lattice precisely at the tricritical point [24] $K_t = 1.6431759(1)$ and $D_t = 3.2301797(2)$. The Monte Carlo simulations used a combination of Metropolis and Wolff steps, which allows fluctuations of the magnetization as well as the density of the vacancies. Periodic boundary conditions were applied, and the system sizes were taken in the range $4 \leq L \leq 32$. The Monte Carlo data for C , P , C_s , and P_s are shown versus $L^{8/5}$ in Fig. 8.2. The approximate linearity of these data lines indicates that all these quantities are specific-heat-like; the scaling behavior is described by Eq. (8.22) with the exponent $y_{t1} = 9/5$. Further, we observed that $\chi \propto \chi_s \propto L^{2y_{h1}-2} = L^{37/20}$ (not shown). The data for the vacancy density ρ is shown versus $L^{y_{t1}-2} = L^{-1/5}$ in Fig. 8.3, where we include the $L \rightarrow \infty$ tricritical value $\rho_t = 0.4549506(2)$, taken from Ref. [24].

For the universal ratios defined in Sec. II, including Q_m , Q_e , Q_ρ , Q_{sm} , Q_{se} , and $Q_{s\rho}$, we fitted the data according to the least-squares criterion by

$$Q(L) = Q + b_1 L^{y_i} + b_2 L^{2y_i}, \tag{8.23}$$

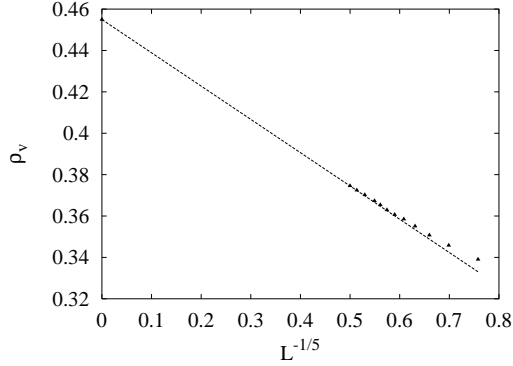


Figure 8.3: Vacancy density ρ of the unconstrained BC model at tricriticality vs. $L^{y_{t1}-2} = L^{-1/5}$.

Table 8.1: Fit results for the dimensionless quantities of the constrained (Constr.) and the unconstrained (Uncon.) Blume-Capel model.

Quant.	Q_m	Q_e	Q_ρ	Q_{sm}	Q_{se}	$Q_{s\rho}$
Uncon.	.6620(5)	.596(2)	.597(2)	.4349(5)	.4720(8)	.4705(8)
Constr.	.9821(1)	.3331(2)	–	.81222(5)	.84810(6)	.84804(6)

where the terms with amplitudes b_1 and b_2 account for corrections with the irrelevant scaling exponent $y_i = -1$ for the $q = 2$ Potts tricritical universality class in two dimensions [17,18,21,22]. The results, shown in Tab. 8.1, indicate that the universal asymptotic values of Q_e and Q_{se} are identical to those of Q_ρ and $Q_{s\rho}$, respectively. This is as expected, since both $\langle e \rangle$ and ρ are energy-like.

Constrained systems

Simulations of the constrained BC model used a combination of Wolff and geometric cluster steps, as discussed earlier. Periodic boundary conditions were used, and the system sizes were taken in the range $6 \leq L \leq 720$. For each system size, about 5×10^7 samples were taken.

Constrained behavior at the tricritical point. The tricritical point was taken from Ref. [24] as $K_t = 1.6431759(1)$, $\rho_t = 0.4549506(2)$. For a finite system L , however, the total number of the vacancies $V_t = L^2 \rho_t$ is generally not an integer. In that case, the actual simulations were performed at $V_- = [V_t]$ and $V_+ = [V_t + 1]$, where brackets $[\]$ denote the integer part. For a sampled quantity A , its tricritical value A_t is then obtained by a linear interpolation as $A_t = xA_+ + (1-x)A_-$, with $x = V_t - V_-$; the statistical error margin of A_t is estimated as $\delta A_t = \sqrt{(x\delta A_+)^2 + [(1-x)\delta A_-]^2}$. The data for the constrained specific heat C and the energy density $\langle e \rangle$ are shown in Figs. 8.4 and 8.5. In comparison with Figs. 8.2 and 8.3, these figures indicate that the scaling behavior of C and $\langle e \rangle$ is indeed modified by the constraint. In particular, the constrained specific heat C reaches only a finite value instead of being divergent for $L \rightarrow \infty$. The exponents used for the horizontal axes in Figs. 8.4 and 8.5 are those predicted in Sec. III. For the tricritical BC model in two dimensions, the Fisher mechanism predicts that the leading thermal singularity in constrained system is determined by the subleading exponent y_{t2} , because the renormalized exponent $2 - y_{t1} = 1/5$ is smaller than $y_{t2} = 4/5$. Thus, one obtains the leading finite-size behavior $\langle e \rangle \propto L^{y_{t2}-2} = L^{-6/5}$ and $C \propto L^{2y_{t2}-2} = L^{-2/5}$, in agreement with Figs. 8.4 and 8.5, respectively. By differentiating Eq. (8.19) with respect to the thermal fields τ_1 and τ_2 , the finite-size dependence of C and $\langle e \rangle$ follows as

$$\begin{aligned}
 C &= c_0 + a_1 L^{2y_{t2}-2} + a_2 L^{y_{t2}-y_{t1}} + a_3 L^{2-2y_{t1}} + \dots, \\
 \langle e \rangle &= e_0 + b_1 L^{y_{t2}-2} + b_2 L^{-y_{t1}} + \dots,
 \end{aligned}
 \tag{8.24}$$

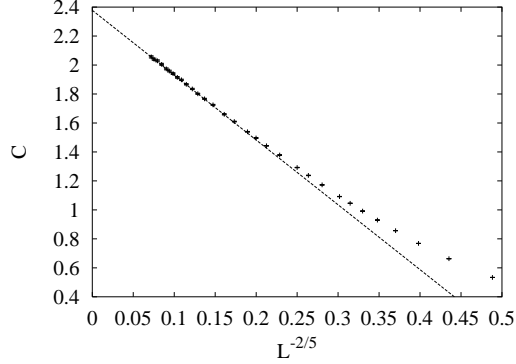


Figure 8.4: Specific heat C of the constrained BC model at tricriticality vs. $L^{2y_{t2}-2} = L^{-2/5}$.

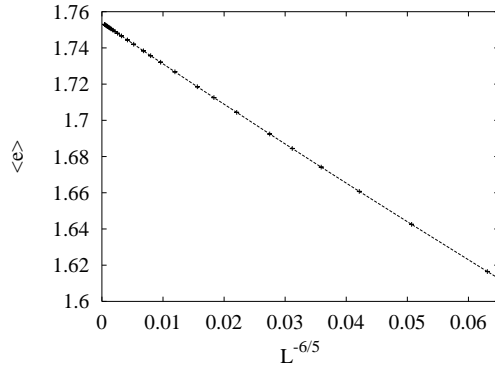


Figure 8.5: Energy density $\langle e \rangle$ of the constrained BC model at tricriticality vs. $L^{y_{t2}-2} = L^{-6/5}$.

where the constants c_0 and e_0 are equal to those in Eq. (8.22). The $\langle e \rangle$ and C data were fitted by Eq. (8.24), with y_{t1} fixed at $9/5$. In order to obtain a satisfactory fit, the data for small system sizes $L \leq 8$ were discarded. We obtain $y_{t2} = 0.798(4)$ and $0.803(4)$ from the fit of C and $\langle e \rangle$, respectively. These results are in good agreement with the exact value $y_{t2} = 4/5$.

The $g_e(r)$ data for $r = \sqrt{2}L/2$ at tricriticality are shown in Fig. 8.6. The approximate linearity indicates that the scaling behavior of g_e is still governed by the leading thermal exponent y_{t1} , i.e., $g_e \propto L^{2y_{t1}-4} = L^{-2/5}$ as described by Eq. (8.22). This confirms that, as expected, the power law describing the spatial correlations is not affected by the constraint, although the amplitude become negative. For an illustration of the influence of the constraint on inhomogeneous fluctuations, we sampled the structure factors C_s and P_s , which display the same scaling behavior as C and P in the unconstrained systems, as shown in Fig. (8.2). The constrained data for C_s and P_s are shown in Fig. 8.7. In contrast to the conventional quantities C and P , the leading behavior of the tricritical structure factors C_s and P_s *remains the same* as in the unconstrained systems. The numerical data were fitted by Eq. (8.22) with the exponent y_{t2} fixed at $4/5$. After a cutoff for small systems sizes $L \leq 8$, we obtain $y_{t1} = 1.799(2)$ and $1.798(2)$ from the fits for C_s and P_s , respectively. These results are in good agreement with the exact value $y_{t1} = 9/5$.

As an illustration of the influence that the energy-like constraint has on magnetic quantities, we sampled the quantities χ and χ_s . The data are shown in Fig. 8.8, where the exponent $37/20$ used for the horizontal scale is equal to $2y_{h1} - 2$ with $y_{h1} = 77/40$ [20–22]. Thus, the constraint does not change the leading scaling behavior of magnetic quantities. This is apparently related to the fact that the chemical potential D , the conjugate parameter of the vacancy density ρ , is not directly coupled to the magnetic field.

The data for the universal ratios, including Q_m , Q_e , Q_ρ , Q_{sm} , Q_{se} , and $Q_{s\rho}$, were also fitted by Eq. (8.23).

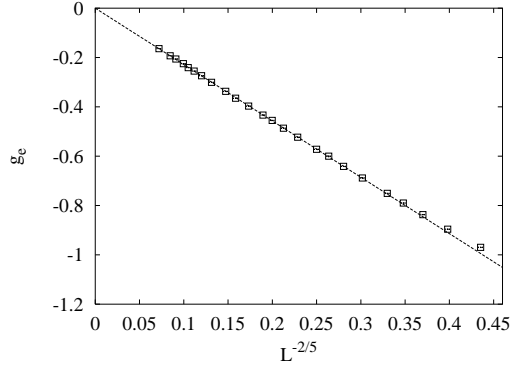


Figure 8.6: Energy-energy correlations $g_e(r)$ of the constrained BC model at tricriticality vs. $L^{2y_{t1}-4} = L^{-2/5}$. The distance r was taken as $L/\sqrt{2}$, the half diagonal system size.

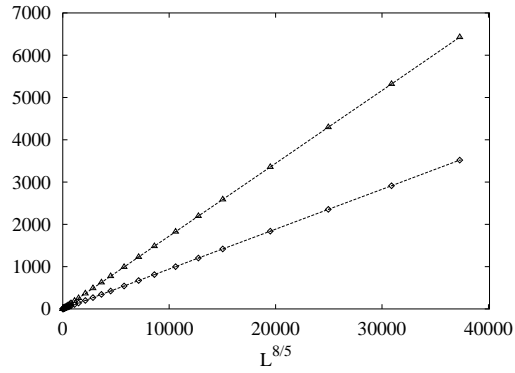


Figure 8.7: Structure factors, $C_s/10$ (Δ) and P_s (\diamond), of the constrained BC model at tricriticality vs. $L^{2y_{t1}-2} = L^{8/5}$.

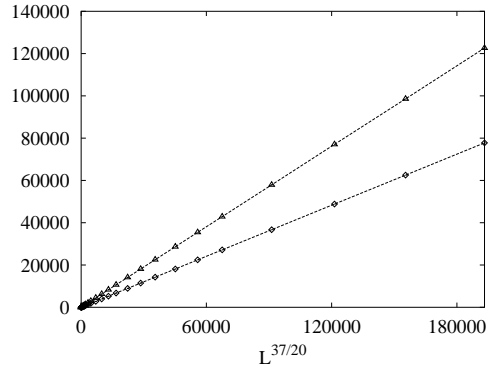


Figure 8.8: Susceptibility-like quantities, χ (\square) and $\chi_s \times 10$ (Δ), of the constrained BC model at tricriticality vs. $L^{2y_{h1}-2} = L^{37/20}$.

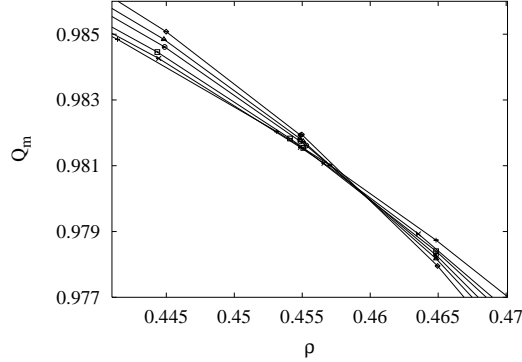


Figure 8.9: Dimensionless ratio Q_m of the constrained BC model with $K = K_t$ vs. vacancy density ρ . The system sizes are $L = 16$ (+), 24 (\times), 32 (\square), 48 (\circ), 64 (\triangle), and 96 (\diamond). The small finite-size dependence of the slopes of these curves indicates that the critical exponent governing the scaling behavior of Q_m as a function of $\rho - \rho_t$ is much smaller than 1.

We assume that, under the constraint, finite-size corrections still mainly arise from the irrelevant field. After a cutoff for small system sizes $L \leq 10$, satisfactory fits can be obtained. The results are shown in Tab. 8.1, where the quoted error margins are two statistical standard deviations. Thus, although the dimensionless ratios are universal, they assume different values in unconstrained and constrained systems. The reason is that these ratios depend on the spatial profile of correlation functions. Here the constraint plays a similar role as the boundary conditions and the aspect ratios, etc. A particular feature in Tab. 8.1 is that the constrained ratio $Q_e = 0.3331(2) \approx 1/3$. This indicates that the fluctuations of the energy density resemble the normal (Gaussian) distribution. As reflected by the fact that the specific heat C remains finite in constrained systems, this is because singularities of energy-related quantities are strongly suppressed so that the ‘background’ (the analytical part of the free energy) plays an enhanced role.

Constrained behavior near the tricritical point. In addition to the tricritical point, the Fisher renormalization mechanism also predicts the scaling behavior as a function of the distances $K - K_t$ and $\rho - \rho_t$. In this case, the dimensionless ratios serve a good choice for such investigations. The Q_m data at $K = K_t$ are partly shown in Fig. 8.9 as a function the vacancy density. They indicate that the exponent y_ρ of the deviation of the vacancy density $\rho - \rho_t$ is much smaller than one, i.e., $y_\rho \ll 1$, in agreement with the prediction by Eq. (8.19). The Q_m data were fitted by

$$Q_m(\rho, L) = Q_m + \sum_{k=1}^4 a_k (\rho - \rho_t)^k L^{k(2-y_{t1})} + b_1 L^{y_i} + b_2 L^{2y_i} + c_1 (\rho - \rho_t) L^{2-y_{t1}+y_i} + c_2 (\rho - \rho_t)^2 L^{2-y_{t1}} + \dots, \quad (8.25)$$

where the term with c_1 describes the ‘mixed’ effect of the leading irrelevant field and the scaling field τ_1 in Eq. (8.19). The term with c_2 arises from the nonlinear dependence of τ_1 on the distance $\rho - \rho_t$. The irrelevant exponent was fixed at $y_i = -1$. Discarding the data for for small system sizes $L \leq 12$, we obtain $y_{t1} = 1.796(5)$, in agreement with the exact value $y_{t1} = 9/5$.

As shown earlier, precisely at the tricritical point, the leading scaling behavior of the structure factors is not renormalized under the constraint. However, we argue here that the constrained scaling behavior of these quantities as a function of the distance to the tricritical point is still governed by Eq. (8.19). Thus, the leading finite-size scaling of $C(\rho, K, L)$ and $C_s(\rho, K, L)$ can be expressed as

$$\begin{aligned} C(\tau_1, \tau_2, L) &= c(\tau_1, \tau_2) + L^{2y_{t2}-2} C(\tau_1 L^{2-y_{t1}}, \tau_2 L^{y_{t2}}), \\ C_s(\tau_1, \tau_2, L) &= c_a(\tau_1, \tau_2) + L^{2y_{t1}-2} C_s(\tau_1 L^{2-y_{t1}}, \tau_2 L^{y_{t2}}), \end{aligned} \quad (8.26)$$

where $\tau_1 = (\rho - \rho_t) + a(K - K_t)$ and $\tau_2 = (K - K_t)$ act as scaling fields. The terms $c(\tau_1, \tau_2)$ and $c_a(\tau_1, \tau_2)$ arise

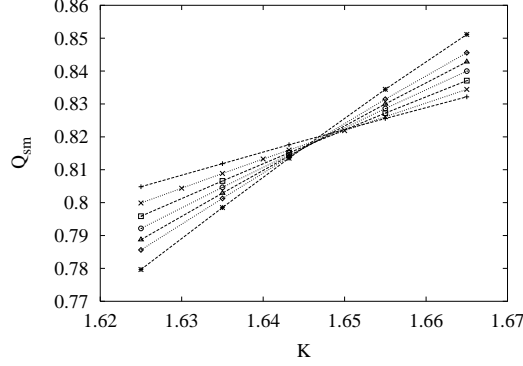


Figure 8.10: Dimensionless ratio Q_{sm} of the constrained tricritical BC model at a fixed tricritical vacancy density $\rho = \rho_t$ vs. coupling constant K . The data points $+$, \times , \square , \circ , \triangle , \diamond , and $*$ represent $L = 24, 32, 40, 48, 56, 64,$ and 80 , respectively.

from the analytical background. For the case $K = K_t$, Taylor expansions of Eq. (8.26) yield the behavior of $C_s(\rho, L)$ as

$$C_s(\rho, L) = c_{a0} + c_{a1}(\rho - \rho_t) + c_{a2}(\rho - \rho_t)^2 + L^{2y_{t1}-2}[d_0 + \sum_k a_k(\rho - \rho_t)^k L^{k(2-y_{t1})} + b_1 L^{y_i} + b_2 L^{2y_i}]. \quad (8.27)$$

We fitted C_s data for $K = K_t$ by Eq. (8.27). After a cutoff for small system sizes $L \leq 10$, we obtain the leading thermal exponent $y_{t1} = 1.793(8) \approx 9/5$.

For an infinite system with the coupling constant $K = K_t$, the specific-heat-like quantities C and C_s behave as $C \propto (\rho - \rho_t)^{-\alpha_\rho}$ and $C_s \propto (\rho - \rho_t)^{-\alpha_{s\rho}}$, respectively. The exponents α_ρ and $\alpha_{s\rho}$ can be obtained by regarding L as a scaling factor, which satisfies $(\rho - \rho_t)L^{2-y_{t1}} = 1$. From Eq. (8.26), one simply has $\alpha_\rho = (2y_{t2} - d)/(d - y_{t1}) = -2$ and $\alpha_{s\rho} = (2y_{t1} - d)/(d - y_{t1}) = 8$. Similarly, for the case $\rho = \rho_t$, the specific heat C and the structure factor C_s behave $C \propto (K - K_t)^{-\alpha}$ and $C_s \propto (K - K_t)^{-\alpha_s}$ in an infinite system, respectively. Following the same procedure, one can obtain $\alpha = (2y_{t2} - d)/y_{t2} = -1$ and $\alpha_s = (2y_{t1} - d)/y_{t2} = 2$.

As an illustration of the renormalization exponents due to the difference of K to the tricritical point, the Q_{sm} data for $\rho = \rho_t$ are partly shown in Fig. 8.10 as a function of K . We fitted these Q_{sm} data by

$$Q_{sm}(K, L) = Q_{sm} + \sum_{k=1}^4 a_{1k}(K - K_t)^k L^{ky_{t2}} + b_1 L^{y_i} + b_2 L^{2y_i} + c_1(K - K_t)L^{y_{t2}+y_i} + c_2(K - K_t)^2 L^{y_{t2}} + \dots \quad (8.28)$$

The exponent y_i were fixed at -1 , and the data for small system sizes $L \leq 10$ were discarded. We obtain $y_{t2} = 0.806(7)$, in agreement with the exact value $y_{t2} = 4/5$.

8.4.3 Baxter's hard-square model

Within the same universality class of the tricritical BC model, we also investigate Baxter's hard-square lattice gas [17,18], which is described by Eq. (8.4). Constrained simulations used the geometric cluster algorithm only, and took place at the exactly known tricritical point $J_t = \ln(3 + \sqrt{5})$ and $\rho_t = (5 + \sqrt{5})/10$. We used periodic boundary conditions and 24 system sizes in the range $4 \leq L \leq 360$. Again, the actual simulations were performed for two integer numbers of vacancies, and the tricritical quantities are obtained by a linear interpolation. This model serves an independent test for the constrained behavior discussed in the above subsection. We observe that, as expected, the constrained tricritical phenomena of this lattice gas

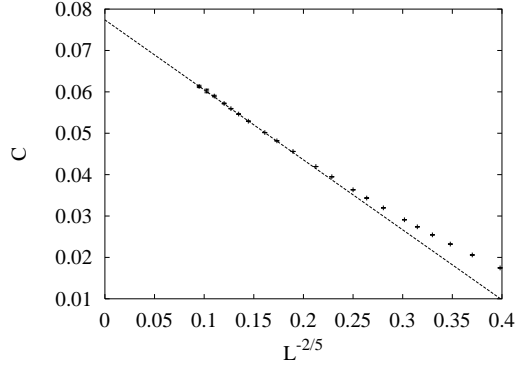


Figure 8.11: Constrained specific heat C of Baxter's hard-square lattice gas at tricriticality vs. $L^{2y_{t2}-2} = L^{-2/5}$.

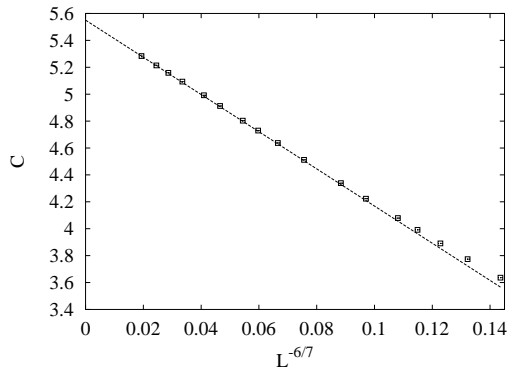


Figure 8.12: Constrained specific heat C of the $q = 3$ Potts model at tricriticality vs. $L^{2y_{t2}-2} = L^{-6/7}$.

and of the BC model are very similar. For instance, the constrained tricritical specific heat of the lattice gas also reaches a finite value as $L^{-2/5}$, illustrated in Fig. (8.11). For this reason, we do not give a detailed account of the numerical results.

8.4.4 Tricritical $q = 3$ Potts model

Using a combination of Metropolis, Wolff, and geometric cluster steps, we first simulated the unconstrained $q = 3$ Potts model with vacancies at the tricritical point [24] $K_t = 1.649913(5)$ and $D_t = 3.15217(1)$. The system sizes were taken in the range $6 \leq L \leq 32$, and the specific heat C and the energy density $\langle e \rangle$ were sampled. As expected, we found that these data are well fitted by Eq. (8.22), with the exact thermal exponents $y_{t1} = 12/7$ and $y_{t2} = 4/7$.

Next, we performed constrained simulations at tricriticality using the determined tricritical vacancy density [24] $\rho_t = 0.34572(5)$. The system sizes were chosen as 20 values in the range $6 \leq L \leq 280$. The Monte Carlo data for C and $\langle e \rangle$ are shown in Figs. 8.12 and 8.13, respectively. Again, the tricritical specific heat C is suppressed and remains finite under the constraint. These figures confirm that the leading behavior of C and $\langle e \rangle$ is governed by the exponents $2 - 2y_{t1}$ and $-y_{t1}$, respectively, as predicted by Eq. (8.24). For a quantitative confirmation, the C data were fitted by Eq. (8.24). First, we fixed y_{t1} at $12/7$ [20–22]. After discarding the data for small system sizes $L \leq 10$, we obtain $y_{t2} = 0.572(3) \approx 4/7$. Next, we fixed y_{t2} at $4/7$ and obtain $y_{t1} = 1.714(2) \approx 12/7$.

The scaling behavior of magnetic quantities and the structure factors also remains unchanged under the constraint, as expected. As an illustration, the C_s data are shown in Fig. 8.14, indicating that at tricriticality

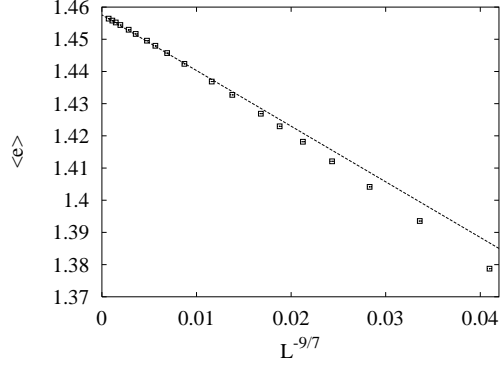


Figure 8.13: Energy density $\langle e \rangle$ of the constrained $q = 3$ Potts model at tricriticality vs. $L^{y_{t2}-2} = L^{-9/7}$.

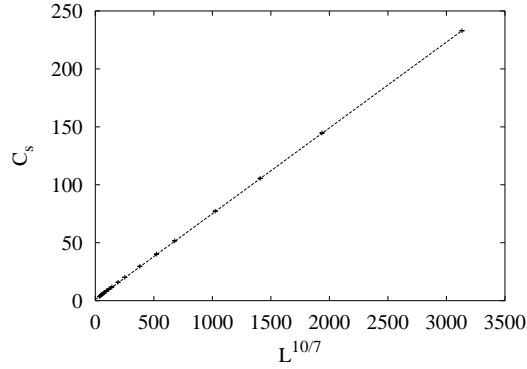


Figure 8.14: Structure factor of the specific heat C_s of the constrained $q = 3$ Potts model at tricriticality vs. $L^{2y_{t1}-2} = L^{10/7}$.

C_s diverges indeed as $L^{2y_{t1}-2} = L^{10/7}$.

8.4.5 Dilute $q = 4$ Potts model

The $q = 4$ Potts model is a marginal case of the tricritical Potts model in the sense that the critical and the tricritical branch merge at $q = 4$; accordingly, the subleading thermal exponent vanishes, i.e., $y_{t2} = 0$ [19]. In this case, we expect that the leading thermal exponent in constrained systems is equal to $2 - y_{t1} = 1/2$. This corresponds with case 2 in Sec. III. Constrained simulations were performed at the ‘fixed’ point, i.e., [24] $K_t = 1.45790(1)$ and $\rho_t = 0.21207(2)$, where logarithmic corrections due to the marginal field associated with y_{t2} are absent. The system sizes took 20 values in the range $12 \leq L \leq 280$. The C_s data are plotted in Fig. 8.15. They show no indication that the constraint introduces slowly-convergent finite-size corrections. According to Eq. (8.24), the C and $\langle e \rangle$ data are plotted versus $1/L$ and $L^{-3/2}$ in Fig. 8.16 and 8.17, respectively. In contrast to the tricritical systems discussed above, the leading terms in Eq. (8.24) are insufficient even to approximately describe these numerical data. Remarkably, the energy density $\langle e \rangle$ has a maximum when the system size L increases. The data were fitted by

$$\langle e \rangle = e_0 + e_1 L^{-3/2} + e_2 L^{-2} + e_3 L^{-5/2}, \quad (8.29)$$

where the exponents were fixed as $-3/2 = -y_{t1}$, $-2 = y_{t2} - 2$, and $-5/2 = -y_{t1} - 1$. After discarding the data for small system sizes $L \leq 12$, the fit yields $e_0 = 1.329377(4)$, $e_1 = 1.53(2)$, $e_2 = -11.0(2)$, and $e_3 = 12.2(4)$, where we quote error margins of two standard deviations. The constants e_1 and e_2 have

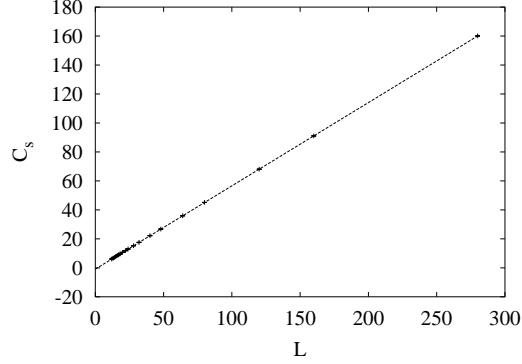


Figure 8.15: Structure factor of the specific heat C_s of the constrained dilute $q = 4$ Potts model at the 'fixed' point vs. $L^{2y_{t1}-2} = L$.

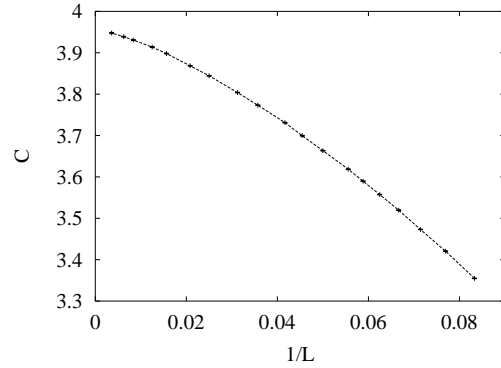


Figure 8.16: Specific heat C of the constrained dilute $q = 4$ Potts model at the fixed point vs. $L^{2-2y_{t1}} = 1/L$.

opposite signs. Similarly, we fitted the C data by

$$C = c_0 + c_1 L^{-1} + c_2 L^{-3/2} . \quad (8.30)$$

and obtain $c_0 = 3.960(4)$, $c_1 = -2.1(4)$, and $c_2 = -23(1)$. The amplitude c_1 is relatively small in comparison with c_2 , which explains the strong nonlinearity in Fig. 8.16.

8.5 Discussion

The geometric cluster method serves well for a detailed investigation of the finite-size scaling behavior of constrained tricritical systems. For the $q = 4$ Potts model with vacancies and the other systems, the constrained data can be explained by the second and the first case of the Fisher renormalization described in Sec. III, respectively. For clarity, a comparison of the unconstrained and constrained tricritical scaling behavior of several quantities is listed in Tab. 8.2. These include the energy density $\langle e \rangle$, the specific heat C , the structure factor C_s , and the magnetic susceptibility χ . These data illustrate that the scaling behavior of conventional energy-like quantities is significantly modified under the constraint, while that of magnetic quantities and structure factors remains unchanged. Generally speaking, the agreement between the numerical results and the theory is *quantitatively* satisfactory.

During the derivations of the scaling formulas in Sec. III, the Fisher renormalization mechanism makes essential use of the universal renormalization exponents in the unconstrained free energy density as described

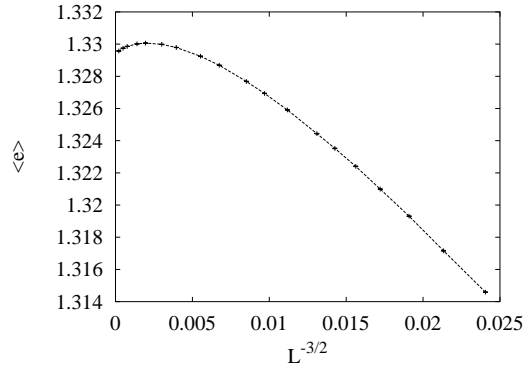


Figure 8.17: Energy density $\langle e \rangle$ of the constrained dilute $q = 4$ Potts model at tricriticality vs. $L^{-y_{t1}} = L^{-3/2}$.

Table 8.2: Leading finite-size scaling behavior of $\langle e \rangle$, C , and C_s of unconstrained (un) and constrained (co) tricritical systems, including dilute $q = 1, 3$, and 4-state Potts models, the Blume-Capel (BC) model, and Baxter's hard-square (HS) model.

Model	$q = 1$	BC	HS	$q = 3$	$q = 4$
$\langle e \rangle^{\text{un}}$	L^{-1}	$L^{-1/5}$	$L^{-1/5}$	$L^{-2/7}$	$L^{-1/2}$
$\langle e \rangle^{\text{co}}$	L^{-1}	$L^{-6/5}$	$L^{-6/5}$	$L^{-9/7}$	$L^{-3/2}$
C^{un}	$L^{7/4}$	$L^{6/5}$	$L^{6/5}$	$L^{10/7}$	L
C^{co}	$\ln L$	$L^{-2/5}$	$L^{-2/5}$	$L^{-6/7}$	L^{-1}
C_s^{un}	$L^{7/4}$	$L^{6/5}$	$L^{6/5}$	$L^{10/7}$	L
C_s^{co}	$L^{7/4}$	$L^{6/5}$	$L^{6/5}$	$L^{10/7}$	L
χ^{un}	$L^{91/48}$	$L^{77/10}$	$L^{77/40}$	$L^{38/21}$	$L^{7/4}$
χ^{co}	$L^{91/48}$	$L^{77/10}$	$L^{77/40}$	$L^{38/21}$	$L^{7/4}$

by Eq. (8.14). This simply means that the present annealed type of constraint does not modify the universality class, and thus the critical exponents in the constrained and unconstrained systems are directly related. We further demonstrate this point by investigating the scaling behavior of the structure factors C_s and P_s , which remains unchanged under the constraint. Therefore, on the basis of the summary in the above paragraph, we conclude that the Fisher renormalization mechanism straightforwardly and completely describes the essential physics of the constrained scaling behavior. It then seems that there is no apparent need to apply other theories. Nevertheless, in this context, we mention Imry's theory [11, 12, 36] for constrained critical phenomena, which is more general and includes the Fisher renormalization mechanism [6] as a special case. This theory has been applied to the Baker-Essam model [35], a compressible Ising model, where a 'special' tricritical point was reported. Such a point, where no renormalization of critical exponents occurs even for systems with $\alpha > 0$, has not been observed in the present investigation. For the experimental data [2] at the λ transition in the ^3He - ^4He mixtures, both the Fisher approach and the renormalization group (RG) calculations of Imry and coworkers [13] can be employed. This has been further confirmed [14] by the Monte Carlo simulations of the tricritical Blume-Capel model in three dimensions. Although the RG calculations [13, 36] can be regarded to correspond with the second case of the Fisher renormalization mechanism, as described in Sec. III, the connection of these two theories is not always obvious. Thus, it seems justified to ask the following questions: 1) in addition to the Baker-Essam model [35], can one further test the theoretical predictions in Refs. [11, 12] in other systems? In particular, can one observe the aforementioned 'special' tricritical point? 2) how are the RG calculations [13] related to the Fisher renormalization mechanism? 3) how can the effect of the subleading thermal field be included in the RG calculations [13]?

Although the mean-field theory is 'unrealistic' in general, it can yield an intuitive physical picture of a phase transition. Moreover, for a sufficiently high spatial dimensionality, the mean-field theory can correctly predict universal parameters. Therefore, we investigated [14] the influence of the constraint on the mean-field version of the Blume-Capel (BC) model. Just as in finite spatial dimensions, the mean-field BC model has a line of second and first-order transitions and a tricritical point. However, under the constraint, it can be shown that the whole transition line reduces to mean-field *critical* Ising-like.

Finally, we remark that, in our application of the Fisher renormalization mechanism, *only* the leading terms are kept, as mentioned in Sec. III. It is obvious that including subleading terms leads to additional finite-size corrections besides those arising from the irrelevant scaling fields.

Bibliography

- [1] I.D. Lawrie and S. Sarbach, *Phase Transitions and Critical Phenomena*, edited by C. Domb and J.L. Lebowitz. (Academic Press, London, 1984), Vol. 9, p 1.
- [2] Y. Achiam and Y. Imry, J. Phys. C **10**, 39 (1977).
- [3] R.B. Stinchcombe, *Phase Transitions and Critical Phenomena*, edited by C. Domb and J.L. Lebowitz. (Academic Press, London, 1984), Vol. 7, p 152, and references therein.
- [4] I. Syozi, Prog. Theor. Phys. **34**, 189 (1965); I. Syozi and S. Miyazima, Prog. Theor. Phys. **36**, 1083 (1966).
- [5] J.W. Essam and H. Garelick, Proc. Phys. Soc. **92**, 136 (1967).
- [6] M.E. Fisher, Phys. Rev. **176**, 257 (1968).
- [7] Y.N. Skryabin and A.V. Shchanov, Phys. Lett. A **234**, 147 (1997).
- [8] M. Krech, e-print, cond-mat/9903288 (1999).
- [9] I.M. Mryglod and R. Folk, Physica A **294**, 351 (2000).
- [10] I.M. Mryglod, I.P. Omelyan, and R. Folk, Phys. Rev. Lett. **86**, 3156 (2001).

- [11] L. Gunther, D.J. Bergman, and Y. Imry, Phys. Rev. Lett. **27**, 558 (1971); Y. Imry, O. Entin-Wohlman, and D.J. Bergman, J. Phys. C **6**, 2846 (1973).
- [12] O. Entin-Wohlman, D.J. Bergman, and Y. Imry, J. Phys. C **7**, 496 (1974).
- [13] Y. Imry, Phys. Rev. Lett. **33**, 1304, (1974); J. Rudnick, D.J. Bergman and Y. Imry, Phys. Lett. A **46**, 448, (1974); Y. Achiam and Y. Imry, Phys. Rev. B **12**, 2768, (1975).
- [14] Y. Deng and H.W.J. Blöte, unpublished.
- [15] M. Blume, Phys. Rev. **141**, 517 (1966).
- [16] H.W. Capel, Physica A **32**, 966 (1966); Phys. Lett. **23**, 327 (1966).
- [17] R.J. Baxter, J. Phys. A **13**, L61 (1980); J. Stat. Phys. **26**, 427 (1981).
- [18] D.A Huse, Phys. Rev. Lett. **49**, 1121 (1982); R.J. Baxter and P.A. Pearce, J. Phys. A **16**, 2239 (1983).
- [19] see e.g., F.Y. Wu, Rev. Mod. Phys. **54**, 235 (1982).
- [20] B. Nienhuis, A.N. Berker, E.K. Riedel, and M. Schick, Phys. Rev. Lett. **43**, 737 (1979).
- [21] B. Nienhuis, *Phase Transitions and Critical Phenomena*, edited by C. Domb and J.L. Lebowitz. (Academic Press, London, 1987), Vol. 11, p 1, and references therein.
- [22] J.L. Cardy, *Phase Transitions and Critical Phenomena*, edited by C. Domb and J.L. Lebowitz. (Academic Press, London, 1987), Vol. 11, p. 55, and references therein.
- [23] D. Friedan, Z. Qiu, and S. Shenker, Phys. Rev. Lett. **52**, 1575 (1984).
- [24] X.F. Qian, Y. Deng, and H.W.J. Blöte, unpublished.
- [25] P.D. Beale, Phys. Rev. B **33**, 1717 (1986).
- [26] B. Nienhuis, J. Phys. A **15**, 199 (1982).
- [27] see e.g., D. Stauffer and A. Aharony, *Introduction to Percolation Theory* (Taylor & Francis, Philadelphia, 1994).
- [28] R.H. Swendsen and J.S. Wang, Phys. Rev. Lett. **62**, 163 (1989).
- [29] U. Wolff, Phys. Rev. Lett. **62**, 361 (1989).
- [30] K. Kawasaki, *Phase Transitions and Critical Phenomena*, edited by C. Domb and M.S. Green. (Academic Press, N.Y., 1972), Vol. 2, p. 443.
- [31] J.R. Heringa and H.W.J. Blöte, Physica A **232**, 369 (1996).
- [32] H.W.J. Blöte, E. Luijten, and J.R. Heringa, J. Phys. A **28**, 6289 (1995).
- [33] J.R. Heringa and H.W.J. Blöte, Phys. Rev. E **57**, 4976 (1998).
- [34] K. Binder, Z. Phys. B: Condens. Matter **43**, 119 (1981).
- [35] G.A. Baker and J.W. Essam, Phys. Rev. Lett. **24**, 447 (1969).
- [36] Y. Imry, private communications (2003).
- [37] Pleimling and Hull JSP 104 971 (2001).
- [38] Kaster JSP 109 133 (2002).

Monte Carlo study of backbone exponents

By means of Monte Carlo simulations and finite-size analyses, we determine the backbone exponent of several q -state Potts model in two and three dimensions.

9.1 The q -state Potts model in two dimensions

We determine the backbone exponent X_b of several critical and tricritical q -state Potts models in two dimensions. The critical systems include the bond percolation, the Ising, the $q = 2 - \sqrt{3}$, 3, and 4-state Potts, and the Baxter-Wu model, and the tricritical ones include the $q = 1$ Potts model and the Blume-Capel model. For this purpose, we formulate several efficient Monte Carlo method and sample the probability P_2 of a pair of points connected via at least two independent paths. Finite-size-scaling analysis of P_2 yields X_b as 0.3566(2), 0.2696(3), 0.2105(3), and 0.127(4) for the critical $q = 2 - \sqrt{3}$, 1, 2, 3, and 4-state Potts model, respectively. At tricriticality, we obtain $X_b = 0.0520(3)$ and 0.0753(6) for the $q = 1$ and 2 Potts model, respectively. For the critical $q \rightarrow 0$ Potts model it is derived that $X_b = 3/4$. From a scaling argument, we find that, at tricriticality, X_b reduces to the magnetic exponent, as confirmed by the numerical results.

9.1.1 Introduction

The integer q -state Potts model [1] is an extension of the Ising model, and has been a subject of intense research interest for decades. It can be generalized to the random-cluster model of all $q \geq 0$ [4]. For a review see [5]. This model has been shown to be very rich in its behavior. In two dimensions, the nature of the critical singularities is now well established. In the study of critical phenomena, the Potts model has become an important testing ground for various methods and approaches.

However, there is still a number of critical exponents, of which the exact values have not been obtained. These exponents characterize geometric properties of the critical Potts models, and seem to have no analogue in the thermodynamics. Among them there are fractal dimensions of ‘backbones’ [7] and of ‘chemical’ paths [18].

Here, we shall briefly review definitions of these quantities, in the language of the percolation model [3], a special case of the Potts model for $q \rightarrow 1$. Consider a bond percolation model on the square lattice; each edge of the lattice is occupied by a ‘conducting’ bond with probability p , or is ‘empty’ with probability $1 - p$. At the critical point $p_c = 1/2$ [3], a percolating cluster, which consists of sites connected via these conducting bonds, will grow arbitrarily large. Suppose one has a percolating cluster, which contains two sites S_1 and S_2 separated by a distance r . The backbone [7] is then defined as the set of sites from which conducting paths exist both to S_1 and S_2 , such that both paths have no bonds in common, i.e., the paths are mutually independent. Thus, if a potential difference is applied to S_1 and S_2 , the backbone consists exactly of those sites through which current would flow, apart from the so-called ‘Wheatstone bridges’. At criticality, the total number of sites or bonds in the backbone scales as $N_b \propto r^{d-X_b}$, where $d = 2$ and X_b are the spatial

and the backbone scaling dimension, respectively. The chemical path [18] is defined as the shortest path between S_1 and S_2 . Its average length at criticality behaves as $l \propto r^{d-X_{\min}}$, with X_{\min} the corresponding scaling dimension. Another exponent of interest is related to the so-called ‘red’ bonds. Suppose a bond in the percolating cluster carries all the current and thus becomes ‘hot’ after some time, then this bond is named a red bond [7, 18]. A cluster with one or more red bonds will, if any red bond is cut, split into disconnected sub-clusters. The total number of red bonds in the percolating cluster behaves as $N_r \propto r^{d-X_r}$, with X_r the red-bond scaling dimension.

As mentioned earlier, the ‘geometric’ exponents, such as X_b , X_r , and X_{\min} , characterize geometric structures of critical systems, and are thus of some physical relevance. For instance, the backbone and red-bond scaling dimensions X_b and X_r are related to the electric conductivity of a random network [26]. The chemical path dimension X_{\min} is the analogue in percolation of the dynamic scaling exponent of critical phenomena [19].

Among these exponents, the red-bond dimension X_r has been identified with another exponent X_p [10,11], which governs the RG flow of the bond probability p for critical systems. As a result, exact values of X_r can be calculated from the theory of the Coulomb gas [9]; these values are also included in the prediction of the conformal field theory [10, 14, 42]. However, except for the special case $q \rightarrow 0$, exact values have not been obtained for X_b and X_{\min} . Numerous theoretical attempts have been carried out. For the percolation model $q \rightarrow 1$, a relation was assumed by Herrmann and Stanley [18] as $X_b = X_r - X_{\min}$, which satisfies numerical tests quite well so far. However, this conjecture apparently cannot be generalized to the critical $q \rightarrow 0$ Potts model, where $X_b = X_r = X_{\min}$, as shown later. It was also assumed that $X_b(q \rightarrow 1) = 7/16$ [15, 16], which is, however, not consistent with current estimations. More recently, $X_b(q \rightarrow 1)$ has been related to a partial differential equation [17], which, unfortunately, appears to be intractable, even numerically.

In parallel with these theoretical attempts, several numerical determinations of X_b have been achieved. Significant progress is obtained by Monte Carlo simulations [18–20]. The basic idea of these simulations is to count the total number of sites or bonds in the backbones. For instance, for the percolation model in the ‘bus-bar’ geometry, Grassberger [19] determined $X_b = 0.3569(8)$. Slow convergence applies to X_b in this case. For the $q = 2$ and 3-state Potts models, it has been estimated [20] that $X_b = 0.25(1)$ and $0.25(2)$, respectively.

Another approach was taken by Jacobsen and Zinn-Justin [22] recently. They applied a transfer-matrix method, and obtained $X_b = 0.3569(6)$ for the percolation model. Instead of the total number of sites in the backbones, they investigated the correlation length of k -connected clusters [43], where $k \geq 1$ is an integer. A cluster is considered to be k -connected if, by eliminating any $k - 1$ sites or conducting bonds, no separation into disconnected sub-clusters is possible. This means that any two sites in the cluster are connected via *at least* k independent paths without any bond in common. At criticality, the behavior of these k -connected clusters is dominated by a family of exponents X_k . Moreover, it has been shown that $X_2 = X_b$ [44], so that one can estimate X_b by studying 2-connected clusters.

In such transfer-matrix calculations, the finite system sizes are restricted to relatively small values, since the computer memory required increases exponentially with linear size L . For instance, in Refs. [22], L is limited to $2 \leq L \leq 10$. This effect, together with the aforementioned slow finite-size convergence, makes it difficult to determine X_b accurately.

In this paper, we present another Monte Carlo study of the backbone exponents. However, in comparison with the earlier Monte Carlo studies [18–20], we apply a new sampling procedure. As mentioned above, the earlier methods involve counting procedures for the number of sites or bonds in the backbone. In other words, for a cluster of interest, all dangling bonds have to be identified and excluded. This appears to be a time-consuming task. Instead, in the present work, we sample the probability $P_2(r)$ that a pair of sites, separated by a distance r , are connected via *at least* two independent paths. For later convenience, we shall refer to the quantity $P_2(r)$ as the ‘backbone correlation function’. The sampling procedure for $P_2(r)$, which will be described in detail later, has a speed at least of the same order as the well-known Wolff cluster method [45]. We note that, in comparison with Refs. [18–20], our procedure to sample $P_2(r)$ is more in line with that used in Ref. [22].

The sampling procedure for $P_2(r)$ can be applied to the general q -state Potts model with any value of $q \geq 0$. Further, with this technique, we simply investigate systems with periodic boundary conditions

rather than in the ‘bus-bar’ geometry [19,20]. Thus, one avoids any finite-size correction associated with the surfaces in the ‘bus-bar’ geometry. This will be confirmed later.

In the present work, several critical and tricritical q -state Potts systems are investigated. The values of q are chosen as $q = 2 - \sqrt{3}$, 1, 2, 3, and 4 for the critical systems, and $q = 1$ and 2 at tricriticality. The critical $q = 1$ and 2 Potts models are just the bond percolation and the Ising model, respectively, and the tricritical $q = 2$ system is the Blume-Capel model [46,47]. For $q = 4$, we avoid slow finite-size convergence by investigating a dilute $q = 4$ Potts model and the Baxter-Wu model [48].

For these systems, extensive simulations were performed to determine X_b . In order to suppress critical slowing down, we make use of various efficient cluster Monte Carlo algorithms. For instance, for the dilute $q = 4$ Potts and the Blume-Capel model, a geometric cluster method [49] was used to move vacancies on lattices. Another example is the simulation of the critical $q = 2 - \sqrt{3}$ Potts model. For this purpose, we formulate a Monte Carlo method for the Potts model with non-integer $q > 0$. This method hardly suffers from critical slowing down for small $q > 0$.

9.1.2 Models

We start from the Hamiltonian of the dilute q -state Potts model on the square lattice [5], which reads

$$\mathcal{H}/k_B T = -K \sum_{\langle i,j \rangle} \delta_{\sigma_i, \sigma_j} (1 - \delta_{\sigma_i, 0}) - D \sum_k \delta_{\sigma_k, 0} \quad (\sigma = 0, 1, \dots, q). \quad (9.1)$$

Each site is occupied by a Potts variable with $\sigma = 1, \dots, q$ or by a vacancy $\sigma = 0$, and the sum $\langle \rangle$ is over all nearest-neighbor sites. The abundance of the vacancies is controlled by the chemical potential D . Nonzero couplings K occur only between equal Potts variables, i.e., variables with nonzero values of σ .

Just as the ‘pure’ Potts model, this model can be represented by Kasteleyn-Fortuin (KF) clusters [4,50], with each site of the lattice also occupied by a vacancy or a Potts variable. A nearest-neighbor bond is placed between each pair of equal, nonzero Potts variables with the probability $p = 1 - \exp(-K)$. We emphasize that, for any pair of nearest-neighbor sites, no bond is present if any of them is a vacancy. The whole lattice is then decomposed into clusters, i.e., the aforementioned KF clusters. This model is also referred to as a random-cluster model with a partition sum

$$Z = \sum_{\{v,b\}} u^{n_b} q^{n_c} w^{n_v}, \quad (u = e^K - 1 \text{ and } w = e^D), \quad (9.2)$$

where the sum is over all mutually consistent vacancy and bond configurations, and n_b , n_c , and n_v are the total number of bonds, KF clusters, and vacancies, respectively. According to finite-size scaling, the average size of these KF clusters at criticality is governed by the magnetic scaling dimension X_h . With the partition sum (9.2), the Potts model is now also well defined for any non-integer $q \geq 0$.

For $D = -\infty$, the vacancies are excluded, and the system reduces to the ‘pure’ Potts model. In this case, the model is self-dual, and the critical point follows [5] as $u_c = \exp(K_c) - 1 = \sqrt{q}$ on the square lattice. With sufficiently abundant vacancies, tricritical systems, described by Eqs. (9.1) and (9.2), can be obtained.

Apart from these KF clusters, we also investigate so-called ‘Potts’ clusters [10,11,42], defined as sets of Potts variables in the same state, connected by nearest-neighbor bonds. In other words, conducting bonds are *always* present between nearest-neighbor Potts variables as long as they are in the same state. Exponents describing Potts clusters are normally different from those for KF clusters. For instance, the $q = 2$ Potts clusters, i.e., Ising clusters, are described by the magnetic exponent of the tricritical $q = 1$ Potts model [9–11], different from that of the critical Ising model. Exponents for $q = 3$ and $q = 4$ Potts clusters have also been predicted as $X_h = 7/80$ and $1/8$ [42].

Among the systems included in the present work, most of the systems can be described by Eqs. (9.1) or (9.2), except the Blume-Capel, and the Baxter-Wu model, which will be described later.

For the $q = 4$ Potts model, logarithmic corrections arise due to the marginal field associated with the fugacity of vacancies [5]. In order to avoid such corrections, we investigate a dilute system at the point where this marginal field vanishes. We shall refer to this point, although somewhat imprecisely, as the

‘fixed’ point. By means of a transfer-matrix calculation [51], we locate this fixed point as $K_{tc} = 1.45790(1)$, $D_{tc} = 2.478438(2)$, and $\rho_{tc} = 0.21207(2)$ for the vacancy density. The precision of this result is considered sufficient for our later investigation of the backbone exponents.

For the case of $q = 4$, besides the aforementioned dilute system, we also investigate the Baxter-Wu model [48], which is defined on the triangular lattice as

$$\mathcal{H}/k_{\text{B}}T = -K \sum_{\Delta, \nabla} \sigma_i \sigma_j \sigma_k, \quad (\sigma = \pm 1), \quad (9.3)$$

where the sum is over every up- and down-triangular face of the lattice. It has been shown that this model belongs to the universality class of the $q = 4$ Potts model, and that logarithmic corrections are absent [48]. This means that the Baxter-Wu model also sits at the aforementioned fixed point. The critical point is given by $K_c = \ln(1 + \sqrt{2})/2$ [48].

For the Ising and the Blume-Capel model, instead of Eq. (9.1), the Hamiltonian reads

$$\mathcal{H}/k_{\text{B}}T = -K^{(I)} \sum_{\langle i, j \rangle} \sigma_i \sigma_j + D^{(I)} \sum_k \sigma_k^2, \quad (\sigma = -1, 0, 1), \quad (9.4)$$

where vacancies are also denoted as $\sigma = 0$. We mention that, instead $p = 1 - \exp(-K)$, the bond probability for the KF clusters is now $p = 1 - \exp(-2K^{(I)})$. Analogously, for the chemical potential $D^{(I)} = -\infty$, the system reduces to the ‘pure’ Ising model, with the critical point at $K_c^{(I)} = \ln(1 + \sqrt{2})/2$. By means of a transfer-matrix calculation [51], we locate, with a sufficient precision, the tricritical point of the Blume-Capel model as $K_{tc}^{(I)} = 1.6431759(1)$, $D_{tc}^{(I)} = 3.2301797(2)$, and $\rho_{tc} = 0.4549506(2)$.

9.1.3 Algorithms

The Monte Carlo investigation of the backbone exponents of the aforementioned systems involves two parts, i.e., the simulation and the sampling procedure.

Monte Carlo simulations

For pure Potts systems with integer q , one can simply use the standard Wolff procedure [45]. In the present paper, these systems include the bond percolation, the Ising, and the $q = 3$ Potts model. For the dilute systems, i.e., the Blume-Capel and the $q = 4$ Potts model, cluster algorithms to flip between vacancies and Potts variables are generally not available. For this reason, we fix the global vacancy density at its equilibrium value, so that critical slowing down due to fluctuations in the number of vacancies is avoided. Cluster steps satisfying this conservation law are realized by a geometric cluster algorithm [49]. It moves groups of vacancies and Potts variables over the lattice in accordance with the Boltzmann distribution. This geometric cluster method is based on spatial symmetries, such as the spatial inversion symmetry. A detailed account can be found in Ref. [49].

Simulations of the Baxter-Wu model [48], which involves three-spin interactions, can be performed as follows [52]. The triangular lattice is divided into three sublattices, one of the sublattices is randomly chosen, and its spins are ‘frozen’. Since each elementary triangle contains one spin from each sublattice, only two-spin interactions remain effectively. Further, the Hamiltonian (9.3) is unchanged if all spins on these two sublattices are flipped. Due to this symmetry, one can now apply the Wolff cluster method on these two sublattices.

For the $0 < q < 1$ Potts model, we formulate a Monte Carlo method on the basis of the random-cluster representation Eq. (9.2), which uses bond variables $l = 0$ or 1 . For simplicity, we illustrate this method precisely at the critical point $u_c = \sqrt{q}$:

1. Randomly choose a bond variable l , connecting sites i and j .
2. Draw a uniformly distributed random number $0 \leq r \leq 1$,
 - (a) if $r < \sqrt{q}/(1 + \sqrt{q})$, the edge l is occupied by a bond, i.e., $l = 1$.

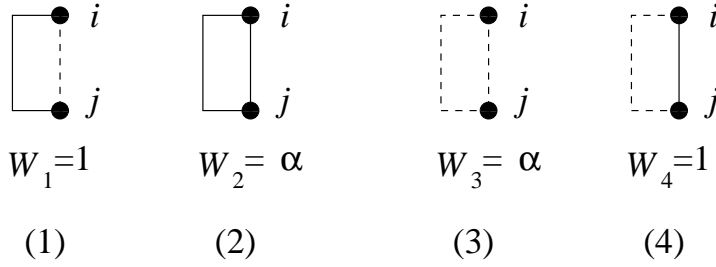


Figure 9.1: Relative weights of the bond variables between neighboring sites i and j for the critical Potts model. Existing paths or bonds are represented by solid lines, while dashed lines means that no path or bond is present. The relative weights between state (1) and (2) and those between (3) and (4) are specified as W_i with $\alpha = \sqrt{q}$.

- (b) if $r > 1/(1 + \sqrt{q})$, no bond is present at the edge l , i.e., $l = 0$.
- (c) if $\sqrt{q}/(1 + \sqrt{q}) \leq r \leq 1/(1 + \sqrt{q})$, set $l = 0$, and check whether sites i and j are connected. If they are not $l = 1$; otherwise $l = 0$.

3. Current Monte Carlo step is completed, and goto 1.

Figure 9.1 illustrates possible connectivities of sites i and j and their relative weights. According to the procedure described above, the transition probability from (1) to (2) is $T_{1 \rightarrow 2} = \sqrt{q}/(1 + \sqrt{q})$, and that from (2) to (1) is $T_{2 \rightarrow 1} = 1/(1 + \sqrt{q})$. Since equilibrium statistics implies that the probability p_1/p_2 is $1/\sqrt{q}$, one has $p_1 T_{1 \rightarrow 2} = p_2 T_{2 \rightarrow 1}$. Thus, the condition of detailed balance is satisfied between states (1) and (2). The same argument applies to states (3) and (4).

For small values of q , we observe that this method hardly suffers from critical slowing down. A similar procedure for $q > 1$ has already been published [53]. Using the procedure described in Ref. [53], we simulated the $q = 2 + \sqrt{3}$ Potts model. In this case, we did observe serious critical slowing down, in agreement with the Li-Sokal bound [54] for the dynamic exponent. This is due to the rather strong energy fluctuations for $q > 2$, especially when the marginal case $q_c = 4$ is approached. In Ref. [53], this Monte Carlo technique was used to locate the marginal value of q_c in three dimensions, and it was claimed that no critical slowing down occurs. This stands, however, in a remarkable contrast with our findings near $q_c = 4$ in two dimensions.

Sampling procedure

Here, we illustrate, in the language of the bond percolation model, the sampling procedure of the backbone correlation function $P_2(r)$.

Step 1, form a KF cluster. We shall illustrate the construction of a KF clusters as follows. Suppose a percolation model is defined on a $L \times L$ square lattice with periodic boundary conditions, and there are two sites A and B separated by a distance $L/2$. The task of this step is to form a KF cluster \mathbb{F} from site A , and then to check whether B is also included in \mathbb{F} , so that A and B are connected via conducting bonds. For the Potts model with integer q , the sites in this KF cluster just form the Wolff cluster [45]. In the standard Wolff algorithm, if two nearest-neighbor sites are already in the cluster, it is not necessary to check whether the bond between them is present or absent. However, we are interested in the backbone correlation function here. If A and B are connected, one then asks how many mutually independent paths exist between A and B . Thus, all edges between nearest-neighbor sites within \mathbb{F} have to be checked. We introduce a variable $C = 0, 1$, and 2 , representing that there is no path, only one path, and *at least* two mutually independent paths between A and B , respectively. First, the edge variables on the lattice are initialized as $e_i = -1$ with $1 \leq i \leq 2L^2$. The value $e_i = 1$ represents that the i th edge is occupied by a bond, and $e_i = 0$ stands for an empty edge. Since only one KF cluster is formed, not all edges of the square lattice are necessarily visited during the formation of \mathbb{F} . The edges, which are not visited, keep their value $e_i = -1$. After this initialization, uniformly distributed random numbers are drawn for each edge connecting to a neighbor in

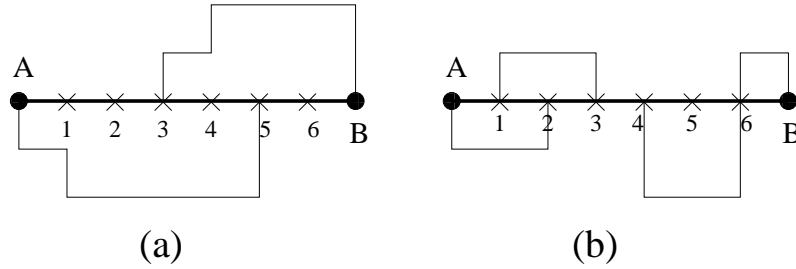


Figure 9.2: Outline of the procedure to determine the connection variable C . The path \mathbb{W} is shown as the thick line, and the remaining conducting bonds are shown as the thin lines. The bonds on \mathbb{W} are temporarily eliminated first. In figure (a), the remaining path stops at 5. After the bonds between A , $1, \dots$, and 5 are restored, the path connects to B , so that $C = 2$. In figure (b), the bond between 3 and 4 is a red bond, and thus the path stops at site 3, so that $C = 1$.

the same state. The edge is occupied by a bond if $r \leq p_c$ and is empty if $r > p_c$. The sites connected via these bonds are included in \mathbb{F} , as stored in a stack memory \mathbb{S} . Next, a site j is read and erased from \mathbb{S} . Then, the edges connecting to site j are checked. If they have not been visited ($e_i = -1$), new random numbers are used to determine whether they are occupied. Repetition of this procedure creates a list of occupied edges and sites, and thus a cluster \mathbb{F} is formed. The determination of the backbone between A and B indeed requires that each bond between sites in \mathbb{F} is visited. This procedure costs some additional computer time in comparison with the algorithm growing a Wolff cluster [3].

If the site B is not in the cluster \mathbb{F} , i.e., A and B are not connected, one has $C = 0$, and the current Monte Carlo step is completed; otherwise, it continues as follows.

Step 2, a path \mathbb{W} is formed between A and B . This can be done by an ‘ant’ walking from A through the conducting bonds. Suppose the ant is currently at site j , it continues its journey by randomly choosing a conducting bond connecting to j , excluding the one it just passed. The ant does not pass a bond twice unless it arrives at a ‘dead’ end. The ‘dead end’ is defined as a site whose connected nearest-neighbor sites have all been visited. In this case, the ant walks back along the ‘old’ road until it finds a ‘new’ bond which it has not visited. Since site B is also in \mathbb{F} , the ant will always arrive at site B . The aforementioned path \mathbb{W} is just composed of the bonds through which the ant has passed once and only once. An example is shown in Fig. 9.2a, where the path \mathbb{W} is represented the thick solid line, and the sites on it are specified as $1, 2, \dots, n$.

The next task is to check whether there is any red bond on \mathbb{W} . If only one independent path can be formed between A and B , then *at least* one red bond occurs on the path \mathbb{W} . Furthermore, if any of these bonds is cut off, the ant cannot arrive at site B . An inefficient way is as follows. Temporarily eliminate a bond b on \mathbb{W} , and then let the ant restart its journey. If the ant can still arrive at B , the bond b cannot be a red bond, and thus is restored. Suppose all the bonds on the path \mathbb{W} pass this test, then no red bond occurs between A and B , so that $C = 2$; Otherwise, $C = 1$. In this way, however, the ant may become too tired to walk. Therefore, we apply a more efficient procedure.

Step 3, temporarily eliminate all the bonds on \mathbb{W} , and let the ant restart its journey from A to B . Suppose the ant cannot arrive at B ; this does not necessarily mean, however, that there are red bonds. For instance, in Fig. 9.2a, after the elimination of the whole path, the ant can only arrive at site 5. This indicates that the bonds between A , $1, \dots$, and 5 are not red bonds, and may thus be restored. Then, the ant continues its journey and arrives at B . In this case, no red bond occurs on the path \mathbb{W} , and $C = 2$. An example of opposite case is given in Fig. 9.2b. Following the same steps the ant cannot go beyond site 3, since the bond between sites 3 and 4 is a red bond. In this case, one has $C = 1$.

In practical applications of this procedure, one can still improve the efficiency by some tricks. For instance, during the formation of the path \mathbb{W} , the site B may act as an ‘attractor’, so that \mathbb{W} will not go too far from B and the ant need not continue its journey randomly. Furthermore, after the elimination of \mathbb{W} , instead of having the ant restart the journey, one can form a new cluster from A on the basis of the remaining bonds, and then check whether it includes B . In the case that B is not included, one restore the

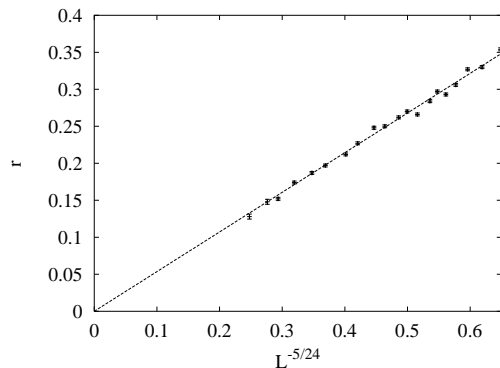


Figure 9.3: The ratio r , between the computer time for steps 2 and 3 and the total time (steps 1, 2, and 3 combined), vs. $L^{-5/24}$ for the percolation model. Every data point involves 10^5 Monte Carlo sweeps, and the system sizes are in the range $8 \leq L \leq 800$. The ratio r extrapolates to 0 for $L \rightarrow \infty$.

‘temporarily eliminated’ bonds on \mathbb{W} which connect sites in A , and then continue to grow cluster A . This procedure ends when either B is included or no growth of A is possible. This avoids the situation that the ant has to walk back from a dead end.

With the connection variable C , the normal magnetic correlation function P_1 and the backbone correlation function P_2 between sites A and B can be defined as

$$P_1 = \langle 1 - \delta_{C,0} \rangle, \quad P_2 = \langle \delta_{C,2} \rangle, \quad (9.5)$$

where the symbol $\langle \rangle$ means the statistical average.

Efficiency of the sampling procedure. As described above, the sampling of P_2 involves up to three steps; the probability that steps 2 and 3 are performed is just the magnetic correlation function P_1 . Step 1 is just a standard Wolff step with a small amount of added computer time, as mentioned above. Steps 2 and 3 involve a number of sites with an upper limit equal to the size of the cluster \mathbb{F} , so that their computer time is also of the same order as the Wolff step. Moreover, the probability P_1 that they are performed decays as L^{-2X_h} , and each sample is only taken between several simulation steps. As a result, the sampling procedure requires less computer time than the Wolff method. As an illustration, we performed 10^5 Monte Carlo steps for the percolation model with system size $8 \leq L \leq 800$. We sampled the ratio r between the computer time for steps 2 and 3 and the total time, i.e., for steps 1, 2, and 3. The data for r are shown in Fig. 9.3 versus $L^{2X_h} = L^{-5/24}$. The approximate linearity indicates that the fraction of the computer time needed by the sampling procedure over the total time goes to 0 as $L \rightarrow \infty$.

9.1.4 Results

As mentioned in Sec. 9.1.1, the backbone correlation function P_2 , and thus the backbone exponent, is related to the behavior of the red bonds. For critical Potts models $0 \leq q \leq 4$, the value of X_r is known to increase with q , which indicates that the KF clusters become less and less ramified. As a result, the backbone correlation function P_2 behaves more and more in line with P_1 , so that X_b may be expected to approach the normal magnetic exponent X_h as $q \rightarrow 4$. For the tricritical Potts model, since $X_r \geq 2$, we expect that the backbone exponent X_b reduces to the magnetic exponent X_h .

For the critical $q \rightarrow 0$ Potts model [4,5], the KF clusters span the whole lattice without any loop, and are thus referred to as spanning trees. In this case, between any pair of points on the lattice, there is precisely only one path \mathbb{P} , so that the backbone correlation function P_2 vanishes. This is due to the vanishing of the amplitude of P_2 as $q \rightarrow 0$. As a consequence, one cannot obtain $X_b(q \rightarrow 0)$ by investigating k -connected clusters, as we will do for other values of $q > 0$. In this case, one can simply make use of the original

definitions of the ‘geometric’ quantities in Sec. 9.1.1, which include the backbone, the red-bond, and the chemical-path exponents. From these definitions, one knows that the aforementioned path \mathbb{P} is just the chemical path, and that the backbone precisely consists of all the bonds on \mathbb{P} . Furthermore, all these bonds are red bonds. Since the red-bond scaling dimension is exactly known $X_r = 3/4$ [10, 55], one simply has that $X_2 = X_b = X_{\min} = 3/4$ for $q \rightarrow 0$. In fact, the statement that $X_b = X_r = X_{\min}$ holds for any type of spanning tree.

In the remaining part of this section, we present our Monte Carlo determinations of X_b for the systems discussed in Sec. 9.1.2. Periodic boundary conditions apply to all these systems. The aforementioned site A was chosen at random, and site B is chosen at a distance $r = L/2$ in the x direction from A . Further, we chose a site D also separated from A a distance $L/2$ but in the y direction.

The correlation functions P_1 and P_2 were sampled both in the x and y directions, such that $P_1 = [P_1^{(x)} + P_1^{(y)}]/2$ and $P_2 = [P_2^{(x)} + P_2^{(y)}]/2$. Moreover, we sampled another backbone correlation function P_{22} that A is simultaneously connected to B and D by *at least* two mutually independent paths.

According to finite-size scaling, the quantities P_1 , P_2 , and P_{22} behave at criticality as

$$P_1 = L^{-2X_h} (a_0 + a_2 L^{y_i} + a_3 L^{-2} + a_4 L^{-3}), \quad (9.6)$$

$$P_2 = L^{-2X_b} (b_0 + b_1 L^{y_{ib}} + b_2 L^{y_i} + b_3 L^{-2} + b_4 L^{-3}), \quad \text{and} \quad (9.7)$$

$$P_{22} = L^{-3X_b} (c_0 + c_1 L^{y_{ib}} + c_2 L^{y_i} + c_3 L^{-2} + c_4 L^{-3}), \quad (9.8)$$

where y_i is the exponent of the leading irrelevant thermal scaling field, and we have assumed integer correction exponents (of $1/L$). The amplitudes a_i , b_i , and c_i are unknown constants. In comparison with the magnetic correlation function P_1 , the ‘geometric’ quantities P_2 and P_{22} may be expected to suffer from additional finite-size corrections, with unknown associated exponents y_{ib} . More rapidly decaying corrections are neglected here. The unknown amplitudes and exponents are determined from multivariate least-square analysis using the Levenberg-Marquardt method [56]. For the systems in the present work, the values of X_h , obtained from the fits of P_1 , are all in excellent agreement with their exact results [9], and need not be discussed in this work.

The bond percolation model

For this model, the system sizes L were taken in the range $8 \leq L \leq 240$. The data for P_2 are shown in Fig. 9.5, and do not indicate the presence of large finite-size corrections. Equation (9.7) was fitted to the Monte Carlo data according to the least-square criterion, and the exponent y_{ib} was left as a free parameter. We observed that the terms with amplitudes b_2 , b_3 , and b_4 do not decrease the residual χ^2 , and thus they were not included in the fit. We obtain $X_b = 0.3566(2)$ and $y_{ib} = -1.27(4)$, where the error bars are twice the statistical standard deviations. Compared to Ref. [19], it seems that our Monte Carlo data suffer less seriously from finite-size corrections. This may be due to our choice of a geometry with periodic boundary conditions instead of the ‘bus-bar’ geometry. For clarity, we plot the value of $P_2 L^{2X_b} - b_0$ as a function of $L^{-1.27}$ in Fig. 9.4, where $X_b = 0.3566(2)$ and $b_0 = 0.742(2)$ are taken from the fit. The apparent linearity indicates that, indeed, finite-size corrections of P_2 can be well accounted for by a single power law $b_1 L^{y_{ib}}$.

The Ising model and the tricritical $q = 1$ Potts model

The simulations were performed for critical Ising systems on square lattices in the range $6 \leq L \leq 240$. The quantities P_2 and P_{22} were sampled both for KF and Ising clusters. As mentioned above, the Ising clusters are described by the magnetic dimension $X_h = 5/96$ of the tricritical $q = 1$ Potts model [9–11]. The Monte Carlo data for P_2 of the KF clusters are shown in Fig. 9.6, which indicates that $2X_b \approx 0.54$. Equations (9.7) and (9.8) were simultaneously fitted to P_2 and P_{22} , respectively, so that X_b and y_{ib} appears in the fit only once. In addition to the terms with y_{ib} , the fit also included a correction with $y_i = -2$. We obtain $X_b = 0.2696(3)$ and $y_{ib} = -0.87(4)$ for KF clusters, and $X_b = 0.0520(3)$ for Ising clusters. Here, the error bars are again two standard deviations. As expected, for the Ising clusters X_b is in a good agreement with $X_h = 5/96 = 0.5208 \dots$ of the tricritical $q = 1$ Potts model.

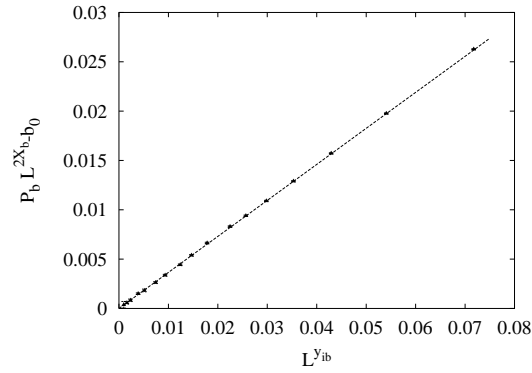


Figure 9.4: Finite-size corrections in P_2 for KF clusters of the critical bond percolation model, vs. $P_2 L^{2X_b} - b_0$ vs. $L^{y_{ib}}$. The values of X_b , b_0 and y_{ib} are taken from the numerical fit: $X_b = 0.3566(2)$, $b_0 = 0.742(2)$, and $y_{ib} = -1.27(4)$.

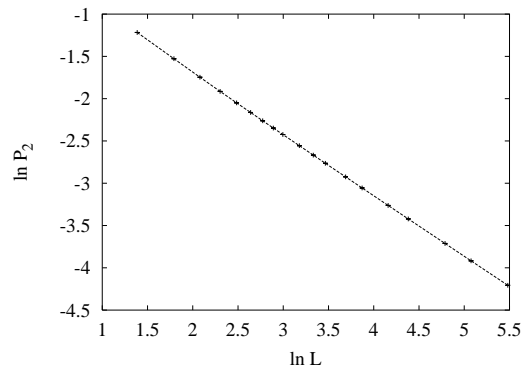


Figure 9.5: Decay of the backbone correlation function P_2 for KF clusters of the critical bond percolation model. The data are shown as $\ln P_2$ vs. $\ln L$.

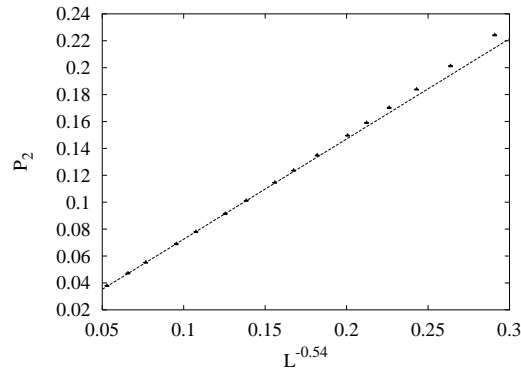


Figure 9.6: Decay of the backbone correlation function P_2 for KF clusters of the critical Ising model. The data are shown as P_2 vs. $L^{-0.537}$.

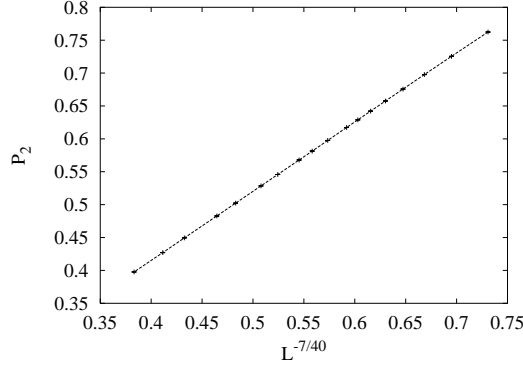


Figure 9.7: Decay of the quantity P_2 for Potts clusters of the critical $q = 3$ Potts model. The data are shown as P_2 vs. $L^{-7/40}$.

The critical $q = 3$ Potts model

The simulations were performed for the $q = 3$ Potts model at criticality with system sizes L in the range $6 \leq L \leq 360$. The quantities P_2 and P_{22} were sampled both for KF and Potts clusters. As mentioned above, the exponent for the Potts clusters has been predicted as $X_h = 7/80$ [42]. As a test, Eq. (9.6) was fitted to the data for P_1 , and we obtain $X_h = 0.0876(2)$, in good agreement with $7/80$. Furthermore, a plot of the data for P_{22} for Potts clusters in Fig. 9.7 also indicates $X_b \approx 7/80$. Again, Eqs. (9.7) and (9.8) were simultaneously fitted to P_2 and P_{22} , respectively. For the $q = 3$ Potts model, the correction term with $y_i = -4/5$ [14] appears difficult to separate from that with y_{ib} , and thus it was neglected in the fit. The corrections with L^{-2} were included, and the fit yields that $X_b = 0.2105(5)$ and $y_{ib} = -0.61(4)$ for the KF clusters, and that $X_b = 0.0873(3) \approx X_h = 7/80$ for the Potts clusters.

The tricritical Blume-Capel model

As mentioned above, the backbone exponent X_b for the tricritical $q = 1$ Potts model has already been determined from the Ising clusters. The result $X_b = 0.0520(3) \approx 5/96$ indicates that X_b reduces to the magnetic exponent X_h for tricritical Potts models. As an independent test, we directly Monte Carlo simulated the tricritical Blume-Capel model. The simulations use the fixed-vacancy-density ensemble, as discussed in Sec. 9.1.2. The system sizes were taken in the range $10 \leq L \leq 360$, and both quantities P_2 and P_{22} were sampled. The numerical fits yield $X_b = 0.0760(8)$ and $0.0753(4)$ for the KF and the Potts cluster, respectively. Both are in good agreement with the tricritical magnetic exponent $X_h = 3/40$ [9, 14].

The Baxter-Wu and the tricritical $q = 4$ Potts model

The $q = 4$ Potts model is a marginal case, not only because the second-leading thermal exponent $X_{t2} = 2$, but also because the red-bond exponent $X_r = 2$ [10, 42]. Thus, the bond-dilution scaling field, conjugate to the red bonds, becomes marginal, and the question arises whether this field is marginally relevant or irrelevant for critical KF and Potts clusters. As independent tests, Monte Carlo simulations were performed both of the aforementioned dilute $q = 4$ Potts model at the fixed point and the Baxter-Wu model. For the latter, the system size L was taken as multiples of 6 and in the range $12 \leq L \leq 240$. For the dilute $q = 4$ model, the system sizes were in the range $10 \leq L \leq 360$. The Monte Carlo data for P_2 of the KF clusters, shown in Fig. (9.8), indicate that $2X_b \approx 1/4$. For these two models, logarithmic finite-size corrections are absent for ‘thermodynamic’ quantities such as the magnetic correlation P_1 . However, we have no solid reason to assume that such logarithmic corrections are absent for ‘geometric’ quantities such as P_2 . Thus, at criticality, we assume that, instead of Eqs. (9.7) and (9.8), P_2 behaves as

$$P_2 = L^{-2X_b} (b_0 + b_1/\ln L + b_2/\ln^2 L + b_3/L^2) . \quad (9.9)$$

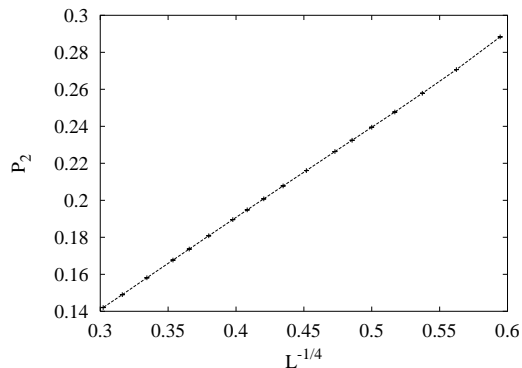


Figure 9.8: Decay of the quantity P_2 for the KF clusters of the dilute $q = 4$ Potts model. The data are shown as P_2 vs. $L^{-1/4}$.

Eq. (9.9) was fitted to the Monte Carlo data for these two models simultaneously. On the basis of the χ^2 criterion, we applied a cutoff for small system sizes $L \leq 12$. We then obtain that $X_b = 0.124(2)$ and $0.127(4)$ for the Potts and the KF clusters, respectively, in agreement with $X_h = 1/8$.

The critical $q = 2 - \sqrt{3}$ Potts model

As a case between $q = 0$ and 1 , we simulated the $q = 2 - \sqrt{3}$ Potts model. The system sizes were taken in the range $6 \leq L \leq 200$, and the quantity P_2 was sampled. We find that, as expected, the finite-size corrections converge rapidly, so that Eq. (9.7) with only the first two terms is sufficient to describe the Monte Carlo data. To obtain a satisfactory χ^2 residual, we applied a cutoff for small system sizes $L < 8$. This leads to $X_b = 0.4953(3)$ and $y_{ib} = -2.3(2)$.

9.1.5 Discussion

We have developed several Monte Carlo methods to determine the backbone exponents of the q -state Potts model. The efficiency of these methods is reflected by the precision of the numerical results, summarized in Tab. 9.1, which significantly improves over existing results. We find that, for critical Potts models, the backbone scaling dimension X_b approaches the magnetic dimension X_h as $q \rightarrow 4$. This reflects the fact that Kasteleyn-Fortuin clusters become more and more compact with increasing q . Further, it has been confirmed numerically that, for the tricritical Potts model, the backbone exponent reduces to the magnetic exponent. In Fig. 9.9, we plot X_b and X_h as a function of the coupling constant of the Coulomb gas g [9]. The relation between g and q is given by $q = 2 + 2 \cos(g\pi/2)$ [9], with $2 \leq g \leq 4$ and $4 \leq g \leq 6$ for the critical and tricritical Potts models, respectively.

The present Monte Carlo methods can also be applied in three dimensions, and simulations for the percolation and the Ising model are currently being performed [51].

9.2 The percolation and the Ising model in three dimensions

Using the sampling technique developed above, we determine the magnetic and backbone exponents $X_h = 0.4768(7)$ and $X_b = 1.125(3)$ for the percolation and $X_h = 0.5178(7)$ and $X_b = 0.829(4)$ for the Ising model in three dimensions.

9.2.1 Introduction

The Ising model and the percolation problem have for many years been of great interest to physicists and mathematicians. While the Ising model presents a very simple theoretical description [2] for *thermodynamic*

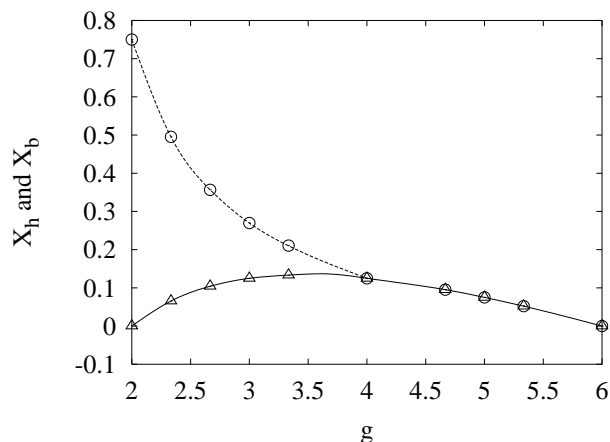


Figure 9.9: The backbone and the magnetic scaling dimension, X_b and X_h , as a function of the coupling constant of the Coulomb gas g . The symbols \triangle and \circ represent X_h and X_b , respectively. The tricritical branch of the Potts model corresponds with $4 \leq g \leq 6$; X_h and X_b coincide in this range.

Table 9.1: Results for the backbone exponent X_b and the associated correction-to-scaling exponent y_{ib} for critical Potts systems. Estimated error margins in the last decimal place, which are twice the standard deviations in the fits, are shown in parentheses. For comparison, the magnetic dimensions X_h and estimations of X_b by other sources are also listed (X_b^* , last column). The numbers given as fractions are exact.

g	Model	X_h	X_b	y_{ib}	X_b^*
2	$q = 0$ Potts	0	$3/4$		
$7/3$	$q = 2 - \sqrt{3}$ Potts	$11/168$	$0.4953(3)$	$-2.3(2)$	
$8/3$	Percolation	$5/48$	$0.3566(2)$	$-1.27(4)$	$0.3569(6)$ [22]
3	Ising	$1/8$	$0.2696(3)$	$-0.87(4)$	$0.25(2)$ [20]
$10/3$	$q = 3$ Potts	$2/15$	$0.2105(5)$	$-0.61(4)$	$0.25(2)$ [20]
4	$q = 4$ Potts	$1/8$	$0.127(4)$	$1/\ln L?$	

phase transitions in magnetic systems, the percolation provides a fascinating illustration [3] of many important concepts of critical phenomena in terms of *geometric* properties. Both models can be exactly mapped onto the random-cluster model [4], in which thermodynamic singularities of the Ising model can also be represented in terms of percolation clusters. For an introduction, we start with the Hamiltonian of the q -state Potts model [5] on the square lattice

$$\mathcal{H}/k_{\text{B}}T = -K \sum_{\langle i,j \rangle} \delta_{\sigma_i, \sigma_j}, \quad (\sigma = 1, 2, \dots, q), \quad (9.10)$$

where the sum is over nearest-neighbor (NN) spins and K is the coupling strength. The random-cluster model is obtained as follows. Between each pair of NN sites, a bond is placed with the probability $p = 1 - \exp(-K)$, so that the whole lattice is decomposed into connected clusters, i.e., the well-known Kasteleyn-Fortuin (KF) clusters [4]. The statistical weight of each bond-variable configuration is given by the partition function of the random-cluster model

$$Z_{rc}(q; K) = \sum_b v^{n_b} q^{n_c}, \quad (v = e^K - 1). \quad (9.11)$$

Here, the sum is over all bond-variable configurations, and n_b and n_c are the total numbers of bonds and KF clusters, respectively. It can be shown [4, 5, 50] that the partition sum of the Potts model (9.10) is equivalent with Z_{rc} in Eq. (9.11). The Ising and percolation models are the special cases with $q = 2$ and $q \rightarrow 1$, respectively. Near the critical point $K_c(q)$, the scaling properties of KF clusters in Eq. (9.11) are governed by the thermal and magnetic scaling fields.

Besides the thermal and magnetic scaling dimensions X_t and X_h , there is still a number of critical exponents, which characterize structure properties of critical KF clusters in Eq. (9.11) and do not have thermodynamic analogue. Among them there are fractal dimensions [7] of ‘backbones’ and of ‘red’ bonds. From the scaling behavior of N_b ,

In comparison with the two-dimensional case, exact results are scarce for critical behavior in three dimensions. Therefore, investigations have to depend on approximations such as ϵ - and series expansions, and Monte Carlo techniques. Extensive studies have been carried out and significant results have been achieved [3, 27–35, 41]. For instance, the percolation threshold of the bond-percolation on the simple-cubic lattice was determined [27] as $p_c = 0.248\,821\,6(5)$, and the backbone dimension was reported [36] as $X_b = 1.145(15)$. From quantities such as the mean cluster size, the thermal and magnetic scaling dimensions were estimated [3, 27, 28, 41] as $X_t = 1.141(3)$ and $X_h = 0.477(3)$, respectively. For the Ising model, there is also some consensus [29–35] that the values of X_t and X_h are 0.413 and 0.518, respectively, with differences only in the last decimal place. However, it seems that so far little attention has been given to the geometric exponents of the Ising model, such as X_b and X_r .

9.2.2 Models

We start with the Hamiltonian of a dilute Ising model on the simple-cubic lattice

$$\mathcal{H}/k_{\text{B}}T = -K \sum_{\langle i,j \rangle} s_i s_j + D \sum_k s_k^2 \quad (s = 0, \pm 1). \quad (9.12)$$

The spins assume the values ± 1 and 0. Those in state $s = 0$ are referred to as vacancies. The abundance of vacancies is controlled by the chemical potential D , and nonzero couplings K occur only between NN Ising spins. For $D \rightarrow -\infty$, the vacancies are excluded, and the model reduces to the ‘pure’ Ising model, i.e., the spin- $\frac{1}{2}$ model [2]. This model has been investigated extensively, and the critical point was determined [35] as $K_c = 0.22\,165\,455(3)$. Along the critical line $K_c(D)$, the amplitude of the irrelevant scaling field with the exponent $y_i = -0.821(5)$ varies as a function of D . It was reported [29, 35] that this amplitude is very small near $D = \ln 2$.

The present paper investigates the dilute Ising model (9.12) with $D = \ln 2$. At this point, the critical coupling and the corresponding vacancy density were determined [29, 35] as $K_c = 0.39\,342\,225(5)$ and $\rho_{vc} = 0.400\,694(1)$, respectively. During the simulations, we fixed the global density of vacancies at the critical

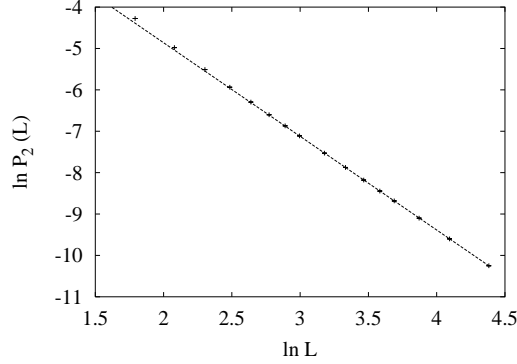


Figure 9.10: The backbone correlation function P_2 for the bond percolation model, shown as $\ln P_2(L)$ v.s. $\ln L$.

value ρ_{vc} , while they are still allowed to move freely over the lattice according to the Boltzmann distribution. This means that an external constraint is imposed. For such a constrained system, it is known [37] that the thermal exponent $y_t = 1.5868(3)$ [35] is renormalized to $y'_t = X_t = 1.4132(3)$. Thus, the constrained specific heat has only a finite cusp at criticality [37, 38] instead of being divergent. Large-scale simulations of the model (9.12) under the constraint are now possible because of the so-called geometric cluster method [49]. This algorithm is developed on the basis of geometric symmetries such as the spatial-inversion symmetry, and has been explained in Ref. [49]. The geometric cluster simulations of these constrained systems suffer little from critical slowing down. This may be related to the fact that the constrained critical specific heat takes a finite value.

9.2.3 Results

Bond-percolation model

The bond-percolation model was investigated on $L \times L \times L$ simple-cubic lattices with periodic boundary conditions, and the bond probability p was set at the critical value [27] $p_c = 0.2488216(5)$. The magnetic and backbone correlation functions $P_1(L/2)$ and $P_2(L/2)$ were sampled for three pairs of points in the x , y , and z directions, respectively, and the average values were calculated. The system sizes were chosen as 16 values in the range $6 \leq L \leq 80$, and a number of 2.1×10^7 samples was taken for each system size. The numerical data for $P_2(L/2)$ are listed in Tab. 9.2. In comparison with the magnetic correlations $P_1(L/2)$, the backbone correlations $P_2(L/2)$ are relatively small, which indicates that critical KF clusters are rather ‘ramified’. According to the least-square criterion, we fitted the data for $P_1(L/2)$ and $P_2(L/2)$ by

$$P_1(L/2) = L^{-2X_h} (a_0 + a_1 L^{y_i} + a_2 L^{-2} + a_3 L^{-3}), \quad (9.13)$$

and

$$P_2(L/2) = L^{-2X_b} (b_0 + b_1 L^{y_i} + b_2 L^{-2} + b_3 L^{-3} + b_4 L^{y_{ib}}), \quad (9.14)$$

where a_i and b_i are unknown parameters. The correction terms with exponent y_i arise from the irrelevant scaling field, of which the exponent y_i has been determined [27] as $y_i = -1.14(15)$. For the backbone correlation P_2 , new finite-size corrections could appear, and thus we include the term with the exponent y_{ib} in Eq. (9.14). Figure 9.10 shows the data for P_2 on a logarithmic scale, i.e., $\ln P_2(L/2)$ versus $\ln L$. The approximate linearity indicates that corrections-to-scaling are not very significant.

If the exponent y_i is left free during the fit for the magnetic correlation P_1 , we have $X_h = 0.4769(6)$ and $y_i = -1.5(3)$, where the quoted error margins are two standard deviations, as obtained from the statistical analysis. The estimation of y_i is consistent with $y_i = -1.14(15)$ [27]. The fit with y_i fixed at -1.14 yields that $X_h = 0.4768(4)$. Taking into account the uncertainties of the percolation threshold p_c ,

Table 9.2: The data for P_1 and $P_2 \times 10$ for the critical bond-percolation model in three dimensions. The numbers in parentheses are the statistical errors at the last decimal place.

	6	8	10	12	14	16
P_1	.20747(3)	.15496(2)	.12411(2)	.10378(2)	.08926(1)	.07839(1)
P_2	.13899(6)	.06889(4)	.04049(3)	.02641(2)	.01846(2)	.01359(2)
	18	20	24	28	32	36
P_1	.06996(1)	.06321(1)	.05301(1)	.045719(9)	.040200(9)	.035905(9)
P_2	.01039(2)	.00815(1)	.00537(1)	.003801(8)	.002803(8)	.002149(7)
	40	48	60	80		
P_1	.032465(9)	.027260(8)	.022031(8)	.016723(8)		
P_2	.001694(7)	.001117(6)	.000676(5)	.000354(5)		

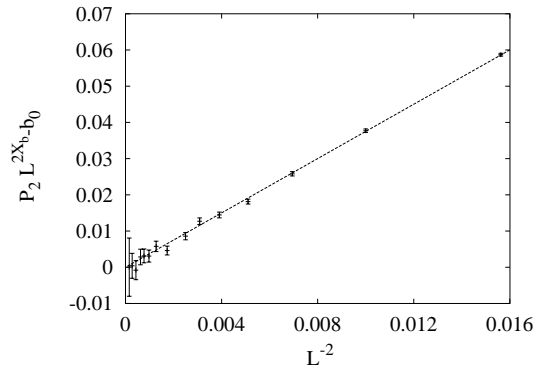


Figure 9.11: Illustration of finite-size corrections in the backbone correlation P_2 for the bond percolation model. This is shown as $P_2 L^{2X_b} - b_0$ v.s. $L^{y_{ib}}$, where the values of X_b , b_0 , and y_{ib} are taken from the numerical fit: $X_b = 1.125(3)$, $b_0 = 0.688(13)$, and $y_{ib} = -2.0(5)$.

we conclude that $X_h = 0.4768(8)$ is a reasonable estimation, which is in agreement with existing results $X_h = 0.477(3)$ [27, 28, 41]. In the fit for the backbone correlation P_2 , it seems unnecessary to include all correction terms described by Eq. (9.14), because not all of them can be well determined, and moreover results do not depend on whether they are present or not. After excluding the terms with a_1 and a_2 , we obtain $X_b = 1.125(3)$ and $y_{ib} = -2.0(5)$, which improves significantly over the existing estimation $X_b = 1.145(15)$ [36]. The fit to the data for P_2 is illustrated by Fig. 9.11.

Dilute Ising model

The dilute Ising model (9.12) on the simple-cubic lattice was also investigated with periodic boundary conditions. Several Monte Carlo cluster steps were performed between subsequent samples. The simulations took place at the critical point [29, 35] $\rho_{vc} = 0.400694(1)$ and $K_c = 0.39342225(5)$. As mentioned earlier, the total number of vacancies is fixed at $V_c = L^2 \rho_{vc}$, and thus a combination of the Wolff [45] and the geometric [49] cluster steps was used. For finite systems L , however, V_c is not an integer. Thus, the actual simulations were performed at two numbers $[V_c]$ and $[V_c] + 1$, where brackets $[]$ denote the integer part. Numerical data at criticality were obtained by linear interpolation between $[V_c]$ and $[V_c] + 1$. System sizes were taken as 14 values in the range $6 \leq L \leq 64$. Apart from the quantities P_1 and P_2 , we also sampled the probability P_{22} that the randomly chosen site A is *simultaneously* connected to B and D by at least two mutually independent paths, where B and D are two points at a distance $L/2$ in the x and y directions,

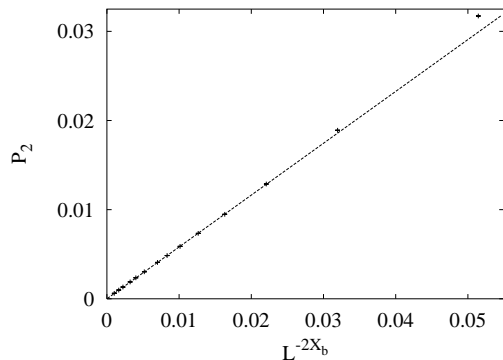


Figure 9.12: The backbone correlation function P_2 for the Ising model, shown as $\ln P_2$ v.s. L^{-2X_b} , where $X_b = 0.829(5)$ is the backbone scaling dimension.

Table 9.3: The data for P_1 , $P_2 \times 10$, and $P_{22} \times 100$ for the dilute Ising model in three dimensions. The numbers in parentheses are the statistical errors at the last decimal place.

	6	8	10	12	14
P_1	.15598(3)	.11571(3)	.09214(2)	.07656(2)	.06550(2)
P_2	.31726(9)	.18909(9)	.12878(8)	.09479(8)	.07339(7)
P_{22}	.4668(2)	.2151(2)	.1211(1)	.07649(9)	.05212(8)
	16	18	20	24	28
P_1	.05722(2)	.05081(2)	.04565(1)	.03794(1)	.03243(1)
P_2	.05881(6)	.04850(6)	.04081(5)	.03030(5)	.02359(4)
P_{22}	.03758(7)	.02818(6)	.02170(5)	.01394(5)	.00956(4)
	32	40	48	64	
P_1	.02832(1)	.02257(1)	.01873(1)	.01395(1)	
P_2	.01893(3)	.01318(2)	.00979(2)	.00613(2)	
P_{22}	.00689(3)	.00400(2)	.00258(1)	.00125(1)	

respectively. The data for P_1 , P_2 and P_{22} are listed in Tab. 9.3. The scaling behavior of P_{22} is described by

$$P_{22}(L/2) = L^{-3X_b} (x_0 + x_1 L^{y_i} + x_2 L^{-2} + x_3 L^{-3} + x_4 L^{y_{ib}}). \quad (9.15)$$

The irrelevant exponent y_i was set at $-0.821(5)$ [35], and the data for P_1 were fitted by Eq. (9.13). We obtain $X_h = 0.5178(7)$, in agreement with the earlier estimation $X_h = 0.5184(1)$ [35], which was obtained from the magnetic susceptibility. For the backbone problem, we *simultaneously* fitted Eqs. (9.14) and (9.15) by the data for P_2 and P_{22} , respectively, such that the backbone dimension X_b appears only once. As in the case of the bond-percolation model, we found no evidence that new correction terms with y_{ib} exist. We obtain $X_b = 0.829(4)$, where the quoted error is again twice the standard deviation. The data for P_2 are shown in Fig. 9.12 versus L^{-2X_b} , where $X_b = 0.829$ was taken from the fit.

9.2.4 Discussion

In conclusion, we have numerically determined the backbone dimension X_b for the bond-percolation and Ising models in three dimensions. As the thermal and magnetic dimensions X_t and X_h , geometric critical exponents are also universal, and thus our results for X_b should also apply to other systems within the percolation and Ising universality class in three dimensions.

Besides the backbone and red-bond dimensions X_b and X_r , there are other exponents characterizing geometric properties of critical systems, e.g., the fractal dimension X_{\min} of ‘chemical’ paths [7]. In perco-

lation theory, these exponents have received significant attention, and they are considered to be of some physical relevance. For instance, the chemical-path dimension X_{\min} is the analog in percolation of dynamic scaling exponent of critical phenomena [7]. However, further explorations of the geometric exponents seem appropriate for other critical systems in three dimensions.

Bibliography

- [1] R.B. Potts, Proc. Cambridge Philos. Soc. **48**, 106 (1952).
- [2] L. Onsager, Phys. Rev. **65**, 117 (1944).
- [3] D. Stauffer and A. Aharony, *Introduction to Percolation Theory* (Taylor & Francis, Philadelphia, 1994), and references therein.
- [4] P.W. Kasteleyn and C.M. Fortuin, J. Phys. Soc. Jpn. **46** (Suppl.), 11 (1969); C.M. Fortuin and P.W. Kasteleyn, Physica **57**, 536 (1972).
- [5] For a review, see e.g., F.Y. Wu, Rev. Mod. Phys. **54**, 235 (1982).
- [6] A. Coniglio and W. Klein, J. Phys. A **12**, 2775 (1980).
- [7] H.J Herrmann and H.E. Stanley, Phys. Rev. Lett. **53**, 1121 (1984); H.J Herrmann, D.C. Hong, and H.E. Stanley, J. Phys. A **17**, L261 (1984).
- [8] B. Nienhuis, J. Phys. A **15**, 199 (1982).
- [9] see e.g., B. Nienhuis, *Phase Transitions and Critical Phenomena*, edited by C. Domb and J.L. Lebowitz. (Academic Press, London, 1987), Vol. 11, p. 1, and references therein.
- [10] A. Coniglio, Phys. Rev. Lett. **62**, 3054 (1989).
- [11] H.W.J. Blöte, Y.M.M. Knops, and B. Nienhuis, Phys. Rev. Lett. **68**, 3440 (1992).
- [12] Y. Deng, H.W.J. Blöte, and B. Nienhuis, Phys. Rev. E **69**, 026123 (2004).
- [13] A.A. Belavin, A.M. Polyakov, and A.B. Zamolodchikov, J. Stat. Phys. **34**, 763 (1984); Nucl. Phys. B **241**, 333 (1984); D. Friedan, Z. Qiu, and S. Shenker, Phys. Rev. Lett. **52**, 1575 (1984).
- [14] J.L. Cardy, *Phase Transitions and Critical Phenomena*, edited by C. Domb and J.L. Lebowitz. (Academic Press, London, 1987), Vol. 11, p. 55, and references therein.
- [15] T.A. Larsson, J. Phys. A **20**, L291 (1987).
- [16] H. Saleur, Nucl. Phys. B **382**, 486 (1992).
- [17] G.F. Lawler, O. Schramm, and W. Werner, e-print math-PR/0108211 (2002).
- [18] H.J Herrmann and H.E. Stanley, J. Phys. A **21**, L829 (1988).
- [19] P. Grassberger, J. Phys. A **25**, 5475 (1992); Physica. A **262**, 251 (1999), and references in.
- [20] E.N. Miranda, Physica. A **175**, 229 (1991).
- [21] Y. Deng, H.W.J. Blöte, and B. Nienhuis, Phys. Rev. E **69**, 026114 (2003).
- [22] J. L. Jacobsen and P. Zinn-Justin, Phys. Rev. E **66**, R055102 (2002); J. Phys. A **35**, 2131 (2002).
- [23] M. Porto, A. Bunde, S. Havlin, and H.E. Roman, Phys. Rev. E **56**, 1667 (1997).
- [24] M. Barthélémy, S.V. Buldyrev, S. Havlin, and H.E. Stanley, Phys. Rev. E **60**, R1123 (1999).

- [25] G. Paul, S.V. Buldyrev, N.V. Dokholyan, S. Havlin, P.R. King, Y. Lee, and H.E. Stanley, Phys. Rev. E **61**, 3435 (2000); G. Paul and H.E. Stanley, Phys. Rev. E **65**, 056126 (2002).
- [26] M. Sahimi, *Applications of Percolation Theory* (Taylor and Francis, London, 1994).
- [27] C.D. Lorenz and R.M. Ziff, Phys. Rev. E **57**, 230 (1997); G. Paul, R.M. Ziff, and H.E. Stanley, Phys. Rev. E **64**, 026115 (2001).
- [28] C.K. Hu, J.A. Chen, N.S. Izmailian, and P. Kleban, Compt. Phys. Comm. **126**, 77 (2000).
- [29] H.W.J. Blöte, E. Luijten, and J.R. Heringa, J. Phys. A **28**, 6289 (1995); H.W.J. Blöte, J.R. Heringa, A. Hoogland, E.W. Meyer, and T.S. Smit, Phys. Rev. Lett. **76**, 2613 (1996); H.W.J. Blöte, L.N. Shchur, and A.L. Talapov, Int. J. Mod. Phys. C **10**, 1137 (1999).
- [30] M. Hasenbusch, K. Pinn, and S. Vinti, Phys. Rev. B **59**, 11471 (1999).
- [31] P. Butera and M. Comi, Phys. Rev. B **56**, 8212 (1997).
- [32] R. Guida and J. Zinn-Justin, J. Phys. A **31**, 8103 (1998).
- [33] K. Binder and E. Luijten, Phys. Rep. **344**, 179 (2001).
- [34] M. Campostrini, A. Pelissetto, P. Rossi, and E. Vicari, Phys. Rev. E **65**, 066127 (2002).
- [35] Y. Deng and H.W.J. Blöte, Phys. Rev. Lett. **88**, 190602 (2002); Phys. Rev. E **68**, 036125 (2003).
- [36] M.D. Rintoul and H. Nakanishi, J. Phys. A **27**, 5445 (1994).
- [37] M.E. Fisher, Phys. Rev. **176**, 257 (1967).
- [38] Y. Deng and H.W.J. Blöte, unpublished.
- [39] J.R. Heringa and H.W.J. Blöte, Physica A **232**, 369 (1995); Phys. Rev. E **57**, 4976 (1998).
- [40] U. Wolff, Phys. Rev. Lett. **62**, 361 (1989).
- [41] M. Sahimi and S. Arbabi, J. Stat Phys. **62**, 1873 (1990).
- [42] C. Vanderzande, J. Phys. A **25**, L75 (1992).
- [43] W.T. Tutte, *Graph Theory* (Cambridge University Press, Cambridge, England, 1984).
- [44] G. Paul and H.E. Stanley, Phys. Rev. E **65**, 056126 (2002).
- [45] U. Wolff, Phys. Rev. Lett. **62**, 361 (1989).
- [46] M. Blume, Phys. Rev. **141**, 1517 (1966).
- [47] H.W. Capel, Physica **32**, 966 (1966); **33**, 295 (1967).
- [48] R.J. Baxter and F.Y. Wu, Phys. Rev. Lett. **31**, 1294 (1973); Aust. J. Phys. **27**, 357 (1974).
- [49] J.R. Heringa and H.W.J. Blöte, Physica A **232**, 369 (1996); Phys. Rev. E **57**, 4976 (1998).
- [50] A. Coniglio and F. Peruggi, J. Phys. A **15**, 1873 (1982).
- [51] Y. Deng and H.W.J. Blöte, unpublished.
- [52] M.A. Novotny and H.G. Evertz, *Computer simulation studies in condensed-matter physics VI*, edited by D.P. Landau, K.K. Mon and H.-B. Schüttler. (Springer Berlin Heidelberg 1993) p.188.
- [53] F. Gliozzi, Phys. Rev. E **66**, 016115 (2002);

- [54] X.J. Li and A.D. Sokal, Phys. Rev. Lett. **63**, 827 (1989).
- [55] B. Duplantier, J. Stat. Phys. **54**, 581 (1989); Phys. Lett. B **228**, 379 (1989).
- [56] see *e.g.* W.H. Press, B.P. Flannery, S.A. Teukolsky and W.T. Vetterling, *Numerical Recipes*, (Cambridge University Press, Cambridge 1986).

Geometric properties of Potts configurations

We investigate the geometric properties of several Potts models in two and three dimensions.

10.1 The critical and tricritical Potts model in two dimensions

We investigate geometric properties of the general q -state Potts model in two dimensions, and define geometric clusters as sets of lattice sites in the same Potts state, connected by nearest-neighbor bonds with variable probability p . We find that, besides the random-cluster fixed point, both the critical and the tricritical Potts model have another fixed point in the p direction. For the critical model, the random-cluster fixed point p_r is unstable and the other point $p_g \geq p_r$ is stable; while p_r is stable and $p_g \leq p_r$ is unstable at tricriticality. Moreover, we show that the fixed point p_g of a critical and tricritical q -state Potts model can be regarded to correspond to p_r of a tricritical and critical q' -state Potts model, respectively. In terms of the coupling constant of the Coulomb gas g , these two models are related as $gg' = 16$. By means of Monte Carlo simulations, we obtain $p_g = 0.6227(2)$ and $0.6395(2)$ for the tricritical Blume-Capel and the $q = 3$ Potts model, respectively, and confirm the predicted values of the magnetic and bond-dilution exponents near p_g .

10.1.1 Introduction

The geometric description of fluctuations near a critical point has been a subject of a long history, which goes back to the formulation of phase transitions in terms of the droplet model [1]. For the general q -state Potts model [8, 47], the critical singularities can be represented in terms of Kasteleyn-Fortuin (KF) clusters [4, 9]. For clarity, we start from the Hamiltonian of the q -state Potts model on the square lattice

$$\mathcal{H}/k_B T = -K \sum_{\langle i,j \rangle} \delta_{\sigma_i, \sigma_j}, \quad (\sigma = 1, 2, \dots, q), \quad (10.1)$$

where the sum is over all nearest-neighbor (NN) sites, and K is the coupling strength. This model can be exactly mapped onto a random-cluster model [9]. Between each pair of NN sites, a bond is placed with the probability $p = 1 - \exp(-K)$, so that the whole lattice is decomposed into connected clusters, i.e., the aforementioned KF clusters. The statistical weight of each bond-variable configuration is expressed by the partition sum of the random-cluster model as

$$Z(q; K) = \sum_b v^{n_b} q^{n_c}, \quad (v = e^K - 1). \quad (10.2)$$

The sum is over all bond-variable configurations, and n_b and n_c are the total numbers of bonds and KF clusters, respectively.

The partition sum (10.2) defines the general Potts model with non-integer $q \geq 0$, which has a continuous and a first-order phase transition for $0 \leq q \leq 4$ and for $4 < q$, respectively. Near the critical point $K_c(q)$, the distribution of KF clusters reflects critical singularities of the Potts model (10.1). For instance, the scaling properties of the average size of critical KF clusters are determined by the magnetic exponent $X_h(q)$. Exact values of $X_h(q)$ have already been obtained by the theory of the Coulomb gas [22, 48], and are also included within the predictions of the conformal field theory [23, 49]. In terms of the coupling constant of the Coulomb gas g , $X_h(g)$ is expressed as

$$X_h(g) = \frac{(g-2)(6-g)}{8g}, \quad (10.3)$$

where g is related to q as $q = 2 + 2 \cos(g\pi/2)$ with $2 \leq g \leq 4$ for the critical branch of the Potts model [22, 48].

Apart from KF clusters, so-called Potts clusters [15–17, 19] have received considerable attentions, which are defined as sets of NN sites in the same Potts state. Thus, bonds are *always* present between any pair of NN sites as long as they are occupied by the same Potts variable. For critical Potts models (10.1), the exponents for the Potts clusters are generally different from those for the KF clusters. A well known example is the Ising model ($q = 2$). The exponent for the Ising clusters, i.e., the $q = 2$ Potts clusters, is $X_h^{(p)} = 5/96$ [15–17], equal to the magnetic exponent of the tricritical $q = 1$ Potts model. Here, the superscript (p) refers to the Potts clusters. For the bond percolation model ($q = 1$), all lattice sites belong to the same Potts cluster, and thus $X_h^{(p)}(q = 1) = 0$. Apparently, $X_h^{(p)}(q) \neq X_h(q)$ in these cases. Within the predictions of the conformal field theory, Vanderzande [19] interpreted $X_h^{(p)} = 7/80$ and $1/8$ for the critical $q = 3$ and 4-state Potts models, respectively. However, for the general non-integer $0 \leq q \leq 4$ Potts model, exact value of $X_h^{(p)}$ has not been reported yet, as far as we know. This is one purpose of the present work.

The tricritical Potts model [8] can be obtained by including vacancies in the ‘pure’ Potts model (10.1). The question then arises what critical exponents describe Potts clusters of the general tricritical q -state Potts model. From Refs. [15–17, 19], it is known that, for the critical Potts model, the exponent $X_h^{(p)}$ approaches the magnetic exponent X_h as q increases. Particularly, $X_h^{(p)} = X_h$ for $q = 4$. Since the tricritical branch of the Potts model is an extension of the critical Potts model [8], we simply assume that, for the tricritical Potts model, the Potts clusters and the KF clusters are described by the same critical exponents. This will be confirmed numerically later.

Moreover, both for the critical and the tricritical Potts model, we investigate a general type of ‘geometric’ clusters, which are defined analogously as the aforementioned KF clusters, but the bond probability can have a variable value $0 \leq p \leq 1$. Thus, KF and Potts clusters are just the special cases of geometric clusters with $p = 1 - \exp(-K)$ and 1, respectively. For the critical Potts model, it is generally believed that, in terms of geometric clusters, the percolation threshold p_g coincides with the critical point of the corresponding Potts model or random-cluster model p_r , i.e., $p_g = p_r = 1 - \exp(-K_c)$. In contrast, at tricritical points K_{tc} , we show that the percolation threshold p_g does not coincide with $p_r = 1 - \exp(-K_{tc})$, but $0 < p_g < p_r$. Furthermore, critical exponents near p_g are different from those near p_r . On the basis of the theory of the Coulomb gas, we predict values of critical exponents near p_g for the tricritical q -state Potts model.

To confirm these predictions, we perform Monte Carlo simulations for the tricritical Blume-Capel [21] and the $q = 3$ Potts model [8]. Numerical data clearly demonstrate the existence of p_g for the tricritical Potts model, and confirm the predicted critical exponents.

10.1.2 General analysis

We start from the critical Potts model, described by Eq. (10.1). For this model, the statistical properties of geometric clusters can be obtained from a ‘mixed’ Potts model [4] with the Hamiltonian

$$\mathcal{H}/k_B T = -J \sum_{\langle i,j \rangle} (\delta_{\tau_i, \tau_j} - 1) \delta_{\sigma_i, \sigma_j} - K \sum_{\langle i,j \rangle} \delta_{\sigma_i, \sigma_j}. \quad (10.4)$$

The second term is just the aforementioned ‘pure’ q -state Potts Hamiltonian (10.1); the first term contains auxiliary Potts variables $\tau = 1, 2, \dots, s$, and controls the distribution of bond variables. One can express

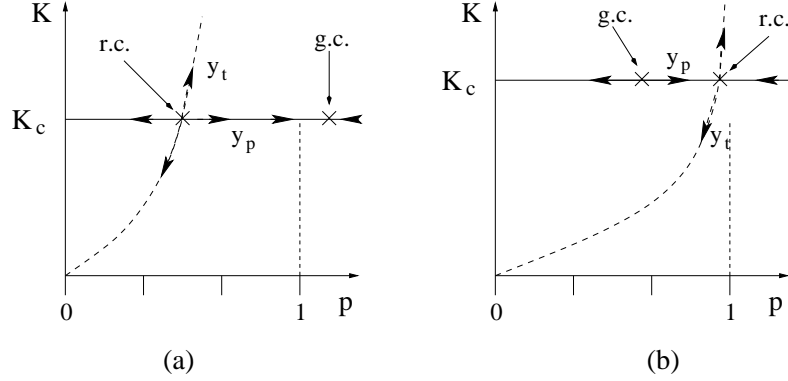


Figure 10.1: RG flows of Potts models in the parameter space (K, p) . Figures (a) and (b) apply to the critical and the tricritical Potts model, respectively. The dashed lines represent the random-cluster model $p = 1 - \exp(-K)$. The points, ‘r.c.’ and ‘g.c.’, represent the random- and the geometric-cluster fixed point, p_r and p_g , respectively. Arrows show the direction of the RG flows.

the partition sum of Eq. (10.4) in bond variables, and differentiate the resulting free energy with respect to the parameter s . Taking the limit $s \rightarrow 1$, one obtains the distribution of geometric clusters with bond probability $p = 1 - \exp(-J)$. Particularly, if one chooses $J = K$, Hamiltonian (10.4) assumes a simple form and describes the random-cluster model (10.2).

For this ‘mixed’ Potts model (10.4), the renormalization-group (RG) flow is sketched in Fig. 10.1(a) in the parameter space (p, K) with $p = 1 - \exp(-J)$. The dashed line represents the random-cluster model with $J = K$. At the critical point $K = K_c$, in terms of geometric clusters, the percolation threshold is just $p_r = 1 - \exp(-K_c)$. Thus, p_r can be considered as a fixed point in the space (p, K) , which is unstable both in the bond-probability direction p and along the dashed line $J = K$. The scaling properties in these two directions are described by the bond-dilution and the thermal scaling field, respectively. We shall denote their associated exponents as y_p and y_t , respectively, where y_p is also referred to be the red-bond exponent [6].

Near the random-cluster fixed point p_r , exact values of the bond-dilution and the thermal exponents, y_p and y_t , have already been obtained by various methods. For instance, on the basis of the theory of the Coulomb gas, it has been derived [6,16,17] that the scaling dimensions, $X_p = 2 - y_p$ and $X_t = 2 - y_t$, satisfy

$$X_p(g) = \frac{1}{8g}(3g - 4)(g + 4), \quad (10.5)$$

and

$$X_t(g) = \frac{6 - g}{g}, \quad (10.6)$$

respectively, where g is the coupling constant of the Coulomb gas, as mentioned before. Furthermore, for integers $0 \leq q \leq 4$, $X_p(q)$ and $X_t(q)$ are also included in the predictions of the conformal field theory. For clarity, we start from the Kac formula describing scalar observables [23,49]

$$X_{i,j}(q) = \frac{[im - j(m+1)]^2 - 1}{2m(m+1)}, \quad (m \geq 1), \quad (10.7)$$

where the positive integer m is related to the conformal anomaly c as $c = 1 - 6/m(m+1)$. For the critical branch of the Potts model, one has $\sqrt{q} = 2 \cos[\pi/(m+1)]$. It is known that $X_p(q)$ and $X_t(q)$ can be identified as $X_{i,j}$ with coordinates $(i=0, j=2)$ and $(i=2, j=1)$, respectively. We also mention that the aforementioned magnetic exponent $X_h(q)$ can be interpreted as $X_{i,j}$ with $i=j=(m+1)/2$.

For the critical Potts model ($2 \leq g \leq 4$), Eq. (10.5) yields $X_p(q) \leq 2$, which indicates that the bond-dilution field is relevant at the random-cluster fixed point p_r , as shown in Fig. 10.1(a). Thus, geometric

clusters at p_r , i.e., KF clusters, and those with the bond-probability $p \neq p_r$ are described by different exponents. For $p < p_r$, we expect that the behavior of geometric clusters is dominated by the trivial $p = 0$ fixed point; while geometric clusters with $p > p_r$, including Potts clusters, are described by a stable fixed point $p_g > p_r$, shown in Fig. 10.1(a). For later convenience, we shall refer to the point p_g as the geometric-cluster fixed point. For the case of the Ising model on the square lattice, it has been found [17] that $p_g \approx 1.08$, in an unphysical region.

The above discussions apply to the critical branch of the Potts model. For the tricritical Potts model, it is already known [22, 48] that the magnetic and thermal exponents, $X_h(q)$ and $X_t(q)$, are still given by Eqs. (10.3) and (10.6), respectively, but with the coupling constant in the range $4 \leq g \leq 6$. Accordingly, for integers $0 \leq q \leq 4$, $X_t(g)$ and $X_h(g)$ can be interpreted as $X_{1,2}$ and $X_{m/2, m/2}$ in the Kac formula (10.7), respectively. On this basis, for the tricritical Potts model, we simply *assume* that the bond-dilution exponent $X_p(q)$ is still given by Eq. (10.5) with $4 \leq g \leq 6$, and thus corresponds to $X_{2,0}$ in the Kac formula (10.7).

To distinguish the critical and the tricritical branch of the Potts model, later, we shall express critical exponents as a function of g only. Table 10.1 lists values of g , $X_p(g)$, and $X_h(g)$ for the Potts model with integer $0 \leq q \leq 4$.

Table 10.1: The bond-dilution and the magnetic exponents, X_p and X_h for the two-dimensional Potts model. The superscripts (r) and (g) represent the random- and the geometric-cluster fixed point, p_r and p_g , respectively. the coupling constant of the Coulomb gas is denoted as g , and the positive integer m is related to the conformal anomaly c as $c = 1 - 6/m(m + 1)$.

Random-cluster fixed point						Geometric-cluster fixed point					
	$q^{(r)}$	$g^{(r)}$	$m^{(r)}$	$X_p^{(r)}$	$X_h^{(r)}$	$X_p^{(g)}$	$X_h^{(g)}$	$m^{(g)}$	$g^{(g)}$	$q^{(g)}$	
critical	0	2	1	3/4	0	15/4	-3/16	1	8		trical
	1	8/3	2	5/4	5/48	35/12	0	2	6	0	
	2	3	3	35/24	1/8	21/8	5/96	3	16/3	1	
	3	10/3	5	33/20	2/15	143/60	7/80	5	24/5	$2 + 2 \cos(2\pi/5)$	
	4	4	∞	2	1/8	2	1/8	∞	4	4	
trical	3	14/3	6	65/28	2/21	143/84	15/112	6	24/7	$2 + 2 \cos(2\pi/7)$	critical
	2	5	4	99/40	3/40	63/40	21/160	4	16/5	$2 + 2 \cos(2\pi/5)$	
	1	16/3	3	21/8	5/96	35/24	1/8	3	3	2	
	0	6	2	35/12	0	5/4	5/48	2	8/3	1	

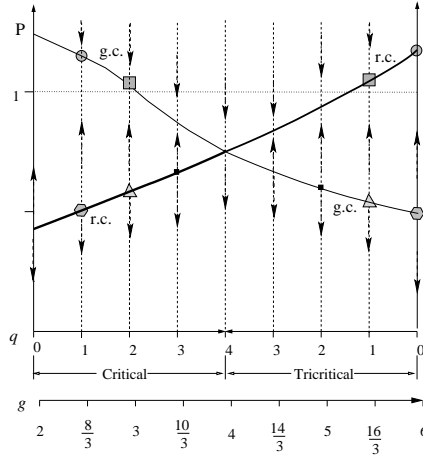


Figure 10.2: RG flows in the plane (q, p) for the general q -state Potts model in two dimensions. The thick and thin solid lines represent the random- and the geometric-cluster fixed point, p_r and p_g , respectively. Pairs of points in the same symbol have the same conformal anomaly. Arrows show the direction of the RG flows. The $q = 4$ Potts model is a marginal case.

As mentioned earlier, for the critical Potts model, the point p_r is a fixed point in the parameter space (p, K) . Here, we *assume* this statement still holds for the tricritical Potts model ($4 < g \leq 6$). Equation (10.5) yields $X_p(g) > 2$, so that the bond-dilution scaling field is irrelevant near the random-cluster fixed point p_r . On the other hand, it is obvious that the trivial $p = 0$ fixed point is stable. On this basis, we expect that, in the p direction, an unstable fixed point p_g occurs in the range $0 \leq p \leq p_r$ for the tricritical Potts model. We shall also refer to this unstable point p_g as the geometric-cluster fixed point. As far as we know, the existence of p_g has not yet been reported. The expected RG flow is shown in Fig. 10.1(b), which will be confirmed numerically later.

In conclusion, according to the predicted values of the bond-dilution exponent X_p [6, 16, 17], we predict that both the critical and the tricritical Potts model have a pair of fixed points, p_r and p_g , on the critical line parametrized by the bond probability p . For the critical branch of the Potts model, the random-cluster fixed point p_r is unstable, and the geometric-cluster fixed point $p_g > p_r$ is stable. In contrast, for the tricritical Potts model, p_r is stable and $p_g < p_r$ is unstable. The $q = 4$ Potts model is a marginal case, and these two fixed points, p_r and p_g , merge together. In the parameter space (p, q) , we illustrate the RG flows in Fig. 10.2.

The question arises what values the critical exponents take near the geometric-cluster fixed point p_g for the general critical and tricritical Potts model. For the Ising model ($q = 2$), it is already known [15–17, 19] that the fixed point p_g corresponds to p_r of the tricritical $q = 1$ Potts model. In other words, p_g of the tricritical $q = 1$ Potts model corresponds to p_r of the Ising model. On this basis, we assume the followings for the general Potts model with $0 \leq q \leq 4$.

Assumption 1, the geometric-cluster fixed point p_g of a *critical (tricritical)* q -state Potts model corresponds to the random-cluster fixed point p_r of a *tricritical (critical)* q' -state Potts model.

Assumption 2, the critical q and tricritical q' -state Potts models have the same conformal anomaly and thus the same number m .

For the critical and the tricritical branch of the Potts model, as is well known, the coupling constant of the Coulomb gas g is related to m as $g = 4m/(m + 1)$ and $g' = 4(m' + 1)/m'$, respectively. Therefore, the aforementioned two models are related by $gg' = 16$.

With these assumptions, critical exponents can be easily obtained for the fixed point p_g . As an example, we consider the magnetic exponent $X_h^{(g)}$ for a model with the coupling constant g . As mentioned earlier,

X_h is given by Eq. (10.3), so that, after the substitution $g = 16/g'$, $X_h^{(g)}(g)$ follows as

$$X_h^{(g)}(g) = \frac{(8-g)(3g-8)}{32g}. \quad (10.8)$$

The same procedure applies to other critical exponents, and the resulting values are consistent with the existing predictions for the critical Potts model with $q = 1, 2, 3$, and 4. For clarity, we list values of $X_h^{(g)}$ and $X_p^{(g)}$ in Tab. 10.1 for integer $0 \leq q \leq 4$.

10.1.3 Monte Carlo investigation

To confirm the predictions in Sec. 10.1.2, we perform Monte Carlo simulations for the tricritical Blume-Capel and $q = 3$ Potts models.

The tricritical Blume-Capel model

The Ising model with vacancies, also called the Blume-Capel model [21], is defined on the square lattice, with the Hamiltonian

$$\mathcal{H}/k_B T = -K \sum_{\langle i,j \rangle} \sigma_i \sigma_j + D \sum_k \sigma_k^2 \quad (\sigma = 0, \pm 1). \quad (10.9)$$

The vacancies are denoted as $\sigma = 0$, and D is the chemical potential of the Ising spins $\sigma = \pm 1$. We mention that, in this case, the bond probability for KF clusters is $p = 1 - \exp(-2K)$.

For $D \rightarrow -\infty$, the vacancies are excluded, and the model reduces to Onsager's spin- $\frac{1}{2}$ model [18]. The critical coupling constant K_c is an increasing function of the chemical potential D , and the critical line $K_c(D)$ terminates at a tricritical point. By means of a sparse transfer matrix technique, we have determined the tricritical point [50] as $K_{tc} = 1.6431759(1)$, $D_{tc} = 3.2301797(2)$, and $\rho_{tc} = 0.4549506(2)$ for the vacancy density. The precision improves significantly over that of the existing results [51] $K_{tc} = 1.64(1)$, $D_{tc} = 3.22(2)$, and is considered to be sufficient for our present investigation.

For this model (10.9), however, no cluster Monte Carlo method to flip between vacancies and Ising spins is generally available. Thus, during the simulations, we fixed the total number of vacancies in order to avoid the critical slowing down due to fluctuations in the number of vacancies. This was realized by a recently developed geometric cluster algorithm [37], which moves groups of vacancies and Ising spins on the lattice in accordance with the Boltzmann distribution. A detailed account of the geometric cluster method can be found in Refs. [37].

The Monte Carlo simulations were performed at the tricritical point. For finite systems, however, the total number of vacancies V at tricriticality is generally not an integer, so that the actual simulations took place at $V_- = [V_{tc}] = [\rho_{tc} L^2]$ and $V_+ = [V_{tc}] + 1$, where square brackets $[]$ denote the integer part of the number in it. For a sampled quantity A , its value A_{tc} at the tricritical point is approximated as

$$A_{tc} = \frac{A_+(V_{tc} - V_-) + A_-(V_+ - V_{tc})}{V_+ - V_-}, \quad (10.10)$$

and the statistical error margin of A_{tc} is taken as

$$\delta A_{tc} = \frac{1}{V_+ - V_-} \sqrt{[\delta A_+(V_{tc} - V_-)]^2 + [\delta A_-(V_+ - V_{tc})]^2}. \quad (10.11)$$

Since we are interested in geometric properties of the Blume-Capel model, the aforementioned geometric clusters have to be constructed with bond probability $0 \leq p \leq 1$ during the sampling procedure. This was realized by a Swendsen-Wang-like algorithm [13]. For a bond- and vacancy-variable configuration, we denote the total number of geometric clusters as N_c , and the size of the i th cluster as s_i . The following quantities were sampled

$$S_2 = \frac{1}{L^2} \left\langle \sum_i^{N_c} s_i^2 \right\rangle, \quad S_4 = \frac{1}{L^4} \left\langle \sum_i^{N_c} s_i^4 \right\rangle, \quad \text{and} \quad r = \langle S_2 \rangle^2 / \langle S_4 \rangle. \quad (10.12)$$

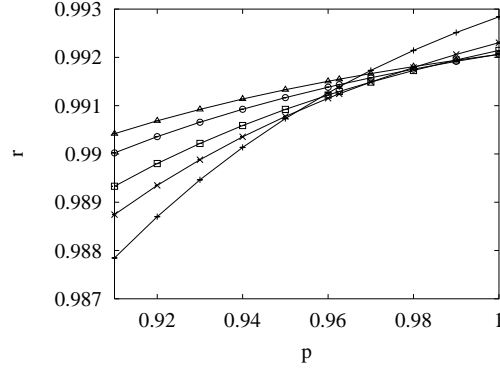


Figure 10.3: The dimensionless ratio r near the random-cluster fixed point p_r for the tricritical Blume-Capel model. The data points $+$, \times , \square , \circ , and \triangle represent $L = 8, 12, 16, 24$, and 32 , respectively.

It can be easily shown that, at the random-cluster fixed point p_r , the quantity S_2 is just the magnetic susceptibility, and the dimensionless ratio r plays a role as the universal Binder cumulant [52] in the Potts model.

Periodic boundary conditions were applied, and near the random-cluster fixed point $p_r = 1 - \exp(-2K_{tc}) \approx 0.96260999$, the system sizes were taken in the range $8 \leq L \leq 120$. Figure 10.3 shows parts of the Monte Carlo data of the dimensionless ratio r , in which the slope of r decreases as the system size L increases. This indicates that the bond-dilution exponent y_p is a negative number, and thus the random-cluster fixed point p_r is stable, as expected. Moreover, according to the least-square criterion, we fitted the following equation to the data of r .

$$r = r_0 + r_1(p - p_c)L^{y_p} + r_2(p - p_c)^2L^{2y_p} + \dots + r_6(p - p_c)^6L^{6y_p} + b_1L^{y_1} + b_2L^{y_2} + b_3L^{y_3} + c_1(p - p_c)L^{y_1+y_p} + n_1(p - p_c)^2L^{y_p}. \quad (10.13)$$

Here, the amplitudes r_i , b_i , c_i , and n_i are unknown parameters, and the term with n_1 accounts for the fact that the bond-dilution scaling field is a nonlinear function of $(p - p_c)$. The terms with b_i describe finite-size corrections, and the associated exponents were simply taken as integer numbers as $y_1 = -1$, $y_2 = -2$, and $y_3 = -3$. Furthermore, we fixed p_c at the random-cluster fixed point $p_r \approx 0.96260999$. After a cutoff for small system sizes $L \leq 10$, we obtain $y_p = -0.48(2)$, in agreement with the prediction $y_p = -19/40$ (Tab. 10.1).

According to Fig. 10.1(b), for tricritical systems, Potts and KF clusters are described by the same critical exponent, i.e., $X_h^{(p)} = X_h$. Thus, we fitted the following equation to the data of S_2 for Potts clusters

$$S_2 = L^{-2X_h}(a_0 + a_1L^{y_1} + a_2L^{y_2} + a_3L^{y_3}). \quad (10.14)$$

Here, the leading finite-size effect arises from the bond-dilution field, so that we set $y_1 = y_p = 2 - X_p = -19/40$, $y_2 = 2y_1 = -19/20$, and $y_3 = -2$. After a cutoff for small system sizes $L \leq 10$, the fit yields $X_h = 0.0747(5)$, in good agreement with $X_h^{(r)}(g = 5) = 3/40$ in Tab. 10.1.

We expect that an unstable geometric-cluster fixed point occurs in the range $0 < p_g < p_r$ for the tricritical Blume-Capel model. This is clearly shown by Fig. 10.4, indicating $p_g \approx 0.62$. Thus, we performed extensive simulations in the range $0.61 \leq p \leq 0.65$, and the system sizes were taken as $8 \leq L \leq 160$. We fitted Eq. (10.13) to the Monte Carlo data of r . After a cutoff for small system sizes $L \leq 12$, we obtain $p_c = 0.6227(1)$ and $y_p = 0.4254(6)$, where the statistical error bars are two standard deviations in the fit. The value of y_p is in good agreement with the expected value $y_p = 2 - X_p = 17/40$ (Tab. 10.1).

At the geometric-cluster fixed point p_g , Tab. 10.1 predicts $X_h^{(g)}(g = 5) = 21/160$. Thus, we fitted the

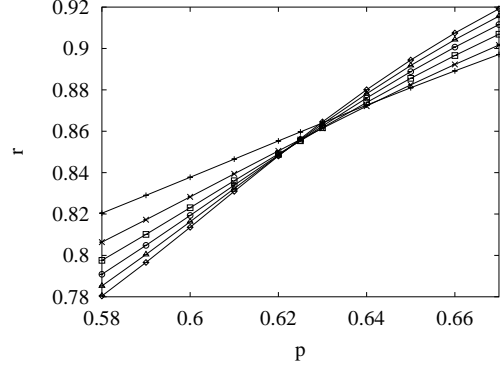


Figure 10.4: The dimensionless ratio r near the geometric-cluster fixed point p_g for the tricritical Blume-Capel model. The data points $+$, \times , \square , \circ , \triangle , and \diamond represent $L = 8, 12, 16, 20, 24$, and 28 , respectively.

following equation to the data of S_2 near p_g

$$S_2 = L^{-2X^{(g)}} [s_0 + s_1(p - p_c)L^{y_p} + s_2(p - p_c)^2L^{2y_p} + \dots + s_6(p - p_c)^6L^{6y_p} + b_1L^{y_1} + b_2L^{y_2} + b_3L^{y_3} + c_1(p - p_c)L^{y_1+y_p} + n_1(p - p_c)^2L^{y_p}] . \quad (10.15)$$

Again, the exponents for finite-size corrections were simply taken as $y_1 = -1$, $y_2 = -2$, and $y_3 = -3$. After a cutoff for small systems $L \leq 12$, we obtain $p_c = 0.62265(10)$ and $X_h^{(g)} = 0.1311(5) \approx 21/160 = 0.13125$.

For the general Blume-Capel model described by Eq. (10.9), the RG flows should, in principle, be shown in the three-parameter space (p, K, D) . For simplicity, we only consider its projection onto the plane (p, K) , which is schematically shown in Fig. 10.5. Areas $K < K_{tc}$ and $K > K_{tc}$ represent a critical sheet and a region for first-order phase transitions, respectively. For $K \rightarrow \infty$, the percolation problem of this Blume-Capel model reduces to the bond-percolation model [8, 12], which has a percolation threshold is $p_c = 1/2$ on the square lattice. For $K < K_{tc}$, the whole area above the solid line, $p = 1 - \exp(-2K)$, is within the percolation thresholds, and critical properties are governed by the fixed point ‘P1’, in the universality class of the tricritical $q = 1$ Potts model. Besides this, there are four other fixed points, ‘I’, ‘TI’, ‘GT’, and ‘BP’, which represent the Ising, the tricritical Blume-Capel, p_g of the tricritical Blume-Capel, and the bond-percolation model, respectively. Arrows show the direction of the RG flows.

The tricritical $q = 3$ Potts model

It has been known [8] that, by including vacancies in the ‘pure’ Potts model (10.1), the tricritical Potts model can be obtained. The Hamiltonian of the tricritical $q = 3$ Potts model on the square lattice reads

$$\mathcal{H}/k_B T = -K \sum_{\langle i, j \rangle} \delta_{\sigma_i, \sigma_j} (1 - \delta_{\sigma_i, 0}) - D \sum_k \delta_{\sigma_k, 0} \quad (\sigma = 0, 1, 2, 3) . \quad (10.16)$$

By means of a sparse transfer matrix technique, we have determined the tricritical points [50] as $K_{tc} = 1.649923(5)$, $D_{tc} = 3.152173(10)$, and $\rho_{tc} = 0.34572(5)$ for the vacancy density.

Analogously, during the Monte Carlo simulations, we fixed the total number of vacancies, and thus used a combination of the Wolff [14] and the geometric cluster [37] steps. The system sizes were taken as $8 \leq L \leq 160$, and periodic boundary conditions were applied. The sampled quantities include S_2 , S_4 , and a dimensionless ratio $Q = \langle S_2 \rangle^2 / \langle 3S_2^2 - 2S_4 \rangle$. Compared to the aforementioned ratio r , the quantity Q is more in line with the well-known Binder ratio [52]. Near the random-cluster fixed point $p_r = 1 - \exp(-K_{tc}) \approx 0.808$, the Monte Carlo data of Q also reveal that the bond-dilution scaling field is irrelevant.

Figure 10.6 shows parts of the Monte Carlo data of Q in the range $p < p_r$, and indicates the geometric-cluster fixed point $p_g \approx 0.64$. According to the least-square criterion, we fitted Eq. (10.13) to the data

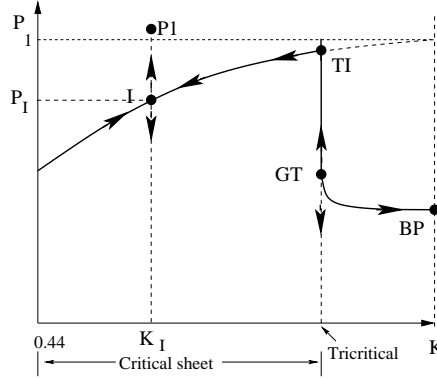


Figure 10.5: RG flows diagram of the Blume-Capel model in the plane (K, P) . The areas $K < K_{tc}$ and $K > K_{tc}$ represent a critical sheet and the region for first-order phase transitions, respectively. The model reduces to the bond-percolation model for $K \rightarrow \infty$, which has a percolation threshold ‘BP’ at $p = 1/2$. There are in total 5 fixed points, ‘I’, ‘P1’, ‘TI’, ‘GT’, and ‘BP’, representing the Ising, the tricritical $q = 1$ Potts, and the tricritical Blume-Capel, the geometric-cluster fixed point of the tricritical Blume-Capel, and the bond-percolation model, respectively. Arrows show the direction of the RG flows.

of Q in the range $0.62 \leq p \leq 0.66$. The value of y_p is fixed at $2 - 2X_r = 25/84$ (Tab. 10.1), we obtain $p_g = 0.6395(2)$, with two standard deviations for the error bar.

We illustrate the data for S_2 at $p_g = 0.6395(2)$ in Fig. 10.7 versus $L = L^{-15/66}$. The approximate linearity indicates that $X_h^{(g)} = 15/112$, as predicted in Tab. 10.1. Moreover, we fitted Eq. (10.15) to the data of S_2 . After a cutoff for small system sizes $L \leq 12$, we obtain $X_h^{(g)} = 0.1337(6)$, in good agreement with $X_h^{(g)} = 15/112$.

The dilute $q = 4$ Potts model

The $q = 4$ Potts model is a marginal case, not only because the second-leading thermal scaling field is marginal $y_{t2} = 0$ [22, 48], but also the bond-dilution exponent $y_p = 0$. We investigate a dilute $q = 4$ Potts model Eq. (10.16) at a point where the second-leading thermal field vanishes. By means of the transfer matrix technique, we have determined this point [50] as $K_c = 1.45790(1)$, $D_c = 2.478438(2)$, and $\rho_c = 0.21207(2)$ for the vacancy density. Analogously, the Monte Carlo simulations use a fixed-vacancy-density ensemble. Periodic boundary conditions were applied, and the system sizes were taken in the range $8 \leq L \leq 280$. At the random-cluster fixed point p_r , we find that Eq. (10.14) is sufficient to describe the data of S_2 , and finite-size corrections decay very rapidly with the leading exponent $y_1 = -2.3(2)$. Furthermore, the fit yields that the magnetic exponent $X_h = 0.1248(3)$, in good agreement with $X_h = 1/8$. This indicates that, as expected, logarithmic corrections due to the marginal second-leading thermal field are absent for the dilute $q = 4$ Potts model at this point. For Potts clusters ($p = 1$), we find that the data of S_2 cannot be described by Eq. (10.14) anymore. Instead, we used the following equation during the numerical fit

$$S_2 = L^{-2X_h} (a_0 + a_1/\ln L + a_2/\ln^2 L + a_3 L^{-2}) . \quad (10.17)$$

This reflects that, for the $q = 4$ Potts model, the bond-dilution scaling field is indeed marginal.

10.1.4 Discussion

We have determined geometric properties of the general critical and tricritical Potts model in two dimensions. Apart from the random-cluster fixed point p_r , we find a geometric-cluster fixed point p_g . Moreover, on the basis of the theory of the Coulomb gas, we predict critical exponents near p_g , which include the magnetic,

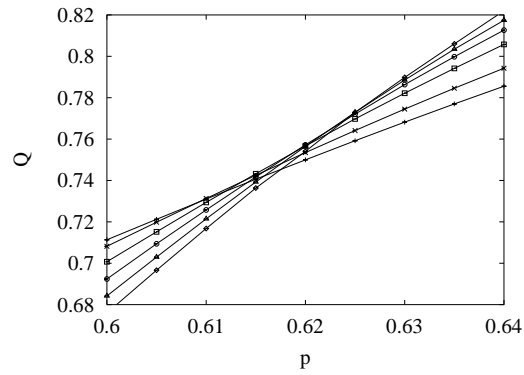


Figure 10.6: The dimensionless ratio Q near the geometric-cluster fixed point p_g for the tricritical $q = 3$ Potts model. The data points $+$, \times , \square , \circ , \triangle , and \diamond represent $L = 12, 16, 24, 32, 40$, and 48 , respectively.

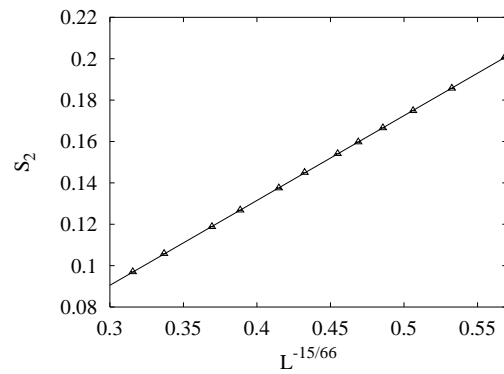


Figure 10.7: The quantity S_2 at the geometric-cluster fixed point p_g for the tricritical $q = 3$ Potts model, versus $L^{-2X_h^{(g)}} = L^{-15/66}$. The system sizes are in the range $12 \leq L \leq 160$.

Table 10.2: The hull-cluster scaling dimensions X_H for the critical and the tricritical Potts model in two dimensions. The superscripts (r) and (g) represent the random- and the geometric-cluster fixed point, p_r and p_g , respectively.

	Critical Potts model					Tricritical Potts model			
q	0	1	2	3	4	3	2	1	0
$X_H^{(r)}$	0	1/4	1/3	2/5	1/2	4/7	3/5	5/8	2/3
$X_H^{(g)}$	3/4	2/3	5/8	7/12	1/2	5/12	3/8	1/3	1/4

the thermal, and the bond-dilution exponent, shown in Tab. 10.1. We have performed extensive Monte Carlo simulations, and confirmed some predictions. As another example, we consider the fractal dimension of the hull or external perimeter of a cluster, which consists of all the absent bonds surrounding the cluster of interest. For the critical Potts model, exact values of the hull-cluster scaling dimension $X_H^{(r)}$ near the random-cluster fixed point p_r have already been given [6] as

$$X_H^{(r)} = (g - 2)/g, \quad (10.18)$$

with g the coupling constant. By assuming that this formula applies to the tricritical branch of the Potts model, and according to the relation $gg' = 16$ between the fixed points p_r and p_g , we obtain near the geometric-cluster fixed point p_g

$$X_H^{(g)} = (8 - g)/8. \quad (10.19)$$

The values of $X_H^{(r)}$ and $X_H^{(g)}$ for integers $0 \leq q \leq 4$ are listed in Tab. 10.2.

From Tab. 10.1, the geometric-fixed point p_g of the bond-percolation model corresponds to p_r of the tricritical $q = 0$ Potts model.

10.2 The critical and the tricritical Ising model in three dimensions

Using the Wolff and geometric cluster algorithms and finite-size scaling analysis, we investigate the critical Ising and the tricritical Blume-Capel model with nearest-neighbor interactions on the simple-cubic lattice. The sampling procedure involves the decomposition of the Ising configuration into geometric clusters, each of which consists of a set of nearest-neighboring spins of the same sign connected with bond probability p . These clusters include the well-known Kasteleyn-Fortuin clusters as a special case for $p = 1 - \exp(-2K)$, where K is the Ising spin-spin coupling. A dimensionless ratio R is then defined on the basis of the size distribution of these geometric clusters. We observe that, unlike the case of two-dimensional tricriticality, the percolation threshold of geometric clusters coincides with Kasteleyn-Fortuin clusters. Further, we determine the corresponding red-bond exponents as $y_r = 0.757(2)$ and $0.501(5)$ for the critical Ising and the tricritical Blume-Capel model, respectively. On this basis, we conjecture $y_r = 1/2$ for the latter model.

10.2.1 Introduction

Second-order thermodynamic transitions are generally accompanied by long-range correlations both in time and space. It is thus plausible that the precise microscopic structure of the system under consideration becomes unimportant as far as the universal aspects of the transition are concerned, and transitions in many different physical systems can be within the same universality class. It has been suspected long time ago [1–6] that, as indicated by the divergence of spatial correlation lengths, thermodynamic singularities near a critical point can be represented in terms of some sort of ‘geometric clusters’. For instance, one may relate spontaneous long-range order below a critical temperature to the formation of an ‘infinite’ cluster. As early as in 1967, Fisher [1] introduced a phenomenological droplet model for the two-dimensional Ising model, in which ‘geometric clusters’ consist of nearest-neighboring (NN) Ising spins of the same sign. These clusters are referred to as Ising clusters, and topological considerations imply [7] that its percolation threshold coincides with the thermal critical point in two dimensions, at least for the square lattice. However, it can also be shown [7] that Ising clusters are too ‘dense’ to correctly describe critical correlations of the Ising model.

For the q -state Potts model (for a review, see Ref. [8]), which includes the Ising model as a special case $q = 2$, a solution was given by Kasteleyn and Fortuin [9, 10] in 1969. The Hamiltonian of a lattice Potts model with nearest-neighbor (NN) interactions only can be expressed as

$$\mathcal{H}/k_{\text{B}}T = -K_p \sum_{\langle ij \rangle} \delta_{\sigma_i \sigma_j}, \quad (\sigma = 1, 2, \dots, q), \quad (10.20)$$

where the sum $\langle \rangle$ is over all NN pairs and K is the coupling constant. A correct geometric representation of this model can be obtained as follows. For each pair of NN spins in the same Potts state, a bond is placed with a probability $p_{\text{KF}} = 1 - \exp(-K_p)$, such that the whole lattice is then decomposed into groups of spins connected via the occupied bonds, which are known as the Kasteleyn-Fortuin (KF) clusters. The statistical weight of each bond-variable configuration is then given by the partition sum

$$Z(u, q) = \sum_b u^{n_b} q^{n_c} \quad (u = e^{K_p} - 1), \quad (10.21)$$

where the sum is over all bond-variable configurations, and n_b and n_c are the total numbers of bonds and KF clusters, respectively. As early as 1932, this partition sum had already appeared in the work of Whitney [11], and the corresponding model is referred to as the random-cluster model. It can be shown [8–10] that the random-cluster model can be exactly mapped onto the q -state Potts model. The percolation threshold of the former occurs precisely at the thermal critical point in the latter. Scaling properties of KF clusters near criticality are governed by critical exponents of the Potts model (10.20). For instance, the fractal dimension of KF clusters at criticality is identical to the magnetic scaling dimension X_h . In fact, one may view the partition sum (10.21) as a generalization of the Potts model to noninteger q . It also includes some special cases such as $q \rightarrow 0$ and 1, where the latter reduces to the uncorrelated bond-percolation model [12]. It was

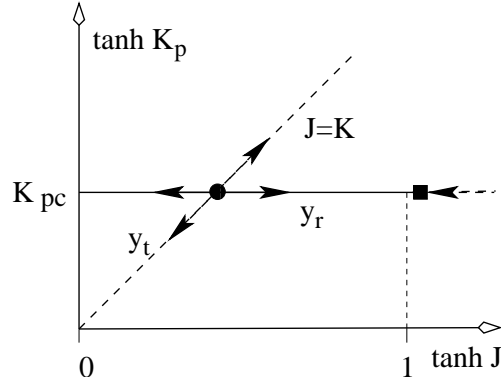


Figure 10.8: Renormalization flow for the mixed Ising model described by Eq. (10.22) with $q = 2$ in two dimensions. The dashed line $J = K_p$ is for the random-cluster representation of the Ising model, and arrows show the directions of renormalization flow.

because of the exact mapping between Eqs. (10.21) and (10.20) that Swendsen and Wang could develop [13] a cluster Monte Carlo method for the Potts model with integer $q = 1, 2, \dots$. This method and its single-cluster version, the Wolff algorithm [14], significantly suppress the critical-slowing-down effect which is very prominent in the standard Metropolis method. Thus, these cluster algorithms have been extensively used in the field of critical phenomena and phase transitions.

The Potts model (10.20) includes the Ising model as a special case for $q = 2$. For other values of q , one can, in the same way as the Ising clusters defined earlier, form Potts clusters [15–17] composed of NN spins in the same Potts state. As expected, these Potts clusters are also on average too ‘large’ [19, 20] to account for thermodynamic singularities of the Potts model. In the context of the renormalization group theory, this can be understood from a ‘mixed’ Potts model, as described by [4, 6]

$$\mathcal{H}/k_B T = -J \sum_{\langle ij \rangle} (\delta_{\tau_i, \tau_j} - 1) \delta_{\sigma_i, \sigma_j} - K \sum_{\langle ij \rangle} \delta_{\sigma_i, \sigma_j}. \quad (10.22)$$

The second term is just the ‘pure’ q -state Potts model (10.20); and the first term contains an auxiliary Potts variable $\tau = 1, 2, \dots, s$. For the case that a pair of NN spins is in the same Potts state both for variables σ and τ , a bond is placed with the probability $p_g = 1 - \exp(-J)$. One can then express the partition sum of Eq. (10.22) in such bond variables, and differentiate the resulting free energy with respect to the parameter s . Taking the limit $s \rightarrow 1$, one obtains the size distribution of geometric clusters composed of NN sites in the same state σ connected with probability p_g . Thus, these clusters include KF and Potts clusters as two special cases for $J = K$ and $p_g = 1$, respectively.

The renormalization flow of the ‘mixed’ Potts model (10.22) in two dimensions is schematically shown [20] in Fig. 10.8, where the dashed line $J = K$ represents the random-cluster model (10.21). Near the random-cluster fixed point $J = K = K_c$, the renormalization flow along the dashed line is governed by the thermal exponent y_t of the Potts model. Further, on the critical line $K = K_c$, the percolation threshold of geometric clusters occurs precisely at $J = J_c = K_c$ [20]. The scaling field parameterizing the critical line near $J = K_c$ is the bond-dilution field, and the associated exponent is called the red-bond exponent y_r . In contrast to the thermal and magnetic ones, the red-bond exponent y_r characterizes geometric properties of the Potts model, and does not have a thermodynamic analogue. The scaling properties of geometric clusters with $p_g > p_{KF}(K_c)$, including Potts clusters, are governed by another fixed point, shown as the black square in Fig. 10.8. This fixed point is irrelevant ($y_r < 0$) in the p_g direction, and we refer to it as the geometric-cluster fixed point [20]. For the two-dimensional Ising model on the square lattice, it occurs in the unphysical region $p_g > 1$ [17].

However, the renormalization scheme in Fig. 10.8 is not generally valid [20] for two-dimensional models.

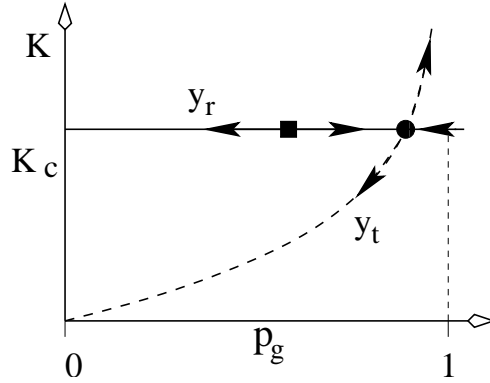


Figure 10.9: Renormalization flow for the two-dimensional tricritical Blume-Capel model (10.23) with D fixed at the tricritical value D_t . The horizontal direction is the bond probability p_g in geometric clusters, and KF clusters are represented by the dashed line $p_g = 1 - \exp(-2K)$.

For instance, we consider the two-dimensional Blume-Capel model [21] with the Hamiltonian

$$\mathcal{H}/k_B T = -K_p \sum_{\langle ij \rangle} s_i s_j + D \sum_k s_k^2, \quad (10.23)$$

where the spins can assume the values ± 1 and 0, and those in state $s = 0$ are referred to as vacancies. The abundance of vacancies is controlled by the chemical potential D . For $D \rightarrow -\infty$, the vacancies are squeezed out, and the model (10.23) reduces to the spin- $\frac{1}{2}$ model. The critical coupling is an increasing function of D , and the critical line $K_c(D)$ terminates at a tricritical point (K_t, D_t) . We mention that, for the Blume-Capel model (10.23), KF clusters should be constructed with the bond-occupation probability $p_{\text{KF}} = 1 - \exp(-2K)$ instead of $p_{\text{KF}} = 1 - \exp(-K)$, due to the difference between the Potts and the Ising Hamiltonian, as shown by Eqs. (10.20) and (10.23), respectively. For the case that the chemical potential D is fixed at the tricritical value D_t , the renormalization flow of the Blume-Capel model [20] is sketched in Fig. 10.9. The bond-dilution field near the random-cluster fixed point $p_{\text{KF}}(K_t)$ is now *irrelevant* ($y_r < 0$); and the percolation threshold p_{g_c} of geometric clusters is smaller than $p_{\text{KF}}(K_t)$. Thus, at tricriticality (K_t, D_t) , the thermodynamic singularities of the Blume-Capel model can be *correctly* represented by geometric clusters *as long as* the bond probability $p_g > p_{g_c}$, including *Ising clusters*. It has been shown [20] that Fig. 10.9 applies to the whole tricritical branch of the Potts model in two dimensions.

As a result of exact solutions, Coulomb gas treatments [22], and conformal field theory [23], the critical behavior of the Potts model (10.20) is now well established in two dimensions. The exact values of a number of critical exponents are known. The geometric- and random-cluster fixed points in Figs. 10.8 and 10.9 were recently conjectured [20] to correspond with a pair of *critical* and *tricritical* Potts systems. These two models share the same conformal anomaly, and are related as $gg' = 16$ in terms of the Coulomb gas coupling constant g [22].

For the three-dimensional Ising model, however, exact information is scarce, so that investigations have to depend on approximations, including Monte Carlo simulations as a powerful tool. A considerable amount of research activities have been carried out [24–31]. For instance, there is some consensus that the thermal and magnetic exponents are $y_t = 1.587$ and $y_h = 2.482$, with uncertainties restricted to the last decimal place. Meanwhile, geometric properties of Ising systems have also received some attention [32–34]. For the spin- $\frac{1}{2}$ model on the simple-cubic lattice, infinite Ising clusters already exist even for zero coupling constant $K = 0$. In the low-temperature phase $K > K_c$, infinite Ising clusters, composed of *minority* Ising spins, occur at about $1.05K_c$ [32–34], before the critical temperature is reached. However, to our knowledge, no systematic investigation has been reported about the renormalization flows such as in shown Figs. 10.8 and 10.9. Particularly, it is not obvious whether or not the percolation threshold of geometric clusters at criticality $K = K_c$ coincides with the random-cluster fixed point; and the red-bond exponent y_r remains to

be determined.

In addition to the critical Ising model, the present work also investigates the tricritical Ising model in three dimensions [35]. Since the upper tricritical dimensionality of $O(n)$ systems is *three*, exact information for some universal quantities is available, one of the rare cases in three dimensions. Exact values of critical exponents can be obtained from renormalization calculations [35] of the Landau-Ginzburg-Wilson Hamiltonian, and even from mean-field analyses. The leading and subleading thermal exponents [35] are $y_{t1} = 2$ and $y_{t2} = 1$, and those magnetic ones are $y_{h1} = 5/2$ and $y_{h2} = 3/2$, respectively. However, no exact results or numerical determinations for the red-bond exponent y_r have been reported to our knowledge; and it is even not obvious where percolation threshold of geometric clusters occurs at tricriticality. It seems thus justified to perform a Monte Carlo investigation for the tricritical Ising model in three dimensions.

10.2.2 Monte Carlo methods and sampled quantities

For simplicity, we chose the spin- $\frac{1}{2}$ and the tricritical Blume-Capel model as the subject of our simulations, so that the Hamiltonian of both models can be expressed by Eq. (10.23). The systems are defined on the $L \times L \times L$ simple-cubic lattice with periodic boundary conditions.

For the spin- $\frac{1}{2}$ model, as described by Eq. (10.23) for $D \rightarrow -\infty$, one can simply apply the Swendsen-Wang and Wolff cluster algorithms. In this case, the critical point on the simple-cubic lattice is known [31] as $K_c = 0.22\,165\,455(3)$, where the number in brackets () is the error margin in the last decimal place. The finite-size analysis in Ref. [31] used a technique that Monte Carlo data for 11 Ising systems were simultaneously fitted, such that universal parameters only occur only once. In the present investigation, the precision of the above determination of K_c is considered to be sufficient.

However, for the general Blume-Capel model (10.23) in the presence of vacancies, the Swendsen-Wang or Wolff cluster simulations become incomplete, since they act only on Ising spins. In this case, the Metropolis method, which allows fluctuations of vacancies, can be used in a combination with these cluster methods. Further, for the special case $D = 2 \ln 2$, a full-cluster simulation has also been developed [25, 36] by mapping the system (10.23) onto a spin- $\frac{1}{2}$ model with two independent variables $\tau_1 = \pm 1$ and $\tau_2 = \pm 1$. Near tricriticality, however, no efficient cluster method is available so far to flip between vacancies and Ising spins. This problem was partly solved in Ref. [38] by means of the so-called geometric cluster method [25, 37]. This algorithm was developed on the basis of spatial symmetries, such as invariance under spatial inversion and rotation operations. It moves groups of Ising spins and vacancies over the lattice in accordance with the Boltzmann distribution, so that the magnetization and the vacancy density are conserved. A combination of the Metropolis, Wolff, and geometric steps significantly suppresses the magnitude of critical-slowness. Such simulations, together with other techniques such as the aforementioned simultaneous finite-size analysis, yield [38] the tricritical point as $K_t = 0.7133(1)$ and $D_t = 2.0332(3)$ on the simple-cubic lattice. The vacancy density ρ_v at the tricritical point is $\rho_v = \rho_{vt} = 0.6485(2)$ [38]. These results are consistent with estimations [39, 40] from other sources $K_t = 0.706(4)$, $D_t = 2.12(6)$, and $\rho_{vt} = 0.652(6)$, within two error margins quoted in the brackets ().

The calculations in the present work include two parts: the Monte Carlo simulations and the formation of geometric clusters with bond-occupation probability p_g . The latter step is performed as follows. For each pair of NN Ising spins of the same sign, a uniformly distributed random number r is drawn, and a bond is placed if $r < p_g$. This is done in an analogous way as in the well-known Swendsen-Wang procedures. In this case, the whole lattice is decomposed into geometric clusters. The size of each cluster, defined as the total number of lattice sites in the cluster, is determined and used to calculate the quantities

$$l_2 = \frac{1}{N^2} \sum_i n_i^2 \quad \text{and} \quad l_4 = \frac{1}{N^4} \sum_i n_i^4, \quad (10.24)$$

where n_i is the size of the i th geometric cluster, and $N = L^3$ is the volume of the system. For KF clusters in which the bond probability $p_g = p_{KF} = 1 - \exp(-2K)$, it can be shown that the quantities in Eq. (10.24) are related to the magnetization m as

$$\langle m^2 \rangle = \langle l_2 \rangle \quad \text{and} \quad \langle m^4 \rangle = 3\langle l_2^2 \rangle - 2\langle l_4 \rangle. \quad (10.25)$$

The first equality in Eq. (10.25) is derived as follows for the spin- $\frac{1}{2}$ model. We denote the numbers of plus and minus spins as N_+ and N_- , respectively, so that the total magnetization is $M = N_+ - N_-$. Since all spins in a KF cluster are of the same sign, M can be written in terms of cluster sizes of KF clusters as $M = \sum_i n_i \tau_i$, where τ_i is the sign of spins in the i th cluster. The sign τ_i assumes $+1$ and -1 with equal probability, and is uncorrelated between different KF clusters. Thus, one has

$$m^2 = \frac{1}{N^2} \sum_i \sum_j n_i n_j \tau_i \tau_j = \frac{1}{N^2} \sum_i n_i^2. \quad (10.26)$$

The derivation of the second equality in Eq. (10.25) follows along similar lines.

On the basis of the quantities l_2 and l_4 , we define a dimensionless ratio R as

$$R = \langle l_2 \rangle^2 / (3 \langle l_2^2 \rangle - 2 \langle l_4 \rangle), \quad (10.27)$$

which is equal to the magnetic ratio $Q = \langle m^2 \rangle^2 / \langle m^4 \rangle$ for KF clusters, i.e., for $p_g = p_{\text{KF}}$. For the bond probability $p_g \neq p_{\text{KF}}$, R will be different from Q ; its value reflects the geometric cluster size distribution. Further, the scaling behavior as a function of the distance $p_g - p_{\text{KF}}$ is governed by the red-bond exponent y_r .

10.2.3 Results

Spin- $\frac{1}{2}$ model

Simulations of the spin- $\frac{1}{2}$ model were performed at $K_c = 0.22\,165\,455(3)$ [31], where the bond-occupation probability in KF clusters satisfies $p_{\text{KF}}(K_c) = 1 - \exp(-2K_c) = 0.35\,809\,124(5)$. The system sizes were taken in the range $6 \leq L \leq 48$, and we sampled the geometric quantities l_2 , l_4 , and R , and the magnetic ratio Q . Several Wolff cluster steps were carried out between consecutive sampling procedures. Part of the data for R is shown in Fig. 10.10, indicating that the percolation threshold of geometric clusters is near $p_{gc} \approx 0.358$, consistent with the random-cluster fixed point $p_{\text{KF}}(K_c)$. According to the least-squares criterion, we fitted the data of R by

$$R(p_g, L) = R_0 + \sum_{k=1}^4 r_k [(p_g - p_{gc}) L^{y_r}]^k + \sum_{j=1}^3 a_j L^{y_j} + c(p_g - p_{gc}) L^{y_1 + y_r} + b(p_g - p_{gc})^2 L^{y_r}, \quad (10.28)$$

where R_0 is the universal number at p_{gc} . The terms with amplitudes r_k describe the effect of the bond-dilution field, and those with a_j accounts for finite-size corrections. We set the exponent $y_1 = y_i = -0.821(5)$ [31], the leading irrelevant exponent of the three-dimensional Ising universality class. Other exponents of the correction terms, as described in Ref. [31], take values as $y_2 = d - 2y_h = -1.964$ and $y_3 = y_t - 2y_h = -3.375$. The term with y_2 arises from the field dependence of the analytic part of the free energy, and that with y_3 is introduced by the nonlinear dependence of the thermal scaling field on the physical magnetic field. The term with amplitude c accounts for the ‘mixed’ effect of the bond-dilution field and the irrelevant thermal field. The last term arises from nonlinear dependence of the bond-dilution field on the bond probability p_g . The data for Q were also included in the fit by Eq. (10.28) with $p_g = p_{\text{KF}}(K_c)$. Further, we included the Q data at K_c , published in Ref. [31]. These data, particular those for larger system sizes $L = 48, 64, 128, \text{ and } 256$, were found very helpful in the numerical analysis. To obtain a satisfactory fit by Eq. (10.28) according to the least-squares criterion, it was necessary to discard the R data for small system sizes $L \leq 6$. We obtain $R_0 = 0.6238(8)$, $p_c = 0.35\,809\,135(15) = p_{\text{KF}}(K_c)$, and $y_r = 0.757(2)$, where the error margins are quoted as two standard deviations. The estimation of R_0 is in good agreement with the Binder ratio $Q = 0.6241(4)$ [31]. We mention that, in Eq. (10.28), the contributions from the terms with b and c are significant. This is indicated by Tab. 10.3, which lists detailed results of the above fit.

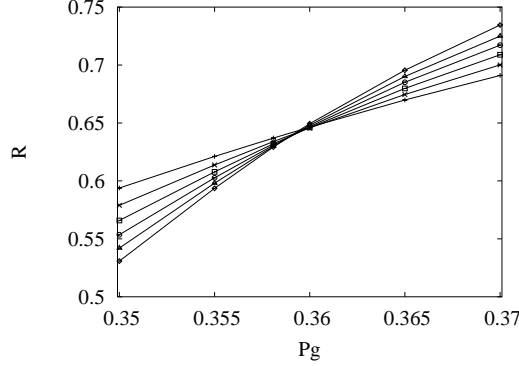


Figure 10.10: Dimensionless ratio R for the critical spin- $\frac{1}{2}$ model in three dimensions, vs. the bond probability p_g . The data points $+$, \times , \square , \circ , \triangle , and \diamond represent finite sizes $L = 12, 16, 20, 24, 28$, and 32 , respectively. The intersections reveal that the location of the percolation threshold agrees with the random-cluster critical point.

Table 10.3: The fit of the dimensionless ratio R for the critical spin- $\frac{1}{2}$ model in three dimensions. The numbers in parentheses are the statistical errors in the last decimal place.

y_r	p_c	R_0	r_1	r_2	r_3
0.757(2)	0.35 809 135(15)	0.6238(5)	-0.811(6)	-1.01(2)	-0.96(3)
r_4	a_1	a_2	a_3	b	c
4.5(5)	0.0965(3)	0.132(3)	1.2(8)	-0.35(2)	0.64(8)

Tricritical Blume-Capel model

Our simulations used a constrained version of the Blume-Capel model described by Eq. (10.23), namely the total number of vacancies is conserved. In this case, the chemical potential D in Eq. (10.23) becomes implicit, and a full-cluster simulation becomes possible by using a combination of Wolff and geometric cluster steps only. A particular feature of such constrained simulations is that they *hardly* suffer from critical-slowness even near the tricritical point. This is consistent with the Li-Sokal criterion [41] which specifies a lower limit for the dynamic exponent, since the constrained specific heat has only reaches a finite cusp instead of being divergent at tricriticality, as already noted in Ref. [38]. Simulations took place at the estimated tricritical point $K_t = 0.7133(1)$ and $\rho_{vt} = 0.6485(2)$. Geometric clusters were formed among Ising spins, and we sampled l_2 , l_4 , R , and Q . The system sizes were taken in the range $6 \leq L \leq 60$. For a finite system L at tricriticality, however, the total number of vacancies $L^3 \rho_{vt}$ is not always an integer. Therefore, the actual simulations were performed at $[L^3 \rho_{vt}]$ and $[L^3 \rho_{vt}] + 1$, where the brackets $[\]$ denote the integer part. Geometric clusters were formed among Ising spins, and we sampled l_2 , l_4 , R , and Q . The value of a sampled quantity at the tricritical point were obtained by a linear interpolation of the Monte Carlo data. For instance, we consider the dimensionless ratio R , and denote the R data at $[L^3 \rho_{vt}]$ and $[L^3 \rho_{vt}] + 1$ as R_a and R_b , respectively. The tricritical value of R and its statistical error margin δR are then

$$R = xR_b + (1 - x)R_a \quad \text{and} \quad \delta R = \sqrt{(x\delta R_b)^2 + [(1 - x)\delta R_a]^2}, \quad (10.29)$$

respectively, where $x = L^3 \rho_{vt} - [L^3 \rho_{vt}]$.

At the tricritical point (K_t, ρ_{vt}) , the bond probability at the random-cluster fixed point is $p_{\text{KF}}(K_t) = 1 - \exp(-2K_t) = 0.7599(1)$. Part of the data for R is shown in Fig. 10.11, which indicates that the percolation

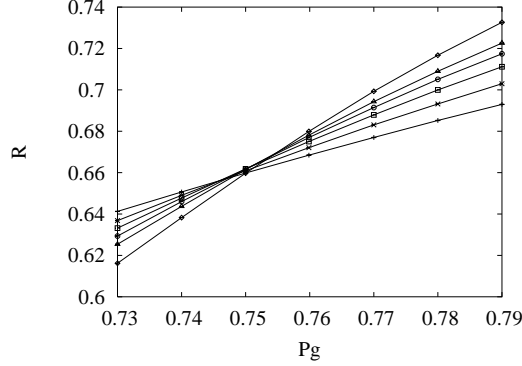


Figure 10.11: Dimensionless ratio R for the tricritical Blume-Capel model in three dimensions, vs. bond probability p_g . The data points $+$, \times , \square , \circ , \triangle , and \diamond represent finite sizes $L = 8, 16, 24, 32, 40$, and 60 , respectively.

Table 10.4: The fit of the dimensionless ratio R for the tricritical Blume-Capel model in three dimensions. The numbers in parentheses are the statistical errors in the last decimal place.

y_r	p_c	R_0	r_1	r_2	r_3
0.501(3)	0.759876(3)	0.690(3)	-0.248(6)	-0.06(1)	0.08(3)
r_4	a_1	a_2	a_3	a_4	a_5
-0.2(2)	-0.0144(5)	0.04(4)	-0.227(5)	1.20(3)	-1.0(2)
a_5	b	c	g		
1.20(3)	4.2(5)	-0.40(5)	-2.8(3)		

threshold of geometric clusters also occurs at $p_{\text{KF}}(K_t)$. The data for R were fitted by

$$\begin{aligned}
 R(p_g, L) = & R_0 + \sum_{k=1}^4 r_k [(p_g - p_{gc})L^{y_r}]^k + a_1/\ln L + a_2/\ln^2 L + a_3/L + \\
 & a_4/L^2 + a_5/L^3 + b(p_g - p_{gc})L^{y_r-1} + c(p_g - p_{gc})^2L^{y_r} + \\
 & g(p_g - p_{gc})/L^2.
 \end{aligned} \tag{10.30}$$

The terms with amplitudes a_1 and a_2 account for logarithmic corrections [35] for the tricritical Ising model in three dimensions, as generally expected at borderline dimensionality of mean-field-like behavior. The last term in Eq. (10.30) arises from the field dependence of the analytical part of the free energy, where the factor $1/L^2$ is obtained as $L^{d-2y_{h1}}$ with $y_{h1} = 5/2$ [35]. In analogy with the procedure for the spin- $\frac{1}{2}$ model, the Q data of Ref. [38] were included in the analysis for R with the corresponding bond probability $p_g = p_{\text{KF}}(K_t)$. After a cutoff for small system sizes $L < 8$, we obtain $R_0 = 0.690(3)$, $y_r = 0.501(3)$, and $p_g = 0.759876(3) \approx p_{\text{KF}}(K_t)$. Detailed results are shown in Tab. 10.4, which indicates that the amplitude a_1 and a_2 for logarithmic corrections are rather small. Further, we observe that the result does not depend on whether the term with a_2 is included. Taking into account the uncertainties of the estimated tricritical point (K_t, ρ_{vt}) , we obtain the red-bond exponent as $y_r = 0.501(5)$.

As mentioned earlier, for the tricritical Ising model in three dimensions, exact values of a number of universal parameters, including the thermal and magnetic exponents, are exactly known as integers or simple fractions [35]. Thus, on the basis of the numerical result $y_r = 0.501(5)$, we *conjecture* that the red-bond exponent $y_r = 1/2$ at the three-dimensional Blume-Capel tricritical random-cluster fixed point.

10.2.4 Discussion

Using Monte Carlo simulations and finite-size analysis, we have investigated geometric properties of the critical Ising and tricritical Ising models in three dimensions. We find that the percolation threshold of critical geometric clusters occurs at the random-cluster fixed point, and the corresponding red-bond exponents are $y_r = 0.757(2)$ and $0.501(5)$ for the above two models, respectively. Just as the thermal and magnetic exponents, the results of the red-bond exponent y_r apply to a large number of systems in the same universality class.

In comparison with the two-dimensional case, geometric properties of the tricritical Ising model are ‘qualitatively’ different in three dimensions. In two dimensions, tricritical KF clusters are so ‘dense’ [20] that the bond-dilution field becomes irrelevant near the random-cluster fixed point; the percolation threshold of geometric clusters occurs before $p_{\text{KF}}(K_t)$, and belongs to a different universality class. In three dimensions, however, the red-bond exponent $y_r > 0$ near $p_{\text{KF}}(K_t)$, so that *only* KF clusters can correctly represent thermodynamic singularities near tricriticality.

As mention earlier, the red-bond exponent y_r describes geometric properties of the system under consideration, and does not have a thermodynamic analogue. As a consequence, the exact value of y_r has not been obtained even for the tricritical Ising model in three dimensions. Although the conjecture $y_r = 1/2$ is in agreement with the numerical determination $y_r = 0.501(5)$, further investigations seem justified. For instance, one may ask the question whether one can derive y_r from mean-field-like considerations.

In addition to the red-bond exponent y_r , there are other geometric critical exponents, such as the fractal dimensions of ‘backbones’ [42–44] and of ‘chemical’ paths [45]. In the percolation theory, these exponents have received considerable attention and are considered to be of some physical relevance. For the $q \rightarrow 1$ Potts model, the red-bond exponent y_r just reduces to the thermal exponent y_t , which is about $1.14(2)$ in three dimensions [46].

Bibliography

- [1] M.E. Fisher, *Physics* (N.Y.) **3**, 25 (1967).
- [2] C.S. Kiang, D. Stauffer, and G.H. Walker, *Phys. Rev. Lett.* **26**, 820 (1971).
- [3] K. Binder, *Ann. Phys.* **98**, 390 (1976).
- [4] A. Coniglio and W. Klein, *J. Phys. A* **12**, 2775 (1980); A. Coniglio and F. Peruggi, *J. Phys. A* **15**, 1873 (1982); A. Coniglio, *Phys. Rev. Lett.* **62**, 3054 (1989).
- [5] M.D. De Meo, D.W. Heermann, and K. Binder, *J. Stat. Phys.* **60**, 585 (1989).
- [6] A. Coniglio, *Nucl. Phys. A* **681**, 451c (2001).
- [7] M. F. Sykes and D.S. Gaunt, *J. Phys. A* **9**, 2131 (1976).
- [8] F.Y. Wu, *Rev. Mod. Phys.* **54**, 235 (1982).
- [9] P.W. Kasteleyn and C.M. Fortuin, *J. Phys. Soc. Jpn.* **46** (Suppl.), 11 (1969).
- [10] C.M. Fortuin and P.W. Kasteleyn, *Physica* **57**, 536 (1972).
- [11] H. Whitney, *Ann. Math. N.Y.* **33**, 688 (1932).
- [12] D. Stauffer and A. Aharony, *Introduction to Percolation Theory* (Taylor & Francis, Philadelphia, 1994).
- [13] R.H. Swendsen and J.S. Wang, *Phys. Rev. Lett.* **58**, 86 (1987).
- [14] U. Wolff, *Phys. Rev. Lett.* **62**, 361 (1989).
- [15] A.L. Stella and C. Vanderzande, *Phys. Rev. Lett.* **62**, 1067 (1989).

- [16] B. Duplantier and H. Saleur, Phys. Rev. Lett. **63**, 2536 (1989).
- [17] H.W.J. Blöte, Y.M.M. Knops, and B. Nienhuis, Phys. Rev. Lett. **68**, 3440 (1992).
- [18] L. Onsager, Phys. Rev. **65**, 117 (1944).
- [19] C. Vanderzande, J. Phys. A **25**, L75 (1992).
- [20] Y. Deng, H.W.J. Blöte, and B. Nienhuis, Phys. Rev. E **69**, 026123 (2004).
- [21] M. Blume, Phys. Rev. **141**, 517 (1966); H.W. Capel Physica **32**, 966 (1966).
- [22] see e.g., B. Nienhuis, *Phase Transitions and Critical Phenomena*, edited by C. Domb and J.L. Lebowitz. (Academic Press, London, 1987), Vol. 11, p. 1.
- [23] J.L. Cardy, *Phase Transitions and Critical Phenomena*, edited by C. Domb and J.L. Lebowitz. (Academic Press, London, 1987), Vol. 11, p. 55.
- [24] D.P. Landau, Physica A **205**, 41 (1994).
- [25] H.W.J. Blöte, E. Luijten, and J.R. Heringa, J. Phys. A **28**, 6289 (1995).
- [26] R. Guida and J. Zinn-Justin, J. Phys. A **31**, 8103 (1998).
- [27] M. Hasenbusch, K. Pinn, and S. Vinti, Phys. Rev. B **59**, 11471 (1999).
- [28] for a review, see e.g., K. Binder and E. Luijten, Phys. Rep. **344**, 179 (2001).
- [29] M. Campostrini, A. Pelissetto, P. Rossi, and E. Vicari, Phys. Rev. E **65**, 066127 (2002).
- [30] Y. Deng and H.W.J. Blöte, Phys. Rev. Lett. **88**, 190602 (2002); Phys. Rev. E **67**, 066116 (2003).
- [31] Y. Deng and H.W.J. Blöte, Phys. Rev. E **68**, 036125 (2003).
- [32] H. Müller-Krumbhaar, Phys. Lett. A **48**, 459 (1974).
- [33] D.W. Heermann and D. Stauffer, Z. Physik A **44**, 339 (1981).
- [34] A. Marro and J. Toral, Physica A **122**, 563 (1983).
- [35] R.B. Stinchcombe, *Phase Transitions and Critical Phenomena*, edited by C. Domb and J.L. Lebowitz. (Academic Press, London, 1984), Vol. 7, p. 152.
- [36] H.W.J. Blöte, L.N. Shchur, and A.L. Talapov, Int. J. Mod. Phys. C **10**, 1137 (1999).
- [37] J.R. Heringa and H.W.J. Blöte, Physica A **232**, 369 (1996); Phys. Rev. E **57**, 4976 (1998).
- [38] Y. Deng and H.W.J. Blöte, unpublished.
- [39] S. Grollau, E. Kierlik, M.L. Rosinberg, and G. Tarjus, Phys. Rev. E **63**, 041111 (2001).
- [40] M. Deserno, Phys. Rev. E **56**, 5204 (1997).
- [41] X.J. Li and A.D. Sokal, Phys. Rev. Lett. **63**, 827 (1989).
- [42] H.J Herrmann and H.E. Stanley, Phys. Rev. Lett. **53**, 1121 (1984).
- [43] P. Grassberger, Physica. A **262**, 251 (1999), and references therein.
- [44] Y. Deng, H.W.J. Blöte, and B. Nienhuis, Phys. Rev. E **69**, 026114 (2004).
- [45] H.J Herrmann, D.C. Hong, and H.E. Stanley, J. Phys. A **17**, L261 (1984).

- [46] G. Paul, R.M. Ziff, and H.E. Stanley, Phys. Rev. E **64**, 026115 (2001).
- [47] R.B. Potts, Proc. Cambridge Philos. Soc. **48**, 106 (1952).
- [48] B. Nienhuis, J. Phys. A **15**, 199 (1982).
- [49] A.A. Belavin, A.M. Polyakov, and A.B. Zamolodchikov, J. Stat. Phys. **34**, 763 (1984); Nucl. Phys. B **241**, 333 (1984); D. Friedan, Z. Qiu, and S. Shenker, Phys. Rev. Lett. **52**, 1575 (1984).
- [50] X.F. Qian, Y. Deng, and H.W.J. Blöte, unpublished.
- [51] P.D. Beale, Phys. Rev. B **33**, 1717 (1986).
- [52] K. Binder, Z. Phys. B: Condens. Matter **43**, 119 (1981).

Edge transitions of two-dimensional tricritical Potts models

Using Monte Carlo techniques and finite-size analysis, we investigate several two-dimensional lattice models with open edges, including the Blume-Capel model and the $q = 1$ and 3 Potts models with vacancies. At bulk tricriticality, we find that the open edges are dominated by the vacancies when the surface couplings K_s and the chemical potential D_s of the vacancies assume the bulk values. When K_s and/or D_s is sufficiently enhanced, an edge phase transition takes place, beyond which spontaneous one-dimensional order occurs on the edges. Edge phase transitions can also be induced by a surface magnetic field H_s . We numerically determine a number of edge critical exponents and derive phase diagrams in terms of K_s , D_s , and H_s . In the low-temperature region, we observe first-order transitions when K_s and D_s are varied; the associated hysteresis loops of surface quantities are remarkably asymmetric. Some further insight in these edge transitions is provided by the exact equivalence of the tricritical $q = 1$ Potts model and the Ising model.

11.1 Introductions

While theoretical physicists frequently study phase transitions in systems with periodic boundary conditions, in reality systems generally have surfaces. Thus, there may be a need to consider the effects due to the presence of surfaces. For a d -dimensional system containing L^d atoms, the relative fraction of atoms at or near a surface is of order $1/L$, and hence for large L it is usually justified to neglect the surface effects on bulk properties of the material. However, near a phase transition, correlations become long-ranged, so that relatively small perturbations can produce large responses. Therefore, surface effects can become significant, and in many cases they cannot be ignored. Indeed surface phase transitions have been the subject of considerable research interest in the past decades [1–11]. Many theoretical and numerical methods have been developed, including mean-field approximations, high- and low-temperature expansions, renormalization group (RG) techniques, conformal field theory, and Monte Carlo simulations etc.

Most of these results apply to three-dimensional systems, and in this context, we briefly review surface critical phenomena of the Ising model on a simple-cubic lattice with two open surfaces in the z direction and periodic boundary conditions in the xy plane [1, 4, 8, 10]. The Hamiltonian of this system can be divided into two parts: bulk terms and surface terms, i.e.,

$$\mathcal{H}/k_{\text{B}}T = -K \sum_{\langle ij \rangle}^{(b)} s_i s_j - H \sum_k^{(b)} s_k - K_s \sum_{\langle lm \rangle}^{(s)} s_l s_m - H_s \sum_n^{(s)} s_n. \quad (11.1)$$

The spins assume values ± 1 , and interactions occur between nearest-neighbor spins. The first two sums account for the bulk, and the last two sums involve spins on the open surfaces. For a finite cube with linear size L , the surface terms concern an area $2L^2$, because there are surfaces both at $z = 0$ and at $z = L$.

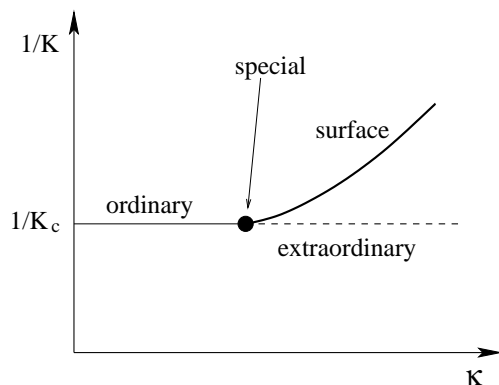


Figure 11.1: Sketch of the surface phase transitions of the Ising model in three dimensions. The vertical axis is the bulk temperature $1/K$, and the parameter $\kappa = (K_s - K)/K$ in the horizontal axis represents the enhancement of the surface couplings. The ‘surface’, the ‘ordinary’, and the ‘extraordinary’ phase transitions are represented by the thick solid, the thin solid, and the dashed line, respectively. The lines meet in a point, shown as the black circle, which is referred to as the ‘special’ phase transition.

In three dimensions, exact information is scarce about the bulk critical behavior of the Ising model described by Eq. (11.1), so that investigations have to depend on approximations. Nevertheless, accurate information has been obtained. For instance, it has been determined [12] that the bulk critical point is $K = K_c = 0.22\ 165\ 455(3)$ and $H = H_c = 0$, and the thermal and magnetic renormalization exponents are $y_t = 1.5\ 868(3)$ and $y_h = 2.4\ 816(1)$, respectively. Surface critical phenomena in this magnetic system (11.1) are now also well analyzed [1, 4, 8, 10]. In the absence of magnetic fields $H = H_s = 0$ and for ferromagnetic couplings $K \geq 0$ and $K_s \geq 0$, the phase diagram is sketched in Fig. 11.1. In the high-temperature region, i.e., the bulk couplings $K < K_c$, the bulk is in the paramagnetic state (‘disordered’), so that the bulk correlations remain finite. However, phase transitions can still occur on the open surfaces when the surface couplings K_s are varied. These transitions, referred to as the ‘surface transitions’, are shown as the curved solid line in Fig. 11.1. Apparently, they belong to the same universality class as Onsager’s Ising model [13] in two dimensions, so that the thermal and magnetic exponents are [13] $y_{ts} = 1$ and $y_{hs} = 15/8$, respectively. At the bulk critical point $K = K_c$, the line of surface transitions terminates at a point (K_c, K_{sc}) , which acts as a multicritical point. For relatively small surface couplings $K_s < K_{sc}$, both the bulk and the surfaces undergo a second-order phase transition at $K = K_c$ when K is varied. However, for larger surface couplings $K_s > K_{sc}$, the surfaces become ferromagnetic at a smaller bulk coupling $K < K_c$, so that the bulk transition $K = K_c$ occurs in the presence of spontaneous surface order. Along the bulk critical line $K = K_c$, the phase transitions for $K_s < K_{sc}$, $K_s = K_{sc}$, and $K_s > K_{sc}$ are referred to as the ‘ordinary’, the ‘special’, and the ‘extraordinary’ transitions, respectively. In order to describe the scaling aspects of these surface transitions, besides the bulk exponents y_t and y_h , additional surface critical exponents are also needed. The ordinary and the extraordinary transitions have one additional relevant surface magnetic scaling field; both the surface thermal and magnetic scaling fields are relevant at the special transition. We denote the corresponding exponents as $y_{hs}^{(o)}$, $y_{hs}^{(e)}$, $y_{ts}^{(s)}$, and $y_{hs}^{(s)}$, respectively, where the superscripts (o), (e), and (s) are for the ordinary, the extraordinary, and the special transitions, respectively. In an analogy with the bulk ones y_t and y_h , exact values of these surface exponents are unavailable. It has been numerically determined [1, 4, 8, 9, 14] that $y_{hs}^{(o)} = 0.737(5)$, $y_{ts}^{(s)} = 0.94(6)$, and $y_{hs}^{(s)} = 1.62(2)$.

The present paper investigates the surface effects on a number of two-dimensional systems. However, in this case, the ‘surfaces’ are just one-dimensional edges. Since one-dimensional systems with short-range interactions are known not to order for any nonzero temperature, the ‘surface transitions’ occurring at $K < K_c$ simply cannot exist on open edges of two-dimensional systems. It may then seem natural that no spontaneous edge order can occur without a long-ranged ordered bulk. In other words, in two dimensions,

it may be expected that only the ordinary transition exists on the one-dimensional surfaces. It has further been argued [1] that the surface dimensionality $d = 2$ is the lower critical dimensionality for the special, the surface, and the extraordinary transitions. This is consistent with exact results for the Ising model in two dimensions. Exact calculations of surface effects in this model [15,16] were not restricted to the critical region but covered in the entire temperature range. At the bulk criticality, it was shown that, for any finite surface coupling K_s , the transition on the open edges is just the ordinary transition. The corresponding surface magnetic exponent is $y_{hs}^{(o)} = 1/2$ [15,16], different from the bulk exponent $y_h = 15/8$ [13]. The surface magnetization density m_s and the surface susceptibility χ_s at the ordinary transition appear to be of logarithmic nature [15,16], i.e.,

$$m_s(H_s) \propto H_s |\ln H_s| \quad (K = K_c, |H_s| \ll 1), \quad (11.2)$$

and

$$\chi_s(t) \propto |\ln |t|| \quad (H_s = 0, |t| = |K - K_c| \ll 1), \quad (11.3)$$

where χ_s is defined as $\partial m_s / \partial H_s$.

The statement that only ordinary transitions occur on the edges can be generalized to the critical branch of the q -state Potts model in two dimensions. For a review of the Potts model, see Ref. [17]. For this model, the nature of the bulk critical singularities is now well established. This is mostly due to exact calculations [18,19], Coulomb gas theory [20], and conformal field theory [3]. In the context of the Coulomb gas theory [20], a sequence of universal exponents can be exactly expressed in terms of a single parameter g , i.e., the coupling strength of the Coulomb gas. The parameter g satisfies $q = 2 + 2 \cos(g\pi/2)$, with $2 \leq g \leq 4$ and $4 \leq g \leq 6$ for the critical and the tricritical branch of the Potts model, respectively. The leading thermal and magnetic exponents of the Potts model are [20,21] $y_t = 3 - 6/g$ and $y_h = (g+2)(g+6)/8g$, respectively. For the ordinary surface transition of the critical Potts model, Cardy [5–7] employed boundary conformal field theory, and expressed the surface magnetic exponent $y_{hs}^{(o)}$ in terms of the bulk thermal exponent y_t as

$$y_{hs}^{(o)} = 2 - 3/(3 - y_t) = 2 - g/2 \quad (2 \leq g \leq 4). \quad (11.4)$$

A remarkable feature of Eq. (11.4) is that $y_{hs}^{(o)}$ is a decreasing function of the Coulomb gas coupling g . In particular, for the $q = 4$ Potts model ($g = 4$), Eq. (11.4) yields $y_{hs}^{(o)} = 0$, so that the surface magnetic scaling field is *marginal*. It seems natural that Eq. (11.4) can also be applied to $g > 4$, just as the above expressions for the bulk exponents y_t and y_h [20,21]. This application then yields that the surface magnetic scaling field is *irrelevant* for the tricritical Potts model. On the other hand, it is known that, near a second-order transition, the strength of critical fluctuations and the sensitivity to perturbations are reflected by the magnitudes of the critical exponents y_t and y_h . For the Potts model, $y_t = 3 - 6/g$ is an increasing function of g , and, for $0 < q < 4$, y_h is larger on the tricritical branch than on the critical one. Thus, one might naively expect that the surface effects, including that of the surface magnetic field H_s , become stronger as g increases. Further exploration of this paradox seems justified.

Recently, boundary conformal field theory has received considerable research interest [22–27]. In the context of statistical physics, this has been applied to the tricritical Ising model in two dimensions. This model is considered to correspond with an integral scattering theory of massive kinks [22], and it preserves superconformal symmetry. By means of factorisable S matrix, fusion rules, and symmetry arguments, various boundary operators were conjectured [23] and the corresponding renormalization flows were constructed. A physical interpretation of these boundary phenomena was then provided by Affleck [24], indicating the possible emergence of spontaneous edge order if the bulk is in the tricritical state. Moreover, this scenario has been numerically confirmed in Ref. [28].

The present paper extends the work in Ref. [28]. First, as a direct illustration of the existence of the edge transitions in tricritical Potts models in two dimensions, we make use of the exact equivalence of the dilute $q = 1$ Potts model with the Ising model in a magnetic field [29]. Thus, the exact information about the edge critical phenomena in the latter model can be reformulated in the language of the former model. Then, using suitable Monte Carlo methods, we simulate the Blume-Capel (BC) model [30,31] and the $q = 3$ Potts model with vacancies. From the finite-size analysis of the numerical data, we derive a number of edge phase diagrams in terms of surface parameters, and determine several surface critical exponents.

11.2 Dilute 1-state Potts model

The dilute Potts model is obtained by including vacancies in the corresponding “pure” Potts model. On the $L \times L$ square lattice with periodic boundary conditions, to which we shall refer as the torus geometry, the Hamiltonian of the dilute q -state model reads

$$\mathcal{H}_P/k_B T = -K \sum_{x,y=1}^L (1 - \delta_{\sigma_{x,y},0}) (\delta_{\sigma_{x,y},\sigma_{x+1,y}} + \delta_{\sigma_{x,y},\sigma_{x,y+1}}) - D \sum_{x,y=1}^L \delta_{\sigma_{x,y},0}, \quad (11.5)$$

where the lattice site is occupied by a vacancy $\sigma = 0$ or a Potts variable with $\sigma = 1, 2, \dots, q$. Nonzero couplings K occur only between Potts variables, and the chemical potential D controls the concentration of the vacancies. In Eq. (11.5), we have introduced the subscript P to represent periodic boundary conditions. For the special case $q = 1$ Eq. (11.5) reduces, apart from a constant, to

$$\mathcal{H}_P/k_B T = -K \sum_{x,y=1}^L \sigma_{x,y} (\sigma_{x+1,y} + \sigma_{x,y+1}) + D \sum_{x,y=1}^L \sigma_{x,y} \quad (\sigma = 0, 1). \quad (11.6)$$

For $D \rightarrow -\infty$, the vacancies are excluded, and the first sum of Eq. (11.6) is just a constant. Nevertheless, the random-cluster representation of Hamiltonian (11.6) corresponds with the bond-percolation model with bond-occupation probability $p = 1 - \exp(-K)$, so that Eq. (11.6) still describes percolation phenomena. In the presence of vacancies, Eq. (11.6) describes a *correlated dilute* bond-percolation model, which can be transformed into the Ising model in a magnetic field. This follows from substitution of $s = 2\sigma - 1$ in Eq. (11.6), which yields

$$\mathcal{H}_P^{(i)}/k_B T = -K^{(i)} \sum_{x,y=1}^L s_{x,y} (s_{x+1,y} + s_{x,y+1}) - H^{(i)} \sum_{x,y=1}^L s_{x,y} \quad (s = \pm 1), \quad (11.7)$$

with the relations

$$K^{(i)} = K/4 \quad \text{and} \quad H^{(i)} = -D/2 + K, \quad (11.8)$$

where the superscript (i) refers to the Ising model. In the absence of a magnetic field $H^{(i)}$, the Ising model (11.7) has a critical point at $K^{(i)} = K_c^{(i)} = \ln(1 + \sqrt{2})/2$ [13]. This point is not percolation-like; it serves as the *tricritical* point of the $q = 1$ Potts system (11.6). Equation (11.8) yields the tricritical point as $K = K_t = 2 \ln(1 + \sqrt{2})$ and $D = D_t = 4 \ln(1 + \sqrt{2})$; the up-down symmetry of Ising spins implies that the tricritical vacancy density is $\rho = 1/2$. Further, it follows from Eq. (11.8) that the leading and the subleading thermal exponents of the tricritical Potts model are equal to the magnetic and the thermal exponent of the Ising model, respectively, so that $y_{t1} = 15/8$ and $y_{t2} = 1$. The leading magnetic exponent is known as $y_{h1} = 187/96$ [20]. In the low-temperature region $K^{(i)} > K_c^{(i)}$, the Ising model undergoes a first-order phase transition when the magnetic field $H^{(i)}$ changes sign. In other words, the dilute $q = 1$ Potts model (11.6) has a line of first-order phase transitions at $D = 2K$ for $K > K_t$.

Because of the attraction between the vacancies, the dilute $q = 1$ model (11.6) is different from the conventional site-bond percolation problem [32]. In the latter system, the vacancies are randomly distributed over the lattice sites, and then bonds are placed with probability $0 \leq p \leq 1$ between all nearest-neighboring occupied sites. Apart from that, sites and bonds are *uncorrelated*. A limiting case is the ‘pure’ site-percolation model, in which the bond-occupation probability is 1. This model is still in the percolation universality, so that no tricritical point exists for the conventional site-bond percolation problem. In contrast, for a correlated dilute q -state Potts model described by Eq. (11.5), it has been found [29, 33] that the tricritical point occurs for any value in the continuous range $0 \leq q \leq 4$.

In order to investigate the surface effects, we define the correlated percolation model (11.6) on an open cylinder, i.e., the $L \times L$ square lattice with periodic and free boundary conditions in the x and the y direction, respectively. As for the three-dimensional case, the surface couplings K_s and the chemical potential D_s can

assume different values from those in the bulk. The Hamiltonian \mathcal{H}_O on the open cylinder can be written as the sum of \mathcal{H}_P in Eq. (11.6) and their difference, which reads

$$\begin{aligned} \mathcal{H}_O/k_B T - \mathcal{H}_P/k_B T = & K \sum_{x=1}^L \sigma_{x,1} \sigma_{x,L} - K \kappa_k \sum_{x=1}^L (\sigma_{x,1} \sigma_{x+1,1} + \\ & \sigma_{x,L} \sigma_{x+1,L}) - D \kappa_d \sum_{x=1}^L (\sigma_{x,1} + \sigma_{x,L}), \end{aligned} \quad (11.9)$$

where $\kappa_k = K_s/K - 1$ and $\kappa_d = D_s/D - 1$ represent the enhancements of the surface coupling and the chemical-potential, respectively. The subscript O is for the open cylinder. The sums in the right-hand side of Eq. (11.9) are only over spins sitting on the edges $y = 1$ and $y = L$. Thus, the surface effects can be regarded to contain two parts: the first term in Eq. (11.9) accounts for the geometric effect due to ‘missing’ neighbors for spins at the surface layers, and the last two sums describe the enhancements of the surface parameters K_s and D_s . Effectively, the first term serves as a perturbation which decreases the correlations along the lines $y = 1$ and $y = L$. After substituting $\sigma = (s + 1)/2$ in Eq. (11.9), one obtains the Ising model on a cylinder with open ends

$$\begin{aligned} \mathcal{H}_O^{(i)}/k_B T - \mathcal{H}_P^{(i)}/k_B T = & \frac{K}{4} \sum_{x=1}^L s_{x,1} s_{x,L} - \frac{K}{4} \kappa_k \sum_{x=1}^L (s_{x,1} s_{x+1,1} + \\ & s_{x,L} s_{x+1,L}) - H_s^{(i)} \sum_{x=1}^L (s_{x,1} + s_{x,L}), \end{aligned} \quad (11.10)$$

with a surface magnetic field $H_s^{(i)}$

$$H_s^{(i)} = [K(2\kappa_k - 1) - 2D\kappa_d]/4. \quad (11.11)$$

Due to the equivalences of Eqs. (11.6) and (11.7), and of Eqs. (11.9) and (11.10), the edge transitions of the Ising model can now be reformulated in the language of the dilute $q = 1$ Potts model. In the high-temperature region $K > K_t$, no transition occurs on the one-dimensional edge. At bulk criticality, the Ising model exhibits an ordinary edge transition at $H_s^{(i)} = 0$, and the surface magnetic exponent is $y_{h_s}^{(o)} = 1/2$ [15, 16]. In the context of the tricritical $q = 1$ Potts model (11.9), this means that, as indicated by the relation (11.11), an edge transition can be induced by varying the surface couplings K_s and the chemical potential D_s . For instance, for the case $\kappa_d = 0$, the edges of the Potts model are dominated by vacancies ($\sigma = 0$) or by Potts variables ($\sigma = 1$) for $\kappa_k < 1/2$ or $\kappa_k > 1/2$, respectively. Since K_s and D_s are temperature-like parameters, we refer to such an edge transition as the ‘special transition’. The surface thermal exponent is simply obtained as $y_{t_s}^{(s)}(q = 1) = 1/2$. In the low-temperature region $K > K_t$, the bulk of the Potts model (11.9) is in a two-phase equilibrium along the line $D/K = 2$, as discussed above. Therefore, a small perturbation due to an enhancement κ_k or κ_d induces a first-order transition, which involves the bulk as well as the edges. Fig. 11.2 sketches the phase diagram of the dilute $q = 1$ Potts model (11.9) for the case $\kappa_d = 0$.

For the $q = 1$ Potts model at bulk tricriticality, Eq. (11.11) yields a line of ‘special’ critical points in the (κ_k, κ_d) plane, as shown in Fig. 11.3.

11.3 Blume-Capel model

The previous section indicates that, also in two-dimensional systems, special phase transitions can occur. However, the dilute $q = 1$ Potts model described by Eq. (11.9) is only a special case. For instance, the coupling constants and the chemical potential in this Potts model are just the magnetic field in the Ising model. In the following two sections, we shall investigate the Blume-Capel (BC) model and the dilute $q = 3$ Potts model.

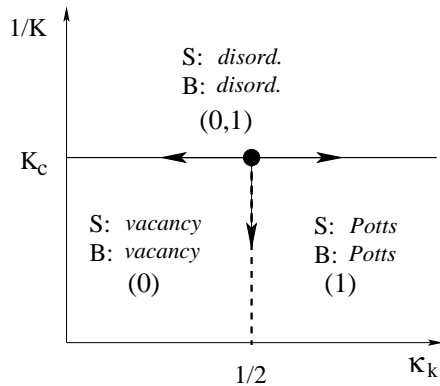


Figure 11.2: Edge phase transitions of the dilute $q = 1$ Potts model in two dimensions, with $K/D = 1/2$ and $\kappa_d = (D_s - D)/D = 0$. For $K < K_c$, both the bulk and the surface are in the ‘disordered’ state, and no edge transition occurs. At bulk tricriticality $K = K_c$, the variation of $\kappa_k = (K_s - K)/K$ yields a ‘special’ edge critical point at $\kappa_k = 1/2$. For $K > K_c$, a line of first-order phase transitions, $\kappa_k = 1/2$, separates the phases dominated by the vacancies and by the Potts variables, respectively. Arrows describe the direction of the renormalization flow.

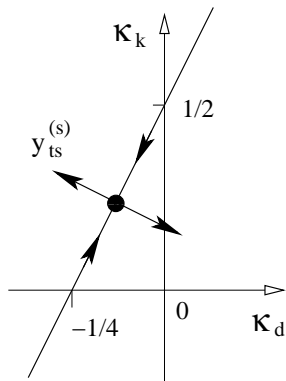


Figure 11.3: Line of ‘special’ transitions in the dilute $q = 1$ Potts model at bulk tricriticality. The fixed point is shown as a black circle, and the arrows represent the direction of the renormalization flow.

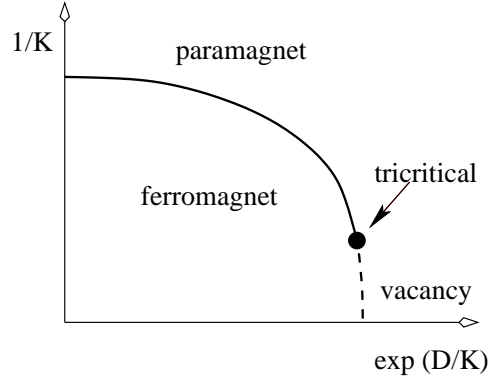


Figure 11.4: Sketch of the bulk phase diagram of the BC model. The tricritical point is denoted as the black circle, the second- and the first-order transition line is represented by the solid and the dashed line, respectively.

The BC model, also referred to as the spin-1 Ising model, was independently introduced by Blume [30] and Capel [31]. This model can be obtained by including vacancies in the Ising model, and it played an important role in the development of the theory of phase transitions and critical phenomena. In the torus geometry, the Hamiltonian reads

$$\mathcal{H}_P/k_B T = -K \sum_{\langle ij \rangle} s_i s_j + D \sum_k s_k^2 \quad (s = 0, \pm 1). \quad (11.12)$$

When the chemical potential D goes to $-\infty$, the vacancies $s = 0$ are excluded, and this model reduces to the spin- $\frac{1}{2}$ Ising model. The critical coupling constant $K_c(D)$ is an increasing function of D , and the critical line $K_c(D)$ terminates at the tricritical point (K_t, D_t) . For $K > K_t$, this line continues as a line of first-order phase transitions. The phase diagram of the bulk transitions is sketched in Fig. 11.4. At the tricritical point, there are four relevant scaling fields; two of them are thermal ones and the other two are magnetic ones. In two dimensions, the renormalization exponents are known as $y_{t1} = 9/5$ and $y_{t2} = 4/5$, and $y_{h1} = 77/40$ and $y_{h2} = 9/8$ [20, 21], respectively. By means of a sparse transfer-matrix technique and finite-size scaling, we located the square-lattice tricritical point [33] as $K_t = 1.643\,175\,9(1)$ and $D_t = 3.230\,179\,7(2)$; the tricritical vacancy density is $\rho_t = 0.454\,950\,6(2)$. This result is obtained from the requirement that both the bulk leading magnetic and energy-energy correlation lengths simultaneously reach their theoretical values. The precision is considered to be sufficient for the present investigation.

On the $L \times L$ open cylinder, as for the dilute $q = 1$ Potts model (11.9), the Hamiltonian of the BC model can be expressed as the sum of the Hamiltonian in the torus geometry and their difference, which reads

$$\begin{aligned} \mathcal{H}_O/k_B T - \mathcal{H}_P/k_B T = & K \sum_{x=1}^L s_{x,1} s_{x,L} - K \kappa_k \sum_{x=1}^L (s_{x,1} s_{x+1,1} + s_{x,L} s_{x+1,L}) + \\ & D \kappa_d \sum_{x=1}^L (s_{x,1}^2 + s_{x,L}^2) - H_s \sum_k (s_{x,1} + s_{x,L}), \end{aligned} \quad (11.13)$$

where H_s is the surface magnetic field. In the right-hand-side of Eq. (11.13), the first term corresponds with the geometric effect, and the remaining three terms describe the effects of the surface parameters K_s , D_s , and H_s .

11.3.1 Bulk criticality $K < K_t$

For bulk couplings $K < K_t$, the phase transition along the critical line $K_c(D)$ is just Ising-like. Thus, in the absence of surface magnetic fields H_s , only the ordinary transitions occur on the open edges, and the

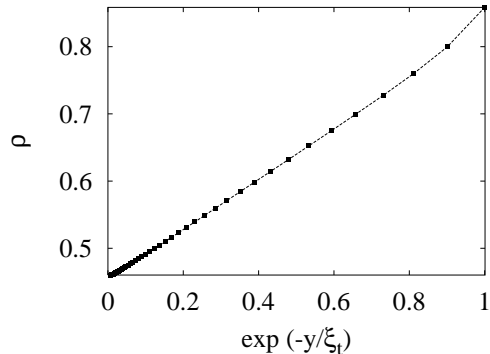


Figure 11.5: Exponential decay of the vacancy density ρ along an $L \times 10L$ cylinder for the tricritical BC model. The system size is chosen as $L = 12$, and r represents the distance to one open end. The correlation length used for the horizontal scale is calculated as $\xi_t = L/(2\pi X_{t1})$, where $X_{t1} = 1/5$ is the bulk thermal scaling dimension. In the middle of the cylinder, ρ is close to the tricritical value $\rho_t = 0.4\ 549\ 506(2)$. Deviations from the exponential behavior occur near the edges (right-hand-side) and near the middle (not visible on this scale).

surface magnetic exponent is $y_{hs}^{(0)} = 1/2$ [15, 16].

11.3.2 Bulk tricriticality: $K = K_t$, $D = D_t$

When the bulk is at the tricritical point, the prediction from conformal field theory described by Eq. (11.4) and the discussions in Sec. II indicate that intriguing phase transitions can occur on the open edges of the BC model.

Ordinary edge transitions

As discussed above, the surface effects can be divided into two parts: the geometric effect and the surface enhancements. To study the former effect only, we investigated the tricritical BC model on an open cylinder with circumference L and length nL for $n = 10$. We took the surface parameters in Eq. (11.13) as $\kappa_k = \kappa_d = 0$ and $H_s = 0$. The system sizes assumed even numbers in the range $8 \leq L \leq 24$. Simulations used a combination of Wolff and Metropolis steps. The former step flips Ising spins, while the latter step also allows fluctuations of the vacancy density. The vacancy density ρ was sampled along the cylinder. The ρ data for $L = 12$ are shown in Fig. 11.5. One observes that, without sufficient enhancements of K_s and D_s , the open edges of the tricritical BC model are mainly occupied by the vacancies. This is analogous to the case of the tricritical $q = 1$ Potts model.

An explanation of the paradox mentioned after Eq. (11.4) can be given as follows. As mentioned in Sec. I, the effect of a temperature-like perturbation is reflected by the bulk thermal exponent y_t , and thus the geometric effect described by the first term in Eq. (11.13) also increases as a function of y_t . For the critical Potts model ($g < 4$), y_t is relatively small, so that the edges maintain strong critical correlations. As g increases, however, the density of the vacancies increases and the edge critical correlations become less strong. As a consequence, the surface magnetic field becomes less ‘effective’. On the tricritical branch ($g > 4$), the geometric effect is so large that the edges are dominated by vacancies, and the surface magnetic field becomes irrelevant. We mention that, although the edges have a considerable degree of disorder, and the decay of this disorder into the bulk can be long-ranged, the bulk tricritical correlation lengths remain divergent. This is reflected by the asymptotically exponential decay of the vacancy density ρ in Fig. 11.5, which takes place with the predicted length scale ξ . Thus, the bulk transition at $K = K_t$ and $D = D_t$ occurs in the presence of ‘disordered’ edges. In analogy with the three-dimensional Ising model, we refer to this phase transition as the ‘ordinary transition’.

Under Cardy's well-known conformal mapping [3], the semi-infinite cylinder is transformed into a semi-infinite plane. The exponential decay of correlations along the cylinder is covariantly transformed into algebraic decay into the bulk of the semi-infinite plane. Thus, the thermal correlation length along the cylinder reads $\xi_t = L/(2\pi X_{t1})$, with the leading thermal scaling dimension $X_{t1} = 2 - y_{t1} = 1/5$ [20, 21]. According to the least-squares criterion, we fitted the ρ data by the formula

$$\rho(r, L) = \rho_t + L^{-2X_{t1}} [\Psi(r) + \Psi(nL - r)] (a_0 + a_1 L^{y_i} + a_2 L^{-2} + \dots), \quad (11.14)$$

with the function

$$\Psi(r) = (e^{r\pi/L} - e^{-r\pi/L})^{-2X_{t1}}, \quad (11.15)$$

where r is the distance to one of the open ends. A justification of Eqs. (11.14) and (11.15) can be found in Refs. [14, 34]. The term $\psi(nL - r)$ in Eq. (11.14) is due to the symmetry between the positions r and $nL - r$. The parameters a_0 , a_1 , and a_2 are unknown constants, and $y_i = -1$ is the leading irrelevant thermal exponent of the tricritical $q = 2$ universality class [20, 21]. For $L \rightarrow \infty$ and $r = L/2$, the bulk vacancy density $\rho(r, L)$ approaches the tricritical value $\rho_t = 0.4\ 549\ 506(2)$ [33]. We fixed the values of y_i and ρ_t , and discarded the data for small system sizes $L \leq 8$ and for small distances $y \leq L/4$. Then, the fit yields $X_{t1} = 0.198(3)$, in good agreement with the theoretical value $X_{t1} = 1/5$.

Special phase transitions

As for the case of the tricritical $q = 1$ Potts model, we expect that the geometric effect in the tricritical BC model can be asymptotically compensated by the enhancements of surface parameters K_s and D_s . To test this expectation, we used a combination of the Wolff and Metropolis methods to simulate the BC model on open cylinders with size $L \times L$. The simulations were performed at bulk tricritical point mentioned above, and we took the surface parameters as $\kappa_d = 0$ and $H_s = 0$. The system sizes assumed 14 odd values in the range $9 \leq L \leq 121$, and we sampled the magnetization density and the vacancy density ρ for several values of κ_k . Further, we defined two dimensionless ratios as

$$Q_b = \langle m_b^2 \rangle^2 / \langle m_b^4 \rangle \quad \text{and} \quad Q_s = \langle m_{s1} m_{s2} \rangle^2 / \langle (m_{s1} m_{s2})^2 \rangle, \quad (11.16)$$

where m_b , m_{s1} , and m_{s2} are the magnetization density on the lines $y = (L + 1)/2$, $y = 1$, and $y = L$, respectively. These dimensionless quantities are closely related to the Binder ratio, and they are useful in Monte Carlo analyses of critical points, because their asymptotic values at criticality are universal.

The absolute value of the surface magnetization $|m_s|$ and the edge vacancy density ρ_s for system size $L = 15$ are shown in Figs. 11.6 and 11.7, respectively. These figures illustrate that, for coupling enhancements $\kappa_k > 0.6$, the open edges are dominated by Ising spins so that *spontaneous order* occurs on the one-dimensional edges. Further, the clean intersection of the Q_b data in Fig. 11.8 reveals a second-order phase transition near $\kappa_k = 0.56$. We fitted the data of Q_b and Q_s by the formula

$$Q(\kappa_k, L) = Q_c + \sum_{k=1}^4 a_k (\kappa_k - \kappa_{kc})^k L^{ky_{ts}^{(s)}} + b_1 L^{y_1} + b_2 L^{y_2} + b_3 L^{y_3} + b_4 L^{y_4} + c (\kappa - \kappa_{kc}) L^{y_{ts}^{(s)} + y_1} + n (\kappa - \kappa_{kc})^2 L^{y_{ts}^{(s)}}, \quad (11.17)$$

where the terms with b_1 , b_2 , and b_3 account for finite-size corrections. The exponent $y_1 = y_i = -1$ arises from the leading irrelevant thermal scaling field [20, 21]. More generally, we expect analytic finite-size corrections with exponents $y_j = -n$ with integer $n \geq 1$. Thus, the exponents y_2 , y_3 , and y_4 were taken as -2 , -3 , and -4 , respectively. The term with c describes the 'mixed' effect of the relevant and the irrelevant thermal scaling field, and the last term in Eq. (11.17) is due to the fact that the surface thermal scaling field can be a nonlinear function of κ_k . After a cutoff for small system sizes $L \leq 11$, the fit of Q_b yields $Q_{bc} = 0.765(4)$, $\kappa_{kc} = 0.5660(4)$, and $y_{ts}^{(s)} = 0.407(8)$, and the fit of Q_s yields $Q_{sc} = 0.566(3)$, $\kappa_{kc} = 0.5664(4)$, and $y_{ts}^{(s)} = 0.395(7)$. These two fits are consistent with each other, and the results for $y_{ts}^{(s)}$ are equal to the exact value $2/5$ [23, 24] within the estimated error margins.

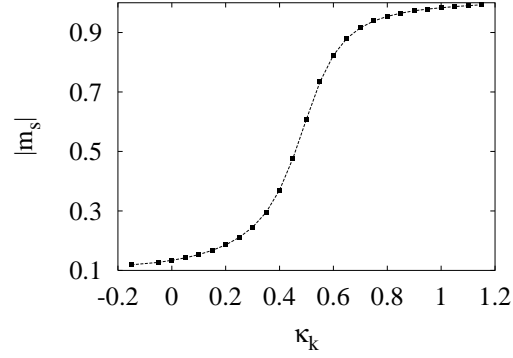


Figure 11.6: Absolute value of the edge magnetization $|m_s|$ of the tricritical BC model vs. coupling enhancement κ_k . The other surface parameters are $\kappa_d = 0$ and $H_s = 0$, and the system size is $L = 15$.

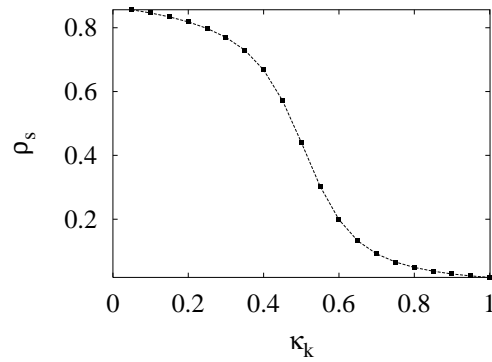


Figure 11.7: Edge vacancy density ρ_s of the tricritical BC model vs. coupling enhancement κ_k . The other surface parameters are $\kappa_d = 0$ and $H_s = 0$, and the system size is $L = 15$.

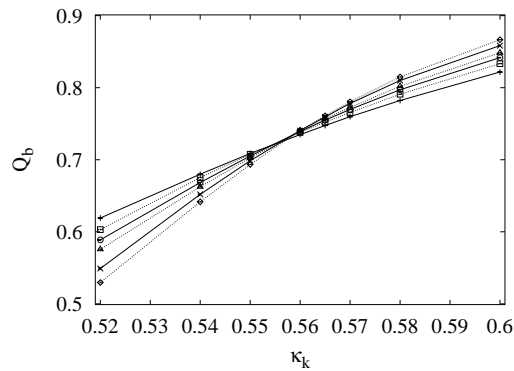


Figure 11.8: Bulk magnetic ratio Q_b of the tricritical BC model vs. coupling enhancement κ_k . The other surface parameters are $\kappa_d = 0$ and $H_s = 0$, and the system sizes are $L = 11$ (+), 15 (\square), 19 (\circ), 23 (\triangle), 31 (\times), and 39 (\diamond).

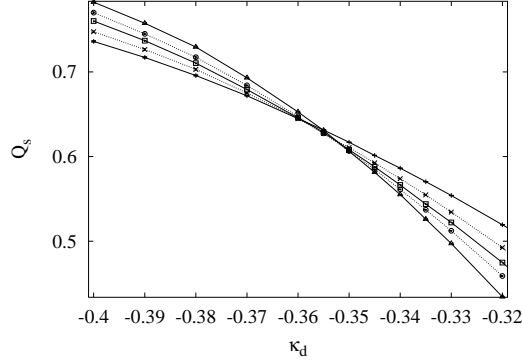


Figure 11.9: Surface magnetic ratio Q_s of the tricritical BC model vs. chemical-potential enhancement κ_d . The other surface parameters are $\kappa_k = 0$ and $H_s = 0$, and the system sizes are $L = 9$ (+), 13 (\times), 17 (\square), 21 (\circ), and 29 (\triangle).

Near the above estimated special transition $\kappa_k = \kappa_{kc}$ and $\kappa_d = 0$, the surface magnetic susceptibility $\chi_s = L\langle m_s^2 \rangle$ was sampled, and the Monte Carlo data were fitted by

$$\chi_s(\kappa_k, L) = r_0 + r_1(\kappa - \kappa_{kc}) + r_2(\kappa - \kappa_{kc})^2 + L^{2y_{hs}^{(s)} - 1} \left[\sum_{k=0}^4 a_k (\kappa - \kappa_{kc})^k L^{ky_{ts}^{(s)}} + b_1 L^{y_1} + b_2 L^{y_2} + b_3 L^{y_3} + c(\kappa - \kappa_{kc}) L^{y_{ts}^{(s)} + y_1} + n(\kappa - \kappa_{kc})^2 L^{y_{ts}^{(s)}} \right]. \quad (11.18)$$

The terms with r_0 , r_1 , and r_2 come from differentiations of the analytical part of the free energy with respect to the surface magnetic scaling field. We fixed the surface thermal exponent $y_{ts}^{(s)}$ at the value $2/5$ [23,24], and obtain $\kappa_{kc} = 0.5658(8)$ and $y_{hs}^{(s)} = 0.914(8)$, where the error margins are quoted as two standard deviations. The corresponding scaling dimension $X_{hs}^{(s)} = 1 - y_{hs}^{(s)} = 0.086(8)$ is marginally consistent with the bulk magnetic scaling dimension $X_h = 3/40$ but also with the exact value $1/10$ [23,24]. We shall come back to this point in Sec. V.

Just as κ_k , the enhancement κ_d of the surface chemical potential also induces a ‘special transition’. This is illustrated by the Q_s data in Fig. 11.9 for the case $\kappa_k = 0$. The fit of the Q_s data by Eq. (11.17) yields a critical point at $\kappa_{dc} = -0.344(2)$. Using the same technique, we have determined a number of special critical points in the parameter space (K_s, D_s) , which are listed in Tab. 11.1. On this basis, the line of special edge transitions is shown in Fig. 11.10. For the limit $K_s \rightarrow \infty$, the edge transition is first-order, and separates a state with edges fully occupied by the vacancies from one with fully magnetized edges. From the relative statistical weights of these phases, the transition is simply obtained as $K_{sc}/D_{sc} = 1$. For the opposite limit $D_s \rightarrow -\infty$, no vacancies occur on the edges. We simulated this limit for system sizes in the range $11 \leq L \leq 111$. We still find a second-order transition at $K_{sc} = K_t(1 + \kappa_{kc}) = 0.1183(8)$. The surface critical coupling strength K_{sc} is quite small in comparison with the bulk tricritical value $K_t = 1.6431759(1)$. Near the critical point K_{sc} , the data of the surface susceptibility χ_s were fitted by Eq. (11.18). We obtain the surface magnetic exponent as $y_{hs}^{(s)} = 0.098(2)$, in good agreement with the exact value $1/10$ [23,24].

As indicated in Fig. 11.10, the line of the special transitions exhibits two bends near the limits $D_s \rightarrow \pm\infty$. To display its behavior for large $D_s \rightarrow -\infty$ in more detail, this line is shown again in Fig. 11.11 in the parameter space (K_s, e^{D_s}) .

Extraordinary phase transitions

In the upper region of the critical line in Fig. 11.10, the edges and the bulk undergo a first- and a second-order transition, respectively, when the bulk coupling K is varied, i.e., the surface magnetization density

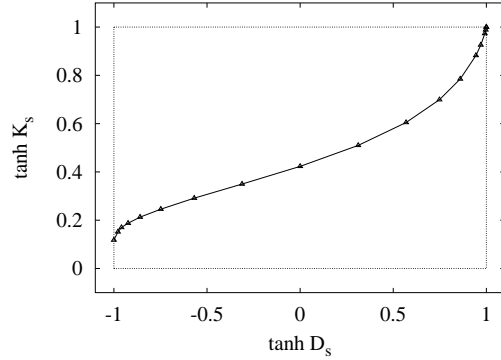


Figure 11.10: Line of special transitions of the tricritical BC model in the parameter space $(\tanh K_s, \tanh D_s)$. The symbols Δ represent the numerical data. When the bulk coupling K is varied, the transition on the edge is first-order in the region above the curve.

Table 11.1: Numerical results for several special edge transition points of the tricritical BC model in the space (K_s, D_s) . The critical values are given in terms of the surface enhancements κ_{kc} and κ_{dc} ; the corresponding values of K_{sc} and D_{sc} are $K_{sc} = K_t(1 + \kappa_{kc})$ and $K_{dc} = D_t(1 + \kappa_{dc})$.

κ_{dc}	$-\infty$	-1.7	-1.6	-1.5	-1.4
κ_{kc}	-0.9280(4)	-0.9050(4)	-0.8964(4)	-0.8845(4)	-0.8686(4)
κ_{dc}	-1.3	-1.2	-1.1	-1.0	-0.9
κ_{kc}	-0.8474(4)	-0.8175(4)	-0.7778(7)	-0.7252(7)	-0.6576(7)
κ_{dc}	-0.8	-0.7	-0.6	-0.45	-0.35
κ_{kc}	-0.5737(8)	-0.4732(8)	-0.3563(9)	-0.1261(8)	-0.0095(9)
κ_{dc}	-0.15	0	0.6		
κ_{kc}	0.3096(8)	0.5662(4)	1.6665(8)		

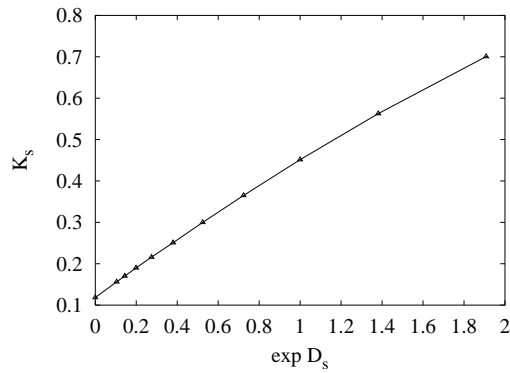


Figure 11.11: Line of special transitions of the tricritical BC model in the parameter space (K_s, e^{D_s}) .

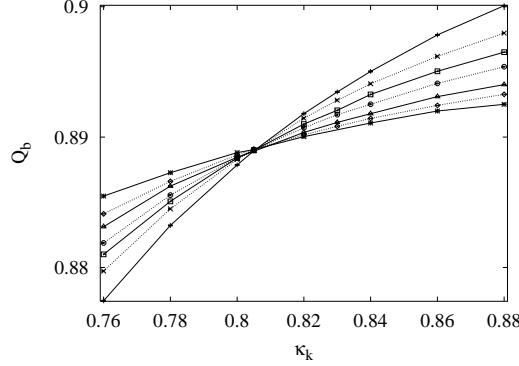


Figure 11.12: Bulk magnetization moment ratio Q_b of the tricritical BC model vs. surface coupling enhancement κ_k . The other surface parameters are $\kappa_d = 0$ and $H_s = 0$. The data points $+$, \times , \square , \circ , \triangle , \diamond , and $*$ represent $L = 7, 9, 11, 13, 17, 21,$ and 29 , respectively. The clean intersection of these data lines implies that, in addition to the ‘special’ transition $\kappa_k = \kappa_{kc} = 0.5662(5)$, there is another ‘fixed’ point at $\kappa_k \approx 0.81$. However, in contrast to Fig. 11.8, the slope of these lines is a decreasing function of the system size L . This means that this fixed point is stable in the κ_k direction.

m_s displays a discontinuity. In comparison with the three-dimensional Ising model, this can be considered to correspond with the coincidence of the ‘surface’ and the ‘extraordinary’ transitions. The existence of spontaneous edge order is only possible because *the bulk is tricritical*. At this point, spins on the edges in effect interact via sufficiently long-ranged bulk correlations, so that also the edge correlations become long-ranged.

It seems reasonable to expect that the bulk critical properties are reflected on the edges even if the edge transition is first order. As a test, we simulated the tricritical BC model for $\kappa_d = 0$ and $\kappa_k > 0.6$. The system sizes were taken in the range $9 \leq L \leq 185$, and part of the Q_b data are shown in Fig. 11.12. The clean intersection in Fig. 11.12 indicates a fixed point near $\kappa_k = 0.81$. The decreasing slope as a function of L indicates that this fixed point is stable in the κ_k direction. Naturally, the question arises what critical exponent governs the renormalization flow in the κ_k direction. For this purpose, we fitted the Q_b data by Eq. (11.17), where the exponent $y_{ts}^{(s)}$ is replaced by $y_{ts}^{(e)}$. After discarding data for small system sizes $L \leq 9$, we obtain $Q_c = 0.892(2)$ and $y_{ts}^{(e)} = -0.80(5)$. We note that, for an arbitrary d -dimensional system, a surface thermal exponent $y_{ts} = -1$ has been reported [35] to occur. However, the result $y_{ts}^{(e)} = -0.80(5)$ is slightly different from this exact value, which dominates the range of the ordinary transitions.

For a further illustration of the edge critical properties in the range of the extraordinary transition, we fitted the m_s^2 data at $\kappa_k = 0.805$, which are listed in Tab. 11.2, by the formula

$$m_s^2 = a_0^2 + L^{-2X_{hs}^{(e)}} (b_0 + b_1 L^{y_{ts}^{(e)}} + b_2 L^{y_i} + b_3 L^{-2} + b_4 L^{-3}), \quad (11.19)$$

where the term a_0 represents the spontaneous edge magnetization density. The exponent $y_{ts}^{(e)}$ was fixed at the estimated value $-0.80(5)$, and we obtain $a_0 = 0.94776(4)$ and $X_{hs}^{(e)} = 0.3987(15) \approx 2/5$. Thus, critical correlations still occur on the edges.

Field-driven edge transition

It seems reasonable that, in analogy with the enhancements of the surface couplings K_s and the chemical potential D_s , the geometric effect can also be compensated by the surface magnetic field H_s . Thus, we simulated the tricritical BC model for surface parameters $\kappa_d = \kappa_k = 0$ but $H_s \neq 0$. The edge magnetization density m_s is shown versus H_s in Fig. 11.13 for system size $L = 32$. It behaves consistently with the

Table 11.2: Monte Carlo data for the second moment m_s^2 of the surface magnetization density at the extraordinary transition in the tricritical BC model. The surface parameters are $H_s = 0$, $\kappa_d = 0$, and $\kappa_k = 0.805$.

L	9	11	13	15	17
m_s^2	.91729(1)	.91560(1)	.91399(1)	.91262(1)	.91145(1)
L	19	21	23	25	29
m_s^2	.91044(1)	.90960(1)	.90886(1)	.90821(1)	.90717(1)
L	33	37	45	55	65
m_s^2	.90631(1)	.90562(1)	.90459(1)	.90367(1)	.90299(1)
L	85	105	145	185	
m_s^2	.90206(1)	.90151(1)	.90076(1)	.90031(1)	

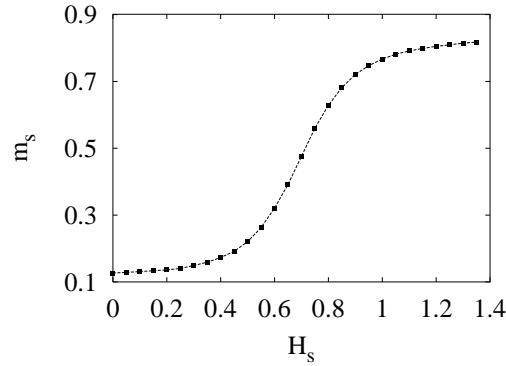


Figure 11.13: Edge magnetization density m_s of the tricritical BC model vs. surface magnetic field H_s . The system size is $L = 32$, and surface parameters are $\kappa_d = 0$ and $\kappa_k = 0$.

above expectation. To test for the presence of a field-driven edge phase transition, we defined the ratio $Q_{sf} = \langle (m_s - \langle m_s \rangle)^2 \rangle^2 / \langle (m_s - \langle m_s \rangle)^4 \rangle$. The Q_{sf} data in the range $8 \leq L \leq 48$ were fitted by Eq. (11.17), and we obtain $Q_{sfc} = 0.4419(10)$, $H_{sc} = 0.6772(10)$, and $y_{hs}^f = 0.405(10) \approx 2/5$. This result, in particular the relevant exponent y_{hs}^f , confirms the existence of the phase transition.

The phase diagram in the parameter space (κ_k, H_s) is sketched in Fig. 11.14 for $\kappa_d = 0$. The numerical results for the estimated critical points, as denoted by \times in Fig. 11.14, are listed in Tab. 11.3. It is clear from Fig. 11.14 that the special transition, at $\kappa_{kc} = 0.5662(4)$, $H_s = 0$, behaves as a ‘multicritical’ point, because several phase transition lines merge in this point.

Table 11.3: Numerical determinations of several field-driven edge transitions for the tricritical BC model in the parameter space (κ_k, H_s) . The surface chemical-potential enhancement is $\kappa_d = 0$.

κ_{kc}	0.45	0.4	0.3	0.2
H_{sc}	0.0661(10)	0.1212(8)	0.2500(10)	0.3880(8)
κ_{kc}	0.1	0	-0.2	-0.5
H_{sc}	0.5315(10)	0.6772(10)	0.9720(10)	1.4080(10)

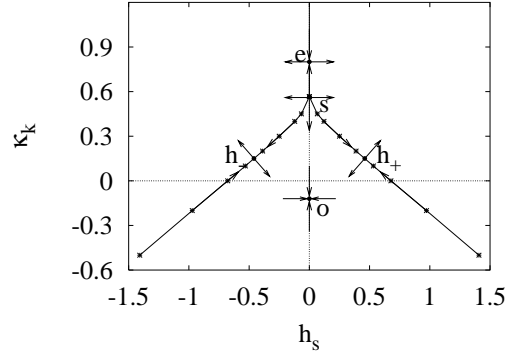


Figure 11.14: Sketch of the phase transitions of the tricritical BC model in the parameter space (κ_k, H_s) with $\kappa_d = 0$. The fixed points are denoted by the black circles, and the arrows show the direction of the renormalization flow.

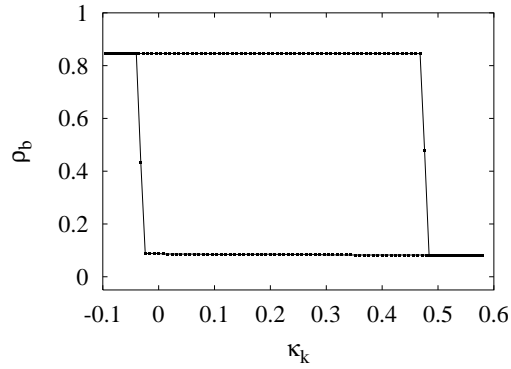


Figure 11.15: Hysteresis loop of the bulk vacancy density ρ_b of the BC model with $K = 1.8$ and $D = 3.55535$, vs. surface coupling enhancement κ_k . The system size is $L = 63$.

11.3.3 Bulk first-order range: $K > K_t$

For $K > K_t$, the bulk of the BC model exhibits a line of first-order transitions, which separates the ferromagnetic phases from the vacancy-dominated phase. On this transition line, just as for the tricritical $q = 1$ Potts model, the surface parameters can also induce first-order transitions. These transitions occur simultaneously on the edges and in the bulk. As an example, we simulated the BC model for $K = 1.8$ and $D = 3.55535$, which is very close to the line of the bulk transitions. The surface parameters were fixed at $\kappa_d = H_s = 0$, and we sampled the bulk and edge vacancy densities, ρ_b and ρ_s , on the lines $y = (L + 1)/2$ and $y = 1, L$, respectively. The hysteresis loops of ρ_b and ρ_s for system size $L = 63$ are shown in Figs. 11.15 and 11.16, respectively. The hysteresis loop of ρ_s is rather *asymmetric*.

According to the investigations in this section, the edge phase transitions of the Blume-Capel model are sketched in Fig. 11.17. The shaded area represents the surface of bulk phase transitions. For $K < K_t$, only the ordinary transitions occur on the edges, so that all renormalization flow lines in this part of the critical surface end in a single fixed point. Along the bulk tricritical line $K = K_t$ and $D = D_t$, there are three fixed points, representing the ordinary, the special, and the extraordinary phase transitions, respectively. For $K > K_t$, there is a line of first-order transitions, which is denoted as the dashed line in Fig. 11.17. On the left- and the right-hand-side of this line, the edges and the bulk of the BC model are dominated by the vacancies and the Ising spins, respectively.

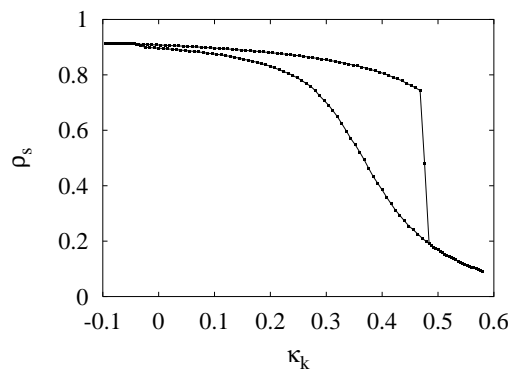


Figure 11.16: Hysteresis loop of the edge vacancy density ρ_s of the BC model with $K = 1.8$ and $D = 3.55535$, vs. surface coupling enhancement κ_k . The system size is $L = 63$.

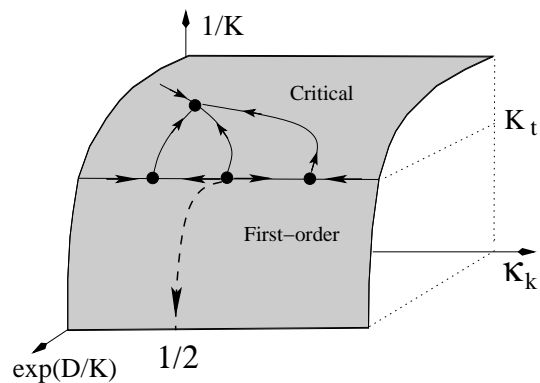


Figure 11.17: Sketch of the edge phase diagram of the BC model for $H_s = 0$. The fixed points are shown as black circles, and the arrows show the renormalization flow.

11.4 Tricritical 3-state Potts model

The Hamiltonian of the dilute $q = 3$ Potts model in the torus geometry is described by Eq. (11.5) with $q = 3$. The bulk phase diagram of this model is analogous to that of the Blume-Capel model described by Eq. (11.12). At tricriticality, the leading and subleading bulk thermal exponents are $y_{t1} = 12/7$ and $y_{t2} = 4/7$, respectively, and the magnetic ones are $y_{h1} = 40/21$ and $y_{h2} = 22/21$ [20, 21]. By means of a sparse transfer-matrix technique, the tricritical point on the square lattice has been determined [33] as $K_t = 1.649\,913(5)$ and $D_t = 3.152\,173(10)$; the tricritical vacancy density is $\rho_t = 0.34\,572(5)$.

On the $L \times L$ open cylinder, the Hamiltonian of the dilute $q = 3$ Potts model reads

$$\begin{aligned} \mathcal{H}_O/k_B T - \mathcal{H}_P/k_B T = & K \sum_{x=1}^L \delta_{\sigma_{x,1}, \sigma_{x,L}} (1 - \delta_{\sigma_{x,1}, 0}) - K \kappa_k \sum_{x=1}^L [\delta_{\sigma_{x,1}, \sigma_{x+1,1}} \\ & (1 - \delta_{\sigma_{x,1}, 0}) + \delta_{\sigma_{x,L}, \sigma_{x+1,L}} (1 - \delta_{\sigma_{x,L}, 0})] - D \kappa_d \sum_{x=1}^L (\delta_{\sigma_{x,1}, 0} + \delta_{\sigma_{x,L}, 0}) - \\ & \frac{H_{s1}}{2} \sum_{k=1}^L (\delta_{\sigma_{x,1,k}} + \delta_{\sigma_{x,L,k}}) + \frac{H_{s1}}{2} \sum_{k=1}^L (\delta_{\sigma_{x,1,2}} + \delta_{\sigma_{x,L,2}}) + \\ & \frac{H_{s1}}{2} \sum_{k=1}^L (\delta_{\sigma_{x,1,3}} + \delta_{\sigma_{x,L,3}}). \end{aligned} \quad (11.20)$$

The surface magnetic field H_{s1} serves to enhance the statistical weight of the Potts state $\sigma = 1$ with respect to states $\sigma = 2$ and $\sigma = 3$.

In analogy with the BC model, the system (11.20) has a line of bulk critical points for $K < K_t$, in the same universality class as the ‘pure’ $q = 3$ Potts model. Thus, only the ordinary phase transition occurs on the open edges, with a surface magnetic exponent $y_{hs}^{(0)} = 1/3$, as predicted by Eq. (11.4). For $K > K_t$, a first-order transition can be induced by enhancements of the surface couplings and the chemical potential. In the present work, we concentrate on the case that the bulk is precisely at the tricritical point.

11.4.1 Special phase transitions

We simulated the tricritical $q = 3$ Potts model (11.20) on the $L \times L$ open cylinder by means of a combination of the Metropolis and Wolff methods, with the linear size in the range $7 \leq L \leq 65$. The bulk parameters were set at the aforementioned tricritical point, and the surface parameters at $H_{s1} = 0$ and $\kappa_d = 0$. The edge order parameter was defined as $m_s^2 = [(\rho_1 - \rho_2)^2 + (\rho_2 - \rho_3)^2 + (\rho_3 - \rho_1)^2]/2$, in which ρ_i is the density of the edge spins in state i . Accordingly, we sampled the ratio $Q_{s1} = \langle m_s^2 \rangle^2 / \langle m_s^4 \rangle$. The Q_{s1} data are partly shown in Fig. 11.18. They indicate a special edge transition near $\kappa_k = 0.7$. The Q_{s1} data were fitted by Eq. (11.17), in which the correction exponents were fixed at $y_1 = y_i = -10/7$ [3], $y_2 = -1$, $y_3 = -2$, and $y_4 = -3$. We obtain $Q_{s1c} = 0.941(2)$, $\kappa_{kc} = 0.702(2)$, and $y_{ts}^{(s)} = 0.282(5)$. Near this special phase transition, i.e., $\kappa_{kc} = 0.702(2)$ and $\kappa_d = 0$, we also analyzed the edge susceptibility χ_s by Eq. (11.18). The fit yields $X_{hs}^{(s)} = 0.133(15)$.

11.4.2 Field-driven edge transitions

Next, we simulated the tricritical $q = 3$ Potts model (11.20) in the presence of the surface magnetic field H_{s1} ; the other surface enhancements were taken as $\kappa_k = \kappa_d = 0$. The system sizes were taken as 10 odd values in the range $7 \leq L \leq 49$, and we sampled the bulk ratio Q_b in Eq. (11.16). Analogous to the case of the tricritical BC model, edge phase transitions are introduced by the field H_{s1} . Nevertheless, the symmetry between the positive and the negative field is now absent. The Q_b data were fitted by Eq. (11.17), and we found two edge transitions at $H_{s1c} = 0.5710(15)$ and $-2.27(3)$. At these two points, the asymptotic values of the ratio Q_b are $0.462(4)$ and $0.232(8)$, respectively; those of the renormalization exponent y_{hs}^f are $0.278(8)$

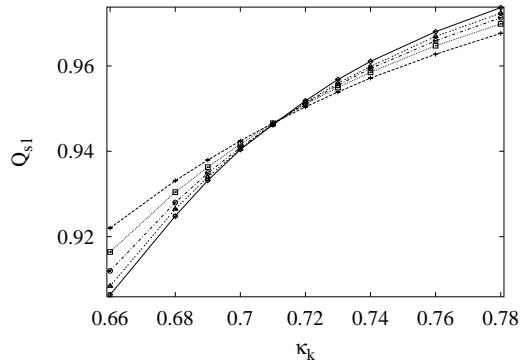


Figure 11.18: Surface magnetic ratio Q_{s1} of the tricritical $q = 3$ model, vs. coupling enhancement κ_k . The data points $+$, \square , \circ , \triangle , and \diamond represent $L = 7, 15, 23, 31,$ and 39 , respectively.

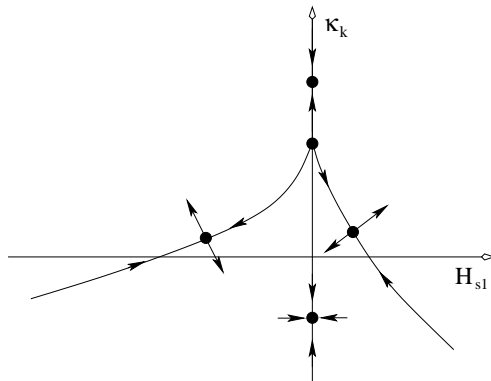


Figure 11.19: Sketch of the edge phase diagram of the tricritical $q = 3$ Potts model in the (H_{s1}, κ_k) plane for $\kappa_d = 0$. The fixed points are denoted by black circles, and the arrows show the renormalization flow.

and 0.280(8), respectively, which are identical to each other within the estimated error margins. From these results, we conjecture the loci of the edge transitions in the plane (κ_k, H_{s1}) as sketched in Fig. 11.19.

In addition to H_{s1} , the surface magnetic fields, H_{s2} and H_{s3} , can also be applied to the Potts system (11.20). Thus, for the case $\kappa_d = \kappa_k = 0$, Fig. 11.20 illustrates the edge phase diagram in the space (H_{s1}, H_{s2}, H_{s3}) .

11.5 Discussion

By means of Monte Carlo simulations and finite-size scaling, we have found that rich surface critical phenomena still occur in two-dimensional systems with short-range interactions only. In particular, when the bulk of a Potts model is at the *tricritical* point, edge transitions are introduced by enhancements of the surface couplings and the chemical potential, and by a surface magnetic field. For the critical branch of the Potts model, however, only the ordinary phase transition exists on the one-dimensional edges. Thus, one concludes that, in two dimensions, it depends on the strength of bulk critical fluctuations whether other types of edge phase transitions can occur.

Let us now address the question what are the exact values of the critical exponents describing the edge phase transitions described in this work. At the special transitions, one has the exact result $y_{ts}^{(s)}(q = 1) = 1/2$ for the tricritical $q = 1$ Potts model. For the case of the tricritical Blume-Capel model, in the context of

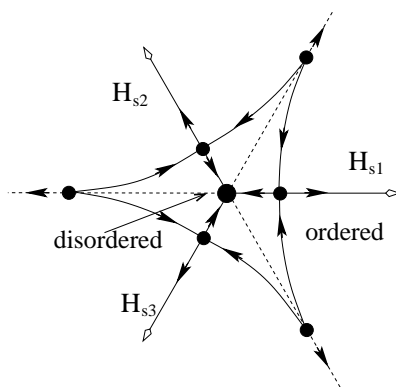


Figure 11.20: Sketch of the edge phase diagram of the tricritical $q = 3$ Potts model as a function the surface fields for $\kappa_d = \kappa_k = 0$. The fixed points are denoted by black circles, and the arrows illustrate the renormalization flows.

Table 11.4: Theoretical predictions of the surface thermal and magnetic exponents, $y_{ts}^{(s)}$ and $y_{hs}^{(s)}$, at the special phase transitions for the tricritical q -state Potts model with $q = 1, 2, 3$, and 4. The parameter g is the Coulomb gas coupling constant.

Model	$q = 0$	$q = 1$	$q = 2$	$q = 3$	$q = 4$
g	6	$16/3$	5	$14/3$	4
$y_{ts}^{(s)}$	$2/3$	$1/2$	$2/5$	$2/7$	0
$y_{hs}^{(s)}$	1	$15/16$	$9/10$	$6/7$	$3/4$

superconformal field theory, it has been predicted that the surface thermal and magnetic exponents are [23,24] $y_{ts}^{(s)} = 2/5$ and $y_{hs}^{(s)} = 9/10$, respectively. For the whole tricritical branch of the Potts model, it has been recently conjectured [28] that, in terms of the Coulomb gas coupling constant g , the exact expressions of $y_{ts}^{(s)}$ and $y_{hs}^{(s)}$ read

$$y_{ts}^{(s)} = (3g - 6)/2g \quad \text{and} \quad y_{hs}^{(s)} = 2 - 8/g, \quad (11.21)$$

respectively. These values of $y_{ts}^{(s)}$ and $y_{hs}^{(s)}$ are one half of the leading and subleading bulk thermal exponents, y_{t1} and y_{t2} , respectively. For the tricritical Potts models with $q = 0, 1, 2, 3$, and 4, the results according to Eq. (11.21) are listed in Tab. 11.4. A remarkable feature is that the expression of $y_{ts}^{(s)}$ in Eq. (11.21) can be simply obtained by substituting $g = 16/g'$ in Eq. (11.4), which describes the surface magnetic exponent $y_{hs}^{(o)}$ at the ordinary phase transitions. The underlying meaning of this procedure is clear for the tricritical $q = 1$ Potts model, because the special transition of this model is just the ordinary transition of the Ising model and the Coulomb gas coupling of these two models are $g = 16/3$ and $g = 3$, respectively. For a pair of critical and tricritical Potts models, we note the relation $gg' = 16$ has been reported [36,37] in other cases. Thus, Eq. (11.21) might mean that the effect of surface couplings K_s in a tricritical Potts model is equivalent with that of the magnetic field H_s in a critical system, the two models being related as $gg' = 16$.

For the tricritical $q = 1$ Potts model, Eq. (11.21) predicts a surface magnetic exponent $y_{hs}^{(s)} = 15/16$. It is known that the bulk Potts magnetic scaling dimension $X_h = 5/96$ is the fractal dimension of Ising clusters, which connect nearest-neighbor Ising spins of the same sign. Thus, one would expect that the exponent $y_{hs}^{(s)}$ governs the scaling behavior of the correlation function $g^{(1)}(r)$, which is defined as the probability that a pair of edge points is in the same Ising cluster. However, it has been shown that the decay of $g^{(1)}(r)$ is described by a geometric scaling dimension $X_p = 1/6$ [28], different from $X_{hs}^{(s)} = 1/16$. The physical interpretation of $y_{hs}^{(s)}$ is so far not clear.

For the tricritical BC model, the results obtained from Eq. (11.21) are in agreement with the predictions in Ref. [23, 24]. In particular, the prediction $y_{ts}^{(s)} = 2/5$ is well confirmed by our numerical result $y_{ts}^{(s)} = 0.395(7)$. However, the exact value $y_{hs}^{(s)} = 9/10$ is only marginally consistent with the result $y_{hs}^{(s)} = 0.914(8)$ for the case $\kappa_d = H_s = 0$ and $\kappa_{kc} = 0.5662(4)$. On the other hand, at the critical point $\kappa_{kc} = -0.9280(4)$, $\kappa_d = -\infty$, the result $y_{hs}^{(s)} = 0.902(2)$ is in good agreement with $y_{hs}^{(s)} = 9/10$. This might be taken as a suggestion that the end point of the line of special transitions at $\kappa_d = -\infty$ in Fig. 11.10 acts as an unstable fixed point with the expected exponent $y_{hs}^{(s)} = 9/10$, while the rest of the line is attracted by another fixed point. However, the numerical evidence is only marginal, and moreover, if the end point at $\kappa_d = -\infty$ is a fixed point, then one would in general expect that the line of special transitions, when parametrized by the activity of the vacancies and the surface coupling enhancement, displays a singularity at $\kappa_d = -\infty$. No sign of such a singularity is visible in Fig. 11.11.

For the tricritical $q = 3$ model, the predictions in Tab. 11.4 are consistent with the numerical determinations $y_{ts}^{(s)} = 0.282(5)$ and $y_{hs}^{(s)} = 0.867(15)$.

The $q = 4$ Potts model is a marginal case for several reasons. First, the critical and the tricritical branch of the Potts model join at $q = 4$. Second, Eq. (11.4) predicts that, at the ordinary phase transitions, the surface magnetic scaling field is marginal, i.e., $y_{hs}^{(o)} = 0$. Third, Eq. (11.21) yields $y_{ts}^{(s)} = 0$, so that the surface coupling and the chemical-potential enhancement become marginal. However, the prediction $y_{hs}^{(s)} = 3/4$ according to Eq. (11.21) is apparently different from the exponent $y_{hs}^{(o)} = 0$. The result $y_{ts}^{(s)} = 0$ also differs from the existing surface thermal exponent $y_{ts} = -1$ [35]. These phenomena indicate that there exists a special phase transition for the $q = 4$ Potts model.

Bibliography

- [1] K. Binder, *Phase Transitions and Critical Phenomena*, edited by C. Domb and J.L. Lebowitz. (Academic Press, London, 1987), Vol. 8, p. 1, and references therein.
- [2] H.W. Diehl, *Phase Transitions and Critical Phenomena*, edited by C. Domb and J.L. Lebowitz. (Academic Press, London, 1987), Vol. 10, p. 76, and references therein.
- [3] J.L. Cardy, *Phase Transitions and Critical Phenomena*, edited by C. Domb and J.L. Lebowitz. (Academic Press, London, 1987), Vol. 11, p. 55, and references therein.
- [4] D.P. Landau and K. Binder, *Phys. Rev. B* **41**, 4663 (1990).
- [5] J.L. Cardy, *Nucl. Phys. B* **240** [FS12], 514 (1984).
- [6] J.L. Cardy, *Nucl. Phys. B* **275** [FS17], 200 (1986).
- [7] J.L. Cardy, *Nucl. Phys. B* **324**, 581 (1989).
- [8] C. Ruge and F. Wagner, *Phys. Rev. B* **52**, 4209 (1995).
- [9] M.P. Nightingale and H.W. Blöte, *Phys. Rev. B* **48**, 13 678 (1993).
- [10] K. Binder, D.P. Landau, and M. Muller, *J. Stat. Phys.* **110**, 1411 (2003).
- [11] H.W. Diehl, *Int. J. Mod. Phys. B* **11**, 3503 (1997).
- [12] M. Campostrini, A. Pelissetto, and E. Vicari, *Phys. Rev. E* **65**, 066127 (2002); Y. Deng and H.W. Blöte, *Phys. Rev. E* **68**, 036125 (2003); and references therein.
- [13] L. Onsager, *Phys. Rev.* **65**, 117 (1944).
- [14] Y. Deng and H.W. Blöte, *Phys. Rev. E* **67**, 066116 (2003).
- [15] B.M. McCoy and T.T. Wu, *Phys. Rev.* **162**, 436 (1967).

- [16] M.E. Fisher and A.E. Ferdinand, Phys. Rev. Lett. **19**, 169 (1967).
- [17] see e.g., F.Y. Wu, Rev. Mod. Phys. **54**, 235 (1982).
- [18] J. Black and V. Emery, Phys. Rev. B **23**, 429 (1981).
- [19] R.J. Baxter, J. Phys. A **13**, L61 (1980).
- [20] B. Nienhuis, *Phase Transitions and Critical Phenomena*, edited by C. Domb and J.L. Lebowitz. (Academic Press, London, 1987), Vol. 11, p. 1, and references therein.
- [21] B. Nienhuis, J. Phys. A **15**, 199 (1982).
- [22] A.B. Zamolodchikov, *Fields, Strings, and Quantum Gravity*, edited by H. Guo, Z. Qiu, and J.L. H. Tye. (Dordun and Breach, 1989).
- [23] L. Chim, Int. J. Mod. Phys. A **11**, 4491 (1996).
- [24] I. Affleck, J. Phys. A **33**, 6473 (2000).
- [25] A. De Martino and M. Moriconi, Nucl. Phys. B **528**, 577 (1998).
- [26] G. Feverati, P.A. Pearce, and F. Ravanini, Phys. Lett. B **534**, 216 (2002); Nucl. Phys. B **675**, 469 (2003).
- [27] R.I. Nepomechie, Int. J. Mod. Phys. A **17**, 3809 (2002).
- [28] Y. Deng and H.W. Blöte, submitted to PRE.
- [29] B. Nienhuis, A.N. Berker, E.K. Riedel, and M. Schick, Phys. Rev. Lett. **43**, 737 (1979).
- [30] M. Blume, Phys. Rev. **141**, 1517 (1966).
- [31] H.W. Capel, Physica **32**, 966 (1966); **33**, 295 (1967).
- [32] see e.g., D. Stauffer and A. Aharony, *Introduction to Percolation Theory* (Taylor & Francis, Philadelphia, 1994).
- [33] X. Qian, H.W.J. Blöte, and Y. Deng (unpublished).
- [34] Y. Deng and H.W. Blöte, Phys. Rev. Lett. **88**, 190602 (2002).
- [35] T.W. Burkhardt and J.L. Cardy, J. Phys. A **20**, L233 (1987).
- [36] B. Duplantier, Phys. Rev. Lett. **84**, 1363 (2000).
- [37] Y. Deng, H.W. Blöte, and B. Nienhuis, Phys. Rev. E **69**, 026123 (2004).

Acknowledgments

The work presented in this thesis is significantly attributed to the support, encouragement, and patience of many people.

The first person I would like to thank is Prof. Henk Blöte. Four days a week we sat in the same office, discussing physics and revising drafts. Often in weekends we spent together enjoying nice weather and discussing physics. I am very impressed by his broad knowledge and great intuition in physics and generosity in every-day life. Henk, your influence on my academic and social life is much more than I can express in words. You are my mentor forever.

I profited a lot from the fruitful and frequent discussions in physics with Dr. Jouke Heringa and from his computer wizardry. Thank you, Jouke, for your patience, kindness, and continuing willingness to help.

I would like to mention the warm support of Prof. Benard Nienhuis, who initiated the work described in Chapter 9. I am very grateful for the fruitful discussions with Profs. J. Cardy, J.M.J. van Leeuwen, and H.W.F. Knops.

I would like to thank Profs. Wenan Guo and Zhanru Yang at Beijing Normal University for introducing me to Prof. Henk Blöte, and to thank Xiaofeng Qian for our collaborations.

Because of the kindness of my colleagues at the Computational Physics Group and the Theoretical Physics Group, my stay in Delft has been very pleasant. In particular, I am indebted to Prof. Simon de Leeuw for his kindness and willingness to help during my search for a new position. I thank Robert Huang Foen Chung for his friendship. I would like to mention Vitaly Kalikmanov, Ovidiu Iancu, Flavius Gligor, Jaap Flohil, Frans Berwald, and Wouter Wetzels.

Often, I received encouragements and help from the people in Delft Chinese Community. In particular, I benefit from Dr. Jianghua Chen both in the scientific research and the social life. I would like to mention Shunli Shang, Jianrong Gao, Haixiang Lin, Jie Han, Jian Cao, Guijie Wang, Rongchao Li, Bingyan Wang, Bing Zhang, Qiang Xu, Ye Zhang, Yasheng Ma, and their families. Most Dutch people I have met are very kind to me. I would like to express my gratitude to Anke Blöte, Jacob Browser, Gerdine, and their families.

I received indispensable help from my friends in China. I am especially indebted to Shuimu Zheng, Wenyong Wang, Jiapan Yang, Xinmei Qian, and Yuzhi Liao for their kindness and willingness to help whenever my family and I have difficulties. I would like to mention Wenhao Deng, Peng Zhang, and Chengbin Zhang in China, Limei Xu in USA, and Jianqiao Hu and Meng Zhan in Singapore.

From September 1st 2004, I will take a postdoctoral position in the group of Prof. Dr. Amarante Böttger. I appreciate the kindness and patience of Amarante Böttger who allows me to finish this thesis.

My gratitude also goes to my parents, brothers, and sisters, who have been a continuing support to me. The most credits, however, should go to the dearest person in my life, Haili Jing. Without her incredible patience, this thesis could never have been done. Recently, we have experienced a new joy from our daughter, Anne Deng, who was born on May 20 2004.

This research was supported by the Dutch FOM foundation (“Stichting voor Fundamenteel Onderzoek

der Materie”) which is financially supported by the NWO (‘Nederlandse Organisatie voor Wetenschappelijk Onderzoek’)

Youjin Deng

Curriculum Vitae

Curriculum Vitae

Youjin Deng
27 April 1974, Fujian, P.R. China

- 1992 – 1997 Beijing Normal University
 Theoretical Physics
 Bachelor degree
- 1997 – 2000 Beijing Normal University
 Nonlinearity in immune systems
 Master of Science
- 2000 – 2004 Delft University of Technology
 Critical phenomena and development of novel algorithms
 PhD degree
- 2004 – Delft University of Technology
 Computational material science
 Postdoctoral position